THÈSE

En vue de l'obtention du

DOCTORAT DE L'UNIVERSITÉ DE TOULOUSE

Délivré par l'Université Toulouse 3 - Paul Sabatier

Présentée et soutenue par

Yachao ZHU

Le 19 novembre 2020

Chemical Engineering of 2D materials for electrochemical energy storage

---

Ecole doctorale : **SDM - SCIENCES DE LA MATIERE - Toulouse**

Spécialité : **Sciences et Génie des Matériaux**

Unité de recherche :
CIRIMAT - Centre Interuniversitaire de Recherche et d'Ingénierie des Matériaux

Thèse dirigée par
Patrice SIMON et Frédéric FAVIER

Jury
M. Mathieu MORCRETTE, Rapporteur
Mme Sophie CASSAIGNON, Rapporteure
Mme Deborah JONES, Examinatrice
Mme Katia FAJERWERG, Examinatrice
M. Christophe LETHIEN, Examinateur
M. Patrice SIMON, Directeur de thèse
M. Frédéric FAVIER, Co-directeur de thèse

Acknowledgments

First of all, I would like to express my gratitude to all those who helped me during the writing of this thesis. I am deeply grateful to Frédéric Favier, my co-supervisor, for his constant motivation, understanding, surpporting and guidance. Thanks for his invaluable expertise in the formulatio of the research topic and methodology in particular. Without his consistent and illuminating instruction, this theis could not have reached its present form. Thanks also to Olivier Fontaine, who has the right scientific attitude and the substance of a genius. His passion and adventure on scientific researches will be always instructive in my future work. Thanks also to Steven Le Vot, who always has a great insight into the research. He is very patient with people and helps me figure out the research questions. Thanks to Khalil Rajoua, who always helped me prepare the sample for characterizations. Thanks to Charlotte Bodin and Pierre Lannelongue, who helped me prepare the electrode and show me the usage of facilities. Thanks to Chandra Sekhar Bongu for the regular discussion about the scientific fundemantal knowledge. Thanks to Halima Tounkara, who really helped me to solve my French questions in my life. I would like to thank for the happy days with all co-workers in AIME, who are Rahma Hachicha, Mathieu Deschanels, Leonard Thommy and Catherine Andreux for their helps in my life and research in Montpellier.

I would like to express my appreciation to my supervisor Professor Patrice Simon for offering me the precious opportunity to work in France, and his specialized knowledge, worthy advice and useful comments on my research. I also thanks to the group members in Toulouse, who are Dr. Pierre-Louise Taberna, Ms. Barbara Daffos, Zifeng Lin, Yinghui Liu, Hui Shao, Jiang lin Ye, Huan Yin, Liyuan Liu, Itchy Wu and Xue Bai.

I would like to state my gratitude to China Scholarship Council (CSC, NO: 201606240097), for the financial surpport from September 2016 to September 2020, without which, all this would not have been possible.

Thanks to the technical assistance from my colleagues in UM2, who are Dr. Bernard Fraisse (XRD), David Bourgogne and Ruiz Josemarie (Raman), Didier Cot and Bertrand Rebiere (SEM), Franck Godiard (TEM) and (TGA).

Last but not the least, I would like to thank all my friends in China and Europe for giving me constant support and encouragement when I got stucked. I warmly thank my family and my girlfriend for loving and surpporting me.

Contents

General abstract

The long-term massive consuming of fossil fuel has induced serious issues, which are energy shortage, environmental pollution, greenhouse gases and a series of other negative effects. The solution to restrict the aftermath is to develop renewable energy sources and devices or technologies. Supercapacitors (SC) have been a promising energy storage device due to the attractive merits complementing those of batteries, which expose short longevity and low power density. Many factors can determine the electrochemical performance of supercapacitors. For example, the properties of electrode materials can lead to distinct charge storage mechanisms. The varieties of electrolyte cause electrochemical ions reactions at/in the electrodes. To optimize the SC device, the electrode materials must be designed with the applicable structures and coupled with suitable electrolytes to facilitate the electron transport and ions diffusion. In this thesis, we initially focused on the preparation, construction and modification of 2D MnO_2-based materials, in which a hydrothermal-method for the preparation of δ typed MnO_2 was proceeded and then modified by introduction of copper ions. The resultant sample, which exposes more active sites, coupling with the intercalated copper cations, boosts the specific capacitance performance for the prepared electrodes. As well, the growth mechanism of 2D δ-MnO_2 was studied by adjusting the reaction time, revealing an architecture development process while the obtained electrodes all show an enhanced cycling stability during upon charge-discharge processes. However, the intrinsic drawbacks of manganese dioxide, such as low conductivity and ions diffusion, resulted in such a poor capacitance. Whereupon, we introduced the battery-type layered double hydroxide (LDH). As expected, cyclability was fairly limited because of the intrinsic flaws of LDH structures but a high capacity was measured on account of the involved redox reactions. By implementing a delamination operation before mixing with MnO_2 powder composite based on LDH layers

wrapping MnO_2 particles was synthesized. As electrode material, it showed a high capacity like LDH but also kept a good cycling stability like MnO_2 in supercapacitors. However, the contribution to the capacitance performance of δ-MnO_2 was. To overcome this limit, we employed and exerted the inherent property of MXene as the substrate to boost the conductivity of MnO_2, therefore generating a composite, in which MnO_2 was embedding MXene layers. Thanks to the synergistic effects, the resulting MnO_2eMXene composite showed an enhanced capacitance and attractive rate capability accompanying with fair cycling stability. Additionally, exfoliated 2D titanium carbide (Ti_3C_2)/MXene is known to suffer the restacking issues after the usual filtration process, thus impeding the ions to connect the inner active sites. Hence, we carried out a templated procedure to produce both expanded MXene and MXene foam. The MXene with expanded interlayers provides more available space for ion transport/diffusion towards active sites, thus improving the capability of charge storage. The MXene foam showing a 3D porous framework offers not only an increased interlayer space but also macropores in through the layers to facilitate the ions diffusion/transport and access to more active sites, leading to the upgraded capacitance performance for supercapacitors.

We also studied carbon-based materials as the electrodes for supercapacitors. Initially, the graphene oxide was reduced, after filtration, then obtaining a dark graphene film. As the electrode, the freestanding graphene film has a good capacitive performance including capacitance, rate capability and lifespan. Operated with a hydrogel, with an expanded porous framework, it exhibits upgraded performance that depended on the temperature at which self-supported graphene films were prepared Furthermore, we coupled MXene with graphene to form a freestanding composite film. It was found that the composite shows a decreased capacitance, but still keeps a great rate capability.

In the end, capacitive carbon cloth were incorporated with battery-like organic salts, aiming to explore new electrochemical behaviors, for supercapacitor-battery hybrid devices. Generally, 3D carbon cloth displays electrical double-layer electrochemical kinetics, which restricts the energy density because of limited accessible area. Hence, to break this barrier, battery-like redox reactions, from organic salts absorbed at carbon cloth surface, contributes to promote the capacitance/ty performance. However, the drawback of poor life-span was imported as well from organic molecules. When coating the modified carbon cloth with MXene layers, it strongly improves the stability and the customized cracks among MXene created a favorable path for ions diffusion, thereby boosting the capacitance and showing the improved cycling performance.

Chapter 1 Introduction

Energy has been an essential and key element of development in the modern world.[1] The consuming of energy in Figure 1.1 (phones, laptops and power tools) in modern society is constantly increasing, and urgently the current energy system market cannot satisfy the consumption of demand. The primary energy supply is still on the dominant position (see Figure 1.2), and leads to sustained detrimental pollution of the environment. The worse situation is that traditional energy storage systems cannot effectively use the energy power, also aggravating the bad pollution problems. Thus, new and eco-friendly energy-storage devices are urgently needed to solve this puzzle. Electrical energy storage devices, such as batteries and supercapacitors (SC), have been among the popular candidates because of the attractive properties, low carbon dioxide emissions, good power density and energy density.

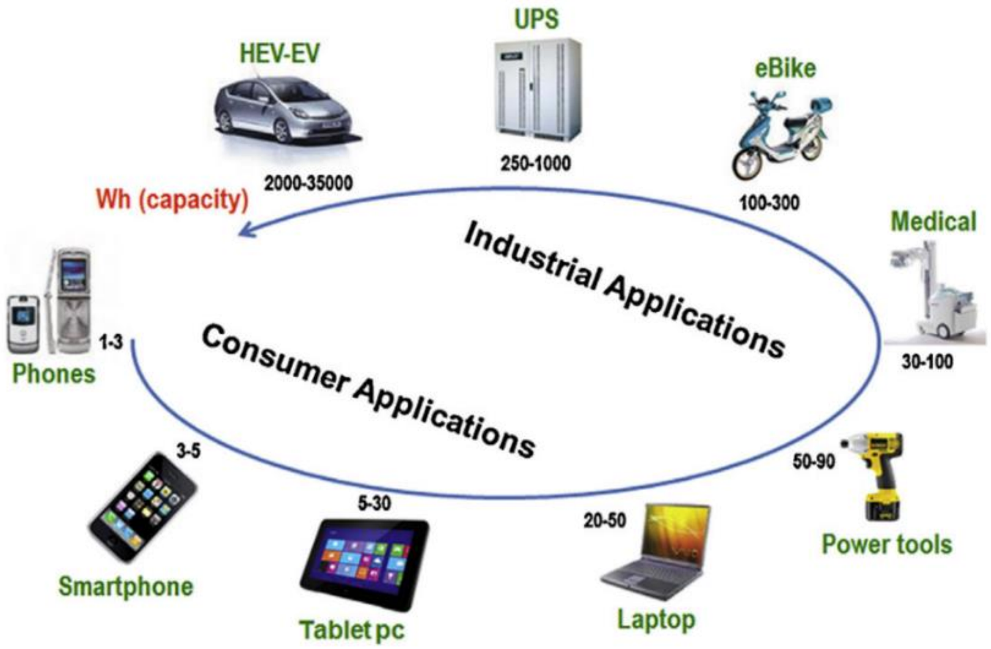

Figure 1.1 The energy consuming in a broad range of applications.[2]

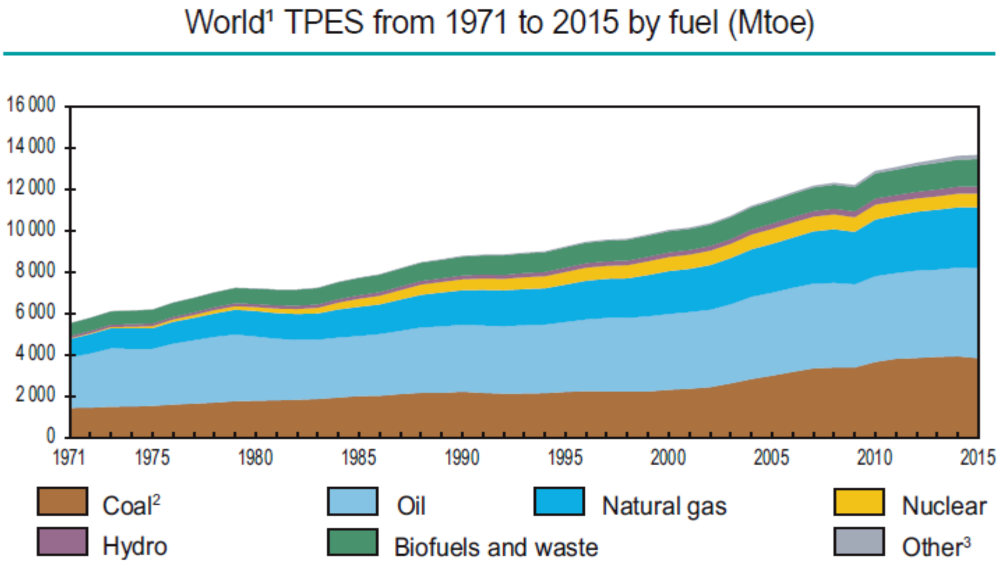

Figure 1.2 World total primary energy supply (TPES) by fuel.[3]

Supercapacitors (SCs), also called electrochemical capacitors, have been studied for many years. Compared with batteries, SCs deliver advantages of fast recharging or discharging (in seconds or less), long-term cycle stability and high-power density. The history of SCs was started by H.I. Becher, who established the early supercapacitor device in 1957. Then Robert A. Rightmire declared the patent for the SCs invention and D. Boos transformed the concept into technology. Afterwards, the new pages are spread by researchers all over the world and some significant related adventures are depicted in Figure 1.3. However, the prevailing SCs is also undergoing some flaws. In the light of the classic Ragone plot (see Figure 1.4), the energy density of SC is lower than batteries, which has hindered and limited the development of SC devices. One of the solution to improve the energy density is to find improved electrode materials for SCs. Superior electrode materials are able to provide a larger potential window and greater capacitance value, thus resulting in gaining greater energy density. So far, many electrode materials have been studied, such as carbon-based materials, oxides, hydroxides, and polymers. And various dimensional materials, from 1D to 3D, have been smartly designed or engineered as electrodes to be applied in SCs.

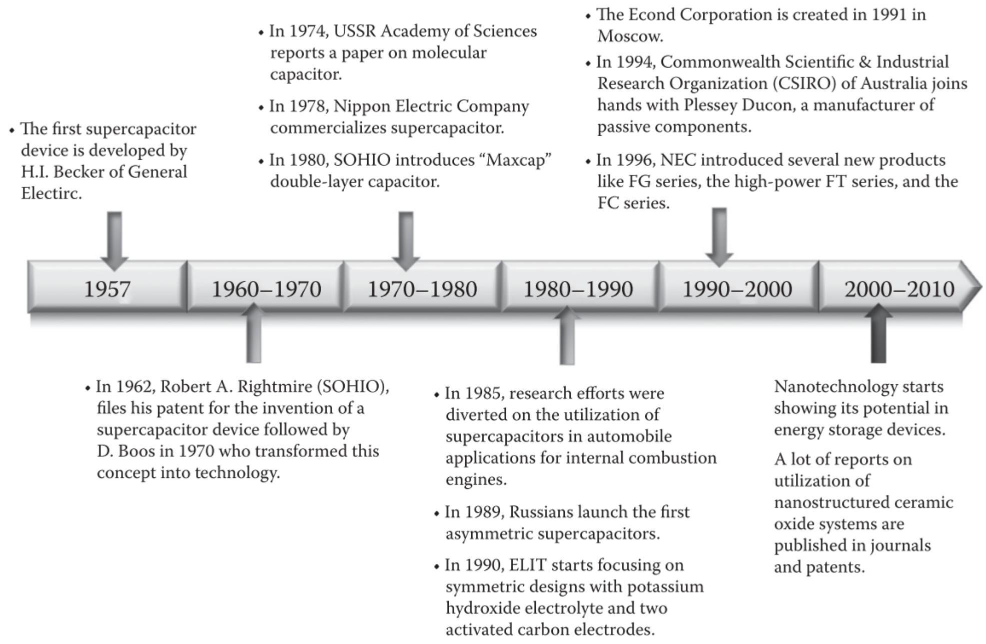

- The first supercapacitor device is developed by H.I. Becker of General Electirc.

- In 1962, Robert A. Rightmire (SOHIO), files his patent for the invention of a supercapacitor device followed by D. Boos in 1970 who transformed this concept into technology.

- In 1974, USSR Academy of Sciences reports a paper on molecular capacitor.
- In 1978, Nippon Electric Company commercializes supercapacitor.
- In 1980, SOHIO introduces "Maxcap" double-layer capacitor.

- In 1985, research efforts were diverted on the utilization of supercapacitors in automobile applications for internal combustion engines.
- In 1989, Russians launch the first asymmetric supercapacitors.
- In 1990, ELIT starts focusing on symmetric designs with potassium hydroxide electrolyte and two activated carbon electrodes.

- The Econd Corporation is created in 1991 in Moscow.
- In 1994, Commonwealth Scientific & Industrial Research Organization (CSIRO) of Australia joins hands with Plessey Ducon, a manufacturer of passive components.
- In 1996, NEC introduced several new products like FG series, the high-power FT series, and the FC series.

Nanotechnology starts showing its potential in energy storage devices.

A lot of reports on utilization of nanostructured ceramic oxide systems are published in journals and patents.

Figure 1.3 Timeline showing the important phases in supercapacitor development.[4]

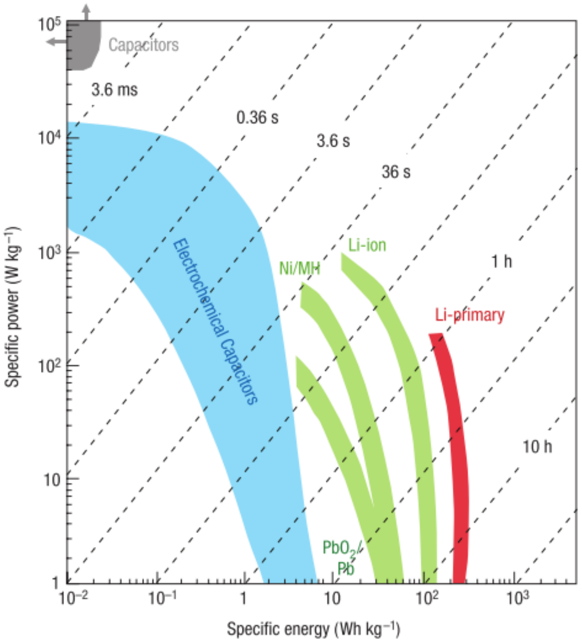

Figure 1.4 Ragone plot (specific power against specific energy) of various electrical energy storage devices.[5]

1.1 Energy storage mechanisms

Supercapacitors and batteries, as advanced technical devices, show different electrochemical energy-storage mechanisms, which lead to different charge-storage properties.[5] In Batteries, lithium ions are first intercalated and accompanied with redox reaction in the bulk electrode materials. Due to slow diffusion-controlled intercalation and phase change, batteries have a high energy density but need slower current rates and longer recharge time. For SCs, generally, there are two concepts of capacitor. In the light of charge-storage mechanisms, one is electrical double-layer capacitors (termed EDLCs), which are charged by electrochemical double layer effect at material surface (Figure 1.5 A and B), where the ions adsorption is reversible, and the other one is pseudocapacitors, which are charged by fast surface redox reactions (Figure 1.5 C), or following rapid sub-surface intercalation processes (Figure 1.5 D).[6] The detailed mechanism difference (phase change, redox reaction, intercalation…) between batteries and supercapacitors are shown in Figure 1.6.

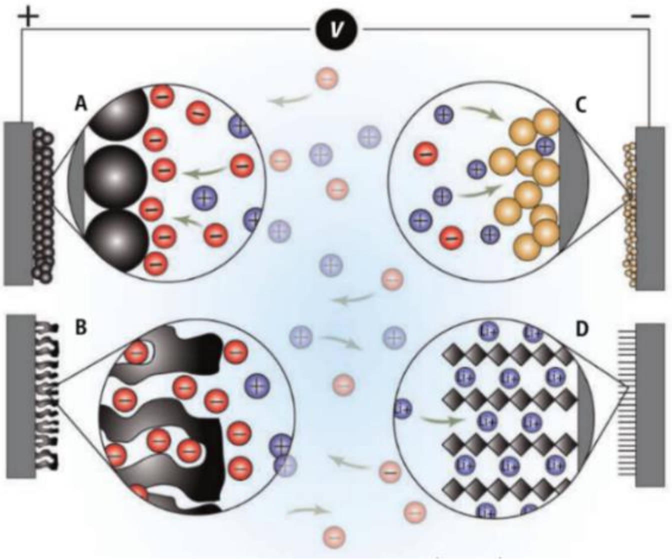

Figure 1.5 Schematic diagram of different mechanism of energy storage.[6]

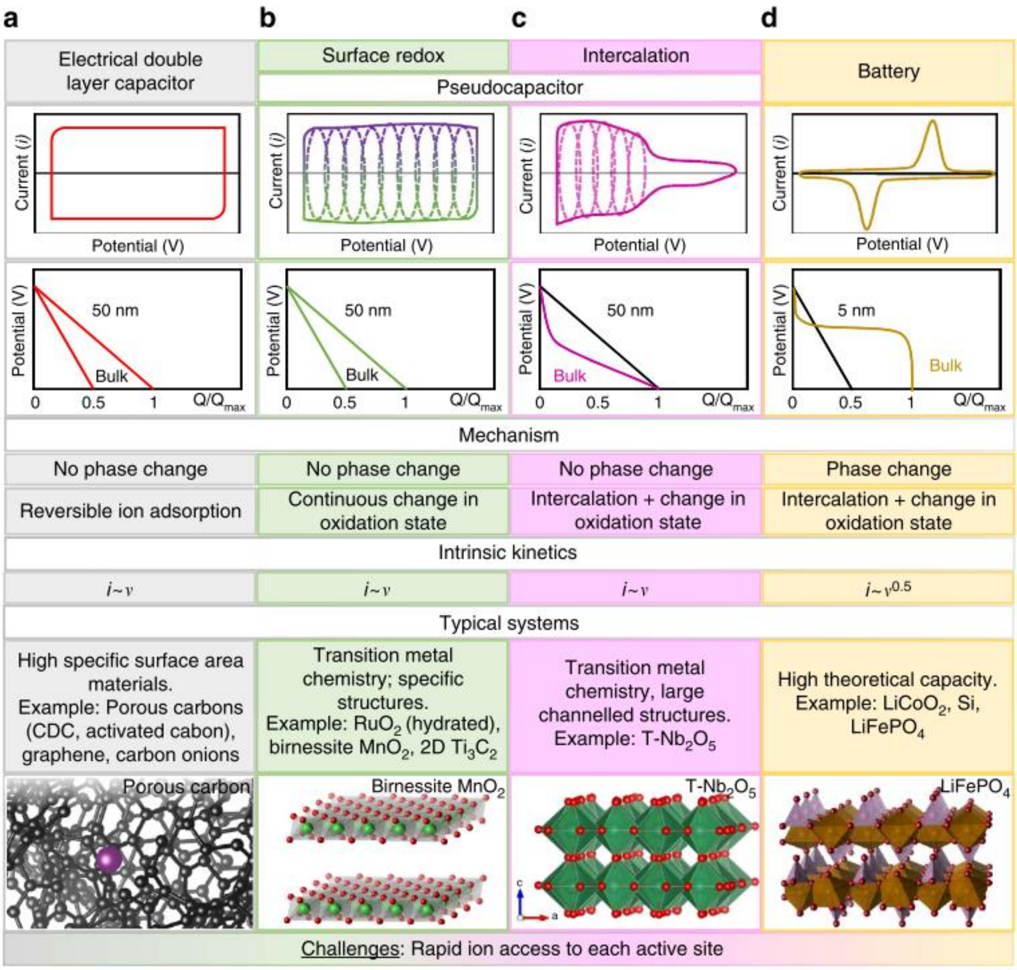

Figure 1.6 Faradaic and capacitive energy storage.[7]

1.1.1 EDLCs

The electrical double layered models imply a strong involvement of the electrode/electrolyte interface, including electrochemical adsorption/desorption of cations and anions at the interface (Figure 1.7). For the Helmholtz model, the polarization of electrode surface induces the separation and diffusion of ions through the electrolyte, thus leading to a structured condensed charge layer, which is called electrical double layers (EDLs). Here is the defined equation of Helmholtz' layer in electrical capacitors:

$$C_H = \varepsilon_0 \cdot \varepsilon_r \cdot S/d \qquad (1)$$

Where ε_0 is the vacuum permittivity, ε_r is the relative permittivity of the dielectric electrolyte, S is the specific surface area of the electrode, and d is the effective thickness of the double layer. Because of ion diffusion in solution and interaction between the dipole moment of the solvent and the electrode, Gouy and Chapman presented the diffusion layer model of EDLs, which is shown in Figure 7(b). Because of the limitation of the Gouy-Chapman model in highly charged double layers, Stern united Helmholtz with Gouy-Chapman models, in Figure 1.7c, presenting the accumulation of ions close to electrode surface (inner layer) and the hydrodynamic motion of ionic species in the diffuse layer (outer layer). However, it is not properly expected that the current carbon-based electrode materials work with the same mechanism in supercapacitors. For instance, carbon nanomaterials have structural and chemical irregularities on the surface, at which the electroactive species are adsorbed by chemical interaction.[8]

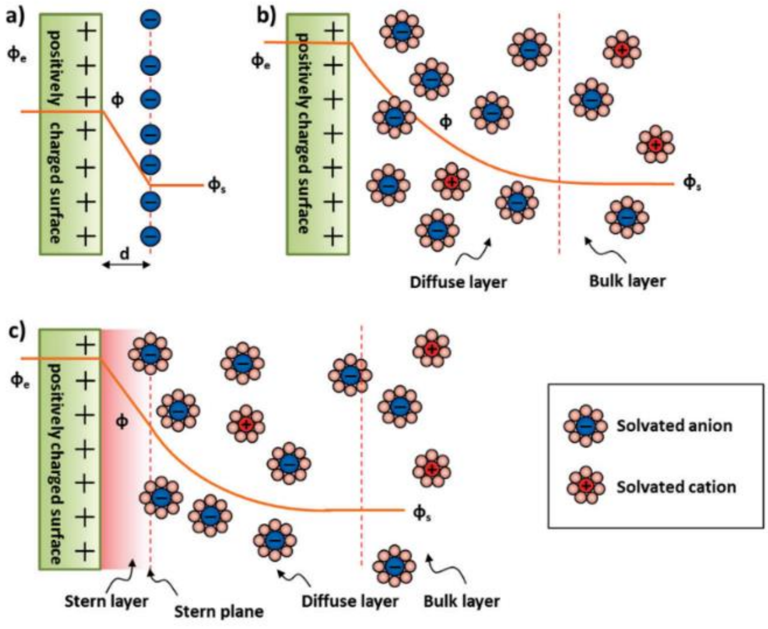

Figure 1.7 The evolution of electrical double-layer model of (a) Helmholtz, (b) Gouy-Chapman and (c) Stern.[9]

1.1.2 Pseudocapacitors

Depending on double layer charging rule, EDLCs are limited by their specific surface area. Furthermore, the furnished active sites in EDLCs are not easily exposed at the surface. In battery electrodes, the deep active sites are accessible within the lattice structure, thus resulting in the diffusion-controlled situation and delaying the charging time[10]. Pseudocapacitors, with the similar active sites like batteries, can store energy via the fast and reversible redox reaction of metal ions on the surface or in the bulk near the surface of a solid electrode, accompanying by the charge across the double layer[11]. Although the electrochemical energy-storage process is similar to batteries, the clear difference is that pseudocapacitors behavior is not controlled by ion diffusion within the crystalline structure of active material.[11] In theory, the kinetic difference can be distinguished by cyclic voltammetric analysis according to this equation[12,13]:

$$i = av^b \tag{2}$$

where i is the current (A), v is the scan rate (mV s^{-1}), a and b are adjustable parameters. When the b value is 0.5, it implies a battery' behavior with a diffusion controlled faradic intercalation process. In contrast, the capacitive behavior without diffusion control can be recognized by the proportional correlation between current and scan rate. In the case of b value equal to 0.5, the correlation between current and sweep rate can be represented as follows[14]:

$$i = nFAC^*D^{1/2}v^{1/2}(\alpha nF/RT)^{1/2}\pi^{1/2}\chi(bt) \tag{3}$$

in which n stands for the number of electrons involved in the electrode reaction; F is the Faraday constant; A is the surface area; C^* stands for the surface concentration; D stands for the chemical diffusion coefficient;α stands for the transfer coefficient; R is the molar gas constant; T is the temperature, and the function (bt) is the normalized current. In another case of b value equaling to 1, the relationship can be described as[15]:

$$i = C_d A \nu \tag{4}$$

where C_d stands for the capacitance and A represents the surface area. Besides, the CV and galvanostatic charge-discharge measurements can exhibit the apparent difference of capacitive/battery' behavior. In the Figure 1.6, it shows a rectangle shape for electric double layer capacitor or that with a small redox peak for pseudocapacitor in cyclic voltammetry curves. For the batteries, it reveals the sharp redox peaks in CV curves and clear potential plateau in discharge process.

1.2 The construction of supercapacitor

Generally, energy storage device is basically composed of the connecting-feature electrolytes and two electrodes, which are separated by an ion-permeable separator. The separator is essentially a membrane that separates the electrons to prohibit the electronic conductance but enable the cross movement of electrolyte ions. Various separators are used in actual devices, such as polymer or paper separators for organic electrolytes, glass fiber separators for aqueous electrolytes. In addition, the current collector, like aluminum foil, platinum disk and nickel foam, is also an important component to support the electrode and conduct electric current to power sources or electrical appliances.[16] The specific constituted elements of supercapacitors are displayed in Figure 1.8.

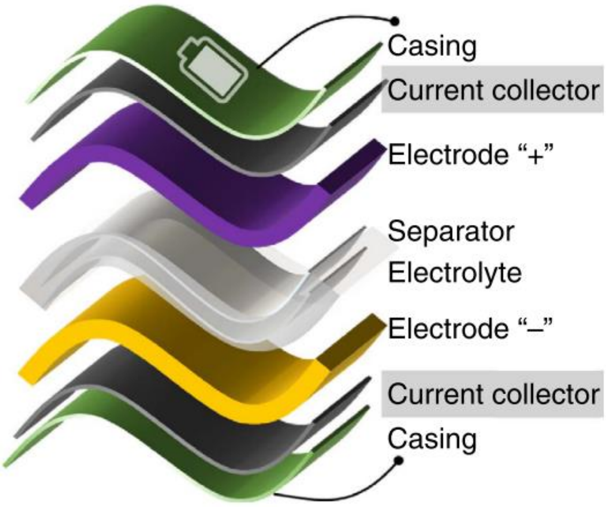

Figure 1.8 Components of typical energy storage device.[7]

1.3 The electrolyte

In nowadays electrolytes, a wide stable working-potential range is a very crucial factor for supercapacitors, which can then access toa high energy density. Generally, electrolytes are sort in three main categories: aqueous electrolytes, organic electrolytes and ionic liquid (ILs). The electrochemical stability window and the ionic conductivity are the two main criteria to select which electrolyte is applied in a device. Devices with aqueous electrolytes can benefit from a higher ionic concentration and lower resistance, therefore showing greater capacitance and power values in comparison with organic electrolytes. Furthermore, they are simpler to prepare, unlike organic electrolytes, which should be process in special condition (like glove box). However, the low-cost and environment-friendly aqueous electrolytes, like KOH, Na_2SO_4 and H_2SO_4, exhibit a narrow working temperature range, high corrosion activity and low discharge voltage, which is limited by the decomposition voltage of water at 1.23V. Breaking this limitation must be considered to increase the aqueous potential window.

1.4 Electrode materials

Electrode materials play a vital role in improving the property for supercapacitors and show the dominant factor on self-discharge, cycling life, capacitance, resistance, etc. The goal of researches on electrode materials is to develop a storage device that can possess high energy and power density, good rate capability and good cycling stability. In the past few years, many materials with various morphologies, structures, pore sizes, etc. have been developed and engineered for supercapacitor electrodes.

1.4.1 carbon-based materials

Among these materials, carbon-based materials prevail in EDLCs due to low price, good electronic conductivity, ease of preparation, and high specific surface area. Carbon-based materials, like porous carbons, carbon nanofibers and graphene, are considered as electrode materials for industrialization

1.4.1.1 Porous carbon

Porous carbons are usually fabricated via first carbonization at high/proper temperatures and then crafted by following post-treatment activation procedures, thereby showing the high porosity, large specific surface area and excellent adsorption capacity. To improve the capacitance, as straightforward strategy is to increase its accessible specific surface area (ASSA) on which the charged ions are physically absorbed. Additionally, many excellent works also focus on the developing/creating or adjusting the porosity, the implementation of defects, heteroatom or functional groups, and even together in carbon-based materials. For instance, Huang [17] prepared a three dimensional hierarchical porous carbon from the micro-sheets PPy reagent that were treated by improved KOH activation procedure. By adjusting the reaction temperature, the obtained porous carbons displayed the evolution of porous structure, shown in Figure 1.9. In the optimal sample, the enhanced porous carbon material exhibited a large specific surface area of 2870 m^2 g^{-1}, togetherwith a high N doping of 7.7 wt%. From these electrodes, a symmetric device, delivered a high specific capacitance (236 F g^{-1} at 2 A g^{-1}) and a remarkable cycling stability (98% after 10k cycles).

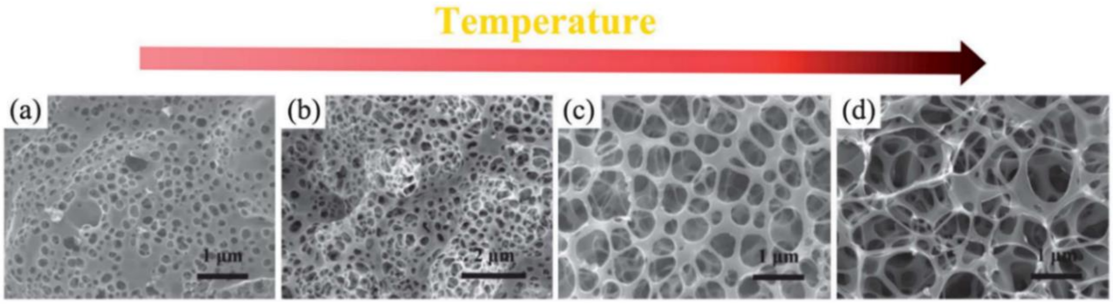

Figure 1.9 SEM images of porous carbon by annealing the slurry of PPy and KOH at various temperatures.[17]

Li[18] developed a graphene-like porous carbon from pretreated biomass, which was punched to generate holes by H_2O_2 reacting with oxidation functions on the surface with layers exfoliating process by using HAc (CH_3COO^-) (Figure 1.10). In details, H_2O_2 can oxidize the cellulose/hemi-cellulose to generate mesoporous structure and in the meantime the HAc partially hydrolyzed the cellulose/hemi-cellulose on the surface to delaminate layers. The elaborated carbon, with upgraded porosity and large surface area, displayed an improved specific capacitance of 340 F g^{-1} at 0.5 A g^{-1} and possessed a great specific energy of 23 Wh kg^{-1}, moreover, holding 98% of longevity after 10k charge-discharge cycles.

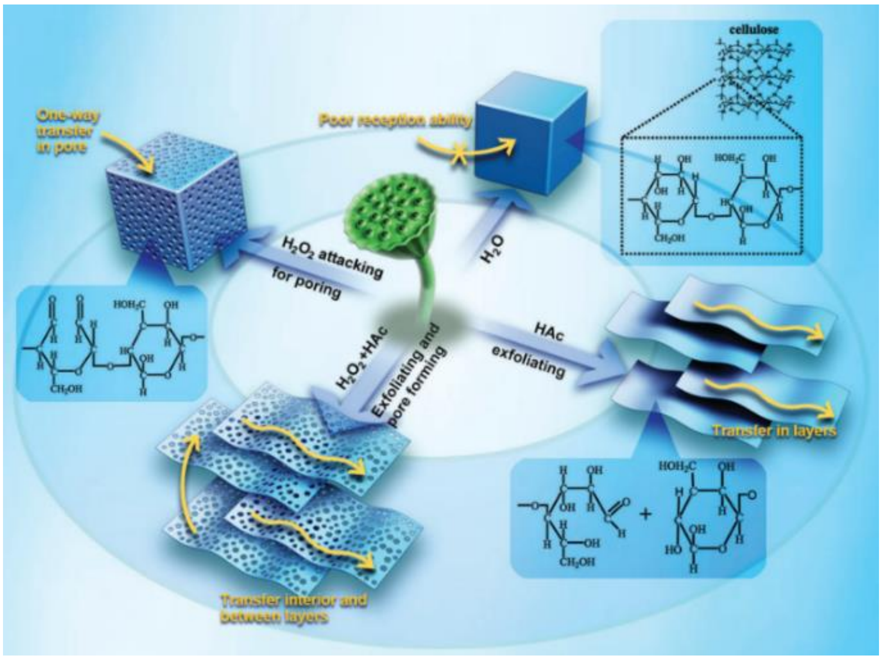

Figure 1.10 The synthesis and mechanism porous active carbon.[18]

In Zheng work[19], a nitrogen-doped and ultrathin nano-sheets porous carbon was reported and constructed via a nice scalable condensation polymerization and followed one-step carbonization/activation operation (Figure 1.11). Assembled with a large surface area (2406 m^2 g^{-1}) of porous carbon, the symmetric device delivered an amazing energy density of 139 Wh kg^{-1}. In addition, the porous carbon was applied in a flexible device, which presented a great volumetric energy (8.4 Wh L^{-1} at 24.9 W L^{-1}) and it could still keep 80% retention when the power density reached 20-fold of original value. Again, with the outstanding cycling life of 96% after 10k cycles, it showed this enhanced porous carbon as promising and prospective electrode for supercapacitiors.

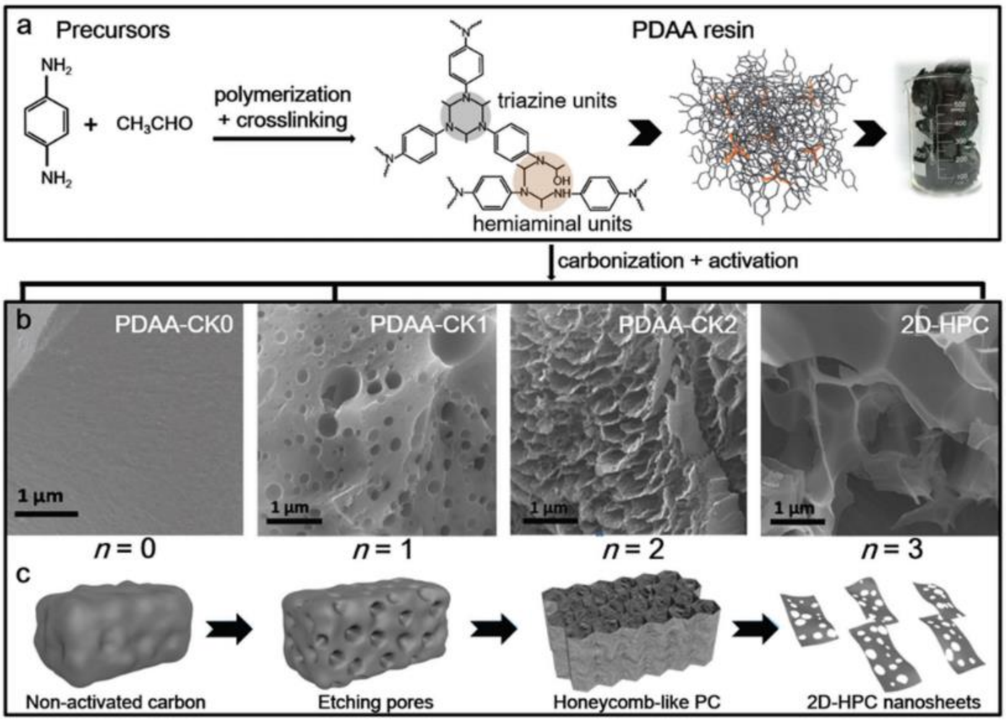

Figure 1.11 Synthesis of 2D hierarchical porous carbon nanosheets based on a one-step pyrolysis of 3D cross-linked polymeric framework. a) The condensation process that gives rise to the polymeric framework PDAA. b) Preparation of carbons from PDAA by carbonization and activation process with different ratios of KOH/PDAA. c) Schematic illustration showing the formation mechanism of samples.[19]

Interestingly, porous carbons can also be used to restrict the restacking for other layered materials. For example, Wang[20] intercalated/introduced a 2D ordered mesoporous carbon unit to rearrange the MXenes interlayer space, thereby solving the restacked issues of exfoliated MXenes layers and facilitating the ion diffusion and electron transfer at even high charge-discharge regimes (Figure 1.12).

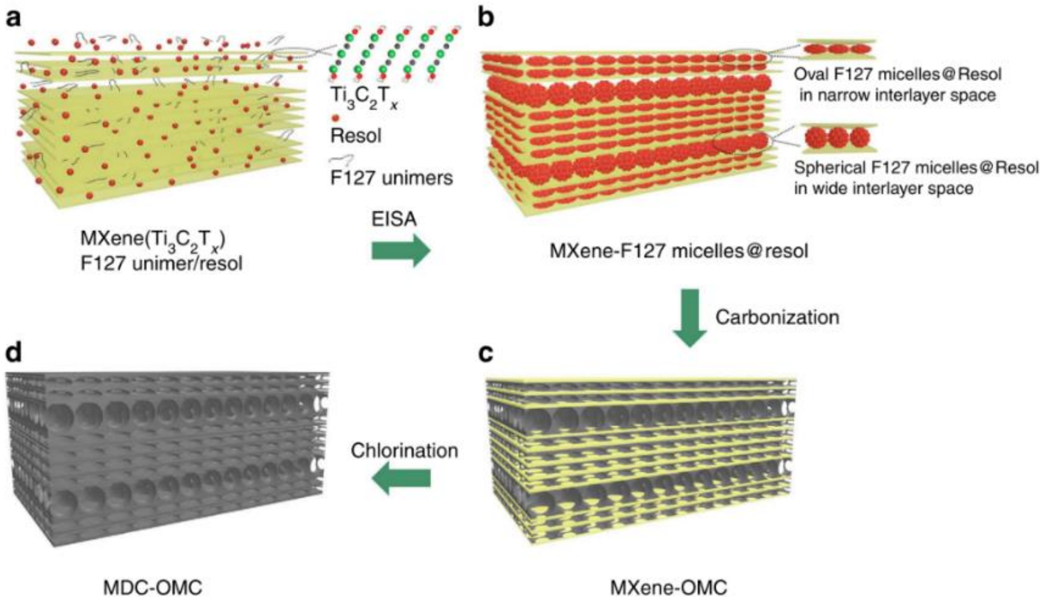

Figure 1.12 Schematic diagram of the porous carbon-based composite.[20]

Interestingly, the distinctive electrochemical mechanism in nanoporous carbon with high advanced capacitive performance triggered a deep exploration to understand/figure out the influence of the nanostructure on storage capabilities. Kaneko and colleagues[21] applied an X-ray scattering experiments with hybrid reverse Monte Carlo (HRMC) analysis to disclose the desolvation process when ionic liquids with matching sized are confined in carbon nanopores (Figure 1.13). They directly prove the role of a superionic state in ionic liquids on the electrochemical behavior. In the case of 1-nm-pore bilayer confinement, the counter ions almost all invades the coordination shell, therefore leading to the preservation of Coulombic ordering. In another case of 0.7-nm-pore monolayer confinement, the molecular-mechanism breaks the alternating array structure of cations and anions, which can lead to closer-distance co-ions because of the reduced Coulombic repulsion. Thanks to the inoperativeness of repulsive force between co-ions, a satisfactorily dense population of con-ions was observed, leading to a great improvement of the capacitance with nanoporous carbons with matching ionic liquids.

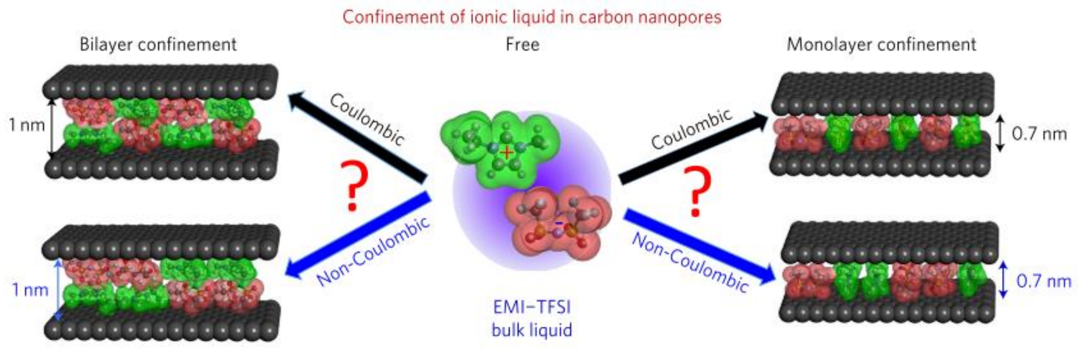

Figure 1.13 Conceptual images of the structure of EMI–TFSI confined inside carbon nanopores with or without Coulombic ordering.[21]

1.4.1.2 CNT

Many CNT-based electrode research works have been applied in supercapacitors. Particularly, the highly ordered carbon nanotube (CNT) presents a well-aligned unique structure, excellent conductivity, low mass density, etc., which endows itself preeminent electrical and electrochemical capabilities for supercapacitors.[22,23] Over the past decades, CNT has elicited many efforts to construct an improved electrode material that possesses the enhanced rate performance and energy density and eventually couple with various other pseudo-capacitive materials to develop an improved composites with high capacitance and long cycling lifetime.[24] Here are some examples to better understand this carbon material. Lee et al.[25] used a new technological gradient biscrolling way to fabricate CNT-based yarns allowing fast-ion-transport (Figure 1.14). Using a metal wire as the current collector, the ~20 µm diameter-upscalable yarns delivered ~179 F cm^{-3} volumetric capacitance and exhibited a linear capacitance increase with scan rates, even reaching up to 80 V s^{-1} with liquid electrolytes and 20 V s^{-1} with solid electrolytes. For a complete supercapacitor, 92% and 99% of cycling stability in 10k cycles were retained with winded and sewed electrodes, respectively. Therefore, this improved technology is a promising application in structuring yarn electrodes for micro-electronic devices.

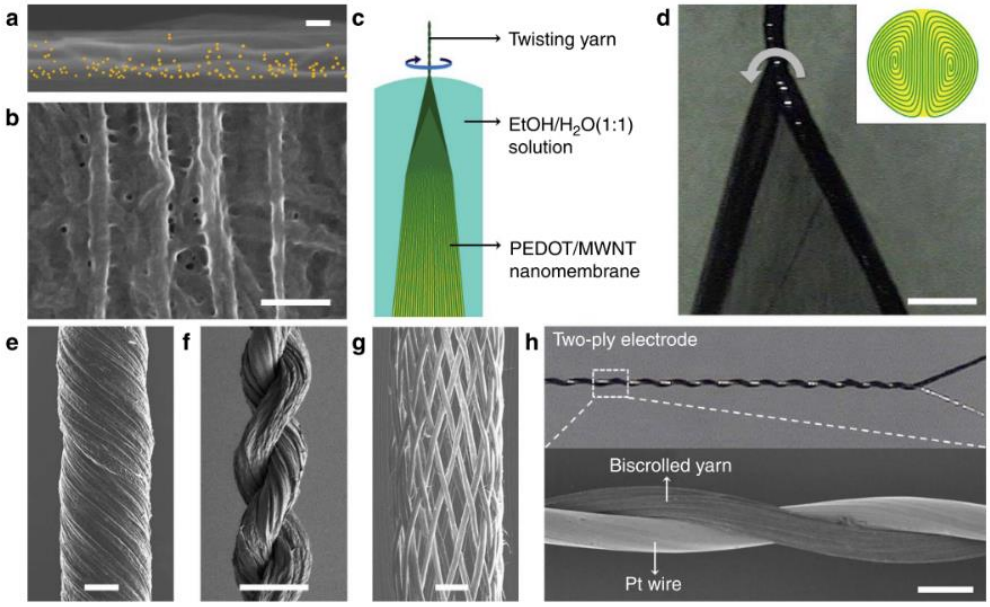

Figure 1.14 The biscrolling method, precursors and derived structures for PEDOT/MWNTyarns.[25]

Choi, et al.[26] reported a wearable yarn based on carbon nanotube –based, in which 90 wt% of pseudocapacitive MnO_2 nanoparticles are trapped by a biscrolling approach. (Figure 1.15) When the flexible and stretchable yarn with solid-state PVA/LiCl electrolyte was assembled and packaged, the fabricated supercapacitor device led to 889 mF cm^{-2} (155 F cm^{-3}) specific capacitance and 35.8 μW cm^{-2} (5.41 mWh cm^{-3}) energy density.

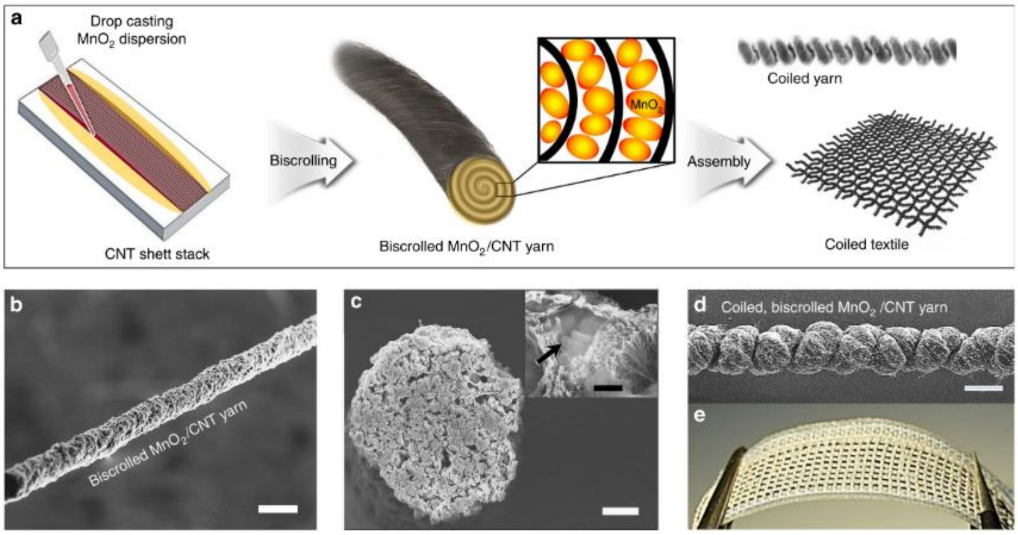

Figure 1.15 Fabrication scheme and images of biscrolled MnO_2/CNT supercapacitor.[26]

1.4.1.3 Graphene

Graphene[27], a two dimensional and hexagonal-lattice carbon monolayer[28], has engaged enormous researches and applications in many fields, ranging from electronic devices[29], biosensors, catalysts[30], DNA sequencing, aerospace, batteries[31], full/solar cells, supercapacitors[32] and other energy-storage applications[33], since Andre Geim and Konstantin Novoselov delaminated a single-atom-thick layered carbon in 2004[34]. Thanks to the unique honeycomb-like structure, it leads to the excellent physical/chemical properties, such as an impressive specific surface area, high electronic conductivity, good chemical and thermal stability and outstanding mechanical flexibility[35,36,37]. Generally, graphene is prepared by many methods, such as mechanical exfoliation, reduction of graphene oxide, liquid-phase exfoliation and so on, which are quite important for the physical/chemical properties in the applications. The summary of production methods is depicted in Figure 1.16. Here, we focus on the defective reduced graphene oxide, which is reduced from graphene oxide with oxygen-containing functional groups by chemical, thermal and electrochemical processes. The graphene oxide is effortlessly coupled with other materials to construct/design enhanced composites because of the exiting of functionalities. Just like the Figure 1.17 showing, the active materials can be carefully encapsulated in graphene network, wrapped between the layers, anchored on the sheets, or trapped like a sandwich.

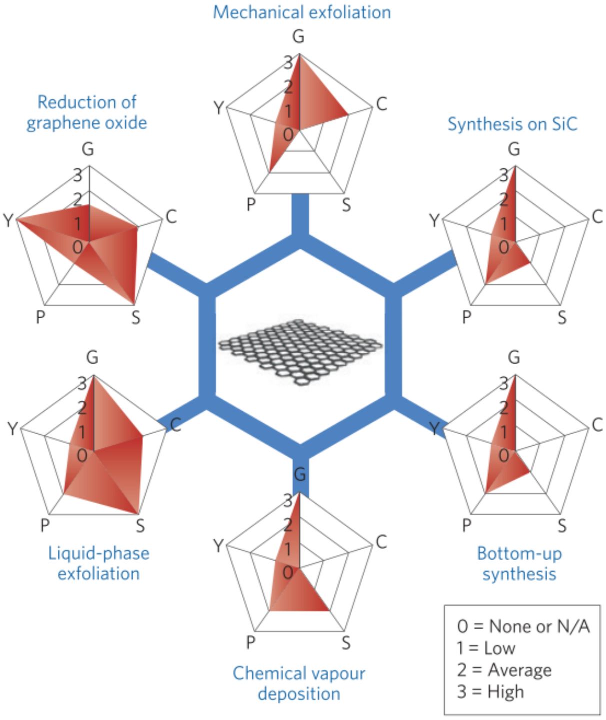

Figure 1.16 Schematic of the most common graphene production methods.[28]

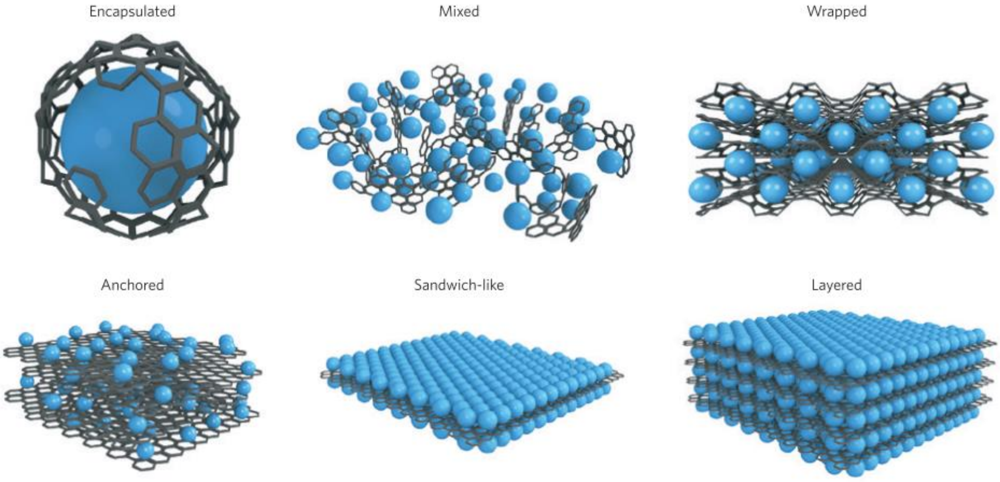

Figure 1.17 Schematic of the different structures of graphene composite electrode materials.[28]

Depending on the talented/versatile skills, numerous and remarkable graphene –based works have been developed for supercapacitors. For example, Kaner, et al.[38] reported a smooth all-solid-state method, in which the graphene oxide was reduced to unstacked graphene films by the laser from a DVD drive (Figure 1.18). The resulting graphene film, with a high conductivity (1738 S m^{-1}) and an attractive surface area (1520 m^2 g^{-1}), as an electrode without binders and the current collector. The fabricated symmetric device presented an excellent energy density in aqueous electrolytes, organic electrolytes and ionic liquids, accompanying a high power density (Figure 1.19). The elegant simple manufacturing method using laser-scribed graphene films provides a promising route towards commercial applications for flexible electronics.

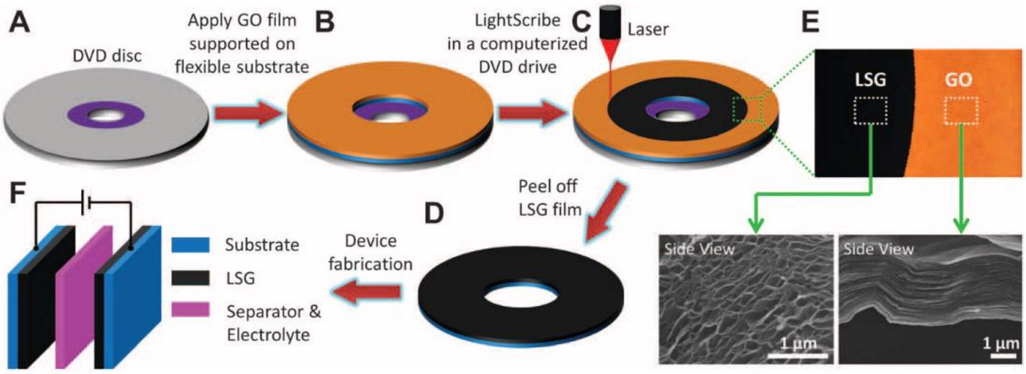

Figure 1.18 Schematic illustration of the fabrication of laser-scribed graphene-based device.[38]

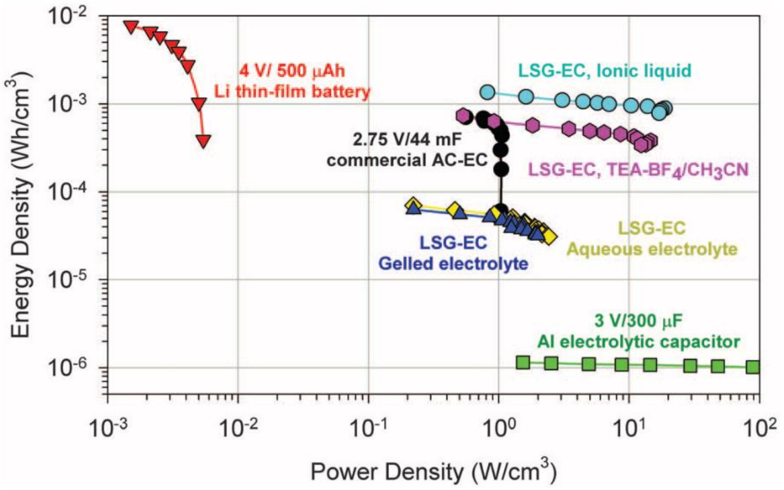

Figure 1.19 Energy and power densities of graphene-based device compared with commercially available AC-EC, aluminum electrolytic capacitors, and a lithium thin-film battery.[38]

Lee and colleagues[39] developed a simple filtration approach to prepare a flexible RGO/MnO_2 paper material without using any template. The obtained freestanding paper can keep its robust shape when it was bent in many ways (Figure 1.20). Thanks to the flexibility of prepared electrode material, the bent asymmetric supercapacitor device exhibited 35.1 μWh cm^{-2} areal energy at 37.5 μW cm^{-2} areal power and display 3.8 mW cm^{-2} areal power (calculated at 1000 mA g^{-1} current density) at 11.5 μWh cm^{-2} areal energy. (Figure 1.21)

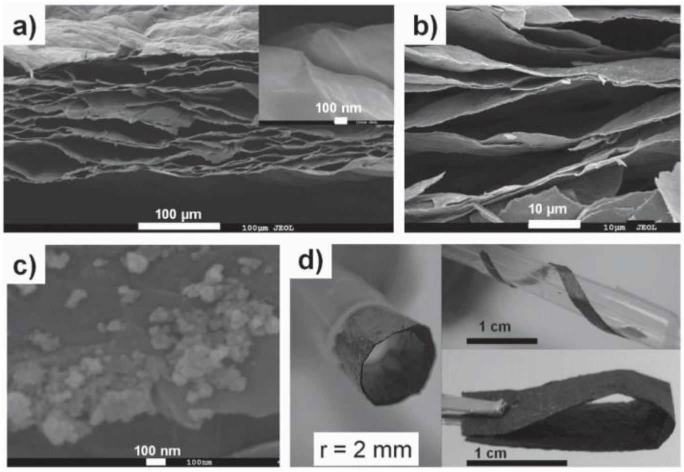

Figure 1.20 Morphology images of RGO/MnO_2 freestanding paper material.[39]

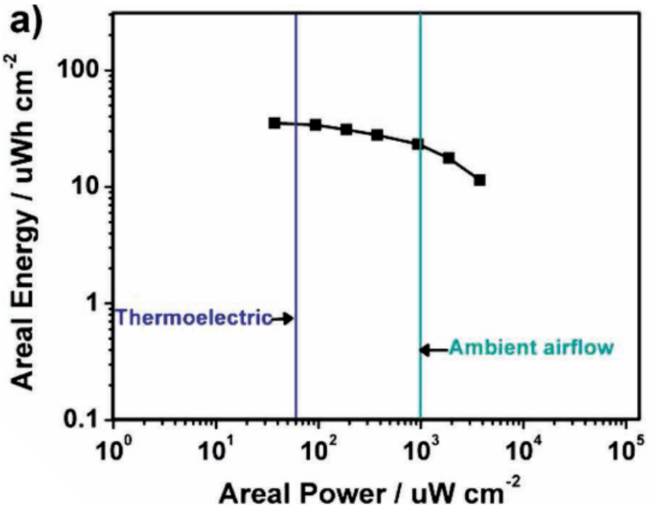

Figure 1.21 Areal performance in a bent asymmetric device.[39]

A pipe mold method is reported (Figure 1.22) and applied to build a flexible and conductive (4700 S m^{-1}) hollow RGO/conducting polymer composite fibers, which can be shaped into knots, rolled up and woven into textiles (Figure 1. 23). As an electrode with poly(vinyl alcohol) PVA/H_3PO_4 gel electrolytes in a symmetric device, it showed an areal capacitance of 304.5 mF cm^{-2} at 0.08 mA cm^{-2}, in the meantime, delivering an excellent 27.1 μWh cm^{-2} energy at 66.5 μW cm^{-2} power densities. Interestingly, the cycling stability after bending 500 times was 96% of the initial capacitance value.

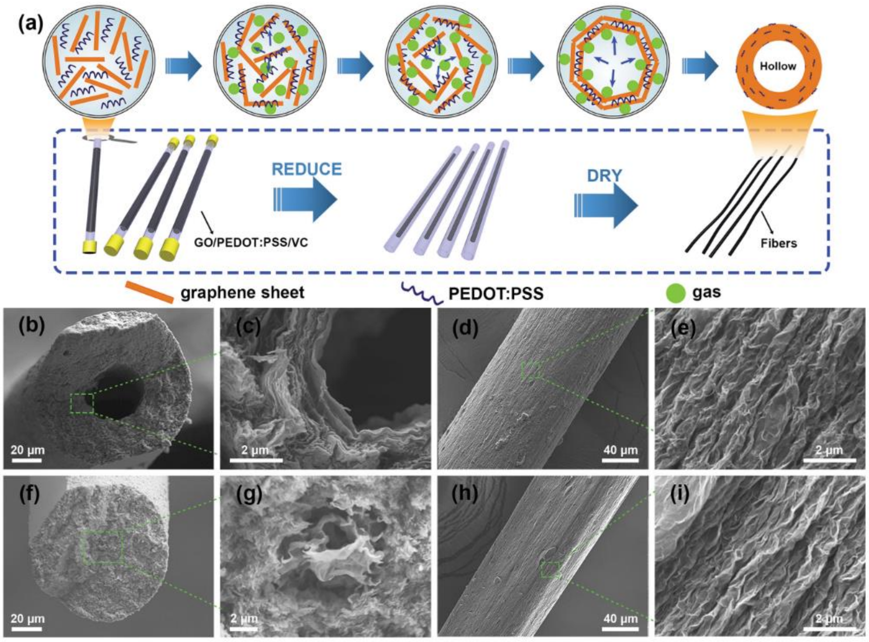

Figure 1.22 Schematic formation and SEM images of Hollow Graphene/Conducting Polymer Fiber Electrode.

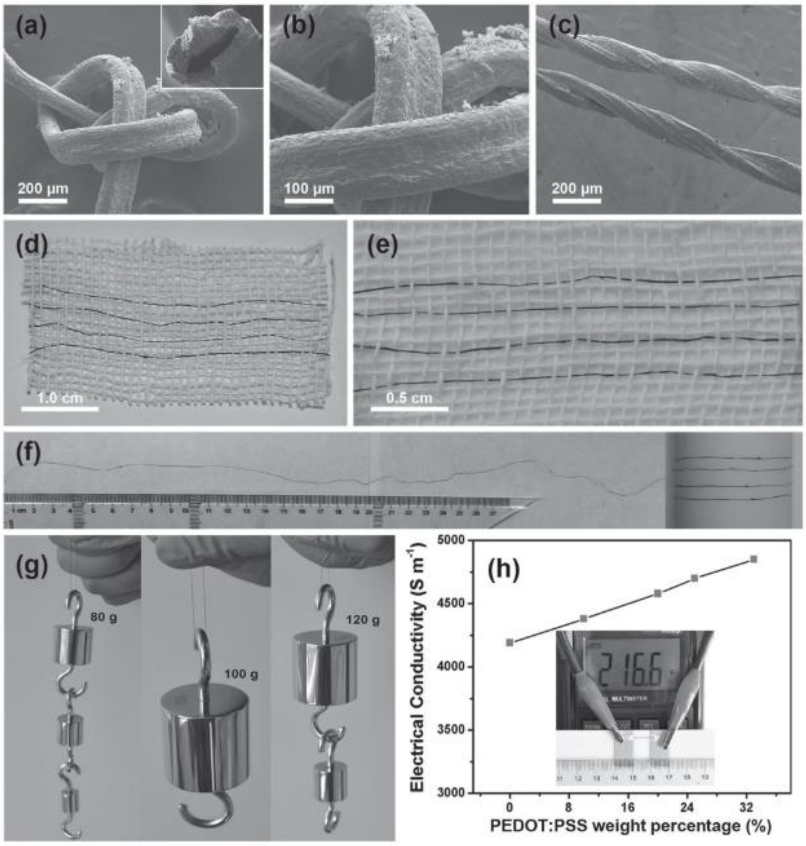

Figure 1.23 Mechanical and electronic properties of Hollow Graphene/Conducting Polymer Fiber Electrode.

1.4.2 Pseudocapacitive materials

In the carbon –based materials, as underlined above, charges are stored in the double layer that is limited by the electrolyte accessible surface area. As a result, the energy density lower than in batteries. Inspiringly, the Faradaic charge-transfer behavior of ruthenium oxide (RuO_2)[40] paved the new path and provided a novel and fundamental understanding for pseudocapacitive mechanism in supercapacitors. During the energy storage process, the ruthenium can fast store charges by redox reactions on the surface.[10] However, the cost of ruthenium oxide limits its development in practical applications.[41] Consequently, more economic pseudocapacitive materials are needed. Since these primary works, more pseudocapacitive materials have been disclosed, such as MnO_2-based materials, specific nanosized transition metal oxides (like Co_3O_4), conductive polymers, and transition metal carbides/nitrides and so on. In this thesis, we concentrate on the construction of 2D pseudocapacitive materials.

1.4.2.1 2D δ-MnO_2

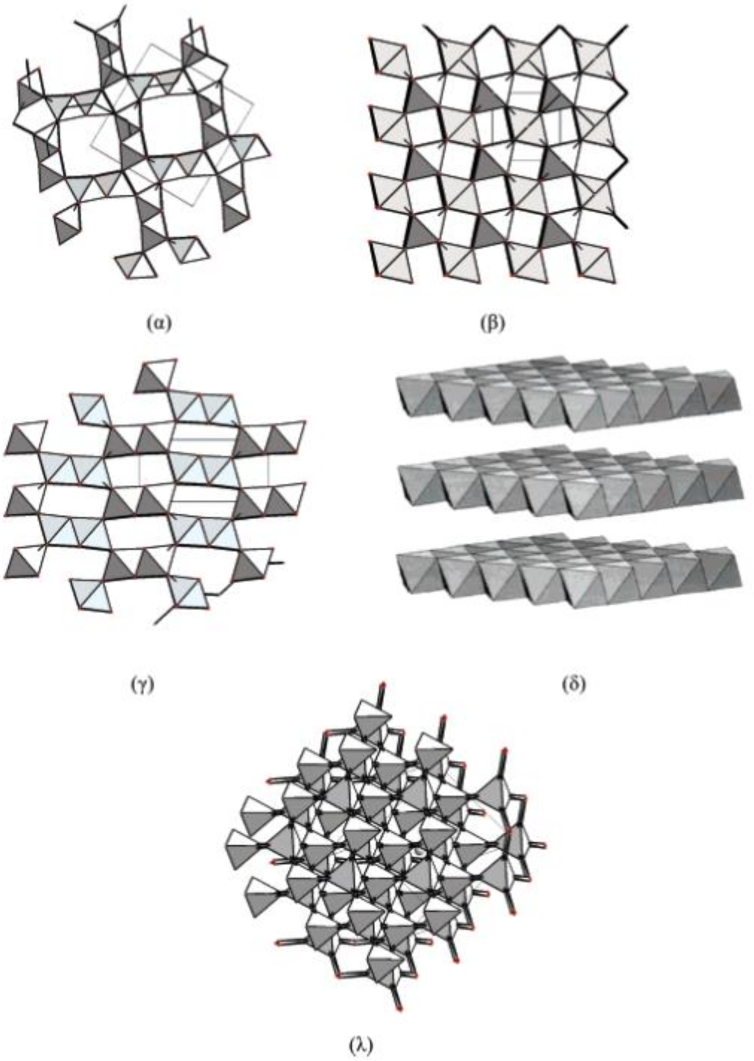

Figure 1.24 Crystallographic structures of α-MnO_2, β-MnO_2, γ-MnO_2, δ-MnO_2, and λ-MnO_2.[42]

Since the initial pseudocapacitive research of MnO_2 was investigated in potassium chloride (KCl) electrolytes by Lee and Goodenough[43], enormous progress has been achieved in MnO_2 –based materials, disclosing a Faradaic reactions between the III and IV oxidation states of Mn ions. And there are various polymorphic forms built on different ways to arrange MnO_6 octahedra They include α-MnO_2, β-MnO_2, γ-MnO_2 showing an 1D channel, δ-MnO_2

possessing 2D layers and spinel having 3D interconnecting channels (see Figure 1.24).[42] In Figure 1.25, various crystallographic structures lead to different ionic conductivities, with a strong correlation with the capacitance performance.[7] Thanks to the planar two-dimensional crystalline structure, the δ-MnO_2 has attracted much attention and been widely applied in designing a performing supercapacitive device for energy storage. Additionally, the abundant and environmentally friendly δ-phase MnO_2 can theoretically deliver up to 1370 F g^{-1} of capacitance over a voltage window of 0.8 V[44]. The charge storage involves a surface Faradaic reaction: $\mathrm{MnO_2 + C^+ + e^- \leftrightarrow MnOOC}$, where C is the electrolytic cation (H^+, Li^+, Na^+ or K^+)[45]. A clear understanding of the charge storage mechanism is needed for a better construction for MnO_2-based electrode materials. Various techniques are applied to evaluate structural changes during electrochemical processes occurring during charge and discharge, such as in situ Raman spectroscopy[46], X-ray photoelectron spectroscopy[47] and X-ray absorption spectroscopy (XAS)[48].

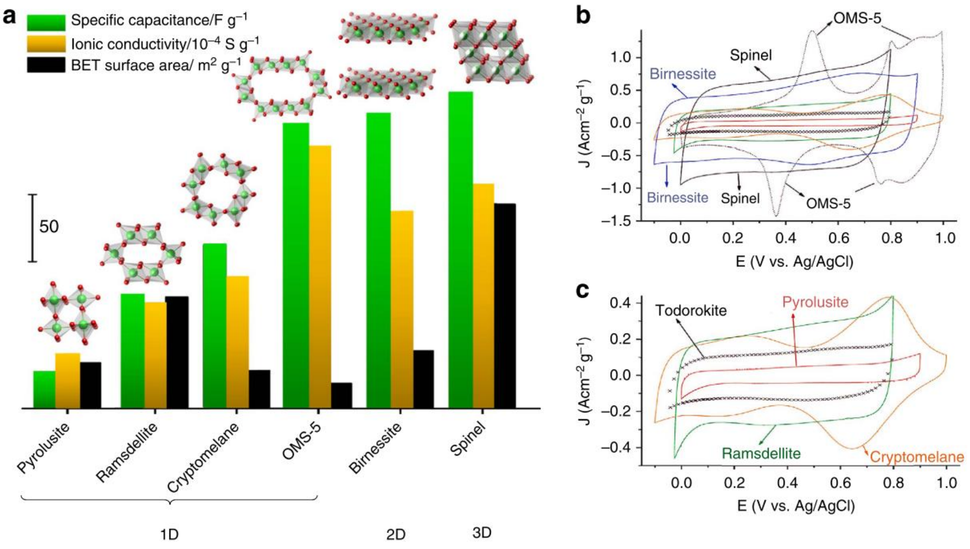

Figure 1.25 Capacitance of various crystallographic forms.[7]

Chen et al. first probed the structure changes via in situ Raman spectroscopy when the model 2D MnO_2 was cycling in 2M $NaNO_3$ electrolytes, finding that the smaller Na^+ cations replaced the larger water molecules between the parallel layers from 0.7V to 0V, which results in the shrinkage of the interlayer spacing because of the less steric hindrance and enhanced electrostatic attractions. In addition, the intercalation/extraction of sodium cations is a reversible process occurring during reduction/oxidation. Furthermore, when other electrolytes were studied using the same procedure, a clear difference in band evolutions was displayed. A 0 V, the band positions were shown to depend on the nature of electrolytes, with the position of v_1 band in correlation with d-spacing and v_2 band position in correlation with d-spacing. The comparison of $I(v_1)/I(v_2)$ values demonstrated the effect of the cation size on charge density and polarizability of the vibrational modes. Because of the influence of the cation size on the Jahn-Teller distortion, the band width is largest in KNO_3 and smallest in $LiNO_3$. Therefore, the in-situ Raman spectroscopy can deliver a direct and clear feedback between interlayer structure and cation size, providing a deep understanding of charge storage mechanism in pseudocapacitive two-dimensional MnO_2.

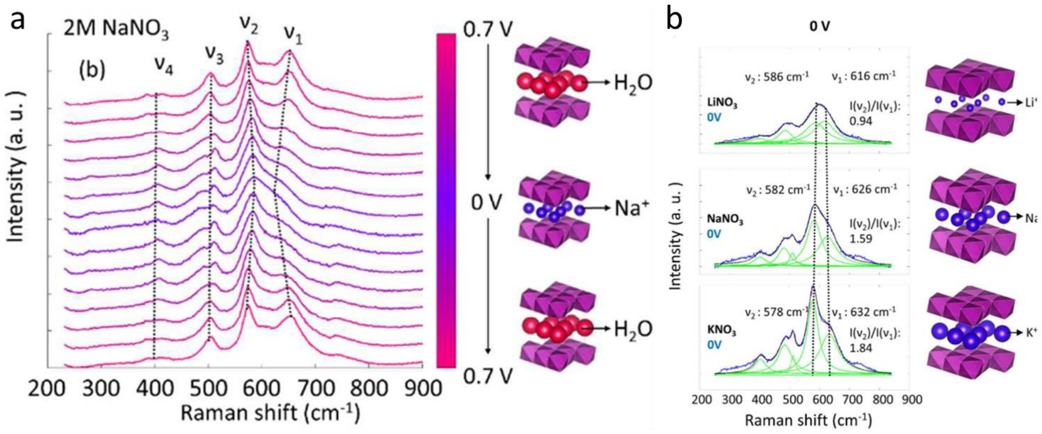

Figure 1.26 (a) The Raman spectroscopic evolution of MnO_2 film in 2M $NaNO_3$ electrolytes.[49] (b) Raman spectra of MnO_2 electrode at the potential 0 V. v_1 represents the symmetric stretching vibration (Mn-O) of MnO_6 groups and v_2 represents the (Mn-O) stretching in the basal plane of MnO_6 sheet.[49]

Chang et al.[50] prepared three composites (MnO_2/C-CNT, MnO_2/RGO, and MnO_2/ RGO-Au) with different charge/discharge behaviors (rate capability, stability) (Figure 1.27a). Then, atomic/electronic structure was studied and elucidated by in situ XAS at Mn K-edge measurement. In Figure 1.27 b, the intensity of pre-peak increased when the MnO_2/C-CNT electrode was charged (0-0.8V), which can be explained by the increase in density of Mn 3d unoccupied states. However, a different irreversible effect in MnO_2/RGO and MnO_2/RGO-Au was observed: gradual increase was first observed at 0.8V and it kept increase tendency at 0.4V. This variation can be explained by the different structures shown in Figure 1.27 a. For MnO_2/C-CNT composite, MnO_2 is deposited into the interior of the C-CNT network and some particles are isolated and not incorporated with C-CNT, while MnO_2 is strongly coated on the outer surfaces of RGO/RGO-Au substrates. It causes narrower tunnels of MnO_2/C-CNT and larger tunnels of MnO_2/RGO-based materials are implied in the charge-discharge process. Therefore MnO_2/RGO-based materials can withstand a larger volume changes without breaking chemical bonds during the electrochemical procedure. The quantified oxidation state of Mn versus energy position at set-up voltages is shown in Figure 1.27c. It implies a low electrochemical involvement of Mn active sites in MnO_2/C-CNT (66%) and MnO_2/RGO (34%). Accordingly, the thin surface layer includes three parts, which are an active MnO_2 redox layer, an inactive MnO_2 layer and a CNT/RGO layer. In light of the low mobilization ratio, plus the less sensitive electrochemical property in MnO_2/RGO, proposing that the double-layer capacitive not pseudocapacitive behavior at 0.4V is the dominant contribution for supercapacitors, meantime any cations are not deintercalated from the interlayer space and the peak intensity keeps constant.

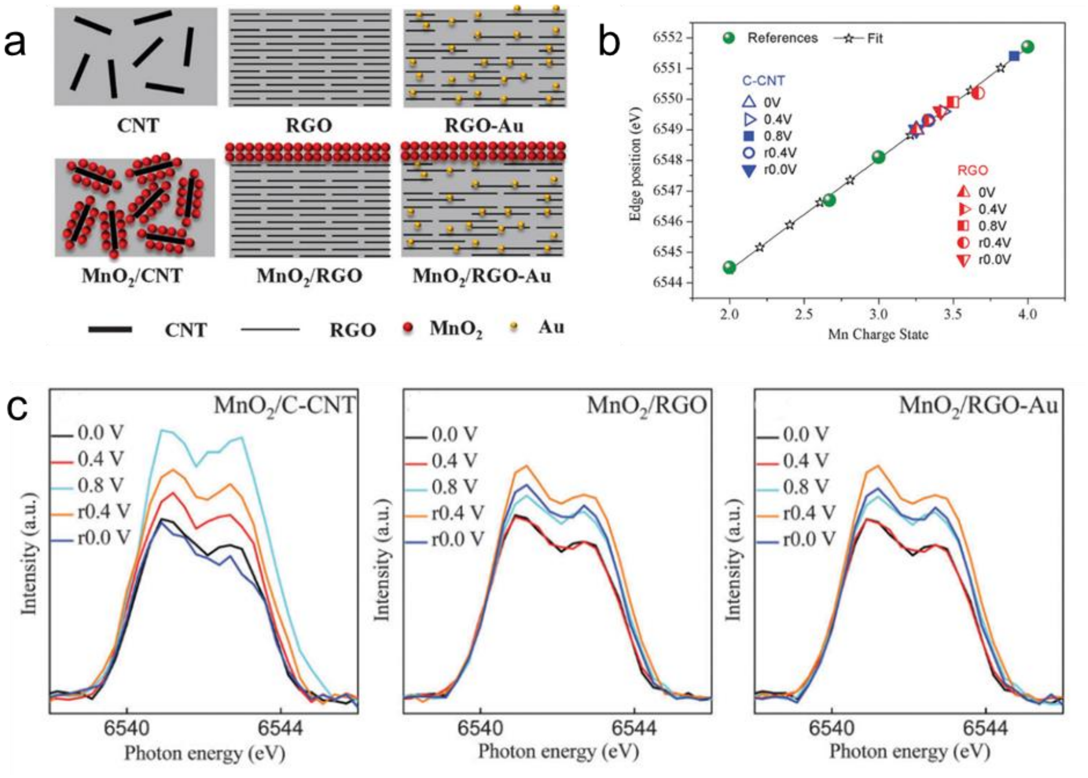

Figure 1.27 (a) Structure Schematic of MnO_2/C-CNT, MnO_2/RGO, and MnO_2/ RGO-Au. (b) Pre-edge region of Mn K-edge XAS of samples at various potentials. (c) Oxidation states of Mn at various applied bias potentials during the redox reaction.[50]

On the other hand, MnO_2–based electrode materials have also received many efforts to improve the limited electrical conductivity and mechanical property These include the incorporation of other metal elements, depositing the MnO_2 layer on conductive material framework and designing MnO_2-polymer composites. Liu et al.[51] reported a nano MnO_2(<2 nm) powder coated on mesoporous carbon fibers (termed PCF@MnO_2, Figure 1.28a), which have a high mass loading (reaching 7 mg cm^{-2}) and great fast charge transfer because of the mesc a ·ous framework. The electrochemical properties of PCF@MnO_2 are displayed in the radar chart, showing a 1148 F g^{-1} of gravimetric capacitance and 3141 mF cm^{-2} of areal capacitance. Again, compared with the performance presented in Figure 1.28c, the capability of PCF@MnO_2

surpasses other previously reported MnO_2-based electrode materials. This construction and synthesis method is adaptable to design other materials for supercapacitors.

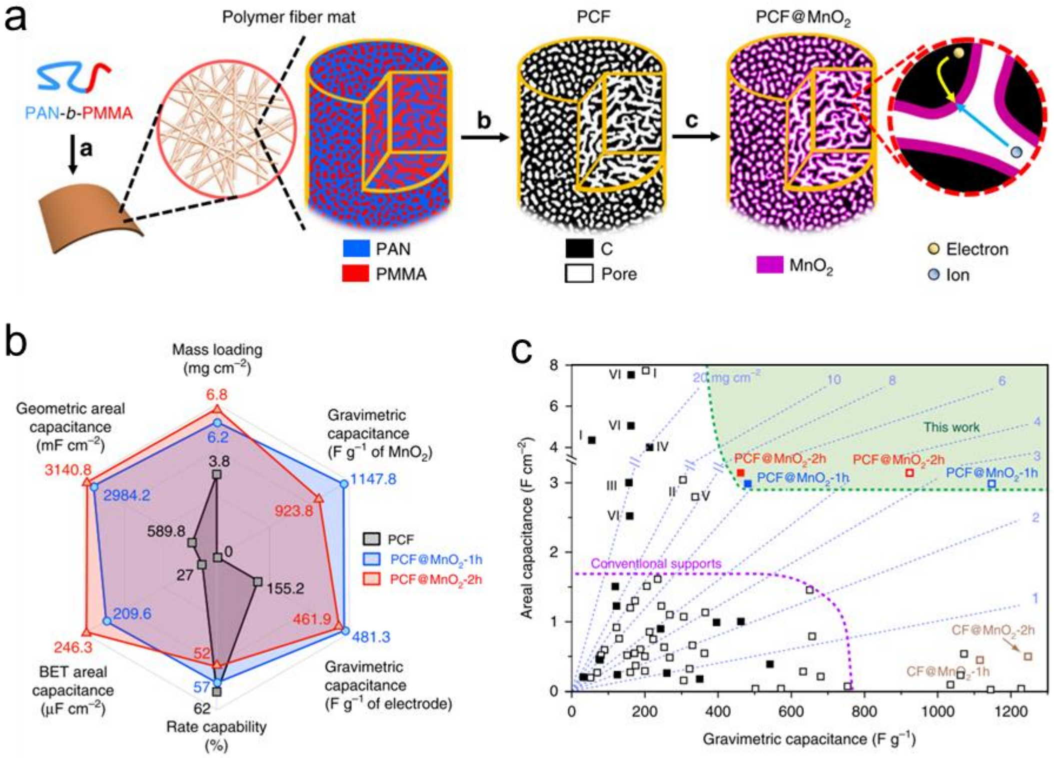

Figure 1.28 (a) Schematic illustration of the synthesis process. (b) The radar chart compares the six figure-of-merits. (c) Mass loading, gravimetric capacitance, and geometric areal capacitance of PCF-based electrodes in comparison with other reported electrodes.[51]

1.4.2.2 MXenes

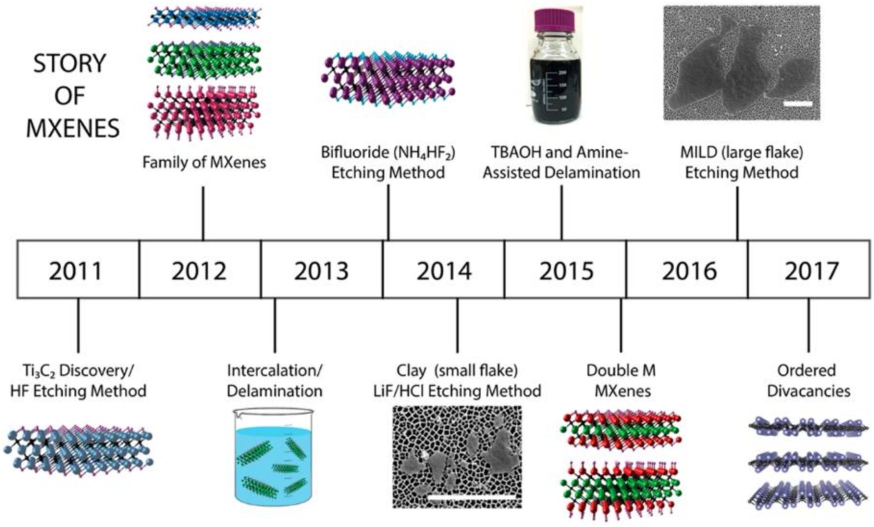

Figure 1.29 Timeline of MXene: from 2011 to 2017.[52]

Two-dimensional transition metal carbides, nitrides and carbonitrides, termed MXenes (M represents transition metals and X represents carbon/nitrogen or both), were discovered in 2011. They show a metallic conductivity ($\sim$6000−8000 S cm^{-1}) and an hydrophilic property.[53] In the original MAX phase from which they derive, A is an element layer like aluminum, which is selectively etched. The timeline of related MXene evolution is shown in Figure 1.29.[52] There are many ways to prepare MXenes exhibiting different properties, such as flake sizes, qualities, or different termination groups. They can be applied in diverse fields, especially energy storage. Numerous MXene -based materials, such as intercalated MXenes, porous MXenes, actived MXenes and MXenes-graphene/carbon fiber/polymer/MnO_2 composite, have been schemed, structured and applied in supercapacitors. Here, we clarify some works about the mechanism of charge storage in MXenes. Wen and colleagues[54] reported the distinct features of cyclic voltammetry curves in H_2SO_4 and KOH electrolytes: capacitance value is greater in acidic electrolytes. Moreover, the rectangular shape can be maintained at high scan rates in KOH rather than H_2SO_4 electrolytes. This can be explained by the different diffusion properties of electrolytic cations. The result of ab initio molecular dynamics (AIMD) simulations are shown in Figure 1.30 and 1.31, and the summary is displayed in table1. It is consistent that water can reduce the activation barriers for hydrated protons/K^+, therefore boosting the 3D movements of ions between the interlayer space. The distinction is that the K+ is located on one side of interlayer space, while the active sites on both sides can accommodate H and H1 (two opposite sides pointing to each other, see Figure 1.31a). As a result, the higher electrolyte concentration offers the MXenes in hydrated H^+ to deliver a greater capacitance. However, the case of H2 with lower proton concentration, which is located on one side, is activated only at the high scan rates, thus leading to the distortion of the corresponding CV curves. Based on the mechanism investigation and discussion, the specific hopping route of ion diffusion between interlayers helps not only to improve the capacitance but also to maintain the capability for MXene-based supercapacitors.

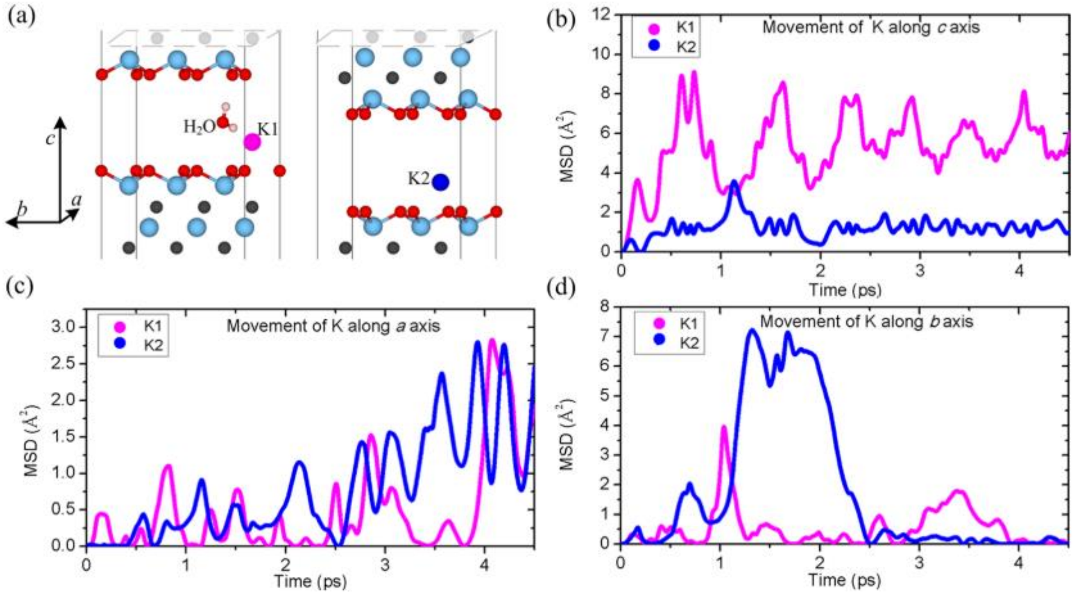

Figure 1.30 Structural configurations of K in the water-containing and water-empty units denoted by K1 and K2 (a) and MSD of K projected along the *c* (b), *a* (c), and *b* (d) axes, respectively.[54]

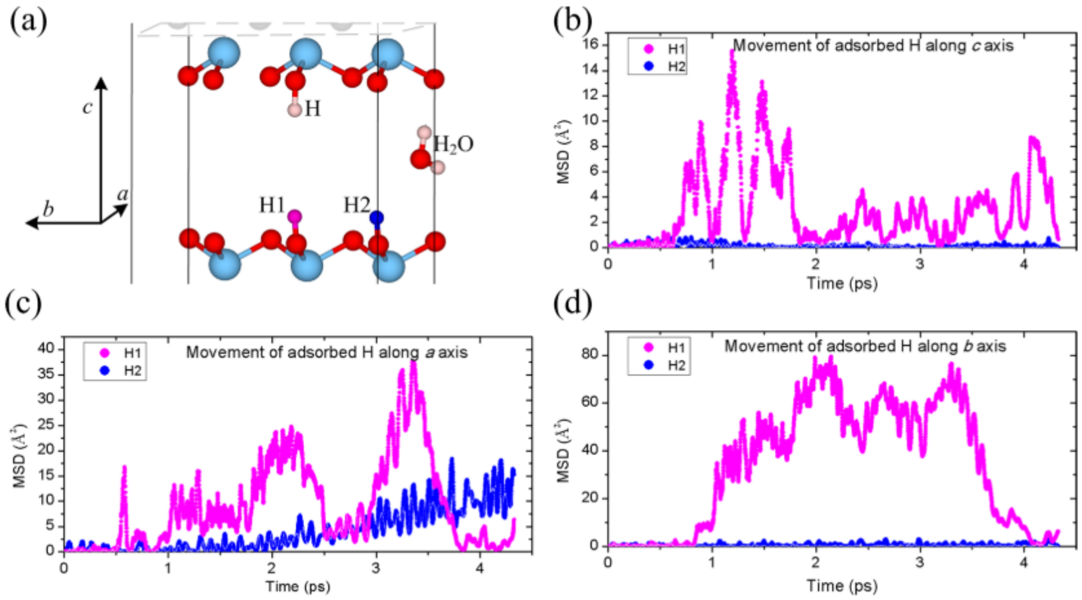

Figure 1.31 Structural configuration (a) and MSD of the adsorbed hydrogen species projected along the *c* (b), *a* (c), and *b* (d) axes, respectively.[54]

Diffusion property	K	Hydrated K	Proton	Hydrated proton
Range	3D 0.21*c*~0.29*c*	Enhanced 3D 0.21*c*~0.29*c*	2D 0.18*c*-plane	3D 0.18*c*~0.32*c*
Migration behavior at high concentration	Continuous movement	Continuous and hopping process	Continuous movement	Continuous and hopping process
Migration behavior at low concentration	Hopping process	Continuous and hopping process	Continuous movement	Hopping process
Allowed occupation layer number	One	One	Two	Two

Table 1.1 Diffusion properties comparison of K ions and protons in the water-empty and water-containing units.[54]

Hu et al.[55] studied the performance of MXene electrodes in three sulfate ion-containing aqueous electrolytes with H+, NH_4^+ and Mg^{2+} cations. The much higher capacitance in H_2SO_4 than in others, implies a distinct electrochemical process. In situ Raman spectroscopy technique was used to explore the in-depth charge mechanisms. The results in Fgure 1.32 express the clear changes (intensity or position) in the case of negatively charged electrode in H_2SO_4 electrolytes. And the specific detail of band evolution from 530 to 770 cm^{-1} is exposed by Lorentzian fitting. From Figure 1.33a, there is an apparent band movement from 726 to 708 cm^{-1}, combining with modes remaining at 630 and 672 cm^{-1} in $Ti_3C_2(OH)_2$. This demonstrates the transformation from $Ti_3C_2O_2$ to $Ti_3C_2O(OH)$ instead of $Ti_3C_2(OH)_2$. As shown in Figure 1.33b, there is ion exchange between interlayers, in which the hydronium of the H_2SO_4 electrolytes bond with the dangling-oxygen active sites, resulting in the reversible redox reactions and observed high-capacitance. Contrarily, the NH4^{+} and Mg^{2+} cations are just adsorbed at the material surface without any ion exchange. This exerts the electric-double-layer capacitive behavior what is lower than the pseudocapacitive contribution. Interestingly, the scenarios related to positive electrodes are invariable in Raman spectra, digging that SO4^{2-} anions are insignificant for electrochemical process.

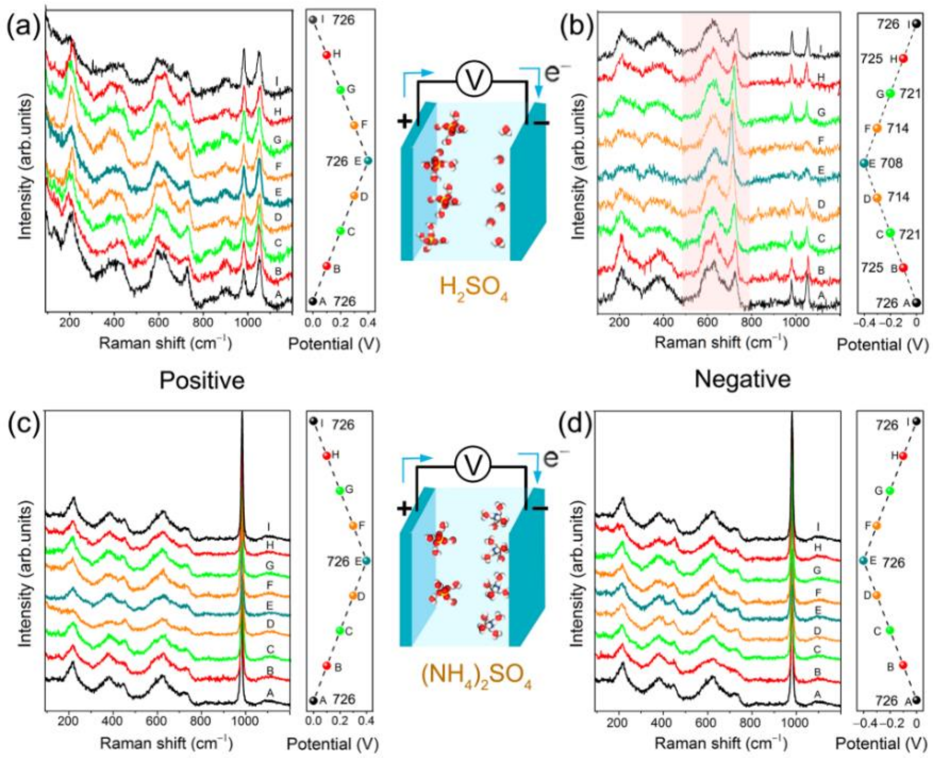

Figure 1.32 In situ Raman spectra of $Ti_3C_2T_x$ MXene in H_2SO_4 and $(NH_4)_2SO_4$ electrolytes.[55]

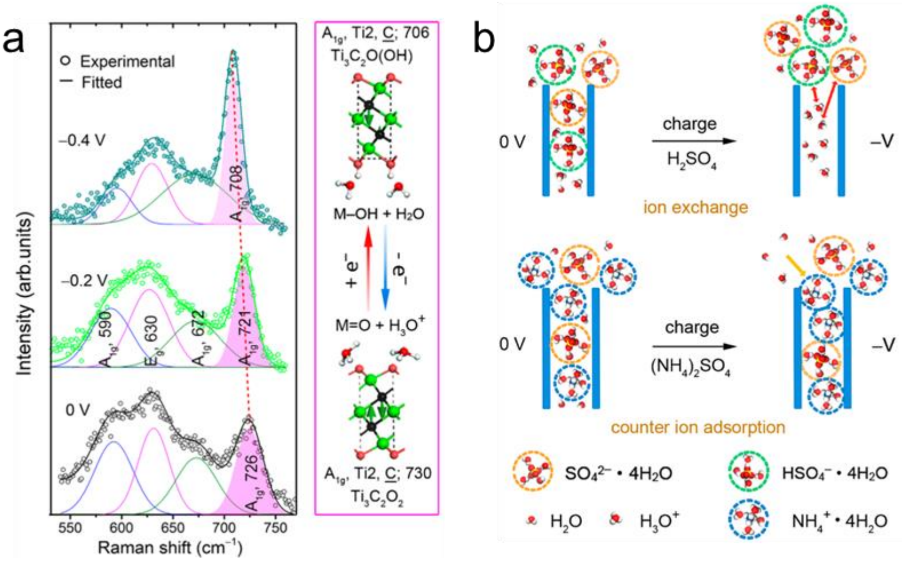

Figure 1.33 (a) Selected spectra and Lorentzian fits of bands of the negative electrode in H_2SO_4. The peak at 726 cm^{-1} and 708 cm^{-1} respectively represent out-of-plane vibrations of C atoms in $Ti_3C_2O_2$ and that in $Ti_3C_2O(OH)$. (b) The schematic of charge mechanisms in different electrolytes.[55]

1.5 Electrochemical technology

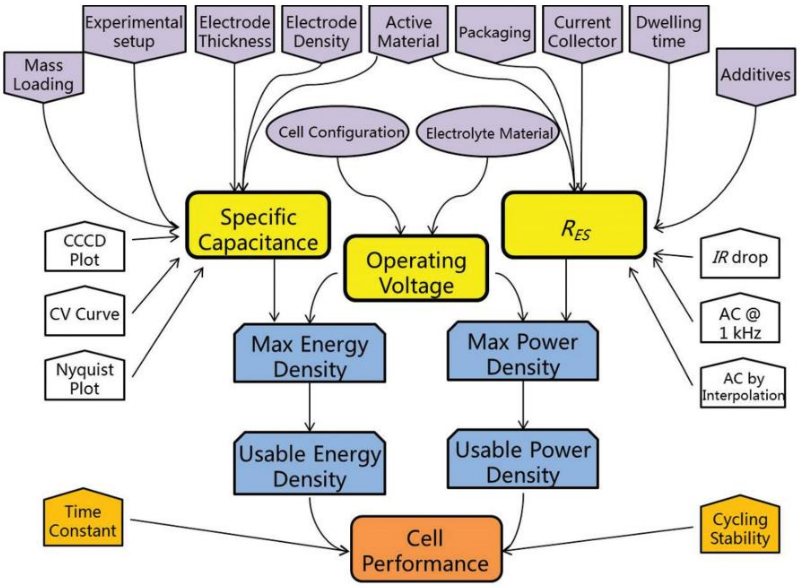

Figure 1.34 An illustration of key performance metrics, test methods, major affecting factors for the evaluation of SCs.[56]

There are various parameters to define the performance of supercapacitors, including capacitance, voltage window, cycling stability, energy density, power density, equivalent series resistance (R_{ES}) and so on. A variety of measurements have been developed and applied to evaluate various criteria: cyclic voltammetry (CV), galvanostatic charge-discharge (GCD)/ constant current charge-discharge (CCCD) and electrochemical impedance spectroscopy (EIS) tests. The detailed inter-correlation and related affecting factors are shown in Figure 1.34. It displays that the core parameters are specific capacitance, operation voltage/potential and equivalent series resistance. These parameters can be obtained from the corresponding test methods in white boxes. In this thesis, we focus on using regular electrochemical measurements for supercapacitors.

1.5.1 Cyclic voltammetry

In cyclic voltammetry (CV), the potential is linearly changed and the current response is monitored until returning to the initial potential to complete the cycle between positive and negative electrodes in a device, or between reference and working electrodes in a three-electrode configuration. The rate of potential change is the scan rate and the applied potential range is the operating potential/potential window. CV is a great technique to elucidate the surface and solution electrochemical reactions, including reaction mechanisms and electrochemical kinetics. For instance, the electric-double-layer capacitors with reversible ions adsorption at the interface possess a squared body CV curve, while batteries have a redox peak due to the Faradaic reactions in the bulk. The detailed differences were shown in Figure 1.6. Furthermore, we generally define the operating potential range by uninterruptedly adjusting the reverse potential in a three-electrode system. Additionally, the capacitance can be obtained in CV curves by corresponding equation (5):

$$C_m = \frac{Q}{2m\Delta V} = \frac{\int_{V_-}^{V_+} I(V)dV}{2mv\Delta V} \tag{5}$$

where C_m is gravimetric capacitance, Q is the total charge, v is the applied scan rate, ΔV is the operating potential window. Similarly, the volumetric and areal capacitances are also calculated by the alike equations.

1.5.2 Galvonastatic charge/discharge

Galvonastatic charge/discharge (GCD) is the one most widely used and reliable test approaches to analyze and inspect the capacitive performance, in which a set-up constant current is applied and flows between the suitable potential limits, resulting in a plot of the potential (V) output with time (s). As with CVs, GCD measurements can also roughly distinguish the different electrochemical behaviors from the shape of potential output. The potential responses of EDLC and pseudocapacitive materials show a linear form during charge/discharge procedures. Interestingly, some pseudocapacitive electrode materials also display tiny slopy voltage plateau regions. However, a long and broad potential plateau is shown in the GCD profiles of batteries, meaning there are phase transformation during involved redox reactions. Details are also depicted in Figure 1.6. Moreover, the GCD technique is skillful to evaluate a series of performance parameters, such as capacitance, energy density, power density, cycling stability, energy efficiency, coulombic efficiency and equivalent series resistance. The gravimetric capacitance is attained by the followed equation (6):

$$\mathrm{C} = \frac{\Delta Q}{m\Delta V} = \frac{i\Delta t}{m\Delta V} \tag{6}$$

Where i is the discharging current, ΔV is the operating potential window, Δt is the discharging time, C_m is the gravimetric capacitance and m is the mass of active materials. Again, the volumetric and areal capacitances are obtained by the similar equations.

The energy and power densities are calculated from equations (7) and (8):

$$\mathrm{E} = \frac{1}{2}C\Delta V^2 \tag{7}$$

$$\mathrm{P} = \frac{E}{3600\Delta t} \tag{8}$$

R_{ES} is evaluated by analyzing the IR drop at the initial step of discharging curve in GCD measurements. According to the Ohm law, R_{ES} is calculated by the equation (9):

$$\mathrm{R}_{ES} = \frac{\Delta V}{\Delta i} \tag{9}$$

where ΔV and Δi represent the voltage and current of IR drop.

The coulombic and energy efficiencies are acquired as follows:

$$\eta_c = \frac{t_D}{t_C} \tag{10}$$

$$\eta_c = \frac{E_{int,D}}{E_{int,C}} \tag{11}$$

where t_D and t_C are the discharging and charging time, $E_{int,D}$ and $E_{int,C}$ are the integral areas discharging and charging processes.

1.5.3 Electrochemical impedance spectroscopy

Electrochemical impedance spectroscopy (EIS) is a frequency-based technique used to measure the impedance data of a system as a function of the modulation frequency by injecting a low-amplitude sinusoidal potential (usually 5 mV).[56] The derived data are conventionally depicted in a Bode plot to exhibit the magnitude and phase responses with frequency or in a Nyquist plot to show the imaginary and real parts of the impedance.[57] Basically, EIS is a meaningful and all-around technology to assess or explore the charge transfer, mass diffusion, capacitance performance and even studying charge storage mechanisms. The capacitance can be obtained from an equation ($\mathrm{C} = 1/(2\pi\mathrm{f}|Z|$) in the bode plot, it is apparent to inspect the capacitance decreases as the frequency increases.[58] Here, we specifically demonstrate the popular Nyquist plot to describe EIS. As shown in the schematic diagram of Figure 1.35a shown, the intercept of Nyquist plot with the real part at the high frequency region is the resistance R_A, which is the equivalent series resistance (R_{es}) that takes into account the bulk electrolyte, the electrode, and the contact resistance between the electrode and the current collector. The diameter R_{AB} of the semicircle stands for charge transfer resistance. And the R_{BC} is the equivalent distribution resistance at the intermedia frequency, which can be represented as equivalent series resistance plus an additional resistance that results from the charge redistribution processes in the electrode pores.[57] The final vertical line at low frequency represents the dominant electric double-layer behavior.[59] A distinct line direction can be used to differentiate the EDLC, pseudocapacitor, and battery behaviors. From Figure 1.35b, the EDLC shows a vertical line and pseudocapacitor displays an approximate 90° straight line with a small semicircle, while the battery offers a 45° straight line with a large semicircle.[60]

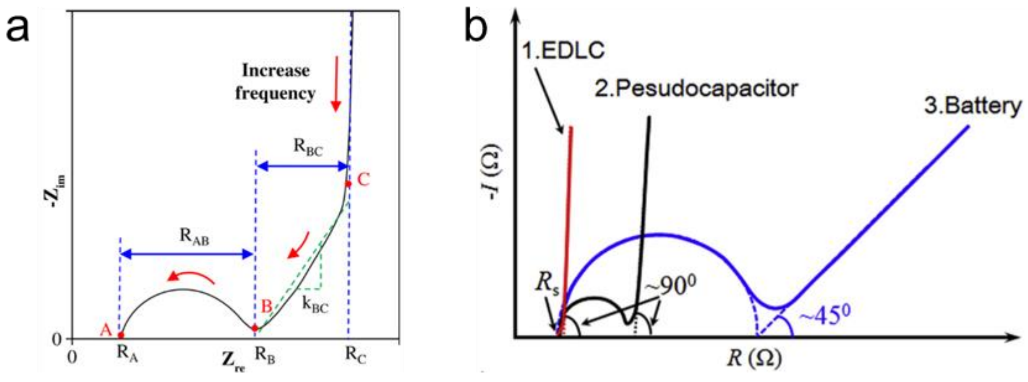

Figure 1.35 (a) Schematic of Nyquist plot.[59] (b) Typical Nyquist plots of ideal EDLCs, pseudocapacitors and batteries.[60]

1.6 Objectives

Since the discovery of graphene, and its shinning physical and chemical properties, two-dimensional (2D) materials can endow the unique structural and surface features for energy storage applications.[61, 62] The purpose of this thesis is to investigate the growth mechanism of 2D δ-MnO_2 and modify its surface morphology by intercalated ions to improve the electrochemical capability. To prevent the restacking problems of hydroxides, MnO_2 units can be used and keep the good stability property for the hydroxide@MnO_2 composites. In addition, we also aim to solve the restacked issues of MXene layers and reveal the more active sites between the interlayers, thus improving the electrochemical property for corresponding supercapacitors. Finally, the MXene layer can be used as a conductive substrate to be loaded MnO_2, as a result, increasing the conductivity and improving the electrochemical performance of MnO_2 for supercapacitors.

1.7 Reference

1. Aneke, M. & Wang, M. Energy storage technologies and real life applications – A state of the art review. Appl. Energy 179, 350–377 (2016).

2. Yoo, H. D., Markevich, E., Salitra, G., Sharon, D. & Aurbach, D. On the challenge of developing advanced technologies for electrochemical energy storage and conversion. Mater. Today 17, 110–121 (2014).

3. Lakshmi, G. S. et al. Energy Statistics. 121 (2017).

4. Jayalekshmi, S. & Puthirath, A. Nanostructured Ceramic Oxides for Supercapacitor Applications. Nanostructured Ceramic Oxides for Supercapacitor Applications (2014). doi:10.1201/b16522

5. Gogotsi, Y. & Simon, P. Materials for electrochemical capacitors. Nat. Mater. 7, 845–854 (2008).

6. Simon, P., Gogotsi, Y. & Dunn, B. Where Do Batteries End and Supercapacitors Begin. Sci. Mag. 343, 1210–1211 (2014).

7. Lukatskaya, M. R., Dunn, B. & Gogotsi, Y. Multidimensional materials and device architectures for future hybrid energy storage. Nat. Commun. 7, 1–13 (2016).

8. Eftekhari, A. The mechanism of ultrafast supercapacitors. J. Mater. Chem. A 6, 2866–2876 (2018).

9. Béguin, F., Presser, V., Balducci, A. & Frackowiak, E. Carbons and electrolytes for advanced supercapacitors. Adv. Mater. 26, 2219–2251 (2014).

10. Eftekhari, A. & Mohamedi, M. Tailoring pseudocapacitive materials from a mechanistic perspective. Mater. Today Energy 6, 211–229 (2017).

11. Wang, G., Zhang, L. & Zhang, J. A review of electrode materials for electrochemical supercapacitors. Chem. Soc. Rev. 41, 797–828 (2012).

12. Lindström, H. et al. Li + Ion Insertion in TiO 2 (Anatase). 2. Voltammetry on Nanoporous Films. J. Phys. Chem. B 101, 7717–7722 (1997).

13. Aikens, D. A. Electrochemical methods, fundamentals and applications. Journal of Chemical Education 60, (2009).

14. Wang, Y., Song, Y. & Xia, Y. Electrochemical capacitors: Mechanism, materials, systems, characterization and applications. Chem. Soc. Rev. 45, 5925–5950 (2016).

15. Wang, F. et al. Latest advances in supercapacitors: From new electrode materials to novel device designs. Chem. Soc. Rev. 46, 6816–6854 (2017).

16. Huang, Y. et al. Hierarchically Mesostructured Aluminum Current Collector for Enhancing the Performance of Supercapacitors. ACS Appl. Mater. Interfaces 10, 16572–16580 (2018).

17. Qie, L. et al. Synthesis of functionalized 3D hierarchical porous carbon for high-performance supercapacitors. Energy Environ. Sci. 6, 2497–2504 (2013).

18. Lu, S. Y. et al. Chemically Exfoliating Biomass into a Graphene-like Porous Active Carbon with Rational Pore Structure, Good Conductivity, and Large Surface Area for High-Performance Supercapacitors. Adv. Energy Mater. 8, 1–9 (2018).

19. Yao, L. et al. Scalable 2D Hierarchical Porous Carbon Nanosheets for Flexible Supercapacitors with Ultrahigh Energy Density. Adv. Mater. 30, 1–9 (2018).

20. Wang, J. et al. Hierarchical porous carbons with layer-by-layer motif architectures from confined soft-template self-assembly in layered materials. Nat. Commun. 8, 1–9 (2017).

21. Futamura, R. et al. Partial breaking of the Coulombic ordering of ionic liquids confined in carbon nanopores. Nat. Mater. 16, 1225–1232 (2017).

22. Li, X., Rong, J. & Wei, B. Electrochemical Behavior of Single- Walled Carbon Nanotube Stress. ACS Nano 4, 6039–6049 (2010).

23. Niu, Z. et al. Compact-designed supercapacitors using free-standing single-walled carbon nanotube films. Energy Environ. Sci. 4, 1440–1446 (2011).

24. Xiong, G. et al. Bioinspired leaves-on-branchlet hybrid carbon nanostructure for supercapacitors. Nat. Commun. 9, (2018).

25. Lee, J. A. et al. Ultrafast charge and discharge biscrolled yarn supercapacitors for textiles and microdevices. Nat. Commun. 4, (2013).

26. Choi, C. et al. Improvement of system capacitance via weavable superelastic biscrolled yarn supercapacitors. Nat. Commun. 7, 1–8 (2016).

27. Meyer, J. C. et al. The structure of suspended graphene sheets. Nature 446, 60–63 (2007).

28. Raccichini, R., Varzi, A., Passerini, S. & Scrosati, B. The role of graphene for electrochemical energy storage. Nat. Mater. 14, 271–279 (2015).

29. Chen, K., Song, S., Liu, F. & Xue, D. Structural design of graphene for use in electrochemical energy storage devices. Chem. Soc. Rev. 44, 6230–6257 (2015).

30. Lin, Z., Waller, G., Liu, Y., Liu, M. & Wong, C. P. Facile synthesis of nitrogen-doped graphene via pyrolysis of graphene oxide and urea, and its electrocatalytic activity toward the oxygen-reduction reaction. Adv. Energy Mater. 2, 884–888 (2012).

31. Lin, D. et al. Layered reduced graphene oxide with nanoscale interlayer gaps as a stable host for lithium metal anodes. Nat. Nanotechnol. 11, 626–632 (2016).

32. Xue, Y. et al. Rationally designed graphene-nanotube 3D architectures with a seamless nodal junction for efficient energy conversion and storage. Sci. Adv. 1, 1–10 (2015).

33. Han, S., Wu, D., Li, S., Zhang, F. & Feng, X. Porous graphene materials for advanced electrochemical energy storage and conversion devices. Adv. Mater. 26, 849–864 (2014).

34. Raimond, J. M., Brune, M., Computation, Q., Martini, F. De & Monroe, C. Electric Field Effect in Atomically Thin Carbon Films. Science (80-.). 306, 666–669 (2004).

35. Shao, Y. et al. Graphene-based materials for flexible supercapacitors. Chem. Soc. Rev. 44, 3639–3665 (2015).

36. Cong, H. P., Chen, J. F. & Yu, S. H. Graphene-based macroscopic assemblies and architectures: An emerging material system. Chem. Soc. Rev. 43, 7295–7325 (2014).

37. Shen, B., Zhai, W. & Zheng, W. Ultrathin flexible graphene film: An excellent thermal conducting material with efficient EMI shielding. Adv. Funct. Mater. 24, 4542–4548 (2014).

38. El-Kady, M. F., Veronica, S., Sergey, D. & Richard, B. K. Laser Scribing of High-Performance and Flexible Graphene-Based Electrochemical Capacitors. Science (80-.). 335, 1326–1330 (2012).

39. Sumboja, A., Foo, C. Y., Wang, X. & Lee, P. S. Large areal mass, flexible and free-standing reduced graphene oxide/manganese dioxide paper for asymmetric supercapacitor device. Adv. Mater. 25, 2809–2815 (2013).

40. Trasatti, S. & Buzzanca, G. Ruthenium dioxide: A new interesting electrode material. Solid state structure and electrochemical behaviour. J. Electroanal. Chem. 29, 4–8 (1971).

41. Augustyn, V., Simon, P. & Dunn, B. Pseudocapacitive oxide materials for high-rate electrochemical energy storage. Energy Environ. Sci. 7, 1597–1614 (2014).

42. Devaraj, S. & Munichandraiah, N. Effect of Crystallographic Structure of MnO 2 on Its Electrochemical Capacitance Properties. J. Phys. Chem. C 112, 4406–4417 (2008).

43. Lee, H. Y. & Goodenough, J. B. Supercapacitor Behavior with KCl Electrolyte. J. Solid State Chem. 144, 220–223 (1999).

44. Ma, Z. et al. Construction of Hierarchical α-MnO2 Nanowires@Ultrathin δ-MnO2 Nanosheets Core-Shell Nanostructure with Excellent Cycling Stability for High-Power Asymmetric Supercapacitor Electrodes. ACS Appl. Mater. Interfaces 8, 9050–9058 (2016).

45. Weifeng Wei,ab Xinwei Cui, a W. C. and D. G. I. Manganese oxide-based materials as electrochemical supercapacitor electrodes. Chem. Soc. Rev 62, 647–652 (2015).

46. Hsu, Y. K., Chen, Y. C., Lin, Y. G., Chen, L. C. & Chen, K. H. Reversible phase transformation of MnO2 nanosheets in an electrochemical capacitor investigated by in situ Raman spectroscopy. Chem. Commun. 47, 1252–1254 (2011).

47. Toupin, M., Brousse, T. & Bélanger, D. Charge storage mechanism of MnO2 electrode used in aqueous electrochemical capacitor. Chem. Mater. 16, 3184–3190 (2004).

48. Nam, K. W., Kim, M. G. & Kim, K. B. In situ Mn K-edge X-ray absorption spectroscopy studies of electrodeposited manganese oxide films for electrochemical capacitors. J. Phys. Chem. C 111, 749–758 (2007).

49. Chen, D. et al. Probing the Charge Storage Mechanism of a Pseudocapacitive MnO2 Electrode Using in Operando Raman Spectroscopy. Chem. Mater. 27, 6608–6619 (2015).

50. Chang, H. W. et al. Electrochemical and: In situ X-ray spectroscopic studies of MnO2/reduced graphene oxide nanocomposites as a supercapacitor. Phys. Chem. Chem. Phys. 18, 18705–18718 (2016).

51. Liu, T., Zhou, Z., Guo, Y., Guo, D. & Liu, G. Block copolymer derived uniform mesopores enable ultrafast electron and ion transport at high mass loadings. Nat. Commun. 10, 1–10 (2019).

52. Alhabeb, M. et al. Guidelines for Synthesis and Processing of Two-Dimensional Titanium Carbide (Ti3C2Tx MXene). Chem. Mater. 29, 7633–7644 (2017).

53. Shahzad, F. et al. Electromagnetic interference shielding with 2D transition metal carbides (MXenes). Science (80-.). 353, 1137–1140 (2016).

54. Wen, J. et al. Understanding the different diffusion mechanisms of hydrated protons and potassium ions in titanium carbide mxene. ACS Appl. Mater. Interfaces 11, 7087–7095 (2019).

55. Hu, M. et al. High-Capacitance Mechanism for Ti3C2Tx MXene by in Situ Electrochemical Raman Spectroscopy Investigation. ACS Nano 10, 11344–11350 (2016).

56. Zhang, S. & Pan, N. Supercapacitors performance evaluation. Adv. Energy Mater. 5, 1–19 (2015).

57. Noori, A., El-Kady, M. F., Rahmanifar, M. S., Kaner, R. B. & Mousavi, M. F. Towards establishing standard performance metrics for batteries, supercapacitors and beyond. Chem. Soc. Rev. 48, 1272–1341 (2019).

58. Raza, W. et al. Recent advancements in supercapacitor technology. Nano Energy 52, 441–473 (2018).

59. Mei, B. A., Munteshari, O., Lau, J., Dunn, B. & Pilon, L. Physical Interpretations of Nyquist Plots for EDLC Electrodes and Devices. J. Phys. Chem. C 122, 194–206 (2018).

60. Xie, J. et al. Puzzles and confusions in supercapacitor and battery: Theory and solutions. J. Power Sources 401, 213–223 (2018).

61. Yu, X. et al. Emergent Pseudocapacitance of 2D Nanomaterials. Adv. Energy Mater. 8, 1–33 (2018).

62. Wang, L., Hu, P., Long, Y., Liu, Z. & He, X. Recent advances in ternary two-dimensional materials: Synthesis, properties and applications. J. Mater. Chem. A 5, 22855–22876 (2017).

Chapter 2 Cu ions modified and regulated MnO_2 impacting on the electrode supercapacitive behavior

2.1 Abstract

In the supercapacitor field, the overall requirements for enhanced energy/power densities, competitive overheads, durable cyclic longevity, and eco-friendliness have stimulated the research for new electrode materials. Pseudocapacitive transition metal oxides led to substantial improvement of energy storage device performance, but both their capacity and rate capability remain too limited, constraining the advance towards practical applications. Herein, a straightforward and competitive approach is specified to derive the layered birnessite δ-MnO_2 functionalized by Cu^{2+} ions, intriguing as the supercapacitor electrode with a superior capacitance of 151 F g^{-1} at 2 A g^{-1} and 106 F g^{-1} at 10 A g^{-1} (73% of initial value). The assembled asymmetric supercapacitor device exhibited a high energy density up to 22 Wh kg^{-1}. Such features notably outscore the raw MnO_2 specimen, explicitly connoting the effectiveness of doping Mn-based materials with Cu^{2+} ions for supercapacitive storage. The greater interlamellar distance and the peerless laminated configuration allow to withstand the volume shrinkage/swelling occurring during charge/discharge processes, contributing to a fair pseudo-capacitive effect with excellent capacity, good rate capability, and long cycling lifetime. While the Cu-modified δ-MnO_2 compound may be not the most cutting-edge electrode material in comparison with some other Mn-based oxides, we endeavor to showcase an ingenious alternative to afford a prospective substituent to explore high-performance energy storage materials.

2.2 Introduction

Burning coal, oil and natural gas are currently causing a series of environmental issues, especially greenhouse effect. The development and commercialization of updated and greener energy storage technologies are in the state of being urgent.[1] Supercapacitor (SC), [2] is an attractive energy device thanks to its high capacity, high power density, long cycling life, etc. compared with lithium ion batteries.[3, 4, 5] For SC, the electrode material is a crucial and essential “territory”, and many promising materials have been engineered[6-10]. Furthermore, the morphology building/tuning is attracting the attention of many researchers[11-13] around the world thanks to enhance the electrochemical performance of electrode material.[14] Generally, “good” electrode materials lead to “good” performance of the corresponding electrochemical supercapacitors.[15] Based on this regulation, various transition metal oxides or –based materials, including manganese oxide[16], ruthenium oxide[17] and so on, have been explored as they are currently considered asimportant components for supercapacitor electrodes. Much interesting works so far have been focused on structuring and conceiving manganese dioxide –based materials as an electrode material for SC.[18] In addition, 2D materials[19, 20, 21] showing a layered morphology structure, like birnessite δ-MnO_2,[22] have opened up a promising prospect in the supercapacitive energy storage field due to their outstanding physical and chemical properties.[23] There is no deny that two dimensional materials present stronger in-plane covalent bonding and weaker out-of-plane interactions,[24] and therefore providing a feasible way to tune the chemical or physical features to obtain enhanced electrode material properties for application in energy storage devices.[25, 26] On the basis of weaker out-of-plane[27] interactions precondition, it is rather simple to implant some molecules, atoms or ions in between the layers. In the meantime, the structure or morphology of the host can be modified or altered following some self-intercalation procedures.[28, 29]

In this paper, we initially fabricated the two-dimensional layered birnessite δ-MnO_2 through a simple hydrothermal method. In a second step, its bulk layered morphology was modified or regulated by using copper ions at various synthetic temperatures and concentrations. As the copper ion concentration was changed, electronic structure of MnO_2 material can be regulated by the ion potential energy, thereby causing interesting physical and chemical transformation phenomenon, such as charge density wave, anisotropic transport performance action. During the course of the present study, Xue and coworkers have assigned the effect of Cu^{2+} doping on the electrochemical performance of MnO_2 electrode material. The electronic structure of the doped material shows copper contribution at the Fermi level narrowing the corresponding band-gap.[30] As such, Cu doping improved the conductivity, ionic transport ability and electrochemical activity of the resulting MnO_2 materials. We argue that the change of bulk layer thickness that we have observed by Cu doping could impact on the electrode performance as well. Again, the resulting enlarged open surface morphology structure can expose more active sites and unsaturated defects, as a result, effectively improving the electrochemical performances. Equipped with this enhanced electrode material, the fabricated device exhibited excellent electrochemical performance with greater specific capacitance, good cycle stability and greater energy density.

2.3 Experimental section

MnO_2 was first prepared by a hydrothermal method. In a typical procedure, 0.2528 g $KMnO_4$ and 0.0321 g $MnSO_4$ were dispersed in 80 mL H_2O following continuous stirring for 15 minutes at room temperature. Then, the solution was transferred into a 100 mL PTFE lined stainless steel autoclave. The sealed autoclave was kept into an oven at 160 °C for 12 h. And then, δ-MnO_2 was obtained after filtering and drying.

Preparation of Cu^{2+} modified δ- MnO_2

Especially, 50 mg δ-MnO_2 was dispersed in a series of Cu^{2+} solutions (50 ml) of various concentrations: (0.5 M, 1 M, and 2 M) at 50 °C. The samples were respectively termed as M-0.5, M-1 and M-2. After filtering and drying, final materials were obtained. Besides, the preparation of the M-1 copper ions modified MnO_2 was also explored at various temperatures. The preparation process is described in the supporting part which is below this chapter. These samples were termed as M-30, M-50 and M-80 for the samples prepared at 30, 50 and 80 ^oC, respectively.

2.4 Characterizations

The structural characteristics of material were analyzed by powder X-ray diffraction (XRD) using a Phillips X'Pert diffractometer with Cu Kα radiation (λ=1.5405Å). The morphology and elemental composition of prepared materials were evaluated by using a JEOL JSM-6300F scanning electron microscope (SEM) coupled energy dispersive X-ray (EDX). Transmission electron microscope (TEM) measurement was conducted on a MET 1200EX2 instrument.

2.5 Electrochemical measurements

Electrochemical measurements in this work were performed at room temperature both in classical three electrode systems and two electrode setups. For three electrode system in 6 M KOH electrolyte, a platinum foil and $Hg/HgO/OH^-$ electrode were used as counter and reference electrode, respectively. When using 1 M Na_2SO_4 electrolyte, an Ag/AgCl reference electrode was used instead. The working electrode was prepared by mixing the active material, carbon black (Sigma Aldrich, USA) and Polytetrafluoroethylene (PTFE) (Sigma Aldrich, USA) with a mass ratio of 60/30/10. The mixed additives were stirred in a proper volume of ethanol, to obtain a homogeneous suspension. Then, the mixture was evaporated at 60 °C to get a slurry that was rolled and, when dry, pressed in between two stainless steel under 10 Mpa for a few tens of second. Finally, the resulting working electrode could be tested. For the two-electrode device in 1 M Na_2SO_4 electrolyte, pre-prepared composite films were used as positive electrode and activated carbon as negative electrode. Electrochemical performance were evaluated through cyclic voltammetry (CV), galvanostatic charge-discharge (GCD) and electrochemical impedance spectroscopy (EIS) (open circuit potential, 0.01-100 kHz). Measurements were performed at room temperature by using a VMP3 multi-channel Bio-Logic electrochemical workstation. CV measurements were carried out at scan rates from 5 mV/s to 100 mV/s. The current density of GCD measurement ranged from 0.5 A g^{-1} or 1 A g^{-1} to 10 A g^{-1}. The specific capacitance was calculated from GCD data.

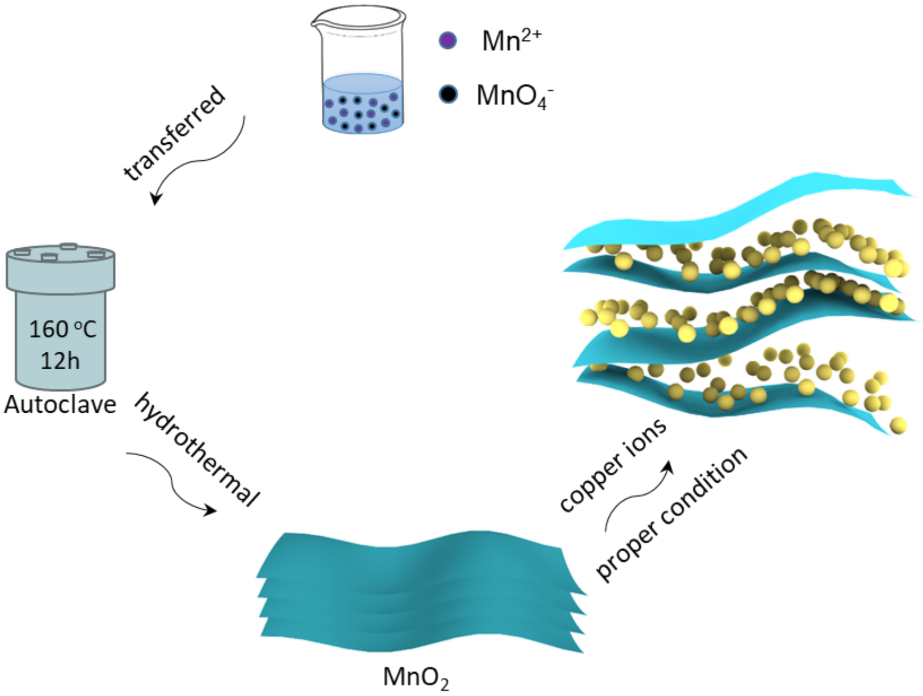

Figure 2.1 Schematic diagram of the preparation process of Cu ions modified δ- MnO_2.

The below related supporting information has been attached after reference.

2.6 Results and discussion

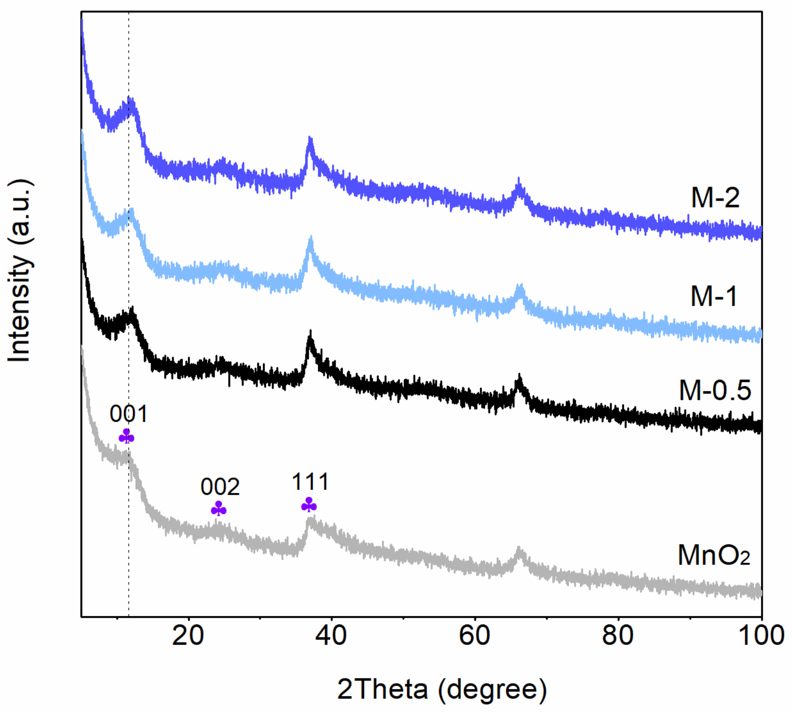

Figure 2.2 XRD patterns of δ-MnO_2, M-0.5, M-1 and M-2 samples.

XRD patterns of as prepared MnO_2, M-0.5, M-1 and M-2 samples are displayed in Figure 2.2. They all show the same features with characteristic peaks of birnessite δ-MnO_2 (001), (002) and (111) at about 11.9°, 24.6°, and 36.9°, respectively. Whatever the concentration of copper solution, the patterns are characteristic of a poorly crystallized material. By increasing the copper ion concentration, the (001) peak, characteristic of the interlayer distance, slightly shifts towards larger diffraction angle. This suggests copper ions to be intercalated in between MnO_2 interlayers, inducing a greater electrostatic attraction and a decrease in the interlayer distance. In addition, Figure S1 shows the XRD patterns of as prepared δ-MnO_2, M-30, M-50 and M-80 samples. Obviously, in the whole MnO_2-based series, X-ray diffraction patterns show consistent peaks at the same degrees of about 11.8°, 24.6° and 36.9° (2θ), which are indexed as the δ-phase MnO_2 diffraction planes (JCPDS 80-1098). However, while MnO_2 was operated at 80 °C (M-80 sample), new diffraction peaks appeared, characteristic of the promotion of at least one extra phase, implying that a new material was generated during the reaction process at this temperature. According to the pattern analysis and the comparison with databases, this multi-peaks substance is certainly recognized as $Cu_xMn_xO_x$.

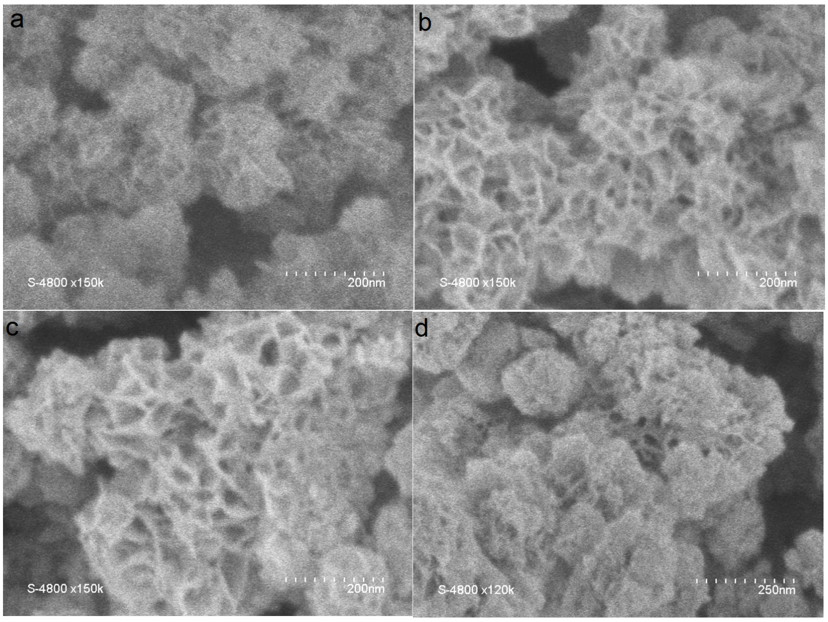

Figure 2.3 SEM images of δ-MnO_2 (a), M-0.5 (b), M-1(c) and M-2 (d).

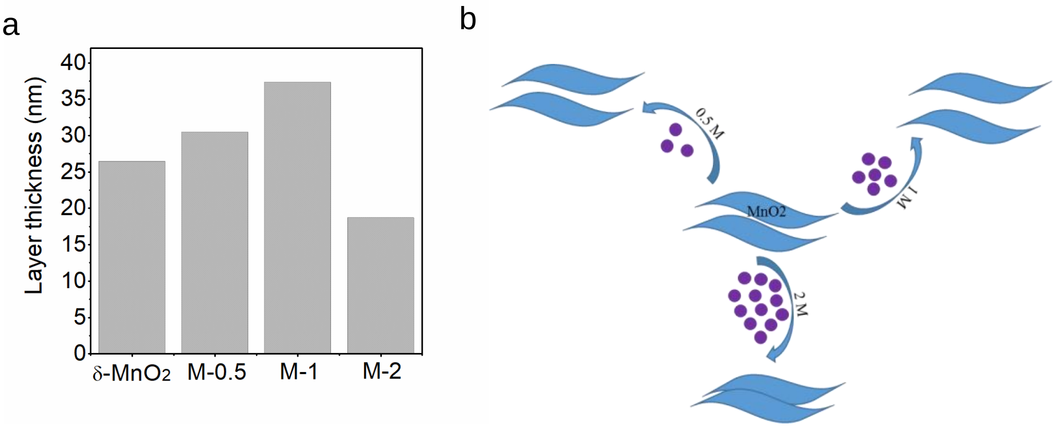

Figure 2.4 The histogram of layer thickness of δ-MnO_2, M-0.5, M-1 and M-2 samples (a). And the principle scheme of different concentrations of Cu^{2+} modified MnO_2 (b).

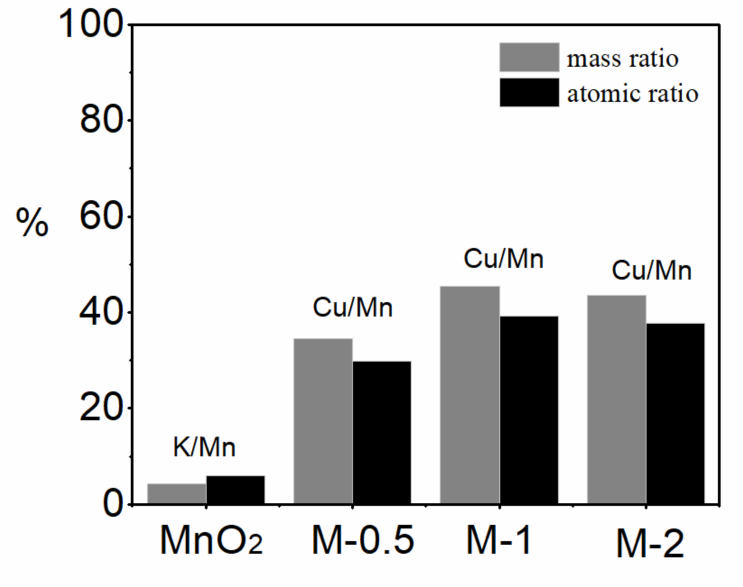

Figure 2.5 The element ratio of samples by EDX at different concentration.

The usually observed cauliflower morphology of prepared materials, deriving from the layered structure of Birnessite (δ-MnO_2), is exhibited by SEM imaging in Figure 2.3. It clearly shows the influences of copper ion solutions of various concentrations on the material morphology. Changes of average inter-flake thickness of the materials are observed. They are measured and shown in Figure 2.4 a. For pristine δ-MnO_2, the average inter-flake thickness is about 26 nm. After modification of δ-MnO_2 during treatment with various concentrations of copper ion solutions, the geometry space changed. From the lowest to greatest Cu^{2+} concentrations, corresponding to M-0.5, M-1 and M-2, the distance/thickness between flakes is reaching 30 nm, 37nm and 19 nm, respectively. The formation principle scheme is displayed in Figure 2.4 b. In the detail, as more copper ions elements are intercalated in MnO_2 units, the inter flake increases, progressively opening the surface morphology. When the concentration reached 2 M, the inter-flake thickness/distance decreased, thus resulting in a less open morphology. We proposed that this opening/closing behavior is associated to a “space effect”. As well known, the layered material holds a specific space, and for every bulk layer, there is a certain space to extend, eventually. Therefore, as the layer grows unceasingly, when, there is not enough accessible room/space to spread, the disorder is introduced in the MnO_2 layer. In consequence, just like in Figure 2.3 and Figure 2.4, the bulk layer was shrunken or even disappeared. As shown in Figure 2.4d, the layered morphology tends to close the available "door". Furthermore, EDX analysis shown in Figure 2.5, suggests that, with the increase of Cu^{2+} concentration, the copper mass ratio in the material first increases (see M-0.5 and M-1) to finally decrease in M-2 material. This point can also be associated to the morphology changes accompanying copper ions reaching a critical concentration. The induced disorder disrupts the bulk layered framework, which blokes the available diffusion path for the copper ions between the layers. Also, as imaged by SEM, the morphologies of as prepared manganese dioxide, M-30, M-50 and M-80 are shown in Figure S2. Again, MnO_2 prepared at various temperatures shows a cauliflower-like morphology structure. Interestingly, in the M-80 sample, together with cauliflower shapes, large sheets are clearly observed in Figure S2 (d). And as we discussed above (XRD results), MnO_2 with a copper ions treatment at 80 ^oC comes out with extra diffraction peaks suggesting the generation of a phase material, which is consistent with SEM result. Further, same as EDX analysis, the ratio of copper element increases with the raise of reaction temperatures. Notably, the ratio of copper in M-80 material shows a dramatic increase (see Figure S3) in comparison with other samples, and the copper content is greater than that of manganese.

Figure 2.6 shows TEM images of raw MnO_2 (a) and M-1 (b) samples. As expected, MnO_2 material displays a layered nano-structure. After introduction of copper ions, M-1 still keeps the layered birnessite structure, which is consistent with XRD result.

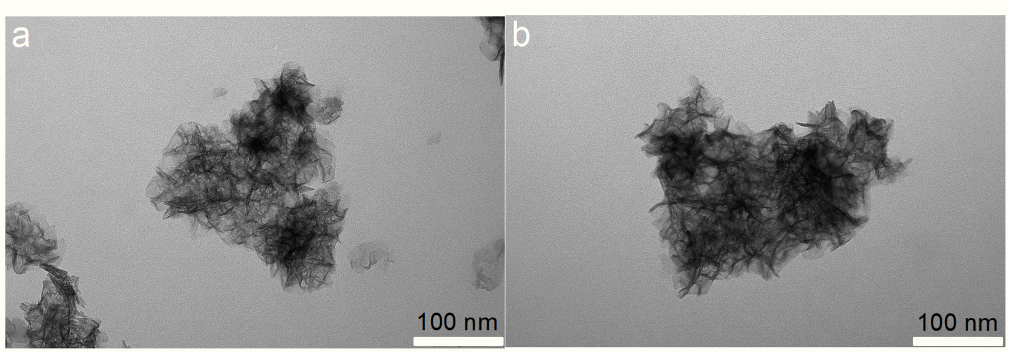

Figure 2.6 TEM images of pure MnO_2 (a) and M-1 (b).

2.7 Electrochemical performance

Initially, Figure 2.7 (a) displays the comparison of CV curves of M-30, M-50 and M-80 –based electrodes at 5 mV s^{-1} in 6 M KOH. Both M-30 and M-50 samples shows the similar integral area in comparison with pure MnO_2, revealing the best electrochemical properties in the series. Differently, after reaction temperature at 80 degrees celsius, the CV of M-80 electrode shows a similar or lower area compared with that of the raw MnO_2 electrode. To further investigate the difference, the specific capacitance was calculated via galvanostatic charge-discharge (GCD) measurements. Correspondingly, the capacitance change is consistent with above result. First, for raw MnO_2, the specific capacitance is 62 F g^{-1} at 0.5 A g^{-1}. After copper ions insertion procedure, remarkably, M-30 and M-50 show specific capacitance values of 152 F g^{-1} and 127 F g^{-1}, respectively, at the same current density.M-50 still exceeds M-30 in capacitance performance at 4 A g^{-1}. In accordance with what was analyzed via CV, M-80 sample behaves the same as that of raw MnO_2. A reaction temperature was therefore considered to elaluate the effect of the Cu^{2+} concentration on the electrochemical performance.

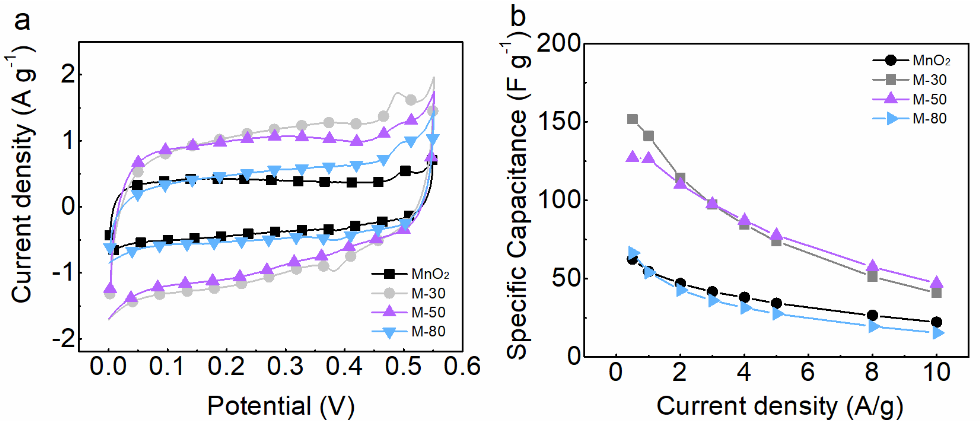

Figure 2.7 Electrochemical performance of MnO_2, M-30, M-50 and M-80 in 6 M KOH. (a) CV curves comparison of samples at 5 mV s^{-1} scan rate. (b) Specific capacitance comparison of samples at various current densities as measured in galvanostatic mode.

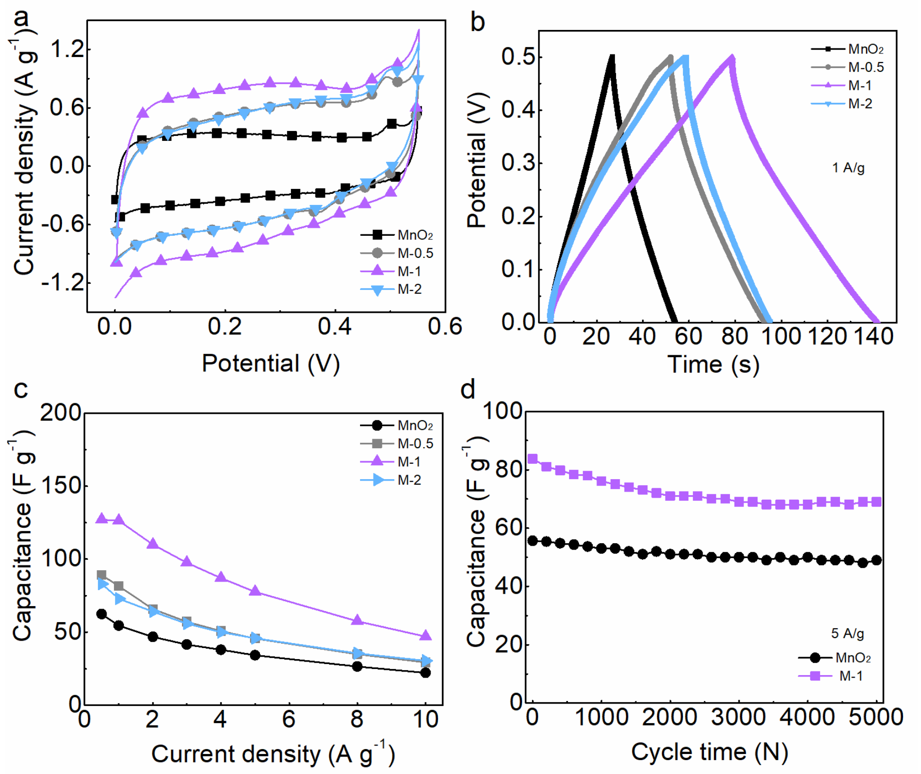

Figure 2.8 Electrochemical performance of MnO_2, M-0.5, M-1 and M-2 in 6 M KOH. (a) CV curves comparison of samples at 5 mV s^{-1} scan rate. (b) Galvanostatic charge-discharge (GCD) measurements of M-1 at various current densities. (c) Specific capacitance comparison of samples at various current densities. (d) The cycling stability of pure MnO_2 and M^{-1} at 5 A g^{-1} current density.

The electrochemical properties of the MnO_2 based electrode material after treatment with various concentration of copper ions at 50 °C (M-0.5, M-1 and M-2) are shown in Figure 2.8. According to CV and GCD, it is clear that the corresponding capacitance of the loaded electrodes firstly shows an increase trend from M-0.5 to M-1. When the copper concentration is up to 1 M, the greatest capacitance is obtained in the series. As the copper ion concentration reaches 2M, the integral area/capacitance decreases back to that of the M-0.5 electrode. The detailed capacitance was also calculated and plotted as a function of the applied current density in Figure 2.8c. Compared with pure MnO_2, the copper ions can definitely improve the capacitance performance for supercapacitors. Up to 1 M copper-ion concentration, the greater the concentration, the greater the capacitance. For a greater concentration, the capacitance dropped down. For instance, for raw MnO_2 -based electrode, the capacitance is 62 F g^{-1} at 0.5 A g^{-1}. The M-0.5 electrode capacitance is 89 F g^{-1} at the same current density, while the M-1 electrode has a capacitance of 127 F g^{-1}. For M-2 electrode, however, the capacitance decreases down to 83 F g^{-1}, which is still greater than the raw MnO_2 electrode.

As mentioned above, the introduction of copper ions not only affects the material morphology but also increases the number of exposed active sites. The concentration difference can open up the sealed structure of MnO_2 and leading to 3D meso/macro structure offering more electroactive sites. Additionally, the cycling stability of pure MnO_2 and M-1 was tested for 5000 cycles at a high current density of 5 A g^{-1} (Figure 2.8 (d)). As depicted, both electrodes display a fair cycle stability. Over the first 3000 cycles, about 89% of the original capacitance of raw MnO_2 electrode is maintained, while that of M-1 sustains about 84% of its initial value. However, during the next 2000 cycles, the raw MnO_2 electrode holds 96% of its remaining capacitance, while M-1 electrode shows an attractive 98% of capacitance retention.

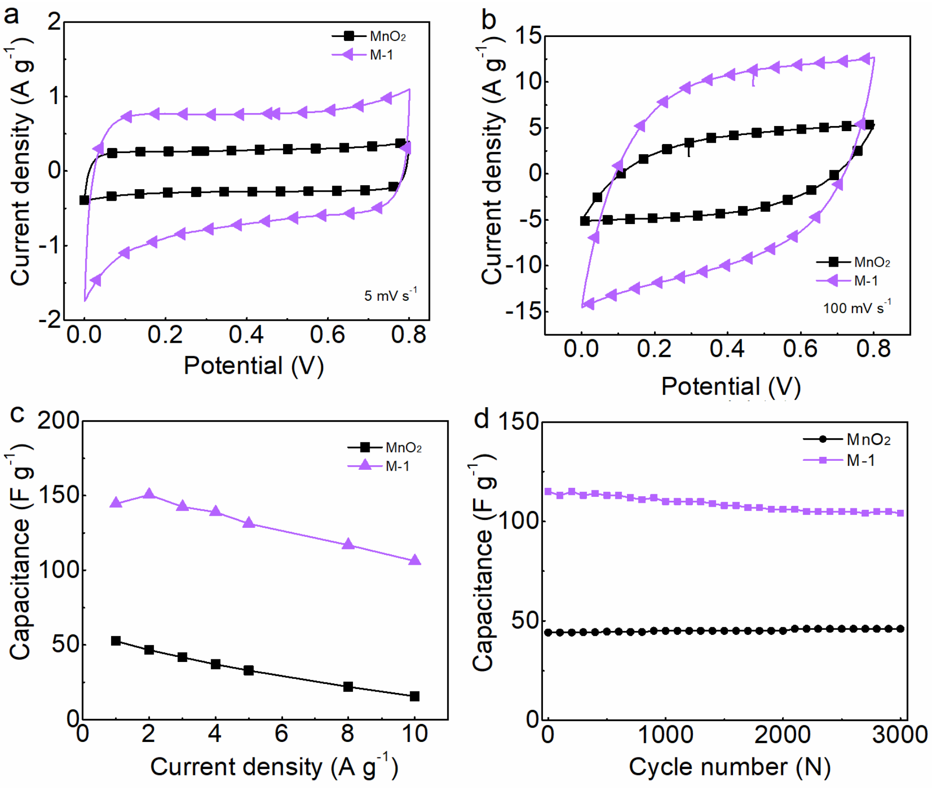

Figure 2.9 Electrochemical performance of electrodes based on raw MnO_2 and M-1 electrodes in 1 M Na_2SO_4. CV curves comparison of samples at 5 mV s^{-1} scan rate (a) and 100 mV s^{-1} (b). Specific capacitance comparison at various current densities (c). Cycling stability at the high current density of 5 A g^{-1} (d).

Then, the electrochemical behavior of raw MnO_2 and M-1 electrodes in 1 M Na_2SO_4 electrolyte was also studied and shown in Figure 2.9. The CV curves of pure MnO_2 at 5 mv s^{-1} presents roughly rectangular shape, but distorted at higher scan rate (100 mV s^{-1}). However, M-1 preserves a more regular frame at the high scan rate, suggesting an advanced rate capability. This is confirmed by the rate curves in Figure 2.9c, which are plotted from GCD measurements. For raw MnO_2 electrode, the capacitance value is 53 F g^{-1} at 1 A g^{-1}. When the current density reaches to 10 A g^{-1}, the capacitance fades down to 16 F g^{-1}, which corresponds to 30% retention only. In contrast, the capacitance of M-1 electrode is 151 F g^{-1} at 2A g^{-1} and 106 F g^{-1} at 10A g^{-1}, revealing a remarkable 73 % retention upon charge/discharge regime. Moreover, the cycling stability in Na_2SO_4 electrolyte was also tested. For M-1 sample, a 91 % retention is kept after 3000 cycles at a current density of 5 A g^{-1}.

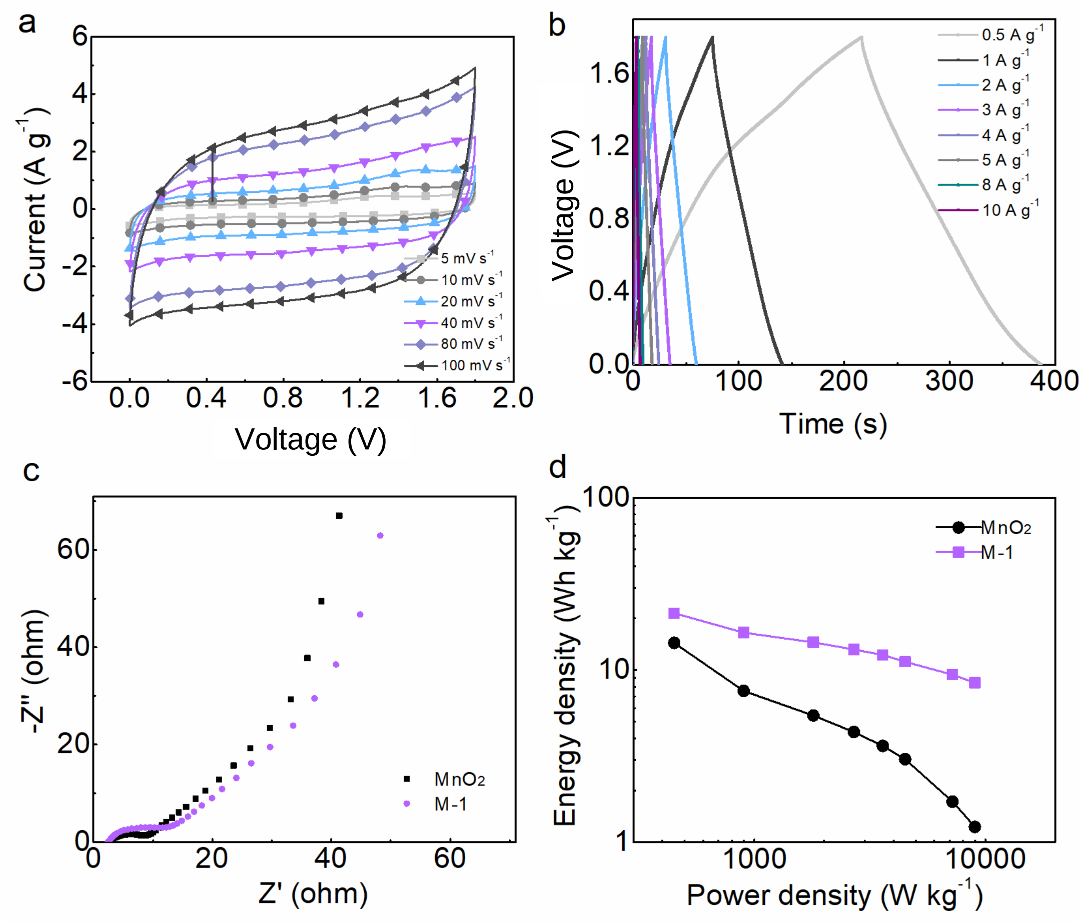

Figure 2.10 Electrochemical performance of pure MnO_2 and M-1 in two-electrode device in 1 M Na_2SO_4. (a) CV curves of M-1 at various scan rates. (b) Galvanostatic charge-discharge curves of M-1 at various current densities. (c) Nyquist plot of samples at frequencies from 100 kHz to 10 mHz. (d) Ragone plot (power density vs energy density).

After measurements in a three-electrode setup, the property of asymmetric supercapacitors with actived carbon (AC) as negative electrode and MnO_2 and M-1 as positive electrodes were evaluated in the 1 M Na_2SO_4 electrolytes. Figure 2.10 (a) shows the cyclic voltammograms of the M-1//AC devices, which was operated at various scan rates. The device delivers a large voltage range of 1.7 V in this aqueous electrolyte. Meanwhile, CVs kept a quite regular rectangular shape, even up to 100 mV s^{-1}, suggesting a fair rate and power capabilities. Figure 2.10 (c) shows Nyquist plots of both MnO_2//AC and M-1//AC devices. They look very similar and the slightly larger RC loop for M-1//AC device in the high frequency range cannot be assigned to any performance discrepancy with raw MnO_2-based device. Galvanostatic charge-discharge measurements were carried out to calculate the device energy and power densities, whose corresponding plots are displayed in Figure 2.10 (d). In the Ragone plot, compared with MnO_2//AC, M-1 -based device produces a more attractive energy density, which is 22 Wh kg^{-1} at a power density of 450 W kg^{-1}.

2.8 Conclusion

In summary, after preparing the layered birnessite δ-MnO_2 material by a simple hydrothermal method. The resulting raw MnO_2 with a cauliflower-like morphology was modified and tailored using copper ions solutions at various concentrations under specific temperatures. In the optimized conditions, the modified MnO_2 shows an opened inter-flake frame offering more access to Mn^{n+} active sites and unsaturated defects. Moreover, trapped copper ions are suggested to provide some extra pseudocapacitance for enhanced device energy. As a result, the M-1 electrode disclosed a capacitance of 127 F g^{-1} at 0.5 A g^{-1} in 6 M KOH electrolyte. This electrode delivered a capacitance of 151 F g^{-1} at 2 A g^{-1} and 106 F g^{-1} at 10 A g^{-1} in 1 M Na_2SO_4 electrolyte, representing a 73 % remarkable rate capability. Equipped with M-1 electrode material and active carbon, a full cell delivered 22 Wh kg^{-1} energy density at 450 W kg^{-1}.

Acknowledgements

This work was supported by China Scholarship Council (CSC).

This chapter is submitting as an article.

2.9 Reference

1 X. Zhang, L. Hou, A. Ciesielski, and Paolo Samorì, Adv. Energy Mater. 2016, 1600671.

2 Y. Gogotsi and P. Simon, Science, 2011, 334, 917.

3 J. Chmiola, C. Largeot, P. Taberna, P. Simon and Y. Gogotsi, Science, 2010, 328, 480.

4 P. Huang, C. Lethien, et al., Y. Gogotsi, P. Simon, Science, 2016, 351, 691.

5 N. Jabeen, A. Hussain, Q. Xia, S. Sun, J. Zhu and H. Xia, Adv. Mater., 2017, 29, 1700804.

6 Q. Mahmood, S. K. Park, K. D. Kwon, S.-J. Chang, J.-Y. Hong, G. Shen, Y. M. Jung, T. J. Park, S. W. Khang, W. S. Kim, J. Kong, H. S. Park, Adv. Energy Mater. 2016, 6, 1501115.

7 B. Anasori, M. R. Lukatskaya, Y. Gogotsi, Nat. Rev. Mater. 2017, 2, 16098.

8 X. Wang, Q. Weng, Y. Yang, Y. Bando, D. Golberg, Chem. Soc. Rev. 2016, 45, 4042.

9 B. Mendoza-Snchez, Y. Gogotsi, Adv. Mater. 2016, 28, 6104.

10 M. Xu, L. Kong, W. Zhou, H. Li, J. Phys. Chem. C 2007, 111, 19141

11 M. R. Lukatskaya, O. Mashtalir, C. E. Ren, Y. Dall'Agnese, P. Rozier, P. L. Taberna, M. Naguib, P. Simon, M. W. Barsoum, Y. Gogotsi, Science 2013, 341, 1502.

12 M. Ghidiu, M. R. Lukatskaya, M. Zhao, Y. Gogotsi & M. W. Barsoum, Nature 2014, 516, 78.

13. C. Yang, M. Shi, X. Song, X. Zhao, L. Zhao, J. Liu, P. Zhang and L. Gao, J. Mater. Chem. A, 2018,6, 5724.

14 L. Li, K. Hui, K. Hui and Y. Cho, J. Mater. Chem. A, 2017.

15 P. Simon and Y. Gogotsi, Nature Materials, 2008, 7.

16 X. Lu, D. Zheng, T. Zhai, Z. Liu, Y. Huang, S. Xie and Y. Tong, Energy Environ. Sci., 2011, 4, 2915.

17 Z. Algharaibeh, X. Liu and P. G. Pickup, Journal of Power Sources, 2009, 187, 640.

18 W. Wei, X. Cui, W. Chen and Douglas G. Ivey, Chem. Soc. Rev., 2011, 40, 1697.

19 R. Mas-Ballesté, C. Navarro, J. Herrero and F. Zamora, Nanoscale, 2011, 3, 20.

20 R. Lv, J. A. Robinson, R. E. Schaak, D. Sun, Y. Sun, T. E. Mallouk, and M. Terrones, Acc. Chem. Res. 2015, 48, 56.

21 Y. Wang, J. Z. Ou, etal., M. S. Strano, and K. Kalantar-zadeh, ACS NANO, 2013, 11, 10083.

22 T. Brousse, P. Taberna, et al., Frédéric Favier, Daniel Belanger and Patrice Simon, Journal of Power Sources, 2007, 173, 633.

23 Q. Wang, K. Kalantar-Zadeh, A. Kis, J. N. Coleman and M. S. Strano, Nature Nanotechnology, 2012, 7.

24 M. Chhowalla, H. S. Shin, G. Eda, L. J. Li, K. P. Loh, H. Zhang, Nat. Chem. 2013, 5, 263.

25 K. S. Novoselov, A. Mishchenko, A. Carvalho and A. H. Castro Neto, Science, 2016, 353, 9439.

26 H. Yuan, H. Wang and Y. Cui, Acc. Chem. Res. 2015, 48, 81.

27 J. Wan, etal., Michael S. Fuhrer and L. Hu, Adv. Energy Mater. 2014, 1401742.

28 Z. Zeng, Z. Yin, X. Huang, H. Li, Q. He, G. Lu, F. Boey, and H. Zhang, Angew. Chem. Int. Ed. 2011, 50, 11093.

29 H. Wang, Z. Lu, S. Xu, D. Kong, etal., Fritz B. Prinz and Y. Cui, PANS, 2013, 110, 19701.

30 Y. Xue, Q. Zhang, W. Wang, H. Cao, Q. Yang, and Lei Fu, Adv. Energy Mater., 2017, 1602684.

Supporting information

The preparation of copper ions modified MnO_2 by various temperatures

50 mg pre-prepared δ-MnO_2 were dispersed into 50 mL, 1 M Cu^{2+} solution. Then the solution was heated at various temperatures (30 °C, 50 °C and 80 °C) and kept for 48h. Finally, the solution was filtrated, and dried to obtain the product powder.

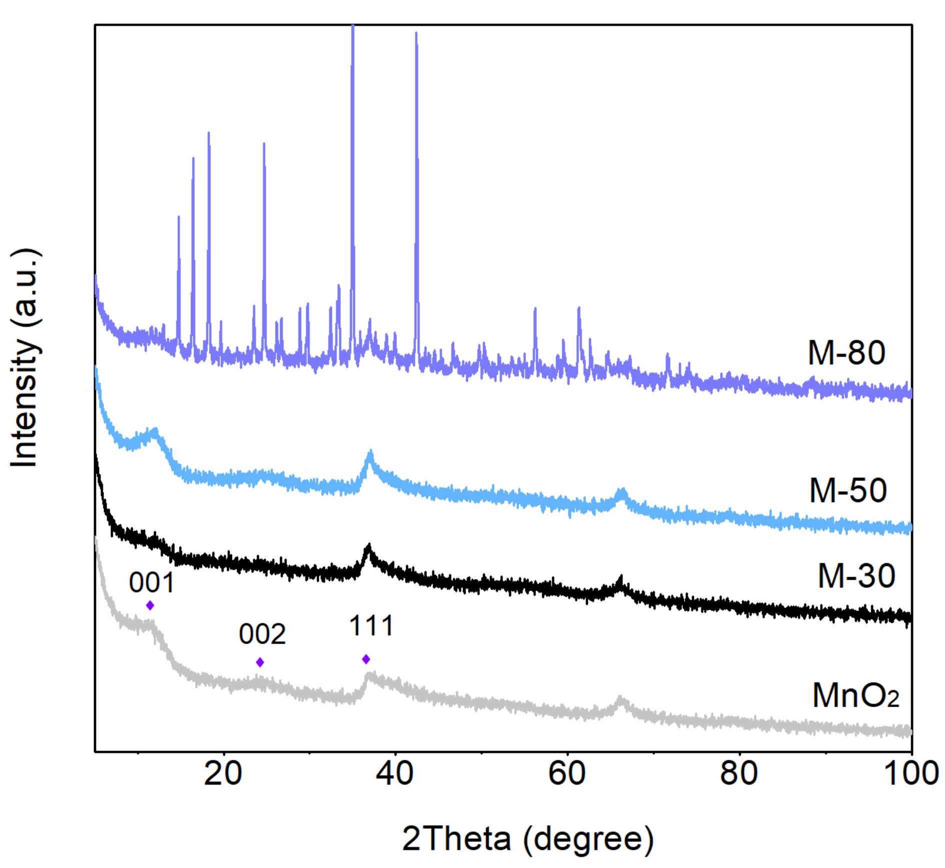

Figure S1 XRD patterns of δ-MnO_2, M-30, M-50 and M-80 samples.

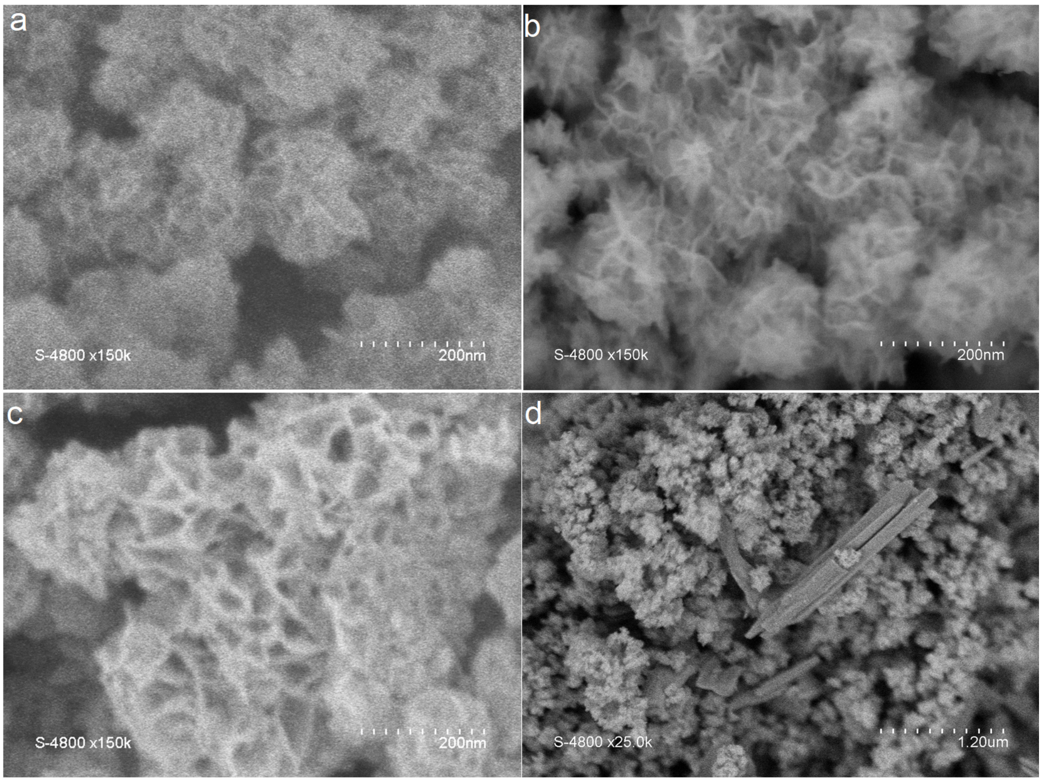

Figure S2 SEM images of δ-MnO_2 (a), M-30 (b), M-50 (c) and M-80 (d) samples.

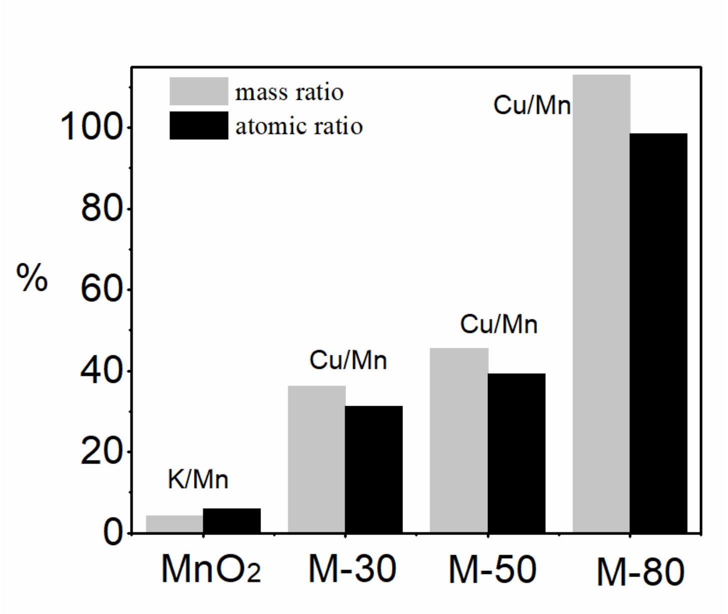

Figure S3 The element ratio of sample by EDX at various temperatures.

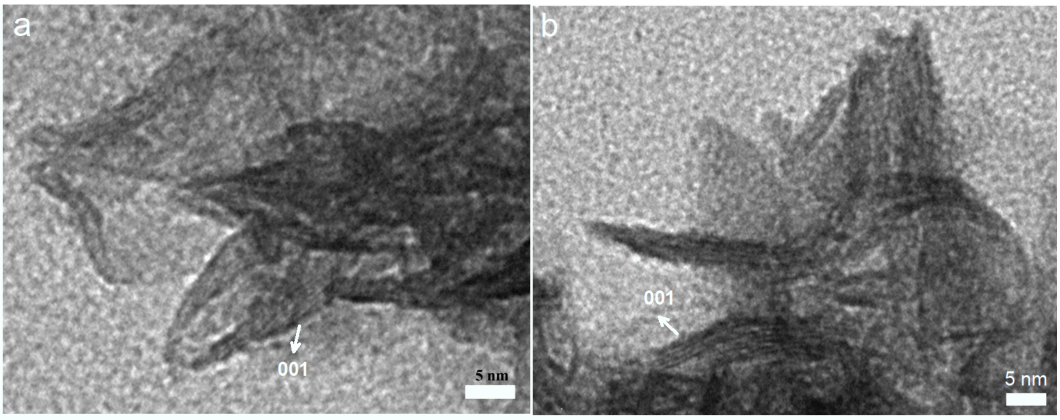

Figure S4 HRTEM images of pure MnO_2 (a) and M-1 (b).

From HRTEM images, the interlayer spacing of lattice fringe is assigned to (001) plane of MnO_2. By analyzing, the d-spacing of exposed MnO_2 lattice plane is 6.7 ± 0.6 Å. For M-1, the d-spacing is 7.3 ± 0.8 Å. The result can be explained by that the measurement of lattice spacing in HRTEM image has a big error. In the XRD analysis, the copper ion modified MnO_2 had a slightly right shift. This slight shift resulted in the small value change of d-spacing. This small change cannot be detected in HRTEM images.

Chapter 3 Design and fabrication of LDH@MnO_2 composites for supercapacitors

3.1 Abstract

High performance electrode materials are critical for the next generation of supercapacitors as they have to show complementary characteristics leading nano-engineered multi-functional composite materials to be considered. In this paper, we successfully designed a LDH@MnO_2 composite electrode material and synthesized it by using electrostatic interactions between exfoliated LDH and birnessite δ-MnO_2 nanoparticles. The optimal composition takes advantages of both components as LDH shows a battery like behavior, storing larger quantities of charges but over a limited number of charge/discharge cycles while MnO_2 displays a greater rate capability and cycle stability. Compared to an electrode based on pure MnO_2, with capacitance at 50 F g^{-1} and 15 F g^{-1} at current densities of 0.5 A g^{-1} and 10 A g^{-1}, respectively, the composite showed up to 308 F g^{-1} and 107 F g^{-1} capacitances at the same regimes. Compared to a LDH -based electrode that kept only 42 % of its initial capacities, the composite displayed 96 % of capacity retention over 4000 cycles at 5 A g^{-1}. A hybrid device with LDH/MnO_2 composite as positive electrode together with an activated carbon negative electrode showed an energy density of 19 Wh kg^{-1} at 400 W Kg^{-1} power density and 7 Wh Kg^{-1} at 10 kW Kg^{-1}.

3.2 Introduction

High power density, rapid charging/discharging and long cycle life are among the main characteristics of supercapacitors (SC)[1,2,3,4]. As in any other electrochemical systems, electrodes are critical components of an SC. As such, device performance strongly depends on those of the electrode materials[5]. Many works have been devoted to the elucidation of the charge-discharge mechanisms and the design of innovative supercapacitive (nanostructured) materials[6]. Many materials have been explored and designed as electrode for supercapacitors. Among them, the two dimensional (2D) materials[7] such as graphene[8], layered transition metal dichalcogenides[9], layered double hydroxides[10] and manganese dioxide (Birnessite type) impart and gain serious attention due to their strong in-plane chemical bond and weak van der Waals or moderate electrostatic coupling between layers[11, 12]. The layered structure is usually easy to delaminate by physical or chemical method, thus leading to a remarkable evolution in their morphological and electronic properties[13]. Moreover, distinct 2D material layers can eventually be restacked to generate new hybrid materials with controlled characteristics and tailored properties[14,15]. Thanks to synergistic effects, prepared composites show improved behaviors. We have used this promising strategy to construct a composite material that integrates a layered double hydroxides (LDH) and layered δ-MnO_2 within a single electrode material. LDHs[15] with a general formula of $[M^{2+}_{1-x}M^{3+}_{x}(OH)_2]^{x+}[A^{n-}_{x/n} \cdot mH_2O]^{x-}$, are composed of brucite-like $M^{2+}(OH)_2$ stacked layers in which some M^{2+} cations can be replaced by M^{3+} cations[16, 17]. The induced charge imbalance results in the intercalation of anions in between the layers to recover the neutrality of charge while stabilizing the layered structure[18]. Despite the electrostatic interaction between layers, LDH are easily delaminated. In the resulting suspension, solids are made of positively charged LDH layers, stabilized by solubilized cations. This state of charge of the LDH layers can provide a convenient path to the fabrication of composite materials by inducing electrostatic interactions with other materials bearing positive charges.[19,20] Generally, as a battery electrode material, LDH shows attractive capacity and fair energy density performance[21]. But the inner structure of LDH is not stable during charge-discharge processes, leading to its reversible swelling inducing strong mechanical stress detrimental to its cyclability. especially at faster charging regimes.[22]

MnO_2 crystallizes as many different polymorphs including α-MnO_2, β-MnO_2 and δ-MnO_2, showing various structural arrangements based on corner or edge - sharing MnO_6 octahedra. These can be developed through 1D tunnels (of various dimensions), 2D layers and more compact 3D structures. MnO_2 polymorphs have been reported as electrode materials for SC for many years[23]. Together with hydrated RuO_2, MnO_2 are often cited as reference pseudocapacitive materials.[24,25,26] In the latter, the electrochemical performance, especially specific capacitance, has been shown to mostly depend on the cationic conductivity of the chosen polymorph, while power is limited by the electronic conductivity of this oxide family.[27] Two dimensional δ-MnO_2 has stimulated many promising works because of its particular stacked layer structure leading to attractive electrochemical performances[28,29]. This 2D structure features the most suited ionic conductivity in the MnO_2 family allowing compensating cations involved in the charge/discharge mechanism to efficiently transfer in between the layers.[30,31,32] Therefore, δ-MnO_2, also known as Birnessite, shows the greatest capacitance and higher rate capability in the MnO_2 series. However, despite advanced development in device fabrication and testing at lab scale [33] and even commercialization initiative,[34]δ-MnO_2 perspectives suffer from an intrinsic poor electronic conductivity[35].

Despite its limited electronic conductivity, MnO_2 shows a way better power capability than any LDH -based battery electrode material and can be cycled over hundreds of thousand charge-discharge cycles. In contrast, LDH electrodes can achieve higher capacity (and should thus lead to devices with greater energy densities). The coupling of these two materials not only should deal with mentioned drawbacks, but should also take synergistically advantages of both LDH and MnO_2 components, consequently attaining greater electrode performance. In the present work, we first prepared bulk LDH material by a co-precipitation method. Then, we investigated the effects of the hydrothermal reaction time on the resulting MnO_2 powder morphology and structure. A LDH@MnO_2 composite material was successfully fabricated by a facile reaction involving the electrostatic interactions between layered LDH and birnessite δ-MnO_2. Some synergy effects were observed, especially when compared with pristine LDH electrode, including a great specific capacity coming from the LDH component, and improved rate capability and capacitance retention upon cycling from MnO_2 part.

3.3 Experimental section

Chemicals and reagents: Manganese chloride ($MnCl_2$) was purchased from Merck Schuchardt and nickel chloride ($NiCl_2$), from Fluka. $CoCl{\cdot}6H_2O$, Sodium hydroxide (NaOH), potassium permanganate ($KMnO_4$), hexamethylenetetramine (HMT), hydrochloric acid (HCl) and formamide were purchased from Sigma-Aldrich. All reagents were used as received without further purification.

Synthesis of nickel cobalt layered double hydroxide (LDH): NiCo-LDH material was prepared by a co-precipitation method. Typically, 1.25 mmol $CoCl·6H_2O$, 0.625 mmol $NiCl_2$ and various quantities of HMT (2.81 mmol, 5.63 mmol and 11.25 mmol) were dissolved in 250 ml H_2O by vigorous stirring. The resulting solutions were heated under reflux at 95 ^oC for 5 h. Finally, pink and green products, depending on the HMT quantity in the pristine solution, were obtained after filtration and drying at 80 ^oC. Samples were referenced as HMT-1, HMT-2 and HMT-3 for powders prepared from 2.81 mmol, 5.63 mmol and 11.25 mmol HMT quantities, respectively. The detailed preparation process is described in Figure S1.

Synthesis of MnO_2 powders: MnO_2 material was synthesized by a hydrothermal method. Typically, 1.66 mmol $KMnO_4$ were dissolved in 70 ml H_2O by stirring. Then, 1 ml 37 % HCl was added to the solution followed by stirring for 10 min in air. The solution was transferred into a stainless steel autoclave before being heated at 140 ^oC for a various duration (0.5h, 1h, 2h, 4h, and 8h). Samples are referred to the corresponding reaction time as M-0.5, M-1, M-2, M-4 and M-8. The detailed preparation process is described in Figure S2.

Synthesis of LDH@MnO_2 composite: The LDH@MnO_2 composite was synthesized by a self-assembling method based on the electrostatic interactions between the positively -charged LDH exfoliated layers and globally negatively -charged MnO_2 particles. Typically, 100 mg prepared HMT-3 and 100 mg M-2 were dispersed into 250 mL formamide/H_2O (1:1) solution. Then, the solutions were heated at 80 ^oC for 12 h under constant stirring in a sealed vial to get a homogeneous suspension. Various weight ratios of LDH and MnO_2 (2:3, 1:1 and 3:2) were used. 10 mL 0.5 M NaOH were added dropwise under constant stirring for 1 hour to disrupt the suspension equilibrium state. Finally, the composite was obtained after filtration and drying at 80 ^oC. Resulting powders are referenced in the following as L@M-1, L@M-2 and L@M-3depending on the LDH/MnO_2 weight ratio at 2:3, 1:1 and 3:2, respectively. A scheme of the synthetic process is shown in Figure 3.1.

3.4 Characterization

X-ray diffraction (XRD) measurements were performed using a Phillips X'Pert diffractometer with Cu Kα radiation (λ=1.5405Å). The morphology and inner structure were imaged using a JEOL JSM-6300F scanning electron microscope (SEM) and MET 1200EX2 transmission electron microscope (TEM).

3.5 Electrochemical measurements

Electrochemical experiments were conducted with a VMP3 multi-channel Bio-Logic electrochemical workstation. The electrochemical performance was evaluated by cyclic voltammetry (CV) and galvanostatic charge/discharge (GCD) experiments. Experiments were performed in both three- and two-electrode setups. For the three-electrode setup, the working electrode was composed of 60% of active materials, 30% of carbon black, and 10% of polytetrafluoroethylene (PTFE). The mixture was first dispersed in ethyl alcohol, and the resulting suspension was heated at 60°C to slowly form a slurry. The slurry was transferred on a smooth glass substrate, and carefully rolled as a film. After drying at 90°C, the film was cut as circle patches that were pressed onto a stainless steel mesh under 10 MPa. A 6 M KOH aqueous solution was used as electrolyte. A Hg/HgO electrode and a platinum foil were used as reference electrode and counter electrode, respectively. For the two-electrode device in 6 M KOH electrolyte, prepared materials were used as positive electrode, and active carbon as negative electrode. The negative mass of active carbon and positive electrode was balanced by using equation (1)[36]. Besides, the power density and energy density were evaluated by using equations (2)[37] and (3)[38].

$$m_+/m_- = \Delta V_- C_- / \Delta V_+ C_+ \qquad (1)$$

$$E = (C \times \Delta V^2) / 7.2 \qquad (2)$$

$$P = E \times 3600 / t \qquad (3)$$

Where C (F g^{-1}) is the specific capacitance, ΔV is the voltage window, E (Wh kg^{-1}) is the energy density, P (W kg^{-1}) is the power density.

The below related supporting information has been attached after reference.

3.6 Results and discussion

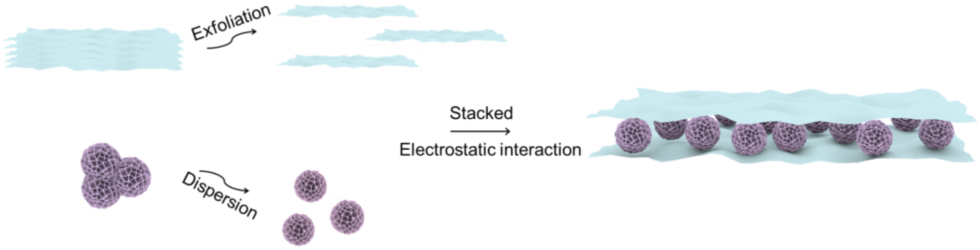

Figure 3.1 Schematic diagram of the preparation process of LDH@MnO_2 hybrid material.

Before the preparation of LDH@MnO_2 composite, we first investigated the structure and morphology of pure LDH and MnO_2 powders. LDHs were prepared by co-precipitating Co and Ni precursors using hexamethylenetetramine (HMT). Figure S3 shows the structural changes in HMT-1, HMT-2 and HMT-3 powders induced by the increase in the HMT content from 2.8 mmol, 5.6 mmol and 11.25 mmol in the pristine solution containing cobalt and nickel chlorides. In HMT-1 XRD pattern, diffraction peaks are characteristic of an hydrotalcite crystal structure[39]. As the HMT content was increased, the corresponding patterns show peaks of nickel hydroxide of increasing intensities, signifying that more nickel hydroxide stacked layer by layer which was triggered by more HMT. For MnO_2, Figure S4 evidences the structural changes occurred as the hydrothermal reaction time was increased. For 0.5h, 1 h and 2h long hydrothermal treatments, powder crystallinities were poor but δ-MnO_2 was unambiguously identified. With the (001) peak at 12.08 2θ getting more intense and shaper, the powder crystallinity obviously improved with reaction time. For longer time, after 4 h and 8 h reactions, α-MnO_2 was obtained. The presence of some remaining δ-MnO_2 traces after 4 hours of treatment cannot be excluded from XRD analysis, but after 8 hours this phase was fully converted and only α-MnO_2 was recovered. Composite materials were obtained by mixing the prepared LDH and MnO_2 powders in a formamide/water solution. This highly polar medium is known to favor the exfoliation of layered materials including LDHs and δ-MnO_2.[15,40,41] The composite synthetic approach is based on the electrostatic assembling of LDH and MnO_2 layers of opposite charges. The XRD patterns of the prepared composites are shown in Figure 3.2. Whatever the LDH/MnO_2 ratio at 2:3, 1:1 or 3:2, patterns of the resulting L@M-1, L@M-2 and L@M-3 powders, respectively, all show diffraction peaks of both components, LDH and MnO_2. As it could be anticipated for a simple physical mixture. However, the loss of crystallinity is indicative that some material structural transformations occurred when powders were in contact with the formamide/water solution, especially for the LDH component. For MnO_2, the amorphization is obviously less marked. A first analysis attempt of the XRD patterns suggests that LDH is rather efficiently exfoliated as more or less individual but positively charged layers in the solution while MnO_2 particles are mostly remaining in their pristine structural and morphological state, As negatively charged particles stabilized by cations at their surface, they electrostatically attract LDH layers that wrap the particles to form a LDH@MnO_2 composite material (Figure 3.1).

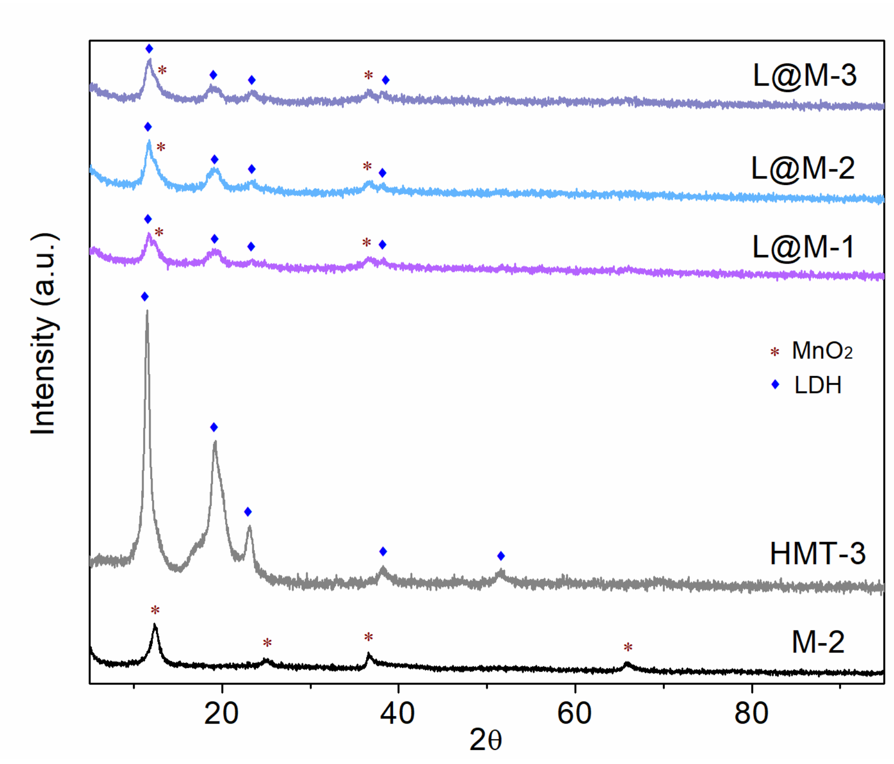

Figure 3.2 XRD patterns of pure LDH, MnO_2 and LDH@MnO_2 hybrid.

The texture and morphology of pure LDH and MnO_2 were first imaged by SEM. The morphology changes when using various HMT contents are evidenced in Figure S5. For HMT-1 powder (from the lowest HMT content in the series), hexagonal shape platelets were obtained. As the HMT content is increased during the syntheses for HMT-2, HMT-3 and HMT-4 samples, pristine hexagonal platelets seemed to merge to form larger flat micro-structures. The evolution of MnO_2 powder morphology when adjusting the reaction time was also investigated by SEM (Figure S6). For M-0.5 as well as for M-1, the powder morphologies displayed a layered spherical structure, sand-rose like, blurred by some surface floccules. However, after 2 hours reaction, the distinct and clean layered structure of M-2 was evidenced. While the reaction time was extended to four hours and more, some lamellas were progressively converted as fiber-like structures. These results are consistent with the XRD pattern analysis which reveals the changes of the crystal structure (Figure S4 and corresponding comments above). The morphologies of L@M-1, L@M-2 and L@M-3 powders are shown in Figure 3.3. The sand-rose -like structure of manganese dioxide was well retained in the samples but particles were covered and wrapped by LDH layers. As shown in Figure 3.3c to 3.3f, there is not much difference between the composite morphologies despite an increase of the LDH loading. In addition, the detailed imaging of the material morphologies was carried out by transmission electron microscope (TEM) as shown in Figure S7. Figure S7a and S7b show the sand-rose morphology of M-2 sample holding a petal-like structure. The high resolution TEM image in Figure S7b displays lattice fringes characteristic of the layered structure of the prepared material. The measured interplanar spacing at 0.72 nm corresponds to the (001) crystal plane of δ-MnO_2. Figure S7c shows large flat LDH layers. The inner morphology of L@M-2 composite is shown in Figure S7d and S7e. These micrographies confirm the presence of roughly spherical MnO_2 particles are embedded/wrapped in/by LDH layers. Such a result reveals the intimate interaction between LDH and MnO_2 components.

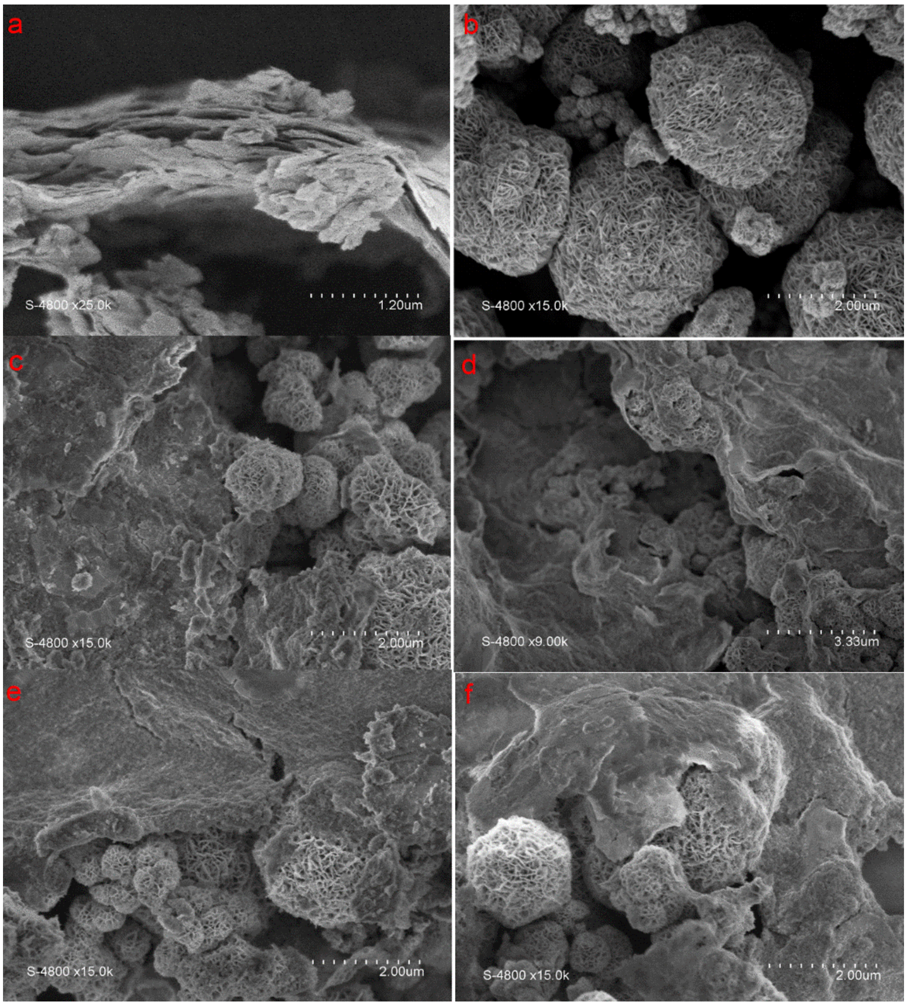

Figure 3.3 SEM images of HMT-3 (a), M-2 (b), L@M-1 (c), L@M-2 (d, e) and L@M-3 (f).

Likewise, electrochemical characteristics of prepared pure MnO_2 and LDH were first explored. Results are shown in Figure S8 and S9. As expected, the rectangular shapes of CVs of MnO_2 -based electrodes in Figure S8a are characteristic of a pseudocapacitive behavior. Specific capacitances were extracted from CV integration as well as from galvanostatic measurements (Figure S8b). Data are reported in Table S1, unambiguously show that capacitances decreased as the reaction time was increased. The greatest capacitance in the series was at 69 F g^{-1} for the electrode from M-0.5 material (at 0.5 A g^{-1}), prepared after 30 minutes autoclaving. For the longest reaction time of 8 hours, the capacitance of M-8 was only 14 Fg^{-1} (at 0.5 A g^{-1}). This capacitance ranking is fully consistent with the XRD phase analysis above (and

Figure S4) as the layered structure of δ-MnO_2 (predominant phase in M-0.5 to M-2) is more favorable to charge storage than the tunneled α-MnO_2 (found in M-4 and M-8). As expected for MnO_2 -based electrodes, the capacitance retention upon scan rate is rather limited, especially for materials prepared after the shortest autoclaving time (M-0.5 to M-2) corresponding to δ-MnO_2. For electrodes mostly incorporating α-MnO_2 (M-4 and M-8), the capacitance retention is known to be better but capacitances are however the lowest in the series.[27]. On the electrode stability upon cycling, capacitance retention was, in contrast, found to weakly depend on the composition and therefore, on the autoclaving duration. As an example of the remarkable stability of MnO_2 based electrodes, M-2 retained 98 % of its initial capacitance after 2000 cycles of charge-discharge at 5 A g^{-1} current density. On the over hand, LDH electrode materials (HMT series) show a typical Faradaic redox behavior (Figure S9a and S9b). Electrode capacity depends on the HMT quantity used to prepare the corresponding LDH electrode materials. The HMT-3 electrode exhibits the largest capacities in the series at 84 mAh g^{-1} (Table S2). However, as previously shown, capacities of prepared LDH electrodes quickly faded down with charge/discharge rate[42,43]. For example, at 8 A g^{-1}, HMT-3 electrode retains only 1/10th of its capacity at 1 A g^{-1} and shows a neglectable capacity at 10 A g^{-1}. The cycle stability of HMT-3 electrode at 5 A g^{-1} is shown in Figure S9d. Nothing surprising for such battery-like material, after 2000 charge-discharge cycles, the capacity faded down to 60 % compared to that at first cycle. Electrochemical results on L@M composite electrodes are shown in Figure 3.4. For ease of comparison, together with CVs and galvanostatic curves of L@M-1, L@M-2 and L@M-3 those of HMT-3 and M-2 are also depicted. These can be commented in both terms of shape and intensity. L@M composite electrodes obviously show a complex Faradaic behavior, mostly battery-like. CVs in Figure 3.4a show two oxidation peaks, one at about 0.3-0.35 V vs Hg/HgO, a second in the range from 0.45 to 0.5 V vs Hg/HgO. By comparison, they can tentatively be assigned to Ni^{2+}/Co^{2+} (LDH) and Mn^{3+} (MnO_2) oxidation, respectively. But for L@M-3 electrode, a single peak can be observed for Ni^{3+}/Co^{3+} reduction below 0.2 V vs Hg/HgO. Another drastic difference when comparing the CV of the LDH -based electrode with those based on the L@M composite is about the voltage differences between oxidation and corresponding reduction peaks of the LDH component. It is rather large for HMT-3 electrode at 0.34 V while strongly decreased when coupling LDH and MnO_2 in the L@M composites, down to 0.12 V for the L@M-1 electrode. This decrease of the peak to peak separation suggets that energy barrier for the activation of the involved redox reaction decreases, so that Ni/Co electrochemical reactions are easier to be activated and to proceed in the composite material. Specific capacitances/capacities were also measured by galvanostatic charge-discharge measurements at various charge/discharge current densities. Corresponding data are displayed in Figure 3.4c. The limited rate capability of LDH HMT-3 is confirmed as the capacity at 84 mAh g^{-1} at 0.5 A g^{-1} faded down to almost zero at 10 A g^{-1}. When MnO_2 is involved, either as pure M-2 electrode material or as part of the L@M composites, the capacitance/capacity retention is improved. Although, performances at low current densities are not as great as for HTM-3 -based electrode, these materials can sustain better rate capabilities. As such, for L@M-2 as well as L@M-3, measured capacities are greater than those for HTM-3 electrode for current densities at 7 A g^{-1} and above. One would argue at this stage, that rate capabilities of the composites are arising from MnO_2 component but, L@M-2 and L@M-3 composite behaviors are almost the same despite a greater MnO_2 loading in the latter. In addition, the introduction of δ-MnO_2 also provide the composite material electrode with enhanced cycle stability, especially for L@M-2 material. After 2000 charge-discharge cycles, this L@M-2 -based electrode still holds 86 % of its initial capacity, while HMT-3 LDH-based electrode only retained 60 % of its capacity at first cycle. As such, L@M-2 composite is the most performing material in the series, either in terms of rate capability and capacity retention upon cycling.

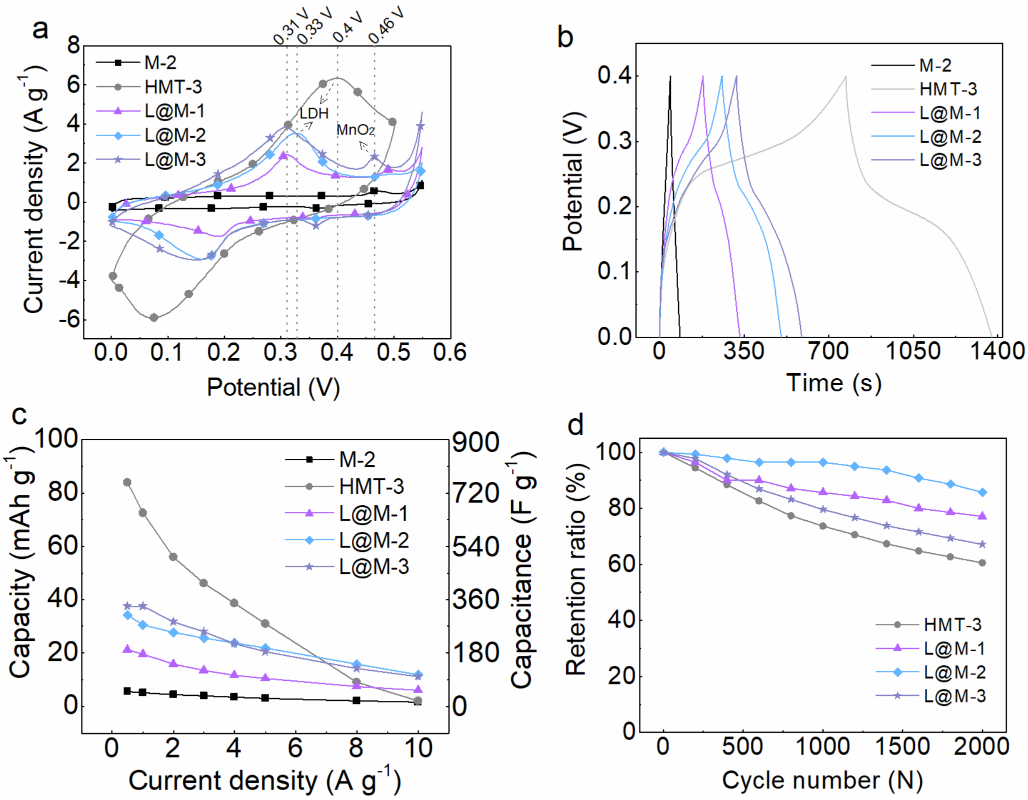

Figure 3.4 Electrochemical characteristics of M-2, HMT-3, L@M-1, L@M-2 and L@M-3 electrodes with 6 M KOH electrolyte solution in three electrode system (a) Comparison of cyclic voltammetry curves (CV) of all samples at a scan rate of 5 mV s^{-1}. (b) Galvanostatic charge-discharge (GCD) curves at a current density of 0.5 A g^{-1}. (c) Specific capacity of all samples at various current densities; capacitance values are given for comparison purpose (d) Cycle stability of all electrode at a current density of 5A g^{-1} in 2000 cycles.

Further electrochemical investigation of electrochemical performance was carried out in a two electrode system. It was built by using L@M-2 composite material as the positive electrode and activated carbon (AC) as the negative one. The results for the L@M-2//AC device are shown in Figure 3.5. CVs measured at scan rates from 5 to 100 mV s^{-1} in Figure 3.5a are characteristic of an asymmetric supercapacitor associating a AC double layer electrode material and a Faradaic redox material. The corresponding capacitance and equivalent series resistance (ESR from ohmic drop) were calculated from galvanostatic charge-discharge measurements (see Figure 3.5b). For comparison purpose, similar measurements were done on a HMT-3//AC hybrid device built using a positive HMT-3 LDH positive battery-type electrode and an AC -based negative EDLC electrode. Therefore, corresponding Ragone plots were obtained. They are shown in Figure 3.5d. The energy density (based on whole weight of two electrodes) of of the L@M-2//AC device is 19 Wh kg^{-1}. In contrast, the HMT-3//AC device, with a 48 Wh kg^{-1} energy density, takes advantage of the LDH battery behavior and performance. However, this attractive energy density drastically faded down at higher power. In contrast, L@M-2//AC device surpasses the HMT-3//AC device in terms of power. But the most severe discrepancy is about device capacitance retentions upon cycling. This is clearly evidenced in Figure 3.5c as the L@M-2//AC device retains 95 % of its initial capacitance while HMT-3//AC loose about 60% of it after 4000 charge-discharge cycles. Characteristic of the poor cyclability of the LDH battery material most of the hybrid device capacitance loss arrises during the first 1000 cycles.

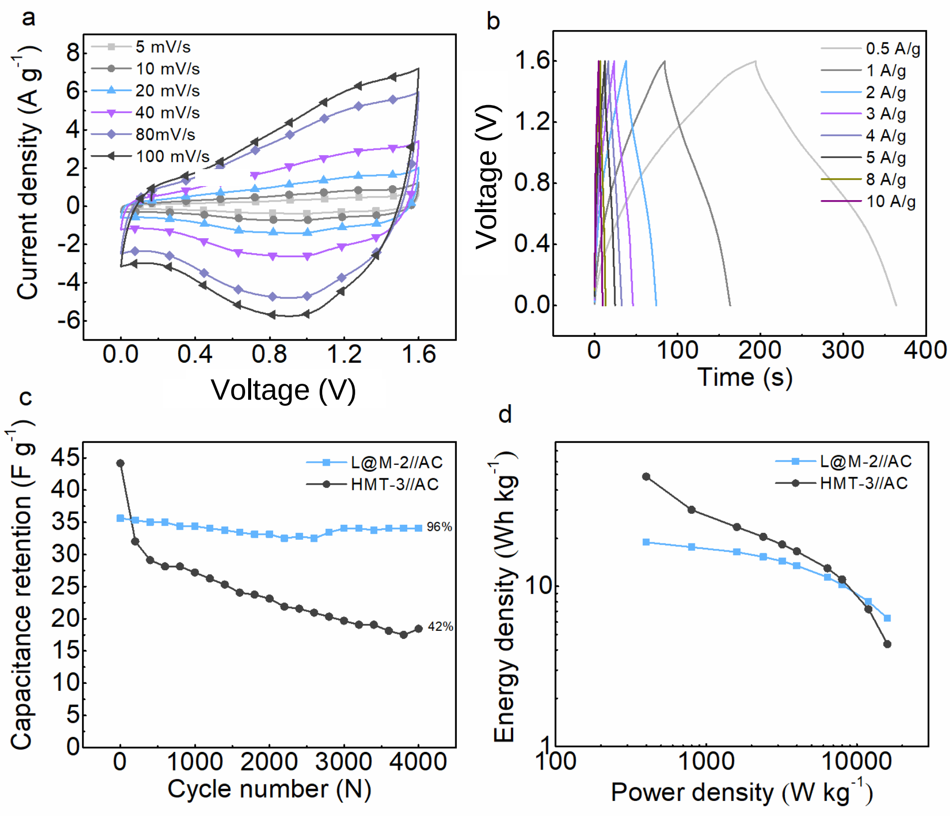

Figure 3.5 Electrochemical characteristics of L@M-2 // AC device (a) Cyclic voltammetry curves at various scan rates. (b) Galvanostatic charge-discharge curves at various current densities. (c) Cycle stability at a current density of 5 A g^{-1} in 4000 cycles. (d) Ragone plots of L@M-2 // AC and HMT-3//AC device.

3.7 Conclusion

This work introduces an original and facile method to prepare LDH@MnO_2 nano-composites by taking advantage of electrostatic interactions between exfoliated LDH layers and δ-MnO_2 birnessite spherical particles. As expected, LDH electrode has a limited rate capability and cycle stability because of its Faradaic battery-like behavior. In contrast, δ-MnO_2 electrode shows better electrode performance on both sides. The designed LDH@MnO_2 composite takes advantage of both components. Thanks to the interaction effect at the nanoscale, the L@M-2 composite used as electrode material, presented attractive electrochemical performance in a three electrode configuration including high specific capacitances upon charge-discharge rate and improved cycle stability. Furthermore, the hybrid supercapacitor device, L@M-2//AC, revealed fair cycle stability and power/energy densities, especially in comparison with a LDH-based device, HMT-3//AC.

Acknowledgements

Y. C. ZHU (NO. 201606240097) is supported by China Scholarship Council (CSC).

This chapter is submitting as an article.

3.8 Reference

1. Y. Wang, Y. Song and Y. Xia, Electrochemical capacitors: mechanism, materials, systems, characterization and applications, Chem. Soc. Rev., 2016, 45, 5925.

2. P. Jezowski, O. Crosnier, E. Deunf, P. Poizot, F. Béguin and T. Brousse, Safe and recyclable lithium-ion capacitors using sacrificial organic lithium salt, Nature Materials, 2018, 17, 167.

3. S. Uppugalla, U. Male and P. Srinivasan, Design and synthesis of heteroatoms doped carbon/polyaniline hybrid material for high performance electrode in supercapacitor application, Electrochimica Acta, 2014, 146, 242.

4. Z. Chen, etal., F. Wei, and Y. Lu, Design and Synthesis of Hierarchical Nanowire Composites for Electrochemical Energy Storage, Adv. Funct. Mater. 2009, 19, 3420.

5. X. Xia, etal., H. Zhang and H. J. Fan, A New Type of Porous Graphite Foams and Their Integrated Composites with Oxide/Polymer Core/Shell Nanowires for Supercapacitors: Structural Design, Fabrication, and Full Supercapacitor Demonstrations, Nano Lett. 2014, 14, 1651.

6. X. Yu, S. Yun, etal., Emergent Pseudocapacitance of 2D Nanomaterials, Adv. Energy Mater. 2018, 1702930.

7. X. Zhang, L. Hou, A. Ciesielski, and P. Samorì, 2D Materials Beyond Graphene for High-Performance Energy Storage Applications, Adv. Energy Mater. 2016, 1600671.

8. R. Liu, Y. Zhang, Z. Ning and Y. Xu, A Catalytic Microwave Process for Superfast Preparation of High-Quality Reduced Graphene Oxide, Angew. Chem. Int. Ed. 2017, 56, 15677.

9. R. Lv, etal., T. E. Mallouk and M. Terrones, Transition Metal Dichalcogenides and Beyond: Synthesis, Properties, and Applications of Single- and Few-Layer Nanosheets, Acc. Chem. Res. 2015, 48, 56.

10. H. Liang, etal., W. Fei and J. Feng, Hierarchical NiCo-LDH@NiOOH core-shell heterostructure on carbon fiber cloth as battery-like electrode for supercapacitor, Journal of Power Sources, 2018, 378, 248.

11. K. S. Novoselov, A. Mishchenko, A. Carvalho and A. H. Castro Neto, 2D materials and van der Waals heterostructures, Science, 2016, 353, 6298.

12. R. Mas-Ballesté, C. Gomez-Navarro, J. Gomez-Herrero and F. Zamora, 2D materials: to graphene and beyond, Nanoscale, 2011, 3, 20.

13. Q. Wang, K. Zadeh, A. Kis, J. N. Coleman, and M. S. Strano, Electronics and optoelectronics of two-dimensional transition metal dichalcogenides, Nature Nanotechnology 2012, 7, 699.

14. Y. Xue, Q. Zhang, W. Wang, H. Cao, Q. Yang, and L. Fu, Opening Two-Dimensional Materials for Energy Conversion and Storage: A Concept, Adv. Energy Mater. 2017, 1602684.

15. Quan, W.; Jiang, C.; Wang, S.; Li, Y.; Zhang, Z.; Tang, Z.; Favier, F. New Nanocomposite Material as Supercapacitor Electrode Prepared via Restacking of Ni-Mn LDH and MnO2 Nanosheets. Electrochim. Acta 2017, 247, 1072–1079. https://doi.org/10.1016/j.electacta.2017.07.010.

15. L. Yu, J. Yang, B. Guan, Y. Lan and X. Wen, Hierarchical Hollow Nanoprisms Based on Ultrathin Ni-Fe Layered Double Hydroxide Nanosheets with Enhanced Electrocatalytic Activity towards Oxygen Evolution, Angew. Chem. Int. Ed. 2018, 57, 172.

16. B.Wang, etal., Fa. Zhao and L. Liu, Two steps in situ structure fabrication of NieAl layered double hydroxide on Ni foam and its electrochemical performance for supercapacitors, Journal of Power Sources 246 (2014) 747.

17. H. Chen, L. Hu, M. Chen, Y. Yan and L. Wu, Nickel–Cobalt Layered Double Hydroxide Nanosheets for High-performance Supercapacitor Electrode Materials, Adv. Funct. Mater. 2014, 24, 934.

18. A. Forticaux, L. Dang, H. Liang and S. Jin, Controlled Synthesis of Layered Double Hydroxide Nanoplates Driven by Screw Dislocations, Nano Lett. 2015, 15, 3403.

19. Acharya, H.; Srivastava, S. K.; Bhowmick, A. K. Synthesis of Partially Exfoliated EPDM/LDH Nanocomposites by Solution Intercalation: Structural Characterization and Properties. Compos. Sci. Technol. 2007, 67 (13), 2807–2816. https://doi.org/10.1016/j.compscitech.2007.01.030.

20. Kang, H.; Huang, G.; Ma, S.; Bai, Y.; Ma, H.; Li, Y.; Yang, X. Coassembly of Inorganic Macromolecule of Exfoliated LDH Nanosheets with Cellulose. J. Phys. Chem. C 2009, 113 (21), 9157–9163. https://doi.org/10.1021/jp900861k.

21. P. Vialat, etal., E. Elkaim and F. Leroux, High-Performing Monometallic Cobalt Layered Double Hydroxide Supercapacitor with Defined Local Structure, Adv. Funct. Mater. 2014, 24, 4831.

22. J. Xiao, L. Wan, S. Yang, F. Xiao and S. Wang, Design Hierarchical Electrodes with Highly Conductive $NiCo_2S_4$ Nanotube Arrays Grown on Carbon Fiber Paper for High-Performance Pseudocapacitors, Nano Lett. 2014, 14, 831.

23. J. Yan, Q. Wang, T. Wei, and Z. Fan, Recent Advances in Design and Fabrication of Electrochemical Supercapacitors with High Energy Densities, Adv. Energy Mater. 2014, 4, 1300816.

24. Choi, C.; Ashby, D. S.; Butts, D. M.; DeBlock, R. H.; Wei, Q.; Lau, J.; Dunn, B. Achieving High Energy Density and High Power Density with Pseudocapacitive Materials. Nat. Rev. Mater. 2020, 5 (1), 5–19. https://doi.org/10.1038/s41578-019-0142-z.

25. Augustyn, V.; Simon, P.; Dunn, B. Pseudocapacitive Oxide Materials for High-Rate Electrochemical Energy Storage. Energy Environ. Sci. 2014, 7 (5), 1597–1614. https://doi.org/10.1039/c3ee44164d.

26. Sun, J.; Wu, C.; Sun, X.; Hu, H.; Zhi, C.; Hou, L.; Yuan, C. Recent Progresses in High-Energy-Density All Pseudocapacitive-Electrode-Materials-Based Asymmetric Supercapacitors. J. Mater. Chem. A 2017, 5 (20), 9443–9464. https://doi.org/10.1039/c7ta00932a.

27. Ghodbane, O.; Pascal, J. L.; Favier, F. Microstructural Effects on Charge-Storage Properties in MnO 2-Based Electrochemical Supercapacitors. ACS Appl. Mater. Interfaces 2009, 1 (5), 1130–1139.

28. Gao, P.; Metz, P.; Hey, T.; Gong, Y.; Liu, D.; Edwards, D. D.; Howe, J. Y.; Huang, R.; Misture, S. T. The Critical Role of Point Defects in Improving the Specific Capacitance of δ-MnO2 Nanosheets. Nat. Commun. 2017, 8 (1), 14559. https://doi.org/10.1038/ncomms14559.

29. Wang, H.; Zhang, J.; Hang, X.; Zhang, X.; Xie, J.; Pan, B.; Xie, Y. Half-Metallicity in Single-Layered Manganese Dioxide Nanosheets by Defect Engineering. Angew. Chemie - Int. Ed. 2015, 54 (4), 1195–1199. https://doi.org/10.1002/anie.201410031.

30. Yeager, M.; Du, W.; Si, R.; Su, D.; Marinković, N.; Teng, X. Highly Efficient K 0.15MnO 2 Birnessite Nanosheets for Stable Pseudocapacitive Cathodes. J. Phys. Chem. C 2012, 116 (38), 20173–20181. https://doi.org/10.1021/jp304809r.

31. Toupin, M.; Brousse, T.; Bélanger, D. Charge Storage Mechanism of MnO2 Electrode Used in Aqueous Electrochemical Capacitor. Chem. Mater. 2004, 16 (16), 3184–3190. https://doi.org/10.1021/cm049649j.

32. Ghodbane, O.; Ataherian, F.; Wu, N.-L.; Favier, F. In Situ Crystallographic Investigations of Charge Storage Mechanisms in MnO2-Based Electrochemical Capacitors. J. Power Sources 2012, 206 (2012), 454–462. https://doi.org/10.1016/j.jpowsour.2012.01.103.

33. Brousse, T.; Taberna, P.-L.; Crosnier, O.; Dugas, R.; Guillemet, P.; Scudeller, Y.; Zhou, Y.; Favier, F.; Bélanger, D.; Simon, P. Long-Term Cycling Behavior of Asymmetric Activated Carbon/MnO2 Aqueous Electrochemical Supercapacitor. J. Power Sources 2007, 173 (1), 633–641. https://doi.org/10.1016/j.jpowsour.2007.04.074.

34. https://en.wikipedia.org/wiki/Aquion_Energy.

35. Y. Liu, D. Yan, etal., P. Yan and Z. Geng, Design, hydrothermal synthesis and electrochemical properties of porous birnessite-type manganese dioxide nanosheets on graphene as a hybrid material for supercapacitors, Journal of Power Sources, 2013, 242, 78.

36 L. Li, Mi. Zhang, X. Zhang and Z. Zhang, New Ti_3C_2 aerogel as promising negative electrode materials for asymmetric supercapacitors, Journal of Power Sources, 2017, 364, 234.

37. Y. Wang and Y. Xia, Recent Progress in Supercapacitors: From Materials Design to System Construction, Adv. Mater. 2013, 25, 5336.

38. G. Zhu, etal., Z. Jin and J. Liu, Pine needle-derived microporous nitrogen-doped carbon frameworks exhibit high performances in electrocatalytic hydrogen evolution reaction and supercapacitors, Nanoscale, 2017, 9, 1237.

39. Yang, J. Yu, C. Hu, C. Wang, M. Li, S.; Huang, H. Bustillo, K. Han, X. Zhao, C. Guo, W. Zeng, Z. Zheng, H. Qiu, J., Surface-Confined Fabrication of Ultrathin Nickel Cobalt-Layered Double Hydroxide Nanosheets for High-Performance Supercapacitors. Adv. Funct. Mater. 2018, 28 (44), 1–11. https://doi.org/10.1002/adfm.201803272.

40. Ma, R. Liu, Z. Li, L. Iyi, N. Sasaki, T., Exfoliating Layered Double Hydroxides in Formamide: A Method to Obtain Positively Charged Nanosheets. J. Mater. Chem. 2006, 16 (39), 3809–3813. https://doi.org/10.1039/b605422f.

41. Huang, S. Peng, H. T. Jiu, W. W. Yang, Z. Zhu, H. Tang, T. Liu, T., Assembling Exfoliated Layered Double Hydroxide (LDH) Nanosheet/Carbon Nanotube (CNT) Hybrids via Electrostatic Force and Fabricating Nylon Nanocomposites. J. Phys. Chem. B 2010, 114 (50), 16766–16772. https://doi.org/10.1021/jp1087256.

42. A.D. Jagadale, G. Guan, X. Li, X. Du, X. Ma, X. Hao, A. Abudula, Ultrathin nanoflakes of cobalt-manganese layered double hydroxide with high reversibility for asymmetric supercapacitor, J. Power Sources. 306 (2016) 526–534. https://doi.org/10.1016/j.jpowsour.2015.12.097.

43. Y. Wang, H. Dou, J. Wang, B. Ding, Y. Xu, Z. Chang, X. Hao, Three-dimensional porous MXene/layered double hydroxide composite for high performance supercapacitors, J. Power Sources. 327 (2016) 221–228. https://doi.org/10.1016/j.jpowsour.2016.07.062.

Supporting information

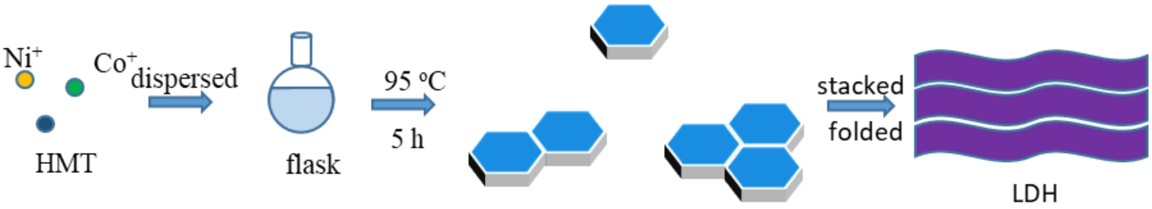

Figure S1 Schematic diagram of preparation process of LDH.

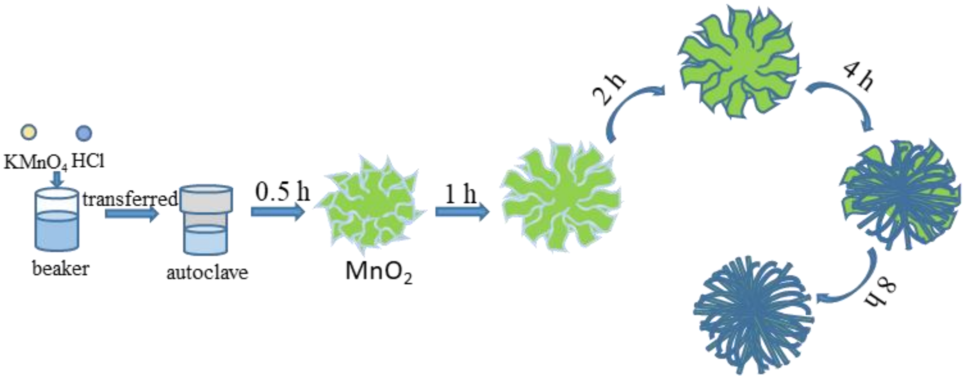

Figure S2 Schematic diagram of MnO_2 fabrication process.

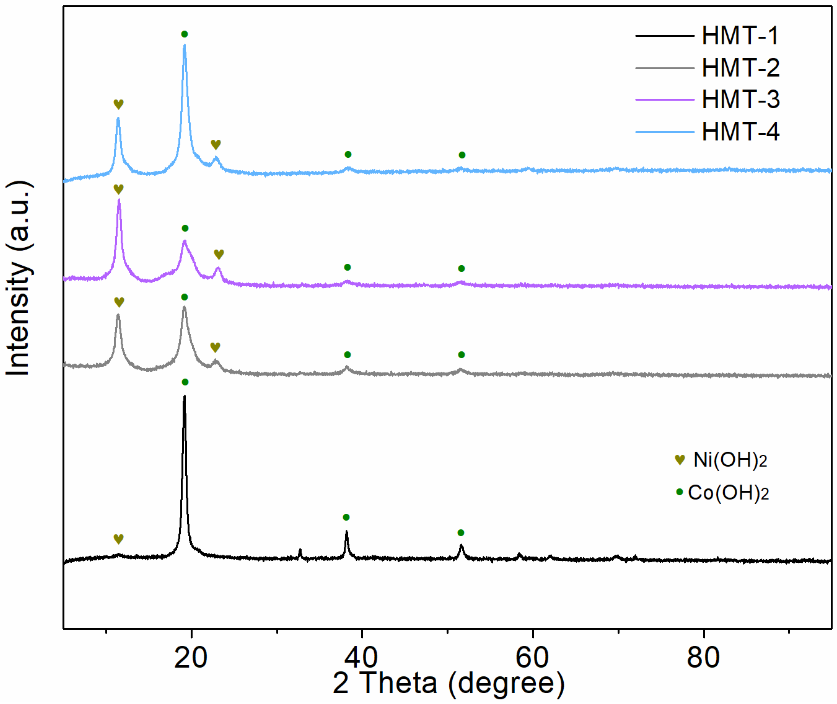

Figure S3 XRD patterns of pure LDH material.

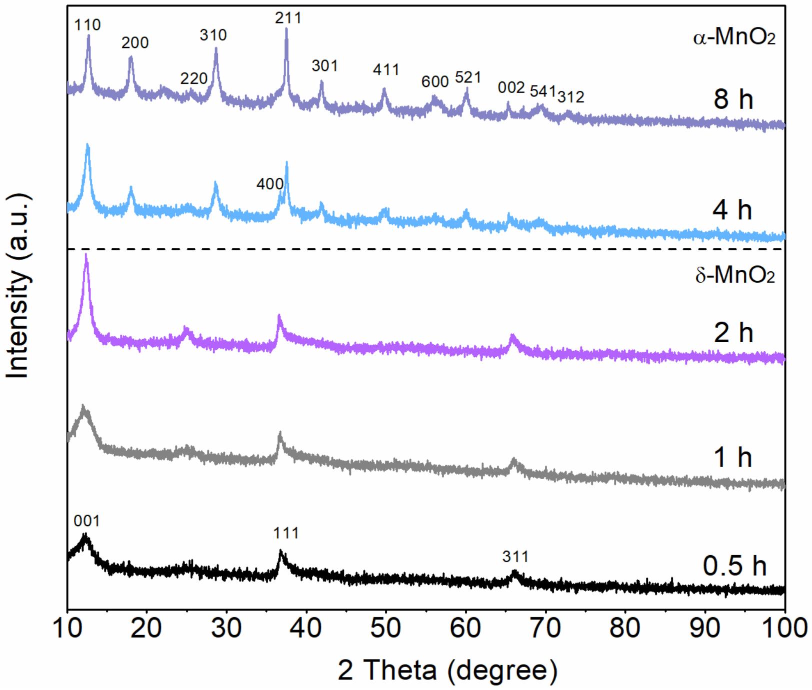

Figure S4 XRD patterns of pure MnO_2.

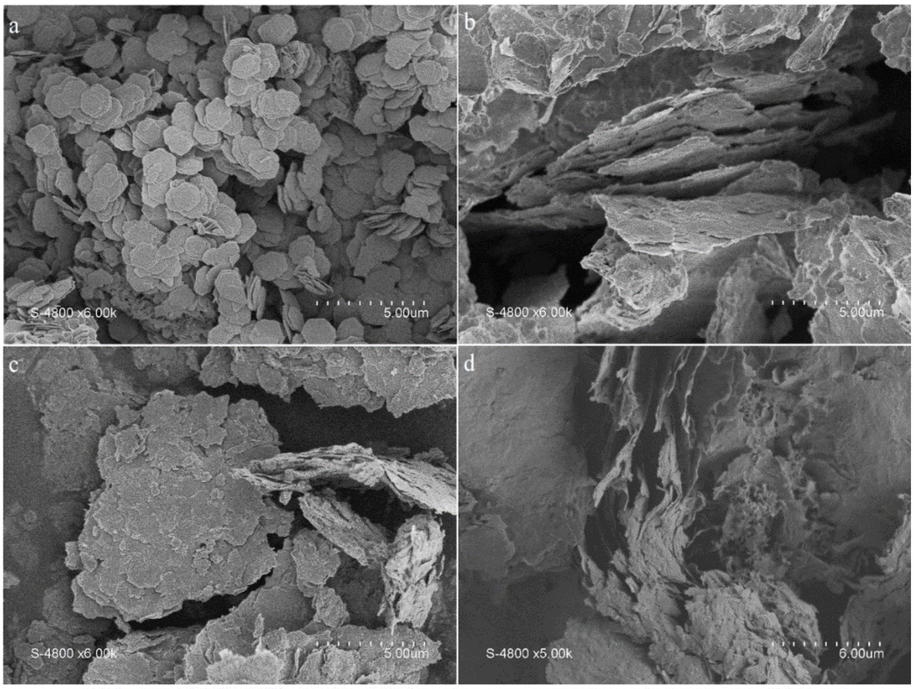

Figure S5 SEM images of HMT-1 (a), HMT-2 (b), HMT-3 (c) and HMT-4 (d).

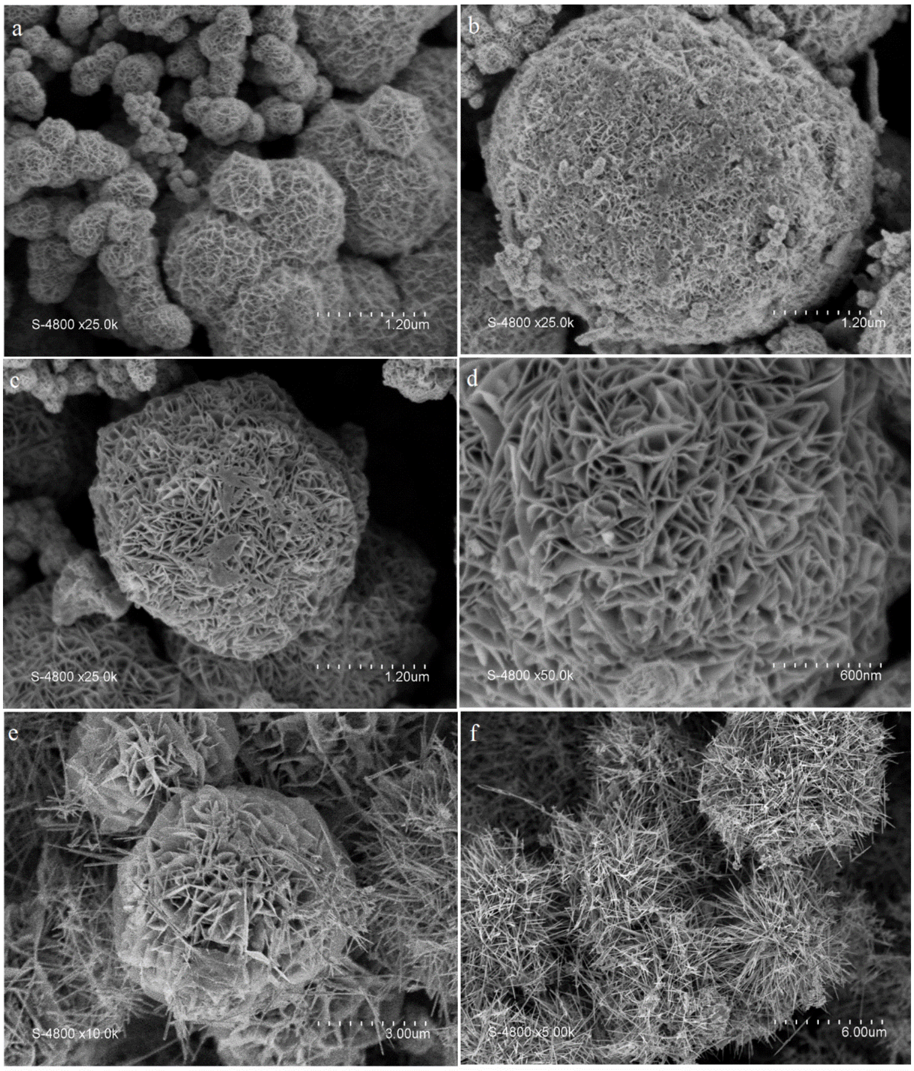

Figure S6 SEM images of M-0.5 (a), M-1 (b), M-2 (c, d), M-4 (e) and M-8 (f).

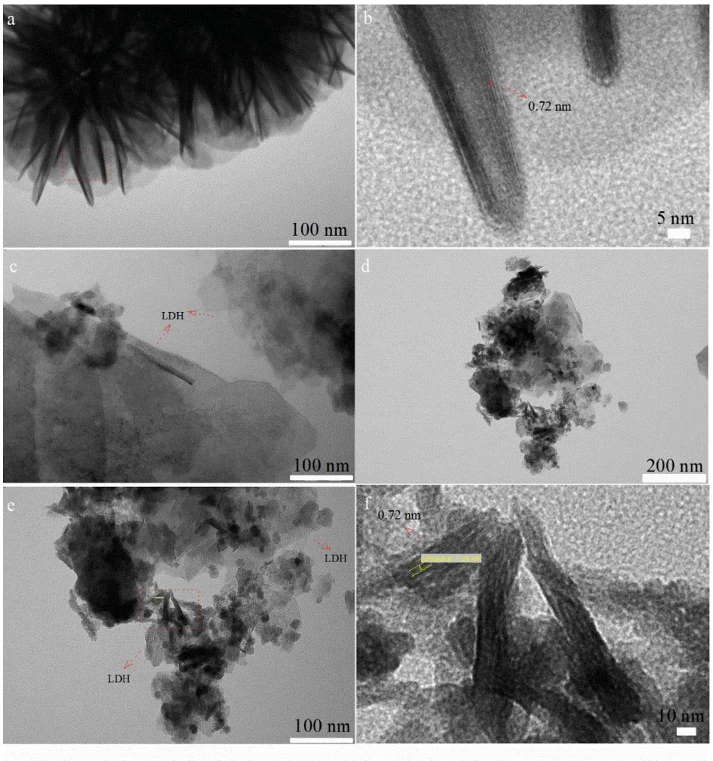

Figure S7 TEM images of M-2 (a, b), HMT-3 (c) and L@M-2 (d-f) samples.

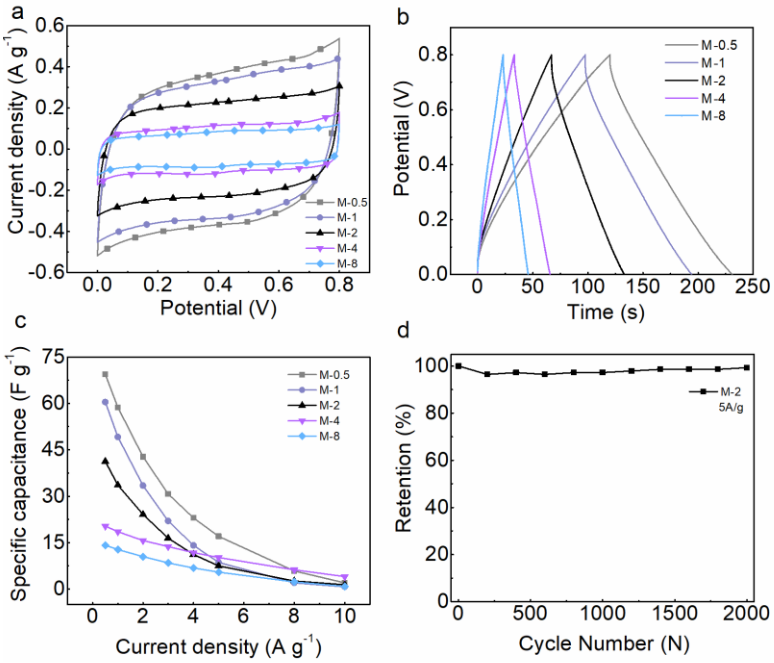

Figure S8 Electrochemical characteristics of M-0.5, M-1, M-2, M-4 and M-8. (a) Comparison of cyclic voltammetry (CV) curves of all samples at a scan rate of 5 mV s^{-1}. (b) Galvanostatic charge-discharge (GCD) curves of samples at a current density of 0.5 A g^{-1}. (c) Specific capacitance of samples at various current densities. (d) Cycle stability of M-5 at a current density of 5 A g^{-1} current density in 2000 cycles. Measurements were done in KOH 6M.

Table S1 Specific capacitances of extracted from CVs and galvanostatic measurements for electrodes fabricated from M-0.5, M-1, M-2, M-4 and M-8 MnO_2 materials.

Capacitances in F g^{-1}	M-0.5	M-1	M-2	M-4	M-8
From cyclic voltammetry at 5 mV s^{-1}	63	56	50	26	22
From galvanostatic measurements at 0.5 A g^{-1}	69	60	41	20	14

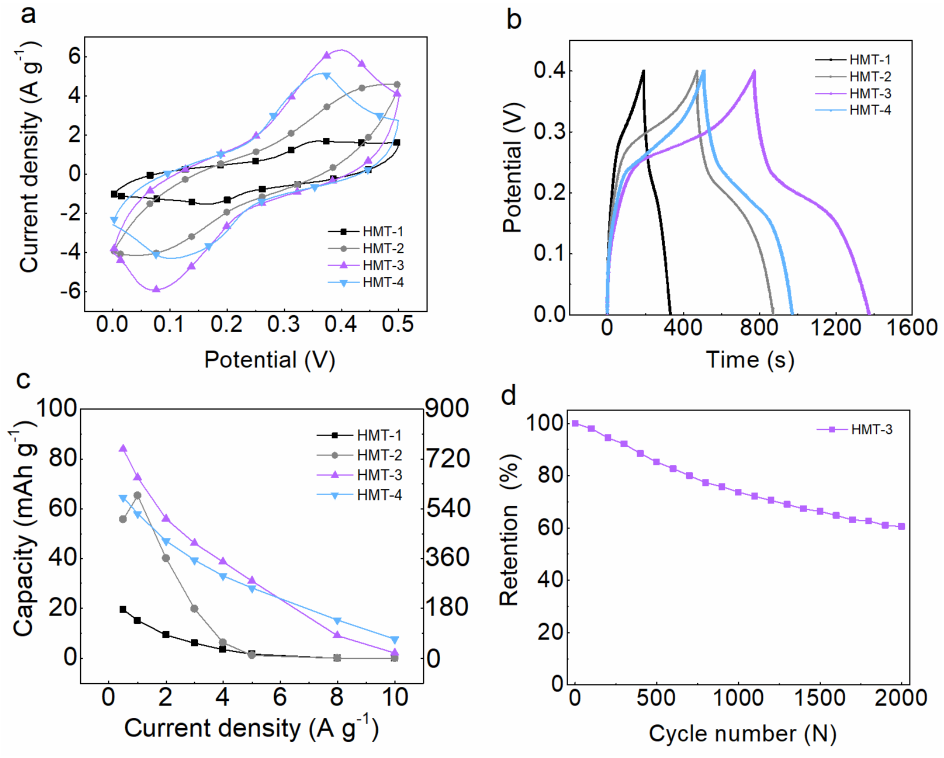

Figure S9 Electrochemical characteristics of HMT-1, HMT-2, HMT-3 and HMT-4 samples. (a) Comparison of cyclic voltammetry (CV) curves at a same scan rate of 5 mV s^{-1}. (b) Galvanostatic charge-discharge (GCD) curves at a current density of 0.5 A g^{-1}. (c) Specific capacitance at various current densities. (d) Cycle stability of HMT-3 at 5 A g^{-1} current density in 2000 cycles. Measurements were done in KOH 6M.

Table S2 Specific capacitancies of extracted from CVs and galvanostatic measurements for electrodes fabricated from HMT-1, HMT-2, HMT-3 and HMT-4 LDH materials. For ease of comparison corresponding capacitances are given in parenthesis

Capacities	HMT-1	HMT-2	HMT-3	HMT-4
From cyclic voltamemtry at 5 mV s^{-1}	21 mAh g^{-1}	56 mAh g^{-1}	85 mAh g^{-1}	40 mAh g^{-1}
From galvanostatic measurements at 0.5 A g^{-1}	20 mAh g^{-1} (176 F g^{-1})	56 mAh g^{-1} (501 F g^{-1})	84 mAh g^{-1} (756 F g^{-1})	65 mAh g^{-1} (581 F g^{-1})

Chapter 4 MnO_2-MXene composite as electrode for supercapacitor

4.1 Abstract

A MnO_2 - MXene composite material is reported, in which MnO_2 particles have been grown onto Ti_3C_2 MXene layers. Thanks to its interconnected structure, it can not only boost the low electrical conductivity of MnO_2, but also suppress the restacking of MXene flakes. As an electrode material in a three-electrode cell, the composite showed higher capacitance and better stability performance than raw MnO_2 in both KOH and Na_2SO_4 aqueous electrolytes. Equipped with MnO_2 – MXene composite material as positive and activated carbon as negative, an asymmetric device using Na_2SO_4 as electrolyte displayed an energy density of 20 Wh kg^{-1} at 500 W kg^{-1} power density. On the other hand, the device operated in KOH electrolyte showed an energy density of 16.8 Wh kg^{-1} at 400 W kg^{-1}, and 11 Wh kg^{-1} at 8 kW kg^{-1}.

4.2 Introduction

Supercapacitors (SCs)[1], including electrochemical double-layer capacitors (EDLCs)[2] and redox-based pseudocapacitors[3], have been extensively studied as promising and efficient candidate for energy storage systems thanks to many attractive features that advantageously supplement those of batteries[4]. These include high power density, fast charge-discharge rate and long cycle life[5,6]. In contrast, their energy density is lower. Carbon-based EDLCs[7] usually show high rate capability thanks to their electrostatic charge storage mechanism based on the reversible adsorption-desorption of electrolytic ions onto the large surface area of the electrode material during quick charge-discharge processes[8]. Various materials such as porous carbons[9-14] and graphene[15-17] have been explored as electrode materials and more than 90% of the supercapacitors commercialized worldwide are activated carbon -based EDLC devices. On the other hand, oxide-based pseudocapacitive materials[18] store the charge through fast and reversible redox reactions near the surface of the material, leading to attractive capacitances[19,20]. In comparison with EDLCs, energy density is greater thanks to the Faradaic contribution but because of the kinetics of the involved redox reactions (intrinsically slower than electrosorption), power is less attractive. Many metal oxides such as RuO_2[21-24] and MnO_2[25-27] have been confirmed as suitable pseudocapacitive electrode materials. The impact on the storage performance of both electronic and crystallographic structures of the oxides has been demonstrated.[28-32]. As an example, storage performance, including rate capabilities, has been demonstrated to depend on the structure of the pseudocapacitive oxide. This is especially true with MnO_2 polymorphs built on 1 to 3D structures, either on channeled, layered or compact arrangements allowing the more or less efficient solid-state diffusion of compensating cations involved in the charge storage mechanism.[35-38] On the other hand, the poor intrinsic electronic conductivity of MnO_2 limits its overall rate capability, which inhibits the electrode capacitance to reach the theoretical value at ~1380 F g^{-1}.[33,34] As such, improving the electronic conductivity of MnO_2-based electrode materials remains a consistent strategy to reach greater performance, especially rate capability, and, consequently, greater device power.

Recently, two-dimensional transition metal nitrides/carbides (MXenes)[39,40] have been successfully prepared by etching of A layers from MAX phases, giving a few atoms thick layered extended family with a general formula $M_{n+1}X_nT_x$, where M represents a transition metal, X is C and/or N, and T_x stands for surface terminations[41-43]. Thanks to their high accessible surface areas promoted by a 2D structure as well as the high electrical conductivity of the carbide-core layer (~4,000 $S.cm^{-1}$), MXene materials can achieve attractive electrochemical performance in aqueous electrolytes, with a capacitance beyond 250 F g^{-1} or 1,500 $F.cm^{-3}$ [44-50].

Back in 2016, Rakhi et al has reported on the synthesis and electrochemical characterization of MnO_2 nanowhiskers on MXene surfaces[51]. This is the ε form of MnO_2, also known as MnO_2 Ramsdelite, which was actually precipitated at the surface of exfoliated flakes of Ti_3C_2. The Ramsdelite structure is built on edge-sharing MnO_6 octaedra in a 1x2 configuration forming channels in which alkali cations are stabilizing the structural arrangement, Therefore, its 1D structure provides ε-MnO_2 with a fair ionic conductivity and, consequently, a pseudocapacitive behavior in neutral aqueous electrolytes with fair charge storage capabilities when used as electrode material in a supercapacitor[52]. As such, these authors claimed up to 212 F g^{-1} capacitance (at 1 A g^{-1} current density) could be obtained with an electrode based on the prepared ε-MnO_2/Ti_3C_2 composite cycled in a 30wt% KOH electrolyte. Despite this attractive performance and the elegance of the synthetic approach, we think there is still room for improvement. This, especially by considering more performing MnO_2 polymorphs to decorate the Ti_3C_2 MXene flakes. This could be MnO_2 birnessite, or δ-MnO_2, which has shown up to twice the capacitance, as electrode material, than that of Ramsdelite thanks to its more open 2D layered structure[52]. Rakhi et al choose to use a symmetric two electrode setup while an asymmetric device with an activated carbon negative electrode, for example, would have been more realistic to discuss power and energy densities. Moreover, they limited their study to a single KOH based electrolyte while MnO_2, as a pseudocapacitive electrode material, is known to show enhanced electrochemical performance when operated in safer neutral sulfate or nitrate - based aqueous electrolytes.[53,54,55,56] Data in Table S1 and associated references are supporting these observations. With the objective to select a more performing MnO_2 material to be incorporated in a nanocomposite with Ti_3C_2 MXene, we initially studied changes in the crystalline structure of MnO_2 and associated electrochemical performance, correlated with the preparation temperature. Interestingly, when increasing the temperature, a material based on layers (δ-MnO_2) together with fibers (α-MnO_2) was obtained, showing an attractive cooperative electrochemical behavior taking advantage of the greater capacitance from the δ phase and greater rate capability from the α phase. Furthermore, exfoliated MXene was used to prepare a composite material in which MnO_2 particles were grown, at the selected temperature, on MXene layers providing an improved conductivity and preventing the restacking of MXenes flakes. Thanks to these advanced features, the MnO_2eMXene (MeM) composite electrode was first evaluated in terms of specific capacitance, rate and cycling capabilities either in KOH and Na_2SO_4 electrolytes. The composite and activated carbon were used as positive and negative electrode, respectively, to fabricate an asymmetric device. Thanks to the large potential window of 2V in Na_2SO_4, AC//MeM-Na device showed attractive energy and power densities. In KOH electrolyte, AC//MeM-K device showed slightly lower but fair energy and power performance.

4.3 Materials and methods

Preparation of Ti_3C_2 MXene suspension and film

1 g LiF and 20 mL of 9 M HCl were mixed and stirred in a plastic bottle. After a few minutes, 1 g Ti_3AlC_2 grey powder was gradually added to the mixture. The etching process was kept at 35 ^{o}C for 24h under constant stirring. Accordingly, Ti_3C_2 MXene flakes were rinsed off by ultrapure water to rise the pH of the effluent up to about 6. After re-dispersing MXene flakes in 250 mL pure water, the flakes were exfoliated by sonication for one hour. The un-exfoliated Ti_3C_2 material was removed away by centrifugation for 1 h. Finally, Ti_3C_2 MXene suspension was obtained. The MXene film was prepared by an easy one-step method. In more details, a given mass of MXene suspension in water was slowly filtered on a PTFE membrane under vacuum. The resulting Ti_3C_2 MXene film was dried in a glass tube under vacuum before storage and use.

Preparation of MnO_2 by co-precipitation

0.1272 g $MnCl_2$ and 0.24 g $KMnO_4$ were respectively dispersed in ultra-pure 20 mL H_2O under constant stirring. Then the $KMnO_4$ solution was added drop by drop to the $MnCl_2$ solution (5 minutes duration operation). The resulting suspension was transferred in a laboratory reflux apparatus and heated at a 120 ^{o}C setpoint temperature for 6 h. After filtration, collected brown MnO_2 powders were dried at 80 ^{o}C in air. Additionally, the effect of the co-precipitation temperature was investigated and syntheses were conducted at 30, 80, 140 °C setpoint temperatures. Corresponding samples are referred as M-30, M-80, M-120 and M-140 depending on the temperature the powder was prepared.

Preparation of MnO_2eMXene

20 mL of a mixture with 20.0 mg Ti_3C_2 MXene and 127.2 mg $MnCl_2$ was first prepared. Using the procedure as described above for the preparation of raw MnO_2, 20 mL $KMnO_4$ solution was slowly added and the resulting suspension was kept at a temperature of 120 °C, for 6 h. This synthesis temperature was

chosen for reasons explained below. After drying, the MnO_2eMXene composite material was obtained.

4.4 XRD, SEM, TEM sampling and equipment

X-ray diffraction patterns of the prepared materials were obtained using a Phillips X'Pert diffractometer with Cu Kα radiation (λ=1.5405Å) in a Bragg-Brentano configuration. A JEOL JSM-6300F scanning electron microscope (SEM) was used to investigate the powder morphologies. Sampling was done on dry powders on carbon tape. The Energy-dispersive X-ray spectroscopy (EDX) and mapping in SEM was applied to analyze elemental compositions and distributions. Transmission electron microscopy (TEM) measurements were done using a JEOL 1200EX2 TEM instrument. Sampling was done on carbon-copper grids.

4.5 Electrochemical characterization

A VMP3 multi-channel Bio-Logic electrochemical workstation was used for all the electrochemical measurements done at controlled room temperature (23 °C) in a three-electrode configuration as well as in a Swagelok setup. Electrode discs were fabricated by first mixing the prepared materials (60%), acetylene black (30%) and PTFE (10%) in ethanol. The resulting paste was then rolled as a film, finally cut as 8 mm diameter round samples using a puncher tool. In the three-electrode setup, the working electrode was the synthesized materials, the reference electrodes were Hg/HgO (KOH) and Ag/AgCl (Na_2SO_4), and the counter electrode was a platinum foil. Gravimetric capacitances were normalized to the active material weight. The mass loadings of pure MnO_2 are displayed in Table S2. The weight loadings of composite are 6.4 and 6.0 mg cm^{-2}, respectively. In the asymmetric device, a commercial activated carbon (PICA) was used as negative electrode. Electrode mass balancing was done by considering capacitances calculated from CVs done on individual electrodes in selected electrolytes. The electrode loading is at about 6.0 mg cm^{-2}.

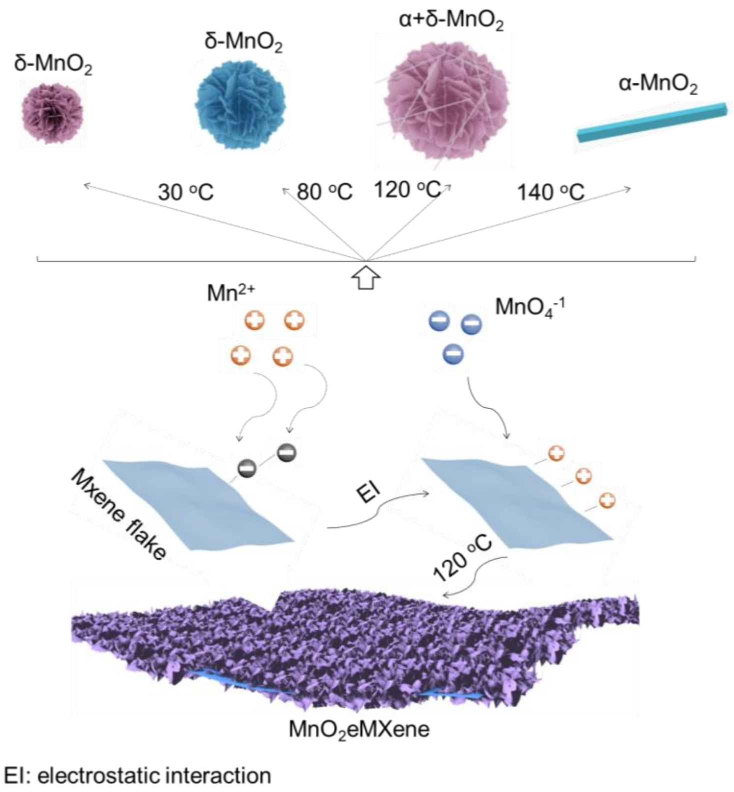

Figure 4.1 Schematic diagram of material preparations.

The below related supporting information has been attached after reference.

4.6 Results and discussion

MnO$_2$ powders were prepared by a co-precipitation method using Mn^{2+} and MnO$_4^{-1}$ as reductant and oxidant, respectively (Figure 4.1, top). Depending on the synthesis temperature (from 80 to 140 °C), resulting MnO$_2$ materials exhibited some discrepancies in their crystalline structure from δ to α phase, additionally following morphological changes from nano sheets to nano fibers. Furthermore, Ti$_3$C$_2$ MXene flakes were used as a template to grow MnO$_2$ by the same co-precipitation method at a synthesis temperature of 120 °C, eventually resulting in a nanostructured MnO$_2$eMXene composite (Figure 4.1, bottom).

Structural changes in MnO$_2$ powders induced by the preparation temperature have been evidenced by XRD measurements (Figure S1). For MnO$_2$-30 (black), MnO$_2$-80 (grey) and MnO$_2$-120 (blue) samples, corresponding to MnO$_2$

powders prepared at 30, 80 and 120 °C, respectively, diffraction peaks are indexed and correspond to δ-MnO_2 (Birnessite, JCPDS 1098[57,58]). This manganese dioxide morphotype shows a layered structure built on 2D layers of edge-sharing [MnO_6] octahedra. Whereas, a clear difference in the crystal structure is distinctly revealed in the XRD pattern of the MnO_2-140 sample, prepared at 140 °C. It exhibits a series of new peaks as well as the absence of the (001) peak previously at 66.28 °2θ. This pattern matches that of α-MnO_2 (Hollandite, JCPDS 44-0141) whose structure is built on 1D tunnels (2x2 edge-sharing MnO_6 octahedra). A closer look at the MnO_2-120 XRD pattern also shows some extra peaks of lower intensity, especially at 56.21 °2θ which corresponds to the (600) diffraction peak of the α-type structure. This suggests a mixture, mostly made of δ-MnO_2 and some α-MnO_2, to be obtained at 120 °C.

As the reaction temperature was increased, the powder morphologies evolved consistently with the structural changes pointed out by XRD analysis. The micro-morphology of prepared powders was studied by scanning electron microscope measurements. In Figure S2, the expected δ-MnO_2 “sand rose” morphologies are clearly observed in MnO_2-30 and MnO_2-80. These roughly spherical particles are made of disordered aggregated MnO_2 platelets. In contrast, at 140 °C, α-MnO_2 nano-rods and needles are mostly observed, together with a few “sand rose” particles. Finally, as suggested by XRD analysis, MnO_2-120 sample is confirmed as a mixture of both types of δ-MnO_2 and α-MnO_2 nano-crystals.

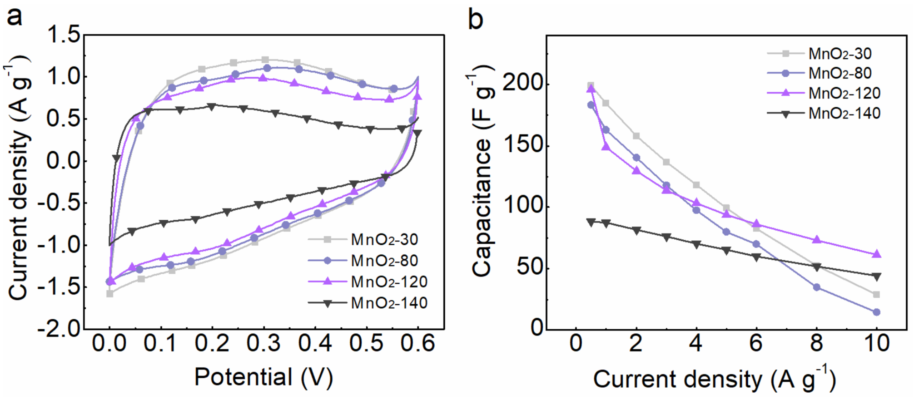

Figure 4.2 Electrochemical performances comparison of MnO_2 with various reaction temperatures in 1 M KOH. (a) Cyclic voltammetry curves at 5 mV s^{-1} scan rate. (b) Specific capacitances comparison at various current densities.

Electrodes based on the prepared MnO_2 materials were tested in a three-electrode setup in 1 M KOH electrolyte with the objective to evaluate the impact of their structure/morphology on their electrochemical behavior. Corresponding capacitances were calculated from cyclic voltammetry measurements at 5 mV s^{-1} scan rate from 0 to 0.6 V versus Hg/HgO reference electrode (Figure 4.2a). Capacitances are detailed in Table S1 but a direct observation of the CV areas allows to compare the various electrode material performance: MnO_2-30 electrode CV displays the largest area in the series and correspondingly, the greatest capacitance at 181 F g^{-1}. As the synthesis temperature was increased, the capacitance of the resulting material decreased, and MnO_2-140 showed the lowest capacitance in the series at 98 F g^{-1}. This evolution is assigned to the structural characteristics of the prepared MnO_2. δ-MnO_2 2D structure has been shown to be highly favorable to the diffusion in between MnO_2 layers of electrolytic cations involved in the charge storage mechanism. As such, corresponding capacitances are the greatest in the MnO_2-based electrode material family[52]. In contrast, α-MnO_2 built on more constraining 1D channels is less performing either in terms of ionic conductivity and capacitance. Measured electrode capacitances are actually related to the δ-MnO_2/α-MnO_2 composition ratio. They decrease as the α-MnO_2 content increases while increasing the synthesis temperature. Capacitances were measured at various charge-discharge rates by galvanostatic measurements (Figure 4.2b). Similarly, to CV measurements, it was found that, at a low current density such as 0.5 A g^{-1}, MnO_2-30 and MnO_2-80 electrode materials, mostly composed of δ-MnO_2, showed larger capacitances than α-MnO_2-rich material such as MnO_2-140. However, capacitances of MnO_2-30 and MnO_2-80 quickly decreased as the current density was increased. For example, the capacitance of MnO_2-30 -based electrode was 29 F g^{-1} and that of MnO_2-80 was 14 F g^{-1} at 10 A g^{-1}. The rate capabilities of these electrodes are as such, fairly limited. In contrast, while the capacitance of MnO_2-140 was limited to 88 F g^{-1} at 0.5 A g^{-1}, it was still 44 F g^{-1} at 10 A g^{-1}. Finally, not only could MnO_2-120 electrode deliver a high capacitance of 196 F g^{-1} at 0.5 A g^{-1}, but it also retained a 62 F g^{-1} capacitance at 10 A g^{-1}. This latter electrode behavior can be explained by its specific composition based on a mixture of δ- and α-MnO_2. At low current density, δ-MnO_2 provides the electrode with its attractive low rate capacitance, while α-MnO_2 component favorably contributes to the capacitance at high current density. Thanks to this peculiar composition in the series, MnO_2-120 electrode material offers the best compromise in terms of rate capabilities, with enhanced capacitances in a wider range of charge-discharge regimes. Because of these well balanced electrochemical properties, 120 °C synthesis temperature was chosen for the preparation of MnO_2eMXene composite based on the precipitation of MnO_2 at the surface of exfoliated Ti_3C_2 MXene flakes. Besides, interestingly, a broad peak is observed in cyclic volumetry of δ-MnO_2 but not pure α-MnO_2 measured in KOH electrolyte. The wide peak can be attributed to the existing of redox reaction during charging-discharging. Over redox process, the alkali cations are intercalated/extracted in the bulk of oxide particles, thereby following the reduction/oxidation of Mn crystal phase.[52] As we mentioned above, the δ-MnO_2 shows an open 2D layered crystal structure, while α-MnO_2 has a 1D crystal channels. Various crystal forms of MnO_2 lead to different electrochemical mechanisms.[28] For α-MnO_2, the distinct redox wave is not noticed in its cyclic volumetry result. It can be interpreted that the intercalation/extraction of alkali cations are limited by the narrow 1D channels nature. The charge mechanism occurred on its surface, on which alkali cations are adsorbed/desorbed during charging-discharging process.[59]

X-ray diffraction (XRD) patterns of the prepared raw MnO_2-120 and MnO_2eMXene composite materials are depicted in Figure 4.3. As expected, MnO_2 powder prepared at 120 °C corresponds to the above described mixture made of δ-MnO_2 (mainly) and some α-MnO_2. The XRD pattern of the Ti_3C_2 MXene shows the usual features of restacked 2D materials with a series of diffraction peaks of decreasing intensity at greater diffraction angle. These correspond to the (002n) atomic layers of Ti_3C_2 MXene and are consistently measured at angles corresponding to the interlayer distance. The XRD pattern of the composite material obtained by precipitation of MnO_2 in presence of exfoliated Ti_3C_2 MXene layers at 120 °C retains the characteristics of the poorly crystallized MnO_2-120 material. Actually, only remain the main peaks from the pristine MnO_2. In contrast, the intense 002 peak of the MXene component almost completely vanishes. This is a proof that this synthetic method prevents exfoliated MXene layers to restack in the composite. This XRD analysis suggests that δ-MnO_2 actually grows at the surface of Ti_3C_2 MXene layers. Moreover, a tendency of the MnO_2 layers to grow parallel to those of MXene is supported by the greater intensity of the (006) peak, characteristic of a preferential orientation of the MnO_2 layers in the composite.

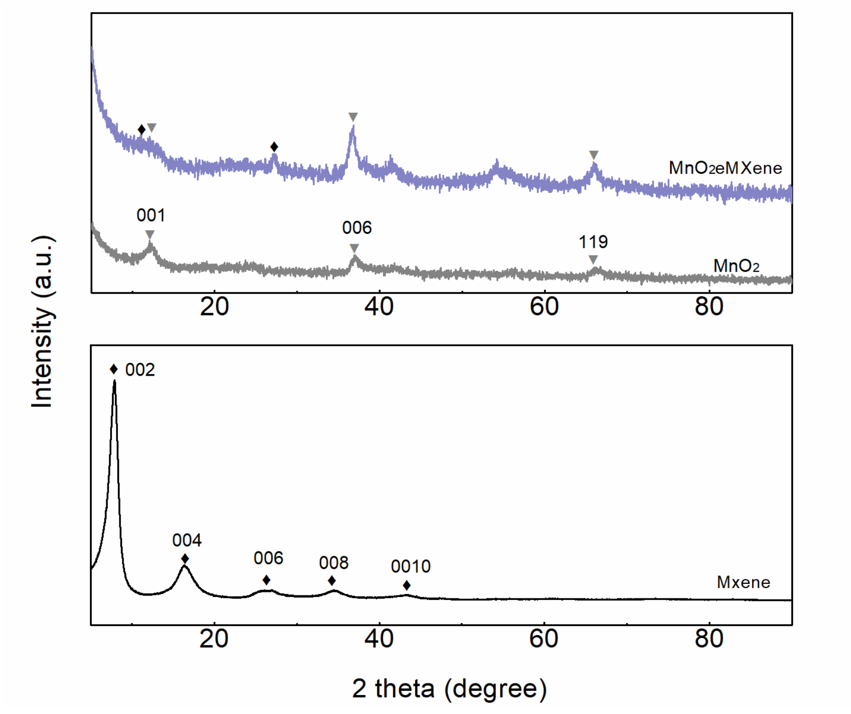

Figure 4.3 XRD patterns of MXene, δ-MnO_2 and MnO_2eMXene composite.

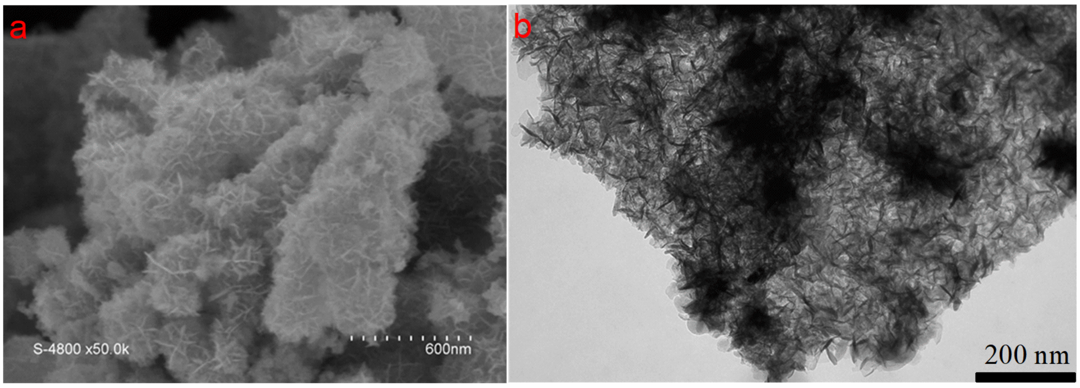

Figure 4.4 SEM and TEM images of MnO_2eMXene composite.

When MXene flakes are introduced as substrates in the synthetic medium, Mn^{2+} cations are first adsorbed on negatively charged MXene layers[60-62] by electrostatic interact ions. Mn^{2+} adsorption is self-limited as it stops when all the Ti_2C_3 flake negative charges are counter-balanced. By reacting with MnO_4^- anions at 120 °C, MnO_2 particles gradually and uniformly grow on the flat MXene template. The resulting material morphology can be evidenced by SEM and TEM imaging. From SEM image in Figure 4.4a, it is difficult to assign any morphology difference between the composite and raw MnO_2 (see Figure S2c for comparison with MnO_2-120). Moreover, it was not possible to identify anything looking like the pristine Ti_3C_2 MXene flakes in the micrographies. At this stage, we argue this is because they are fully covered by MnO_2 particles. TEM image in Figure 4.4b is more indicative as it shows a rather homogeneous thick layer of MnO_2 grown at the surface of a microsized Ti_3C_2 MXene flake. The same morphology was found all over the analyzed sample and, either by SEM or TEM, it was not possible to identify any small or individual MnO_2 particles nor individual neither uncovered nor partially covered. Consistently, EDX mappings shown in Figure S6 demonstrates the homogeneous distribution of the various components Mn, O, Ti and C, all over the surface of the sample, characteristic of an intimate mixture of MnO_2 and Ti_3C_2 MXene in the composite and confirming the preferential growth of MnO_2 particles at the surface of MXene flakes. Consistently with the self-limited adsorption of Mn^{2+} cations at MXene surface, the same composition was found on every spots analyzed by EDX mapping. EDX analysis (Table S2) also evidenced the presence of K in the composite, as expected intercalated cations in between the layers of δ-MnO_2. As suggested by the SEM images, MnO_2 appears as the predominant component while Ti_3C_2, underneath the MnO_2 thicker layer, is more difficult to accurately detect and analyze.

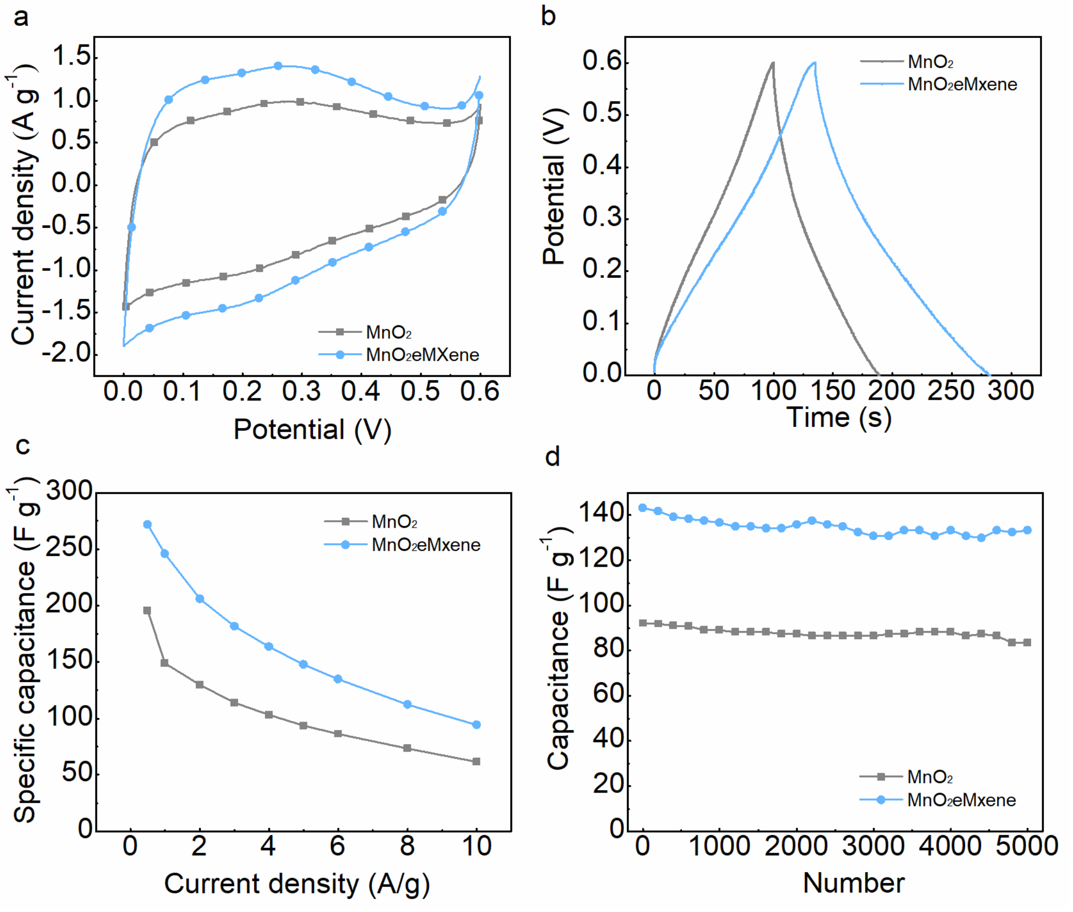

Figure 4.5 Electrochemical characteristics of MnO_2eMXene composite and MnO_2-120 -based electrodes in 1 M KOH electrolyte. (a) Cyclic voltammetry measurement at 5 mV s^{-1} scan rate. (b) Galvanostatic charge-discharge curves at 1 A g^{-1} current density. (c) Specific capacitance comparison at various current densities. (d) Cycling capability over 5k charge-discharge cycles at 5 A g^{-1}.

MnO_2-120 and MnO_2eMXene -based electrodes were used for electrochemical characterization in a three-electrode setup in KOH as well as in Na_2SO_4 electrolytes. In 1M KOH, cyclic voltammograms measured at 5 mV s^{-1} between 0 and 0.6 V versus Hg/HgO reference electrode in Figure 4.5a are characteristic of a pseudocapacitive electrode material. These CVs, but also the corresponding galvanostatic curves in the same potential range (Figure 4.5b), show that the composite displays a greater capacitance than MnO_2-120 electrode. However, both electrode materials have similar rate capabilities

(Figure 4.5c). As such, the composite can deliver a capacitance of 272 F g^{-1} at 0.5 A g^{-1}, fairly more than MnO_2-120 at 196 F g^{-1} at the same current density, that decreases by 55 % down to 148 F g^{-1} at 5 A g^{-1}. For MnO_2-120 electrode, the capacity loss at 5 A g^{-1} is of 47 % at 94 F g^{-1}. As anticipated, the MnO_2eMXene -based electrode inherits the rate capability of MnO_2-120 demonstrated above. On the other hand, the composite capacitance at 5 A g^{-1} is 133 F g^{-1} after 5k charge-discharge cycles, corresponding to 93% of its initial capacitance (Figure 4.5d). Conversely, the capacitance of MnO_2-120 electrode at 83 F g^{-1} after the same electrochemical cycling program is characteristic of 90% retention, about the same as the MnO_2eMXene composite electrode. Electrochemical characteristics of the prepared electrode materials were also tested in sodium sulfate electrolyte. Results are shown in Figure 4.6. Here again, both MnO_2-120 and MnO_2eMXene -based electrode CVs show roughly rectangular shapes. Corresponding capacitances were calculated at various current densities by galvanostatic cycling. For MnO_2-120 electrode, the capacitance is 114 F g^{-1} at 0.5 A g^{-1} but fades down to 8 F g^{-1} at 10 A g^{-1}, demonstrating the poor rate performance (7%) usually observed for MnO_2-based electrodes in neutral electrolyte. Oppositely, at higher current, the electrode made of MnO_2eMXene composite can hold almost 50% of its low current capacitance, delivering 165 F g^{-1} (0.5 A g^{-1}) and 81 F g^{-1} (10 A g^{-1}) (Figure 6c). In neutral electrolyte, the greater rate capabilities of MnO_2eMXene can hardly be assigned to some α-MnO_2 contribution as in KOH electrolyte for two reasons. Firstly, the rate capability of α-MnO_2 has been shown to be very limited in Na_2SO_4 1M.[63] Secondly, despite the same synthesis temperature, there is not much evidence of any needle in the SEM/TEM micrographies of MnO_2eMXene composite or α-MnO_2 diffraction peaks in its XRD pattern. The enhanced rate performance of MnO_2eMXene should be assigned to the enhanced electronic conductivity thanks to the MXene component. The cycling capability over 5k cycles was evaluated at 5 A g^{-1} current density (Figure 6d). For both prepared electrode materials, there is not any noticeable capacitance fading, demonstrating the good stability of these pseudocapacitive materials upon cycling at this quite realistic regime (from 40 to 60 sec. for a complete charge discharge cycle).

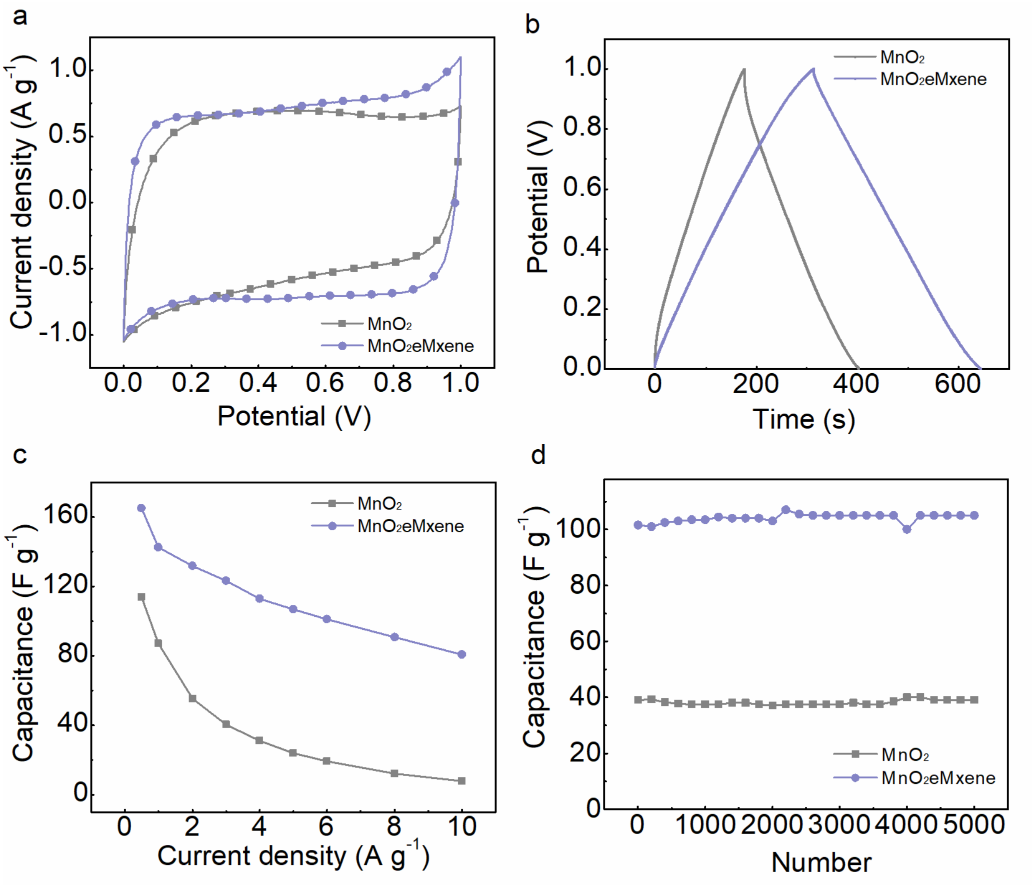

Figure 4.6 Electrochemical characteristics of of MnO_2eMXene composite and MnO_2-120 -based electrodes in 1 M Na_2SO_4 electrolyte. (a) CV curves at 5 mV s^{-1} scan rate. (b) Galvanostatic charge discharge curves at 0.5 A g^{-1} current density. (c) Specific capacitance comparison at various current densities. (d) Cyclic stability after 5k charge-discharge cycles at 5 A g^{-1}.

Two-electrode asymmetric devices were assembled from an activated carbon (AC) used as negative electrode and MnO_2eMXene composite (MeM) as positive electrode. Mass loadings were balanced based on capacitance values calculated from galvanostatic charge-discharge measurements at the same current density in corresponding electrolytes. They were tested in KOH as well as Na_2SO_4 electrolytes. From CV as well as from galvanostatic measurements (Figure 4.7a and 4.7b), the AC//MeM device was operated in a greater voltage window of 2.0 V in Na_2SO_4 electrolyte (AC//MeM-Na)[64] while it was limited to 1.6 V in KOH (AC//MeM-K). In contrast, the capacitance of the device (relative to the mass of both electrodes) is lower in Na_2SO_4 electrolyte (35 F g^{-1}) than in

KOH (47 F g^{-1}) and the difference is obviously assigned to the greater capacitance of the MnO_2eMXene positive electrode in the latter electrolyte (Figure 4.5a and 4.6a: 272 F g^{-1} in KOH versus 165 F g^{-1} than in Na_2SO_4). This balance of both device capacitance and voltage leads to energy densities in the same range (Figure 4.7c). These were calculated from galvanostatic charge-discharge data. The AC//MeM-Na device shows an energy density of 19.3 Wh kg^{-1} at 500 W kg^{-1}, while the value decreased to 4.4 Wh kg^{-1} at 10k W kg^{-1}. AC//MeM-K device presents 11 Wh kg^{-1} energy density at 8k W kg^{-1}, although it showed 16.8 Wh kg^{-1} at 400 W kg^{-1}, revealing an attractive energy-density retention at high power. The cycling stability was also evaluated for both devices (Figure 4.7d). After 10k charge-discharge cycles, capacitances of both devices operated in KOH and Na_2SO_4 electrolytes decreased to about 77% of their initial capacitance. Most of the loses occurred during the first 2k cycles. To assign the origin of these fadings, Ohmic drop as well as Coulombic and energy efficiencies were analyzed (Figure S3). In KOH electrolyte, the apparent decrease of specific capacitance during the first 2000 cycles can be assigned to the observed evident reduction of the energy efficiency. Then, the device suffered a normal gradual capacitive decay in extra cycles. On the other hand, there are also a visible fading of the energy efficiency over initial 1000 cycles when the device was operated in Na_2SO_4 electrolyte, though the capacitance fading is more limited. Additionally, it exhibits slight increase of ohmic drop over cycles in both applied electrolytes.

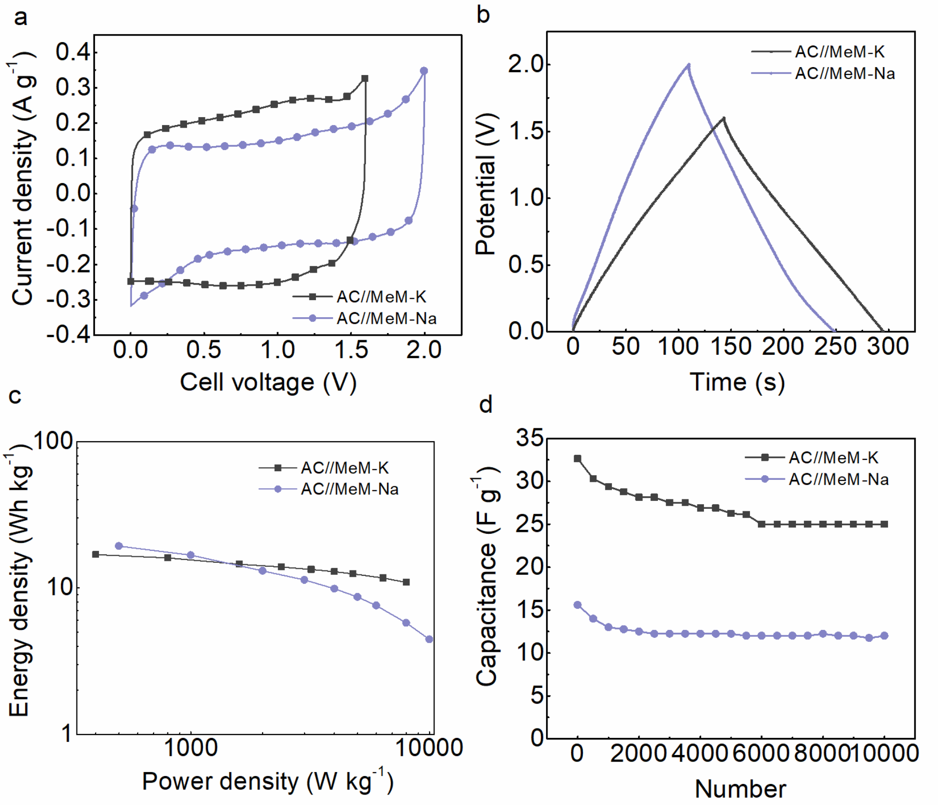

Figure 4.7 The electrochemical performance of AC//MeM-K and AC//MeM-Na devices in neutral (Na_2SO_4 1 M) and alkaline electrolytes (KOH 1 M). (a) Cyclic voltammetry test at 20 mV s^{-1}. (b) galvanostatic charge discharge curve at 0,5 A g^{-1}. (b) Ragone plots for the full cell. Power and energy densities are normalized by the mass of both electrodes. (d) Cycling Longevity in 10k charge-discharge cycles.

4.7 Conclusion

Two different MnO_2 polymorphs and their mixtures were synthesized by adjusting the temperature of the co-precipitation reaction. According to XRD patterns and SEM images, below 80 °C, δ-MnO_2 was obtained while α-MnO_2 was prepared at greater temperatures. This structural change was evidenced as the powder morphology evolved from δ-MnO_2 nano-sheets to α-MnO_2 nano-fibers. Moreover, MnO_2-120 sample prepared at 120 °C appeared as a mixture of δ and α phases with nano-sheets and fibers. As an electrode in a three-electrode setup, MnO_2-120 electrode not only exhibited a high capacitance (196 F g^{-1} at 0.5 A g^{-1}) just like δ-MnO_2, but also held the rate performance of α-

MnO_2. Exfoliated Ti_3C_2 MXene layers with negative surface charges were introduced in the co-precipitation medium, allowing Mn^{2+} cations to adsorb while reacting at 120 °C with Mn^{7+} to give MnO_2 sand-roses particles grown at the MXene layer surface. The resulting composite was characterized by X-ray powder diffraction and electron microscope measurements. An MnO_2eMXene -based electrode was initialy studied in a three-electrode cell, using KOH and Na_2SO_4 electrolytes. In KOH it delivered a capacitance performance of 272 F g^{-1} at 0.5 A g^{-1} and kept 93% of capacitance retention over 5k charge-discharge cycles at a current density as high as 5 A g^{-1}. On the other hand, in Na_2SO_4 electrolyte, MnO_2eMXene electrode showed a 165 F g^{-1} capacitance at 0.5 A $g^{-1}$and 81 F g^{-1} at 10 A g^{-1}, implying a 50% of rate capability in this current range. In a second step, asymmetric devices built on MnO_2eMXene (MeM) and commercial activated carbon in both electrolytes were fabricated and evaluated. Compared with the AC//MeM-K operated in KOH owning a 1.6 V working voltage window, AC//MeM-Na device takes benefit from a larger potential window of 2 V in Na2SO4, confirming the advantages of neutral electrolytes. As such, AC//MeM-Na displayed a 19.3 Wh kg^{-1} (500 W kg^{-1} power density) energy density while it was 16.8 Wh kg^{-1} at 400 W kg^{-1} for AC//MeM-K. In contrast, AC//MeM-Na showed a drastic energy-density fading at 4.4 Wh kg^{-1} at 10 KW kg^{-1}, while AC//MeM-K device kept a remarkable energy density of 11 Wh kg^{-1} at a 8 KW kg^{-1} power density.

Acknowledgements

Y. C. ZHU (NO. 201606240097) is supported by China Scholarship Council (CSC).

This chapter is submitting as an article.

4.8 Reference

1. Y. Gogotsi, P. Simon, Materials for electrochemical capacitors, Nat. Mater. 7 (2008) 845–854.

2. F. Béguin, V. Presser, A. Balducci, E. Frackowiak, Carbons and electrolytes for advanced supercapacitors, Adv. Mater. 26 (2014) 2219–2251.

3. D. Kaufman, K.L. Hudson, R. Mcclamrock, Where Do Batteries End and Supercapacitors Begin?, Sci. Mag. 343 (2014) 1210–1211.

4. W. Bao, L. Liu, C. Wang, S. Choi, D. Wang, G. Wang, Facile Synthesis of Crumpled Nitrogen-Doped MXene Nanosheets as a New Sulfur Host for Lithium–Sulfur Batteries, Adv. Energy Mater. 8 (2018) 1–11..

5. M. Salanne, B. Rotenberg, K. Naoi, K. Kaneko, P.-L. Taberna, C.P. Grey, B. Dunn, P. Simon, Efficient storage mechanisms for building better supercapacitors, Nat. Energy. 1 (2016) 16070.

6. F. Wang, X. Wu, X. Yuan, Z. Liu, Y. Zhang, L. Fu, et al., Latest advances in supercapacitors: From new electrode materials to novel device designs, Chem. Soc. Rev. 46 (2017) 6816–6854.

7. X. Chen, R. Paul, L. Dai, Carbon-based supercapacitors for efficient energy storage, Natl. Sci. Rev. 4 (2017) 453–489.

8. S. Bose, T. Kuila, A.K. Mishra, R. Rajasekar, N.H. Kim, J.H. Lee, Carbon-based nanostructured materials and their composites as supercapacitor electrodes, J. Mater. Chem. 22 (2012) 767–784.

9. C. Merlet, B. Rotenberg, P.A. Madden, P.L. Taberna, P. Simon, Y. Gogotsi, et al., On the molecular origin of supercapacitance in nanoporous carbon electrodes, Nat. Mater. 11 (2012) 306–310.

10. J. Wang, J. Tang, B. Ding, V. Malgras, Z. Chang, X. Hao, et al., Hierarchical porous carbons with layer-by-layer motif architectures from confined soft-template self-assembly in layered materials, Nat. Commun. 8 (2017) 1–9.

11. G. Li, J. Sun, W. Hou, S. Jiang, Y. Huang, J. Geng, Three-dimensional porous carbon composites containing high sulfur nanoparticle content for high-performance lithium-sulfur batteries, Nat. Commun. 7 (2016) 1–10.

12. M. Yang, Z. Zhou, Recent Breakthroughs in Supercapacitors Boosted by Nitrogen-Rich Porous Carbon Materials, Adv. Sci. 4 (2017) 1600408.

13. A.M. Abioye, F.N. Ani, Recent development in the production of activated carbon electrodes from agricultural waste biomass for supercapacitors: A review, Renew. Sustain. Energy Rev. 52 (2015) 1282–1293.

14. A. Borenstein, O. Hanna, R. Attias, S. Luski, T. Brousse, D. Aurbach, Carbon-based composite materials for supercapacitor electrodes: A review, J. Mater. Chem. A. 5 (2017) 12653–12672.

15. W. Hooch Antink, Y. Choi, K.D. Seong, J.M. Kim, Y. Piao, Recent Progress in Porous Graphene and Reduced Graphene Oxide-Based Nanomaterials for Electrochemical Energy Storage Devices, Adv. Mater. Interfaces. 5 (2018) 1–19.

16. R. Raccichini, A. Varzi, S. Passerini, B. Scrosati, The role of graphene for electrochemical energy storage, Nat. Mater. 14 (2015) 271–279.

17. M.F. El-Kady, S. Veronica, D. Sergey, B.K. Richard, Laser Scribing of High-Performance and Flexible Graphene-Based Electrochemical Capacitors, Science (80-.). 335 (2012) 1326–1330.

18. A. Eftekhari, The mechanism of ultrafast supercapacitors, J. Mater. Chem. A. 6 (2018) 2866–2876.

19. D.P. Dubal, O. Ayyad, V. Ruiz, P. Gómez-Romero, Hybrid energy storage: The merging of battery and supercapacitor chemistries, Chem. Soc. Rev. 44 (2015) 1777–1790.

20. M. Zhi, C. Xiang, J. Li, M. Li, N. Wu, Nanostructured carbon-metal oxide composite electrodes for supercapacitors: A review, Nanoscale. 5 (2013) 72–88.

21. C. (John) Zhang, T.M. Higgins, S.H. Park, S.E. O’Brien, D. Long, J.N. Coleman, V. Nicolosi, Highly flexible and transparent solid-state

supercapacitors based on RuO2/PEDOT:PSS conductive ultrathin films, Nano Energy, 28 (2016) 495–505.

22. H. Li, X. Li, J. Liang, Y. Chen, Hydrous RuO 2 -Decorated MXene Coordinating with Silver Nanowire Inks Enabling Fully Printed Micro-Supercapacitors with Extraordinary Volumetric Performance, Adv.Energy Mater.9(2019), 1803987.

23. H. Ma, D. Kong, Y. Xu, X. Xie, Y. Tao, Z. Xiao, W. Lv, H.D. Jang, J. Huang, Q.H. Yang, Disassembly–Reassembly Approach to RuO2/Graphene Composites for Ultrahigh Volumetric Capacitance Supercapacitor, Small. 13 (2017) 1–7.

24. Y. Wang, D. Gu, J. Guo, M. Xu, H. Sun, J. Li, L. Wang, L. Shen, Maximized Energy Density of RuO2//RuO2 Supercapacitors through Potential Dependence of Specific Capacitance, ChemElectroChem. 7 (2020) 928–936. https://doi.org/10.1002/celc.201901898.

25. T. Liu, Z. Zhou, Y. Guo, D. Guo, G. Liu, Block copolymer derived uniform mesopores enable ultrafast electron and ion transport at high mass loadings, Nat. Commun. 10 (2019) 1–10.

26. N. Zhang, F. Cheng, J. Liu, L. Wang, X. Long, X. Liu, et al., Rechargeable aqueous zinc-manganese dioxide batteries with high energy and power densities, Nat. Commun. 8 (2017) 1–9.

27. H. Chen, L. Hu, Y. Yan, R. Che, M. Chen, L. Wu, One-step fabrication of ultrathin porous nickel hydroxide-manganese dioxide hybrid nanosheets for supercapacitor electrodes with excellent capacitive performance, Adv. Energy Mater. 3 (2013) 1636–1646.

28. M.R. Lukatskaya, B. Dunn, Y. Gogotsi, Multidimensional materials and device architectures for future hybrid energy storage, Nat. Commun. 7 (2016) 1–13.

29. S. Yoon, E. Kang, J.K. Kim, C.W. Lee, J. Lee, Development of high-performance supercapacitor electrodes using novel ordered mesoporous

tungsten oxide materials with high electrical conductivity, Chem. Commun. 47 (2011) 1021–1023.

30. D.P. Dubal, S.H. Lee, J.G. Kim, W.B. Kim, C.D. Lokhande, Porous polypyrrole clusters prepared by electropolymerization for a high performance supercapacitor, J. Mater. Chem. 22 (2012) 3044–3052.

31. G. Yu, L. Hu, N. Liu, H. Wang, M. Vosgueritchian, Y. Yang, Y. Cui, Z. Bao, Enhancing the supercapacitor performance of graphene/MnO2 nanostructured electrodes by conductive wrapping, Nano Lett. 11 (2011) 4438–4442.

32. M. Kim, C. Lee, J. Jang, Fabrication of highly flexible, scalable, and high-performance supercapacitors using polyaniline/reduced graphene oxide film with enhanced electrical conductivity and crystallinity, Adv. Funct. Mater. 24 (2014) 2489–2499.

33. Z. Ma, G. Shao, Y. Fan, G. Wang, J. Song, D. Shen, Construction of Hierarchical α-MnO2 Nanowires@Ultrathin δ-MnO2 Nanosheets Core-Shell Nanostructure with Excellent Cycling Stability for High-Power Asymmetric Supercapacitor Electrodes, ACS Appl. Mater. Interfaces, 8 (2016) 9050–9058.

34. X. Zhao, L. Zhang, S. Murali, M.D. Stoller, Q. Zhang, Y. Zhu, R.S. Ruoff, Incorporation of manganese dioxide within ultraporous activated graphene for high-performance electrochemical capacitors, ACSNano.,6(2012)5404–5412.

35. D.Y. Sung, I.Y. Kim, T.W. Kim, M.S. Song, S.J. Hwang, Room temperature synthesis routes to the 2D nanoplates and 1D nanowires/nanorods of manganese oxides with highly stable pseudocapacitance behaviors, J. Phys. Chem. C. 115 (2011) 13171–13179.

36. Z. Lv, Y. Luo, Y. Tang, J. Wei, Z. Zhu, X. Zhou, W. Li, Y. Zeng, W. Zhang, Y. Zhang, D. Qi, S. Pan, X.J. Loh, X. Chen, Editable Supercapacitors with Customizable Stretchability Based on Mechanically Strengthened Ultralong MnO2 Nanowire Composite, Adv. Mater. 30 (2018).

37. A. Cross, A. Morel, A. Cormie, T. Hollenkamp, S. Donne, Enhanced manganese dioxide supercapacitor electrodes produced by electrodeposition, J. Power Sources. 196 (2011) 7847–7853.

38. C. Choi, K.M. Kim, K.J. Kim, X. Lepró, G.M. Spinks, R.H. Baughman, S.J. Kim, Improvement of system capacitance via weavable superelastic biscrolled yarn supercapacitors, Nat. Commun. 7 (2016) 1–8.

39. M. Ghidiu, M.R. Lukatskaya, M.Q. Zhao, Y. Gogotsi, M.W. Barsoum, Conductive two-dimensional titaniumcarbide ‘clay’ with high volumetric capacitance, Nature. 516 (2015) 78–81.

40. F. Shahzad, M. Alhabeb, C.B. Hatter, B. Anasori, S.M. Hong, C.M. Koo, et al., Electromagnetic interference shielding with 2D transition metal carbides (MXenes), Science (80). 353 (2016) 1137–1140.

41. M. Khazaei, M. Arai, T. Sasaki, C.Y. Chung, N.S. Venkataramanan, M. Estili, et al., Novel electronic and magnetic properties of two-dimensional transition metal carbides and nitrides, Adv. Funct. Mater. 23 (2013) 2185–2192.

42. X. Liang, A. Garsuch, L.F. Nazar, Sulfur Cathodes Based on ConductiveMXene Nanosheets for High- Performance Lithium–Sulfur Batteries, Angew. Chemie-Int. Ed. 54 (2015) 3907–3911.

43. L. Ding, Y. Wei, Y. Wang, H. Chen, J. Caro, H. Wang, A Two-Dimensional Lamellar Membrane:MXene NanosheetStacks, Angew. Chemie - Int. Ed. 56 (2017) 1825–1829.

44. M.R. Lukatskaya, S. Kota, Z. Lin, M.Q. Zhao, N. Shpigel, M.D. Levi, J. Halim, P.L. Taberna, M.W. Barsoum, P. Simon, Y. Gogotsi, Ultra-high-rate pseudocapacitive energy storage in two-dimensional transition metal carbides, Nat. Energy. 6 (2017) 1–6.

45. C. Couly, M. Alhabeb, K.L. Van Aken, N. Kurra, L. Gomes, A.M. Navarro-Suárez, B. Anasori, H.N. Alshareef, Y. Gogotsi, Asymmetric Flexible MXene-Reduced Graphene Oxide Micro-Supercapacitor, Adv. Electron. Mater. 4 (2018) 1–8.

46. Q. Xue, Z. Pei, Y. Huang, M. Zhu, Z. Tang, H. Li, Y. Huang, N. Li, H. Zhang, C. Zhi, Mn3O4 nanoparticles on layer-structured Ti3C2 MXene towards the oxygen reduction reaction and zinc-air batteries, J. Mater. Chem. A. 5 (2017) 20818–20823.

47. C. Chen, X. Xie, B. Anasori, A. Sarycheva, T. Makaryan, M. Zhao, P. Urbankowski, L. Miao, J. Jiang, Y. Gogotsi, MoS2-on-MXene Heterostructures as Highly Reversible Anode Materials for Lithium-Ion Batteries, Angew. Chemie - Int. Ed. 57 (2018) 1846–1850.

48. S. Niu, Z. Wang, M. Yu, M. Yu, L. Xiu, S. Wang, X. Wu, J. Qiu, MXene-Based Electrode with Enhanced Pseudocapacitance and Volumetric Capacity for Power-Type and Ultra-Long Life Lithium Storage, ACS Nano. 12 (2018) 3928–3937.

49. L. Yu, L. Hu, B. Anasori, Y.T. Liu, Q. Zhu, P. Zhang, Y. Gogotsi, B. Xu, MXene-Bonded Activated Carbon as a Flexible Electrode for High-Performance Supercapacitors, ACS Energy Lett. 3 (2018) 1597–1603.

50. C. Yang, Y. Tang, Y. Tian, Y. Luo, Y. He, X. Yin, W. Que, Achieving of Flexible, Free-Standing, Ultracompact Delaminated Titanium Carbide Films for High Volumetric Performance and Heat-Resistant Symmetric Supercapacitors, Adv. Funct. Mater. 28 (2018) 1705487.

51. R.B. Rakhi, B. Ahmed, D. Anjum, H.N. Alshareef, Direct Chemical Synthesis of MnO 2 Nanowhiskers on Transition-Metal Carbide Surfaces for Supercapacitor Applications, ACS Appl. Mater. Interfaces. 8 (2016) 18806–18814.

52. O. Ghodbane, J.L. Pascal, F. Favier, Microstructural effects on charge-storage properties in MnO 2-based electrochemical supercapacitors, ACS Appl. Mater. Interfaces. 1 (2009) 1130–1139.

53. L. Athouël, F. Moser, R. Dugas, O. Crosnier, D. Bélanger, T. Brousse, Variation of the MnO2 birnessite structure upon charge/discharge in an electrochemical supercapacitor electrode in aqueous Na2SO 4 electrolyte, J. Phys. Chem. C. 112 (2008) 7270–7277.

54. T. Brousse, P.-L. Taberna, O. Crosnier, R. Dugas, P. Guillemet, Y. Scudeller, Y. Zhou, F. Favier, D. Bélanger, P. Simon, Long-term cycling behavior of asymmetric activated carbon/MnO2 aqueous electrochemical supercapacitor, J. Power Sources. 173 (2007) 633–641.

55. M. Toupin, T. Brousse, D. Bélanger, Charge storage mechanism of MnO2 electrode used in aqueous electrochemical capacitor, Chem. Mater. 16 (2004) 3184–3190.

56. A. Gambou-Bosca, D. Bélanger, Electrochemical characterization of MnO2-based composite in the presence of salt-in-water and water-in-salt electrolytes as electrode for electrochemical capacitors, J. Power Sources. 326 (2016) 595–603.

57. A.A. Voskanyan, C.-K. Ho, K.Y. Chan, 3D δ-MnO2 nanostructure with ultralarge mesopores as high-performance lithium-ion battery anode fabricated via colloidal solution combustion synthesis, J. Power Sources. 421 (2019) 162–168.

58. Cong Guo, Qihao Zhou, Huimin Liu, Shuo Tian, Binglei Chen, Jian Zhao, Jingfa Li, A case study of β- and δ-MnO_2 with different crystallographic forms on ion-storage in rechargeable aqueous zinc ion battery, Electrochimica Acta 324 (2019) 134867.

59. S. Devaraj, N. Munichandraiah, Effect of Crystallographic Structure of MnO_2 on Its Electrochemical Capacitance Properties, J. Phys. Chem. C. 112 (2008) 4406–4417.

60. J. Yan, C.E. Ren, K. Maleski, C.B. Hatter, B. Anasori, P. Urbankowski, A. Sarycheva, Y. Gogotsi, Flexible MXene/Graphene Films for Ultrafast Supercapacitors with Outstanding Volumetric Capacitance, Adv. Funct. Mater. 27 (2017) 1–10.

61. K. Huang, Z. Li, J. Lin, G. Han, P. Huang, Two-dimensional transition metal carbides and nitrides (MXenes) for biomedical applications, Chem. Soc. Rev. 47 (2018) 5109–5124.

62. L. Ding, Y. Wei, Y. Wang, H. Chen, J. Caro, H. Wang, A Two-Dimensional Lamellar Membrane: MXene Nanosheet Stacks, Angew. Chemie - Int. Ed. 56 (2017) 1825–1829.

63. H.U. Shah, F. Wang, M.S. Javed, R. Saleem, M.S. Nazir, J. Zhan, Z.U.H. Khan, M.U. Farooq, S. Ali, Synthesis, characterization and electrochemical

properties of α-MnO2 nanowires as electrode material for supercapacitors, Int. J. Electrochem. Sci. 13 (2018) 6426–6435.

64. T. Brousse, P.-L. Taberna, O. Crosnier, R. Dugas, P. Guillemet, Y. Scudeller, Y. Zhou, F. Favier, D. Bélanger, P. Simon, Long-term cycling behavior of asymmetric activated carbon/MnO2 aqueous electrochemical supercapacitor, J. Power Sources. 173 (2007) 633 – 641.

Supporting information

Table S1 Comparison of electrochemical performance for Ti3C2, MnO2 and composite material -based electrodes

material	capacitance	Current density/ Scan rate	Energy	Types of electrolyte	Ref
MnO_2eMXene	272F g^{-1}	0.5 A g^{-1}	17 Wh kg^{-1} (400 W kg^{-1}) And 11 Wh kg^{-1} (8 KW kg^{-1})	1 M KOH	This work
MnO_2eMXene	165 F g^{-1}	0.5 A g^{-1}	20 Wh kg^{-1}(400 W kg-1)	1M Na_2SO_4	This work
ε-MnO_2/Ti_2CT_x_Ar	212 F g^{-1}	1 A g^{-1}	14 Wh kg-1(700 W kg-1)	30 wt% KOH	1
d-Ti_3C_2Tx film on NF	140 F g^{-1}	5 mV s^{-1}	/	1M KOH	2
Ti_3C_2Tx/RGO	154 F g^{-1}	1 A g^{-1}	/	2 M KOH	3
TiO_2-Ti_3C_2	143 F g^{-1}	5 mV s^{-1}	/	6M KOH	4
Ti_3C_2Tx	63 F g^{-1}	5 mV s^{-1}	/	1M KOH	5
Ti_3C_2/ZnO	120 F g^{-1}	2 mV s^{-1}	/	1M KOH	6
PANI@TiO_2/Ti_3C_2Tx	109 F g^{-1}	0.5 A g^{-1}	/	1M KOH	7
α-MnO_2-G	90 F g^{-1}	1 A g^{-1}	/	1M Na_2SO_4	8

$GrMnO_2$	310 F g^{-1}	5 mV s^{-1}	9 Wh kg^{-1}(3 KW kg^{-1})	1M Na_2SO_4	9
MnO_2/carbon nanotube	/	/	13 Wh kg^{-1} (316 W kg^{-1})	0.5M Na_2SO_4	10
CNT/MnO_2	105 F g^{-1}	1 A g^{-1}	/	1M Na_2SO_4	11
MnO_2/CuO	148 F g^{-1}	0.5 A g^{-1}	/	1M Na_2SO_4	12
MnO_2 nanosheets	100 F g^{-1}	0.5 A g^{-1}	/	0.5M Na_2SO_4	13
$K0.15MnO_2$/PEDOT	91 F g^{-1}	1 A g^{-1}	15 Wh kg^{-1}	0.1M Na_2SO_4	14
MnO_2/CNTs	201 F g^{-1}	1 A g^{-1}	13 Wh kg^{-1} (600 W kg^{-1})	1M Na_2SO_4	15
Carbon@MnO_2	129 F g^{-1}	0.5 A g^{-1}	/	1M Na_2SO_4	16
Graphite/PEDOT/MnO_2	158 F g^{-1}	1 A g^{-1}	1 Wh kg^{-1} (4.5 KW kg^{-1})	0.5M Na_2SO_4	17
MnO_2 nanorods	156 F g^{-1}	2 A g^{-1}	/	4 M KOH with p-phenylenediamine	18
carbon nanofiber/graphene/MnO_2	225 F g^{-1}	1 mA cm^{-2}	15 Wh kg^{-1} (583 W kg^{-1})	6 M KOH	19
CNTs@MXene	81 F g^{-1}	5 A g^{-1}	3 Wh kg^{-1} (311 W kg^{-1})	6M KOH	20
NiO@MnO_2 core/shell	266 F g^{-1}	0.5 A g^{-1}	/	2M KOH	21

1. R. Jiang, C. Cui, H. Ma, Using graphene nanosheets as a conductive additive to enhance the capacitive performance of α-MnO2, Electrochim. Acta. 104 (2013) 198–207. https://doi.org/10.1016/j.electacta.2013.04.125.

2. J. Chang, M. Jin, F. Yao, T.H. Kim, V.T. Le, H. Yue, F. Gunes, B. Li, A. Ghosh, S. Xie, Y.H. Lee, Asymmetric supercapacitors based on graphene/MnO2 nanospheres and graphene/MoO3 nanosheets with high energy density, Adv. Funct. Mater. 23 (2013) 5074–5083. https://doi.org/10.1002/adfm201301851.

3. R.B. Rakhi, B. Ahmed, D. Anjum, H.N. Alshareef, Direct Chemical Synthesis of MnO 2 Nanowhiskers on Transition-Metal Carbide Surfaces for Supercapacitor Applications, ACS Appl. Mater. Interfaces. 8 (2016) 18806–18814. https://doi.org/10.1021/acsami.6b04481.

4. Y. Su, I. Zhitomirsky, Hybrid MnO2/carbon nanotube-VN/carbon nanotube supercapacitors, J. Power Sources. 267 (2014) 235–242. https://doi.org/10.1016/j.jpowsour.2014.05.091.

5. Y. Jin, H. Chen, M. Chen, N. Liu, Q. Li, Graphene-patched CNT/MnO2 nanocomposite papers for the electrode of high-performance flexible asymmetric supercapacitors, ACS Appl. Mater. Interfaces. 5 (2013) 3408–3416. https://doi.org/10.1021/am400457x.

6. Y. Xin Zhang, F. Li, M. Huang, One-step hydrothermal synthesis of hierarchical MnO2-coated CuO flower-like nanostructures with enhanced electrochemical properties for supercapacitor, Mater. Lett. 112 (2013) 203–206. https://doi.org/10.1016/j.matlet.2013.09.032.

7. C. Tanggarnjanavalukul, N. Phattharasupakun, J. Wutthiprom, P. Kidkhunthod, M. Sawangphruk, Charge storage mechanisms of birnessite-type MnO2 nanosheets in Na2SO4 electrolytes with different pH values: In situ electrochemical X-ray absorption spectroscopy investigation, Electrochim. Acta. 273 (2018) 17–25. https://doi.org/10.1016/j.electacta.2018.04.022.

8. S. Xu, G. Wei, J. Li, Y. Ji, N. Klyui, V. Izotov, W. Han, Binder-free Ti3C2Tx MXene electrode film for supercapacitor produced by electrophoretic deposition method, Chem. Eng. J. 317 (2017) 1026–1036. https://doi.org/10.1016/j.cej.2017.02.144.

9. M. Yeager, W. Du, R. Si, D. Su, N. Marinković, X. Teng, Highly efficient K 0.15MnO 2 birnessite nanosheets for stable pseudocapacitive cathodes, J. Phys. Chem. C. 116 (2012) 20173–20181. https://doi.org/10.1021/jp304809r.

10. L. Li, Z.A. Hu, N. An, Y.Y. Yang, Z.M. Li, H.Y. Wu, Facile synthesis of MnO2/CNTs composite for supercapacitor electrodes with long cycle stability, J. Phys. Chem. C. 118 (2014) 22865–22872. https://doi.org/10.1021/jp505744p.

11. Y. Zhao, Y. Meng, P. Jiang, Carbon@MnO2 core-shell nanospheres for flexible high-performance supercapacitor electrode materials, J. Power Sources. 259 (2014) 219–226. https://doi.org/10.1016/j.jpowsour.2014.02.086.

12. P. Tang, L. Han, L. Zhang, Facile synthesis of graphite/PEDOT/MnO2 composites on commercial supercapacitor separator membranes as flexible and high-performance supercapacitor electrodes, ACS Appl. Mater. Interfaces. 6 (2014) 10506–10515. https://doi.org/10.1021/am5021028.

13. L. Su, L. Gong, H. Lü, Q. Xü, Enhanced low-temperature capacitance of MnO2 nanorods in a redox-active electrolyte, J. Power Sources. 248 (2014) 212–217. https://doi.org/10.1016/j.jpowsour.2013.09.047.

14. D.G. Lee, Y.A. Kim, B.H. Kim, Capacitive properties of hierarchically structured carbon nanofiber/graphene/MnO2 hybrid electrode with nitrogen and oxygen heteroatoms, Carbon N. Y. 107 (2016) 783–791. https://doi.org/10.1016/j.carbon.2016.06.093.

15. L. Yang, W. Zheng, P. Zhang, J. Chen, W.B. Tian, Y.M. Zhang, Z.M. Sun, MXene/CNTs films prepared by electrophoretic deposition for supercapacitor electrodes, J. Electroanal. Chem. 830–831 (2018) 1–6. https://doi.org/10.1016/j.jelechem.2018.10.024.

16. C. Zhao, Q. Wang, H. Zhang, S. Passerini, X. Qian, Two-Dimensional Titanium Carbide/RGO Composite for High-Performance Supercapacitors, ACS Appl. Mater. Interfaces. 8 (2016) 15661–15667. https://doi.org/10.1021/acsami.6b04767.

17. J.F. Zhu, Y. Tang, C.H. Yang, F. Wang, M.J. Cao, Composites of TiO2 nanoparticles deposited on Ti3C2 mxene nanosheets with enhanced

electrochemical performance, J. Electrochem. Soc. 163 (2016) A785–A791. https://doi.org/10.1149/2.0981605jes.

18. M.R. Lukatskaya, O. Mashtalir, C.E. Ren, Y. Dall'Agnese, P. Rozier, P.L. Taberna, M. Naguib, P. Simon, M.W. Barsoum, Y. Gogotsi, Cation Intercalation and High Volumetric Capacitance of Two-Dimensional Titanium Carbide, Science (80-.). 341 (2013) 1502 – 1505. https://doi.org/10.1126/science.1241488.

19. F. Wang, M. Cao, Y. Qin, J. Zhu, L. Wang, Y. Tang, ZnO nanoparticle-decorated two-dimensional titanium carbide with enhanced supercapacitive performance, RSC Adv. 6 (2016) 88934–88942. https://doi.org/10.1039/c6ra15384d.

20. X. Lu, J. Zhu, W. Wu, B. Zhang, Hierarchical architecture of PANI@TiO2/Ti3C2Tx ternary composite electrode for enhanced electrochemical performance, Electrochim. Acta. 228 (2017) 282–289. https://doi.org/10.1016/j.electacta.2017.01.025.

21. J. Chen, Y. Huang, C. Li, X. Chen, X. Zhang, Synthesis of NiO@MnO 2 core/shell nanocomposites for supercapacitor application, Appl. Surf. Sci. 360 (2016) 534–539. https://doi.org/10.1016/j.apsusc.2015.10.187.

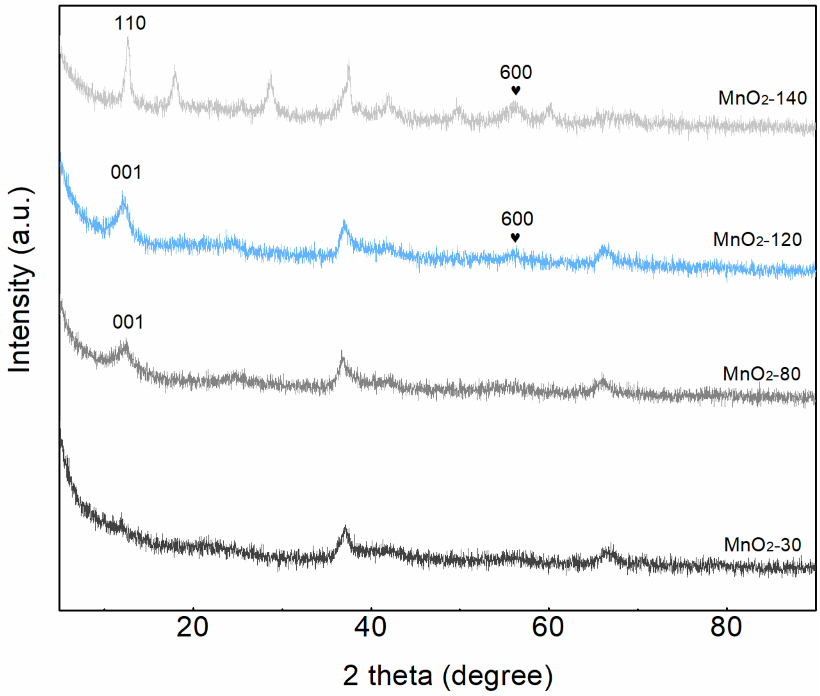

Figure S1 XRD patterns of as-prepared MnO_2 samples.

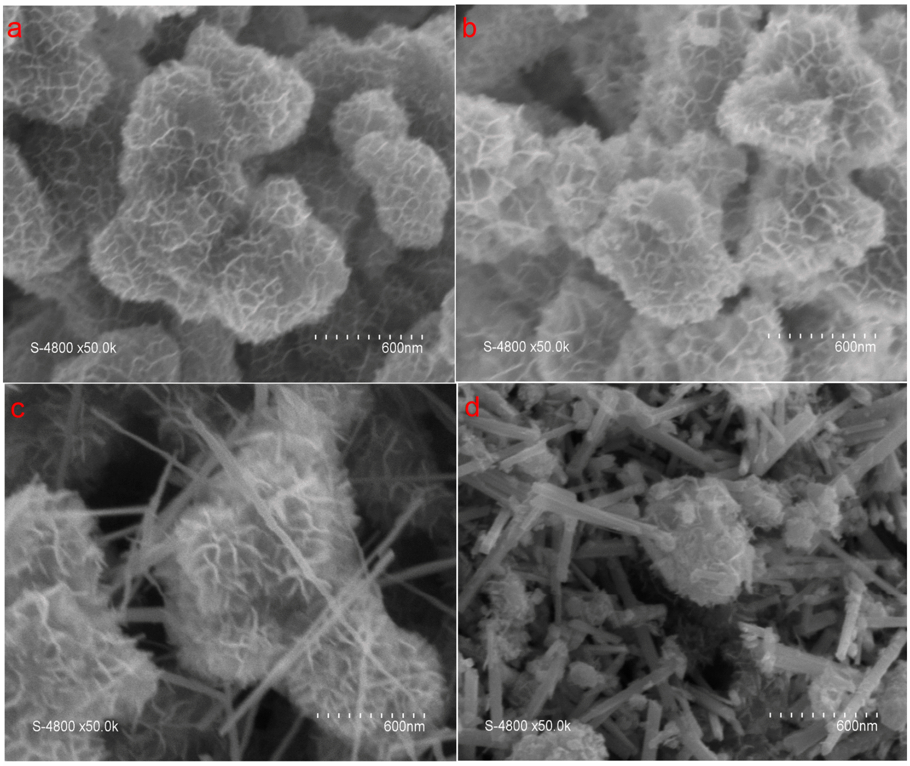

Figure S2 SEM images of MnO_2-30 (a), MnO_2-80 (b), MnO_2-120 (c) and MnO_2-140 (d).

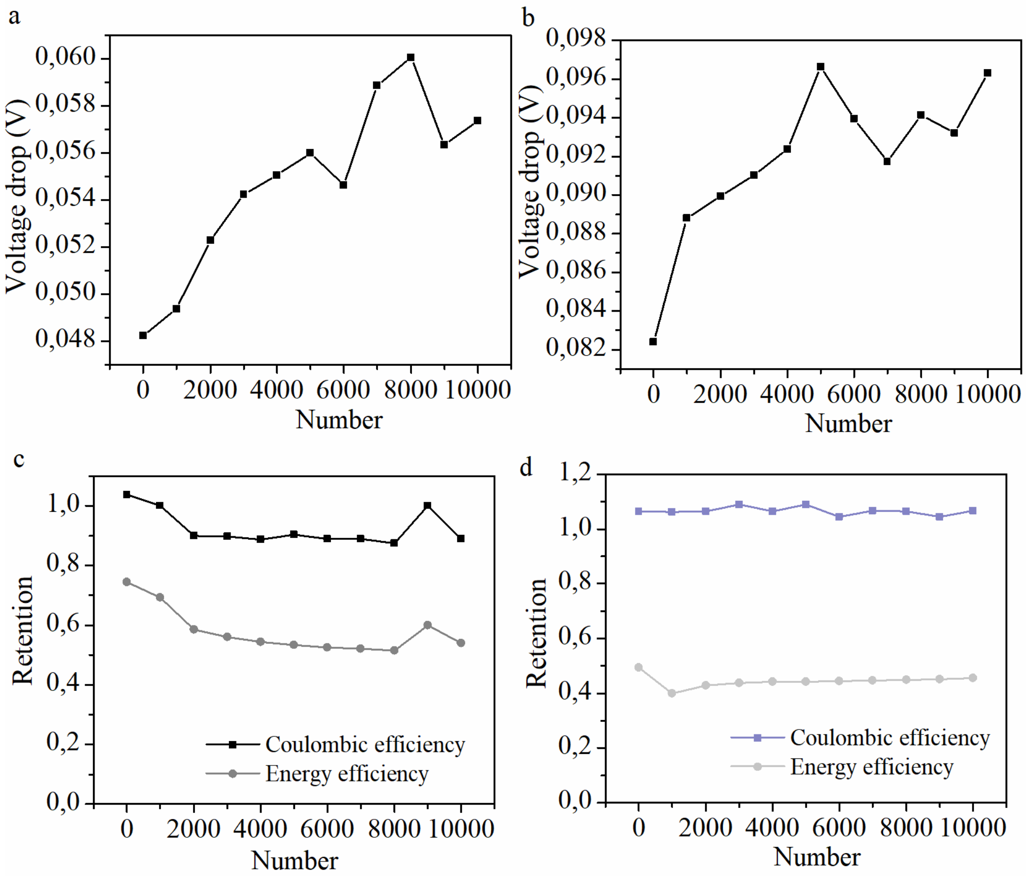

Figure S3 The voltage drop in (a) KOH and (b) Na_2SO_4. Coulombic and energy efficiency in (c) KOH and (d) Na_2SO_4.

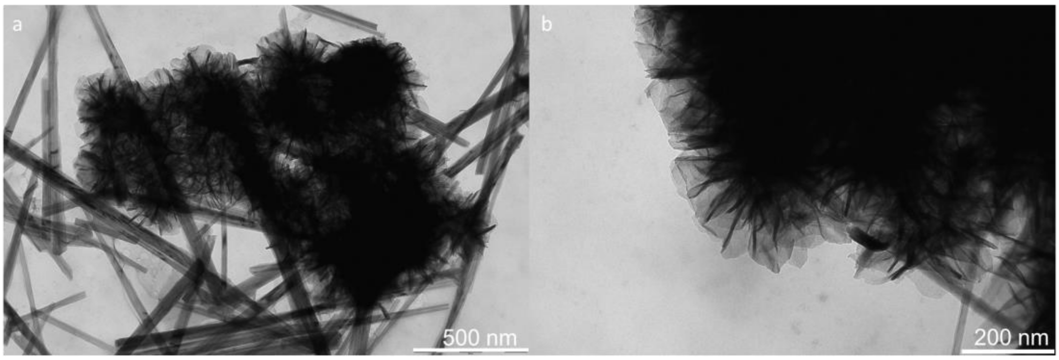

Figure S4 TEM (Transmission Electron microscopy) images of MnO_2-120.

Samples	MnO_2-30 (6.0 mg cm^{-2})	MnO_2-80 (7.5 mg cm^{-2})	MnO_2-120 (7.5 mg cm^{-2})	MnO_2-140 (5.8 mg cm^{-2})
Capacitance (F g^{-1})	181	160	154	98

Table S2 The detailed specific capacitances of samples at 5 mV s^{-1} in three electrode system; The capacitance calculation is based on active material mass which is displayed in the table.

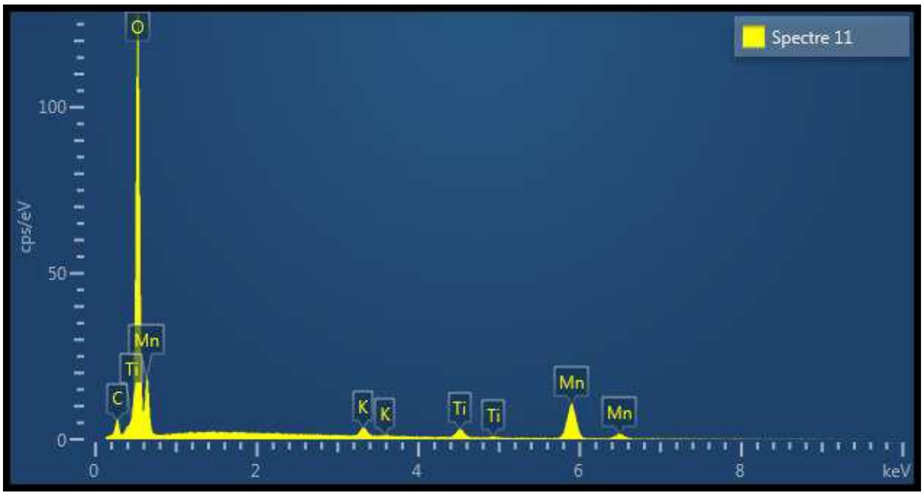

Figure S5 Energy Dispersive X-ray Spectroscopy (EDX) of MnO_2eMXene.

Element	Mass%	Atom%
C	2.33	5.77
O	30.62	57.04
K	2.01	1.53
Ti	4.61	2.87
Mn	60.43	32.79
Total:	100.00	100.00

Table S2 The element composition analysis in MnO_2eMXene.

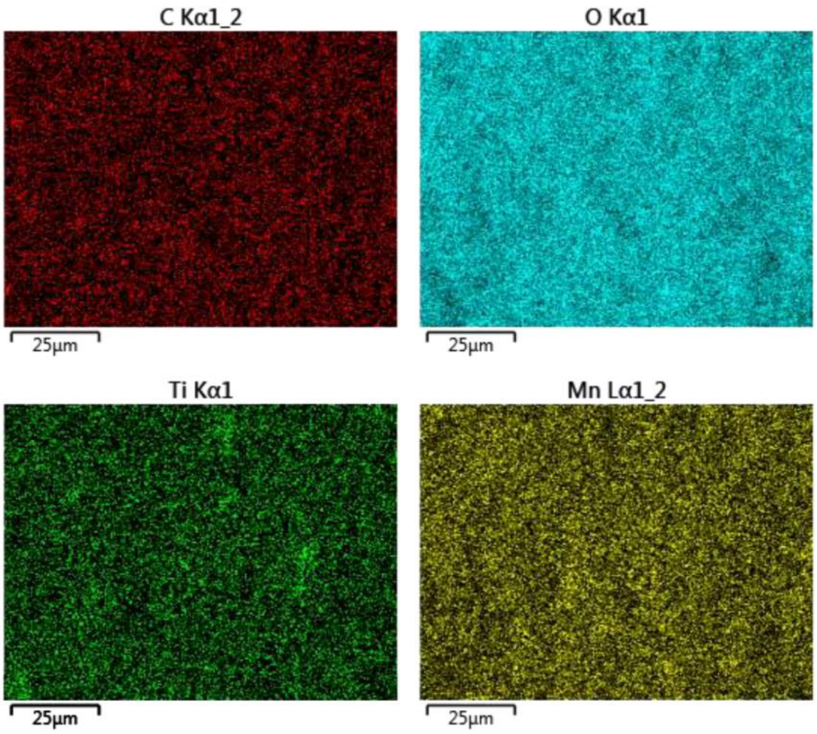

Figure S6 SEM-EDX mapping of elemental distribution in MnO_2eMXene.

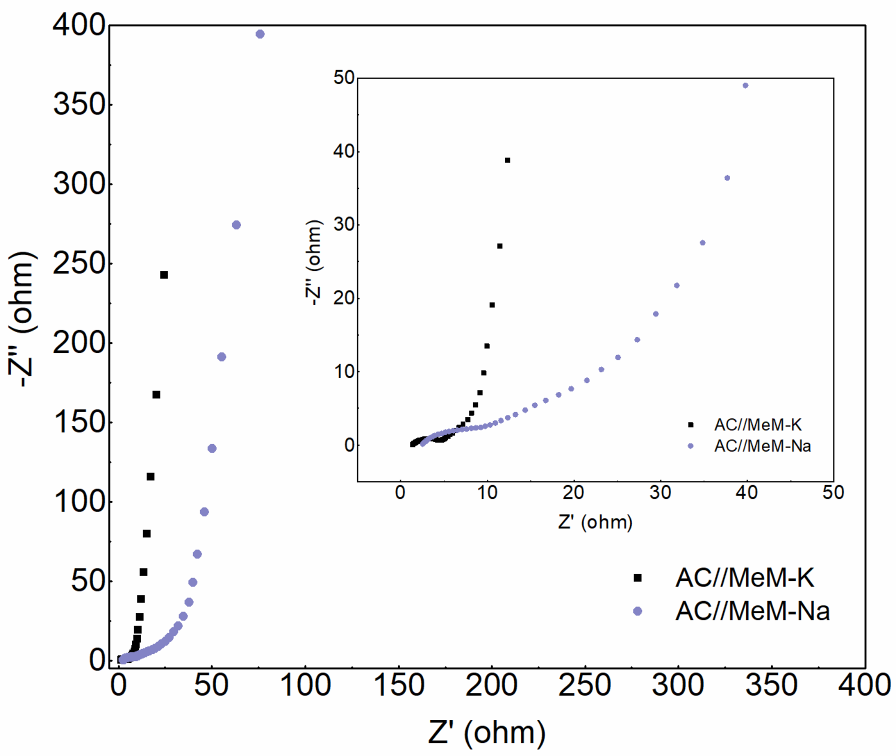

Figure S7 Nyquist plots of EIS.

Chapter 5 Modifications of MXene Layers for Supercapacitors

5.1 Abstract

The re-stacking of $Ti_3C_2T_x$-MXene layers has been prevented by using two different approaches: a facile hard templating method and a pore-forming approach. The expanded MXene obtained by using MgO nanoparticles as hard templates displayed an open morphology based on crumpled layers. The corresponding electrode material delivered 180 F g^{-1} of capacitance at 1 A g^{-1} and maintained 99 % of its initial capacitance at 5 A g^{-1} over five thousand charge-discharge cycles. On the other hand, the MXene foam prepared after heating a MXene-urea composite at 550°C, showed numerous macropores on the surface layer and a complex open 3D inner-architecture. Thanks to this foamy porous structure, the binder-free electrode based on the resulting MXene foam displayed a great capacitance of 203 F g^{-1} at 5 A g^{-1} current density, 99 % of which was retained after five thousand cycles. In comparison, the pristine MXene –based electrode delivered 82 F g^{-1}, only, in the same operating conditions. An asymmetric device built on a negative MXene foam electrode and a positive MnO_2 electrode exhibited an attractive energy density of 16.5 Wh kg^{-1} (or 10 Wh L^{-1}) and 160 W kg^{-1} (or 8.5 kW L^{-1}) power density. Altogether, the enhanced performances of these nano- engineered 2D materials are a clear demonstration of the efficiency of the chosen synthetic approaches to work out the re-stacking issue of MXene layers.

5.2 Introduction

In the wake of graphene[1], other two dimensional materials[2], such as, δ-MnO2 [3, 4, 5], MoS_2[6, 7] and MXene[8, 9, 10], have received a surge of interest from the material science community, as they offer, together with their unique "planar" physical peculiarities, an infinite number of surface chemistry opportunities, especially when compared with their carbonaceous flagship.[11] These opportunities have been explored in many application fields including electrochemical energy storage.[12-14] In the corresponding devices, both basal planes and defected edges are usually contributing to charge storage.[15] As a result, one can take profit of the strong in-plane covalent bonding and weak out-of-plane Van der Waals interactions between layers[16], to develop chemical strategies to provide or tune further active sites. These proceed by many chemical and physical methods including exfoliation[17], intercalation[18] and hybridization[19]. The main idea is to prevent the natural tendency of the individual 2D layers to restack to minimize the surface energy just as in the pristine material(s). By chemical engineering at the nanoscale, associating layers of 2D materials of different chemical compositions and physical properties offers wonderful opportunities to take advantage of resulting synergistic effects[20]. Potential combinations are unnumbered, imagination is probably the limit. As such, in the resulting composite, expanded, hybrid… materials, the opened 2D space between the layers can, for example, provide a "path" strongly suited for ion adsorption and transport. These characteristics have made 2D materials as very attractive electrode materials in batteries[21] and supercapacitors[22]. Two different kinds of supercapacitors (SC), can be distinguished, on the basis of the corresponding charge storage mechanism: electrostatic interactions in electrical double layer capacitors (EDLCs), and fast redox reactions near the surface material in pseudocapacitors.[23] With 2D materials, this classification remains as graphene is probably mostly EDLC type while exfoliated MnO_2 birnessite is pseudocapacitive.[24-29] Composites obtained by stacking of EDLC and pseudocapacitive, EDLC and battery type, or battery type and pseudocapative 2D materials have been recently reported.[30-33] However, the anisotropy of material properties could also be a critical drawback for 2D materials, especially in energy storage electrode materials. Although, both in-plane ionic and electronic conductivities can be remarkable, through-plane conductivities can be fairly limited. Depending on the layer orientation toward the current collector surface, perpendicular or parallel, electrode overall performance can be down-graded.

MXene[34], as a remarkable 2D material, containing a conductive carbide core along with transition metal oxide-like surfaces and intercalated water molecules,[35] triggered much attention and attracted worldwide researches in the field of energy storage and more specifically for supercapacitors.[36-40] MXene is prepared from the corresponding MAX phase by a chemical etching method, usually using a fluorine-containing solution. MAX phases are layered ternary carbides and nitrides with the formula $M_{n+1}AX_n$, where M is an early transition metal (such as Ti, V and Nb), A is an element from A-group (usually Al or Si) and X is carbon and/or nitrogen.[8,41,42] $Ti_3C_2T_x$-MXene could be obtained by etching Ti_3AlC_2 in a mixture of LiF and HCl. T_x stands for the termination moieties at the layer surface. Their chemical nature depends on the etching process. They have a strong impact on the electrolyte/electrode interface especially through the hydrophilic/hydrophobic surface balance. $Ti_3C_2T_x$-MXene also shows up to ≈ 6700 $S.cm^{-1}$ of metallic conductivity which is highly favorable to fast electron transfer.[43-45] However, as for other 2D materials, the MXene flakes tend to restack during the preparation process, resulting in a drastic loss of the developed electroactive surface area, and hindering the electrolyte ion access into the electrode bulk[15]. To prevent this re-stacking issue and simultaneously enhance the through-plane ionic conductivities, alternative methods based, for instance, on the modification of the layer morphology and texture have to be considered.

In this study, exfoliated $Ti_3C_2T_x$-MXene was first prepared by a chemical etching method from Ti_3AlC_2 corresponding MAX phase. To prevent the re-stacking of the resulting individual layers, several routes were explored. First, nano-sized MgO particles were used as solid spacer. After removal of the particles adsorbed at the layer surface, electrolytic ions were able to be efficiently transported in between the layers of the resulting expanded MXene during the charge-discharge process. Therefore, prepared expanded MXene (EM) electrodes showed enhanced electrochemical performances when compared to regular MXene. Alternatively, urea was used as molecular spacer or template. After a thermal treatment under argon atmosphere, a $Ti_3C_2T_x$-MXene foam (MF) was obtained. The resulting MF electrode showed an attractive and seriously improved capacitance performance, especially at high rate. When associated to a MnO_2 positive-electrode in an MF//MnO_2 asymmetric device, an attractive energy density of 16.5 Wh kg^{-1} (or 10 Wh L^{-1}) was obtained at 160 W kg^{-1} (or 8.5 kW L^{-1}) power density.

5.3 Experimental details

Preparation of MXene-$Ti_3C_2T_x$ suspension and pure MXene: 1 g LiF (Sigma, 99.98%) and 20 ml 9 M HCl (Sigma, 37%) solution were mixed in a plastic beaker and stirred for a few of minutes. 1 g Ti_3AlC_2 powders was then slowly added to the solution. The reaction temperature was kept at 35 °C for 24 h under constant stirring. The resulting $Ti_3C_2T_x$ flakes were washed with water and separated by centrifugation until the pH value was ~ 6. The flakes were dispersed in 250 ml H_2O and treated by sonication for 1 h. Finally, the resulting $Ti_3C_2T_x$ was recovered by a 1 h centrifuge step at 3500 rpm. The average size of resulting MXene flakes is centered at 0.2 and 2 µm (Figure S1). The pure MXene film was prepared by a simple vacuum filtration procedure on a PTFE membrane by using 3500 rpm rotating speed.

Preparation of expanded MXene by hard templating method: 23.26 ml $Ti_3C_2T_x$ MXene suspension (50 mg, 2.15 mg/ml) were dispersed in 26.74 ml, 200 mg MgO (Sigma, nanopowder ≤ 50 nm particle diameter) solution, and the solution was stirred for 24 h. During the filtration process, 40 ml, 3 M acetic acid (Sigma, 99.8%) were slowly added to remove the MgO template. After washing three times with pure water, the film was dried at 50 °C under vacuum.

Preparation of the MXene foam and overlapped MXene foam: 23.26 ml $Ti_3C_2T_x$ MXene suspension (50 mg, 2.15 $mg.ml^{-1}$) was mixed with 23.26 ml urea (Sigma) solution (200 mg with or without 0.1 M HCl). The resulting solution was stirred for 2 h. A thick disk was obtained by vacuum filtration. After drying it at 50 °C under vacuum, the resulting film was placed in a porcelain crucible and treated at 550 °C for 2 hours under argon atmosphere.

Preparation of MnO_2: 0.1272 g $MnCl_2$ (Merck Schuchardt, anhydrous) was dispersed in 20 mL H_2O under continuous stirring. The same was done with 0.24 g $KMnO_4$ (Sigma, 99.0%). The $KMnO_4$ solution was slowly added to $MnCl_2$ solution. The resulting mixture was heated at 100 ^oC and kept for 6 h at this temperature under constant stirring. After filtration and rinsing with water, the powder was obtained by drying at 80 ^oC overnight. From the XRD pattern, the prepared powder was assigned to δ-MnO_2 (Figure S2). Corresponding SEM and TEM images are depicted in Figures S3 and S4, respectively.

Material characterization: The crystal phase and structure of the prepared material films were examined by X-ray diffraction (XRD) using a Phillips X'Pert diffractometer with Cu Kα radiation (λ=1.5405Å). Morphologies were imaged by using a JEOL JSM-6300F scanning electron microscope (SEM). The element composition was analyzed by Energy-dispersive X-ray spectroscopy (EDX) in SEM. The thermal decomposition of MF was followed by thermo-gravimetry coupled mass-spectrometry (TG-MS) under Ar from room temperature to 800 °C (rate 5 °C/min).

Electrochemical characterization: Electrochemical measurements were performed in three electrode systems, symmetric device and asymmetric at ambient temperature by using a VMP3 multi-channel Bio-Logic electrochemical workstation. In three-electrode system, platinum foil and Hg/HgO/OH^- electrode were used as counter and reference electrode respectively. The working electrode was assembled by two clean nickel foam with sandwiched binder-free MXene film in between two stainless steel under 10 Mpa for 30 seconds. Finally, the system was tested in 1 M KOH electrolyte. In the symmetric device, two identical working electrodes were prepared as follows. The electrode was prepared by mixing the active material, carbon black and Polytetrafluoroethylene (PTFE) with a mass ratio of 60/30/10. The mixture was dispersed in a proper volume of ethanol under constant stirring. Then, the mixture was evaporated at 60 °C to get a slurry. With the adapted behavior, the slurry was rolled and, when dry, pressed in between two stainless steel under 10 Mpa for a few tens of second. Finally, the cut suitable film was assembled into the Swagelok device. For asymmetric device, MnO_2 was used as a positive electrode. For individual electrodes, capacitances are relative to the mass of active material while for devices, they are relative to the cu;ulative mass of active materials in both electrodes.

The below related supporting information has been attached after reference.

5.4 Results and discussion

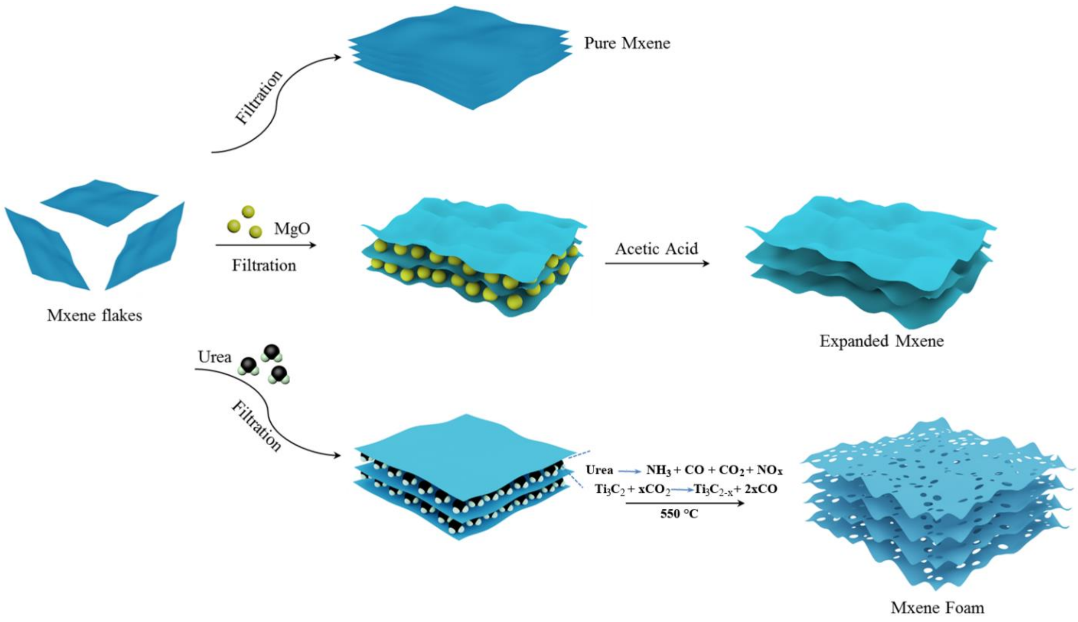

Figure 5.1 Synthesis scheme of the preparation of various forms of MXene, as re-stacked material after exfoliation (top), expanded MXene after re-stacking in presence of MgO nanoparticles (middle), and MXene foam from thermal treatment in presence of urea (bottom).

The specific synthetic routes are depicted in Figure 5.1. A suspension of exfoliated MXene flakes was first prepared as described in the experimental section (see *Experimental details* below). In the present study, it was used as starting material for the preparation of other MXene-based materials. The drastic changes in the corresponding XRD patterns shown in Figure 5.2 are a crystallographic proof of the conversion of Ti_3AlC_2 MAX phase (Figure 5.2a) to MXene (Figure 5.2b). As usually observed for 2D materials, only the peak series characteristic of the layered structure of MXene, remains after conversion while the other peaks, especially around 39° 2θ, disappear. An inter-layer distance of 11.15 Å was calculated for the prepared MXene from the 2θ position of the (002) diffraction peak at 7.87° 2θ. From Ti_3AlC_2 MAX phase (Figure 5.3a) to MXene (Figure 5.3b), the more open and disordered 2D morphology is also evidenced by looking at the corresponding SEM micrographies.

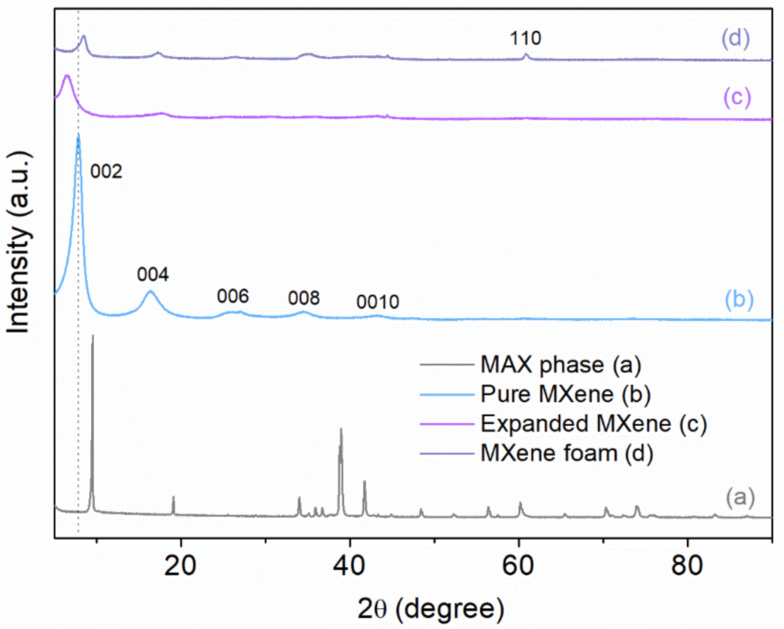

Figure 5.2 XRD patterns of Ti_3AlC_2 MAX phase (a), MXene (b), Expanded MXene (c), and Mxene Foam (d).

To prevent the re-stacking of the MXene layers and eventually to get an even more open 2D structure, magnesium oxide was considered as a solid nano-spacer (Figure 5.1, middle). Such a hard template has already been used for the preparation of carbons with hierarchical porosities including activated or doped carbons, graphene.[46,47,48] It appears as suited for this purpose as it is easy to prepare and/or commercially available as nanoparticles that efficiently absorb material precursors, either in molecular, polymeric or solid states, through Van der Waals interactions and hydrogen bonds. Moreover, as such a template, it can be easily removed using a mild acidic post-treatment. MgO particles were first homogeneously dispersed in the suspension of Ti_3C_2Tx-MXene flakes by ultrasonication and vigorous stirring. Once the composite suspension filtrated, MgO nanoparticles are randomly and uniformly distributed in between the MXene layers. Commercial MgO particles were actually chosen for their diameter below 50 nm to fit the MXene flake size distribution (at 0.2 and 2 µm, Figure S1). This size ratio promoted a consistent 2D sandwich composite structure build on flakes large enough to cover “many” particles instead of a simple/single particle wrapping that would restrain the development of the targeted expanded framework. Afterwards, MgO particles were slowly "digested" by gently pouring an acetic acid solution, and progressively washed away. The resulting film of expanded MXene was recovered after washing and drying. When comparing the XRD pattern of the expanded MXene as shown in Figure 5.2 with that of the exfoliated MXene used as precursor, the structural impact of the MgO hard templating is obvious: While the MXene layered structure remains, despite a severe amorphization of the material related to the loss of the long range order, a strong shift of the (002) peak towards lower angles is observed (Figure 5.2c). As such, the interlayer distance increases from 11.15 to 13.60 Å along the c-axis thanks to hard templating with MgO nanoparticles.

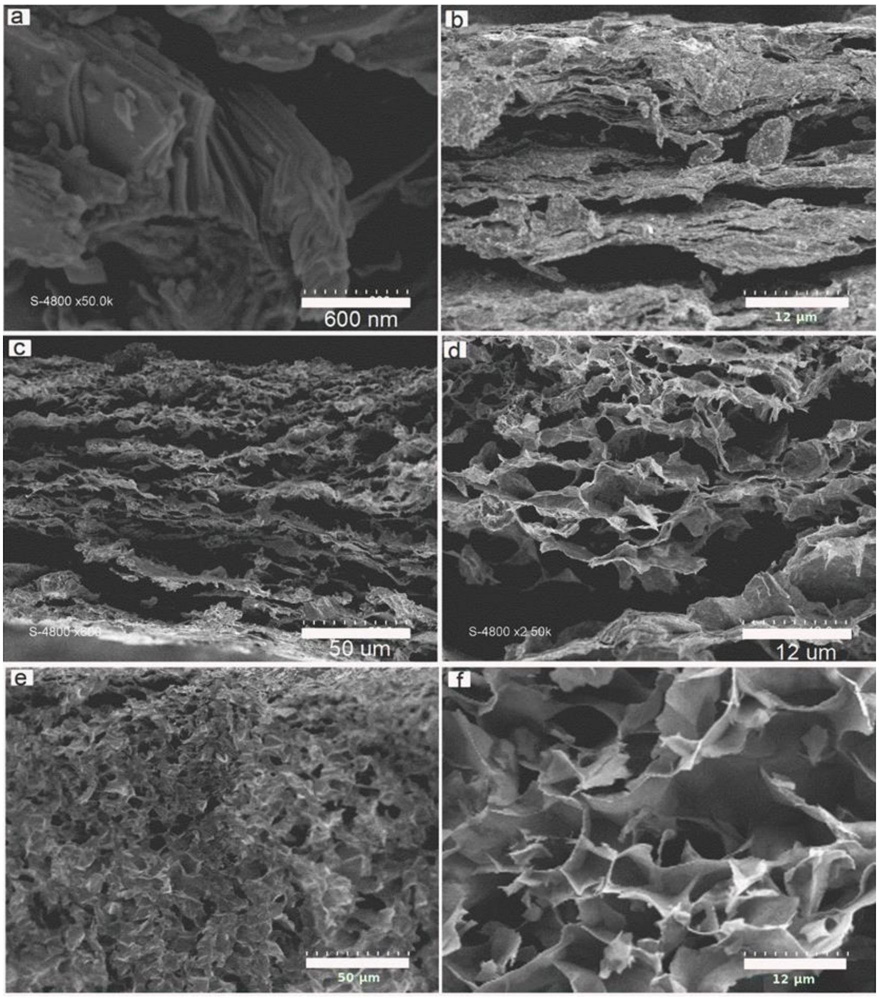

Figure 5.3 Side views from SEM images of Ti_3AlC_2 MAX phase (a), $Ti_3C_2T_x$-MXene (b), Expanded $Ti_3C_2T_x$-MXene (c, d) and $Ti_3C_2T_x$-Mxene foam (e, f).

SEM images in Figure 5.3 (c, d) show the side view of the prepared expanded MXene. The complex structure is built on large voids in between crumpled MXene layers. While voids are originating from the dissolution of MgO nanoparticles by acidic treatment, layer crumpling could be assigned to the mechanical stress induced by capillary forces during material drying. The resulting open 3D architecture, with interconnected channels and conductive walls, is anticipated to promote suitable ion diffusion and electronic percolation through the whole material volume.

On the other hand, urea has been widely used as a reactant to synthesize N-doped materials through a pyrolysis process, including nanostructured metal oxides[49], carbides[50], carbons[51,52], etc. Although, such a doping is a conventional strategy in semiconductor processes, it has been more recently introduced in the synthesis of energy conversion and storage electrode materials, for oxygen reduction[53], supercapacitors[54] or LiS batteries[55], leading to enhanced electrochemical performances and stability. After mixing the $Ti_3C_2T_x$-MXene with urea, a thick disk was obtained by vacuum filtration. The re-staking of MXene layers is prevented by urea molecules trapped in between. In such a slightly acidic medium, cationic protonated urea strongly absorbs at the negatively charged MXene flakes and the layers are efficiently kept apart when going to solid state. The resulting MXene@urea composite material was pyrolyzed at 550 °C under argon atmosphere. All synthetic details are given in the experimental part above. SEM micrographies of the pyrolized Mxene@urea composites are depicted in Figure 5.3e, 5.3f and Figure 5.4b to 5.4d. Although the side view (Figure 5.3e and 5.3f) is characteristic of the opening of the structure of the material induced by the synthetic process, the layered morphology of the pristine MXene (Figure 5.3b) is hardly identified in the resulting disordered honey-comb structure. Moreover, discrepancies in the top views in Figure 5.4 of MXene and the resulting material are spectacular. While MXene shows a flat and “plain” surface build on $Ti_3C_2T_x$ layers (Figure 5.4a), the pyrolysis of MXene/urea composite obviously generate numerous macro-pores through the layers, i.e. perpendicular to the surface (Figure 5.4b-4d). The resulting 3D structure based on a disordered self-assembling of exfoliated and porous layers displays a complex foam architecture. When comparing with the pristine MXene, the (002) peaks of MXene Foam (MF) slightly shift towards greater 2θ angles, suggesting a decrease of the inter-layer distance induced by the synthetic process (Figure 5.2d). Such a shrinking can be assigned to the de-intercalation of H_2O molecules during the thermal treatment, either free or solvating urea molecules, originally trapped in between the MXene layers. Moreover, during the process, MXene flakes are self-assembling as a foam structure by a pore-forming process that is confirmed by the appearance of a (110) peak at about 60.85° 2θ. This peak is characteristic of the ordering induced in the non-basal directions. Meantime, as confirmed by the (002n) peaks, some c-axis ordering remains.[56]

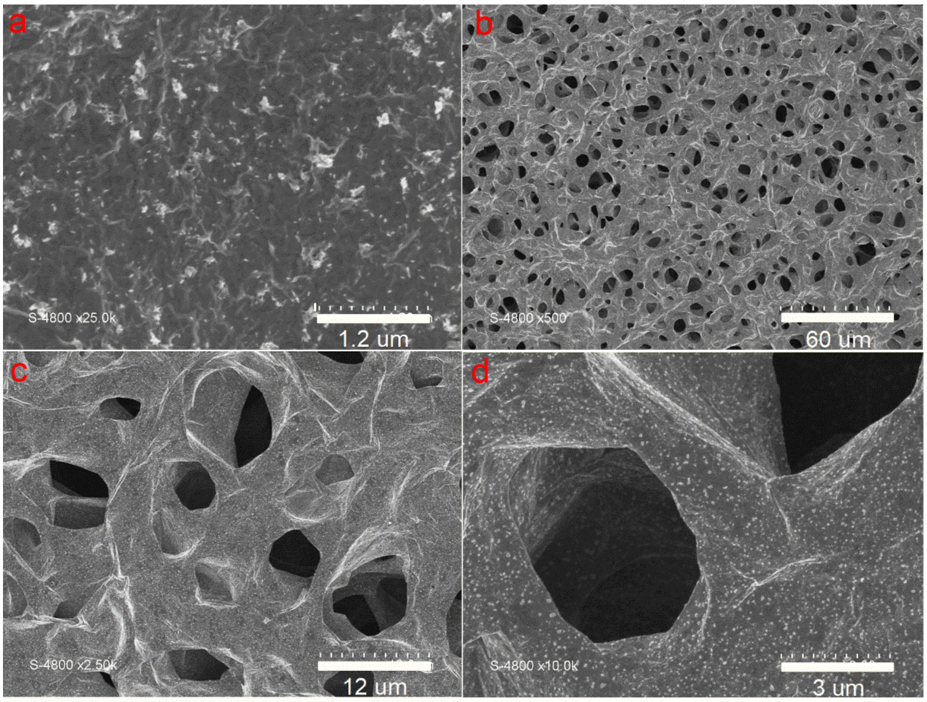

Figure 5.4 The SEM images of pristine MXene (a) and MXene Foam (b-d) surface view.

As already mentioned, many authors have reported on the use of urea to N-dope various materials including carbons and carbides. To the best of our knowledge, any of these have mentioned such a drastic impact on the resulting material morphology, especially on pore generation. In the present case, the reactivity of urea towards $Ti_3C_2T_x$ layers at 550 °C can be assigned to the pore forming process and generation of the complex 3D foam structure. Surprisingly, it was not possible to demonstrate the presence of nitrogen as dopant in the resulting material by SEM-EDX (Figure S5 and S6 and Table S1). The TG-MS analysis performed on an MXene/urea composite up to 800 °C, confirms the thermal decomposition of urea as ammonia, carbon monoxide, carbon dioxide and nitrous oxides. The mechanism of formation of MXene foams involves these gases as generated CO_2 etches the carbon from $Ti_3C_{2.2}T_x$–MXene (as calculated from EDX measurements in Table S1) to drill holes in the layers, resulting in a $Ti_3C_{1.7}T_x$-MXene foam. Generated gases, while confined during the thermal treatment, are suspected to induce mechanical deformations of the layers before to escape from the complex macroporous structure.

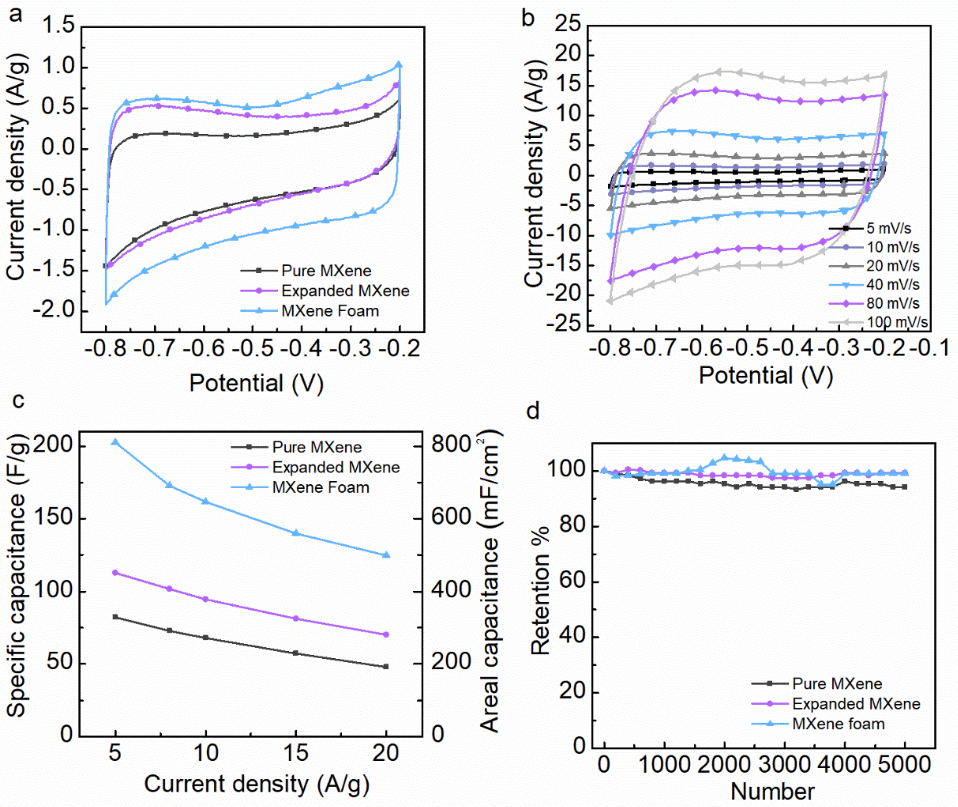

Figure 5.5 Electrochemical characteristics of binder-free electrodes in three electrode configurations using 1 M KOH as electrolyte. (a) Comparison of CV curves of the prepared materials at 5 mV s^{-1} scan rate. (b) CV curves of MXene foam electrode at various scan rates. (c) Comparison of the specific capacitances of the prepared material as a function of the applied current densities. (d) Comparison of the capacity retention of pristine MXene, expanded MXene and MXene foam at 5 A g^{-1} over 5000 charge-discharge cycles.

Electrochemical performance of prepared electrode materials was investigated in three electrode configuration in 1M KOH electrolyte. In Figure 5.5a, the roughly rectangular shape of CVs at 5 mV s^{-1} demonstrates the pseudocapacitive behavior of prepared MXene-based materials. A similar behavior was also observed in 1M Na_2SO_4 neutral electrolyte while in acetonitrile organic electrolyte, the electrochemical activity was limited (Figure S7). As demonstrated by the CVs of the MXene foam–based electrode in Figure 5.5b, this behavior remains at higher scan rate, up to 100 mV s^{-1} at least, as only slight distortions are observed. In the series, a quick comparison of the corresponding integral area at 5 mV s^{-1} scan rate suggests that the MXene foam -based electrode presents the greatest capacitance. This was confirmed by the galvanostatic charge-discharge measurements at 5 A g^{-1} (Figure S8a) used for specific capacitance calculations. The specific capacitance of pristine MXene is the lowest at 80 F g^{-1}. For expanded MXene, capacitances is 112 F g^{-1}. Finally, the greatest specific capacitance at 5 A g^{-1} was measured at 203 F g^{-1} (811 mF cm^{-2}) for the MXene foam –based electrode. This enhancement can certainly be assigned to the progressive opening of the material structures in the series leading to a larger electrochemical interface and greater number of sites available for electrolytic ions involved in charge compensation. The improvement in the ion transport capabilities of the materials is also confirmed by the specific capacitance retention at higher scan rate (Figure 5.5b). In addition, the achieved capacitance of MXene foam in this paper exceeds other MXene-based supercapacitors. For instance, Zhao et al.[57] prepared a composite, in which RGO plays a role of conductive "bridge" to link with $Ti_3C_2T_x$ blocks, thus showing a specific capacitance of 154 F g^{-1} at 2 A g^{-1}. Zhu and co-workers[58] decorated the TiO_2 on the Ti_3C_2 layers by using a simple in situ hydrolysis and heat-treatment process. The synthesized composite revealed a high specific capacitance of 143 F g^{-1} at 5 mV s^{-1}. Yang et al.[59] deposited the binder-free Ti_3C_2 MXene/carbon nanotubes films onto graphite paper by the electrophoretic deposition method. The as-prepared electrode displayed 134 F g^{-1} at 1 A g^{-1}. Shi et al.[60] synthesized the MXene foam by using a thermal treatment method to restrain the restacking issue. The obtained MXene foam exhibited a high capacitance of 123 F g^{-1} at 5 mV s^{-1}. Starting with pristine MXene electrode at 48 F g^{-1}, specific capacitances at 20 A g^{-1} ranked about the same as expanded MXene electrode shows 70 F g^{-1} and MXene foam a remarkable 125 F g^{-1} specific capacitances (Figure 5.5c and Figure S8b). Moreover, the observed asymmetry of the galvanostatic curves is characteristic of limited Coulombic efficiencies. This behavior is actually shared by many MXene-based electrode materials.[61, 62, 63, 64] It is assigned to parasitic redox reactions, especially those involving the electrolyte and/or the MXene surface groups. The Faradaic origin of this (slow) phenomenon is supported by the improvement of the measured Coulombic efficiency as the scan rate (or current density) is increased. A more detailed analysis was done on the kinetics of the charge storage in the the various prepared Mxene-based electrode materials. First, the Log-Log current versus scan rate curves were plotted from CV data at various scan rates (Figure S9). b slopes were calculated at 1.06 (pure MXene), 0.99 (Expanded MXene) and 1.02 (MXene foam) and correspond to $i = av^b$ relationship[65, 66, 67]. Being close to 1, they suggest the charge storage mechanism in the corresponding materials to mostly proceed through fast surface-controlled processes, hardly limited by diffusion of electrolytic ions in the electrode bulk. Second, the stronger contribution of the surface material was especially confirmed for the MXene foam electrode by separating capacitive (surface) versus diffusion-limited currents in the corresponding CVs operated at various scan rates (Figure S10). The corresponding capacitive ratio are reported as an histogramm in Figure S11. It should be noticed that it is 71% at 5 mV s^{-1}, implying a significant capacitive/surface contribution to the overall measured capacitance, even at such a low scan rate. Furthermore, the capacitive contribution increases while raising the scan rate, signifying that, at high rates, MXene foam stores charges mostly through surface reactions in the EDL.

Nyquist plots shown in Figure S12 confirm the similar behavior of the perpared electrodes at high frequency, especially in terms of charge transfert resistance, but the straigth and sharp increase of the imaginary part of the impedance (-Z'') of the MF -based electrode in the low frequency range confirms this material attractive capacitive performance. On the other hand, the cycle stability was tested for 5000 cycles by galvanostatic charge-discharge measurements at 5 A g^{-1} current density. The results are shown in Figure 5.5d for MXene–based electrodes. A closer look at the charge-discharge curves reveals some measurement artefacts (Figure S13), especially between cycles #2000 and #3000, leading to calculation errors and overestimated corresponding capacitance values. Finally, the pristine MXene keeps 94 % of its initial specific capacitance, while expanded MXene and MXene foam show excellent 99 % capacitance retention.

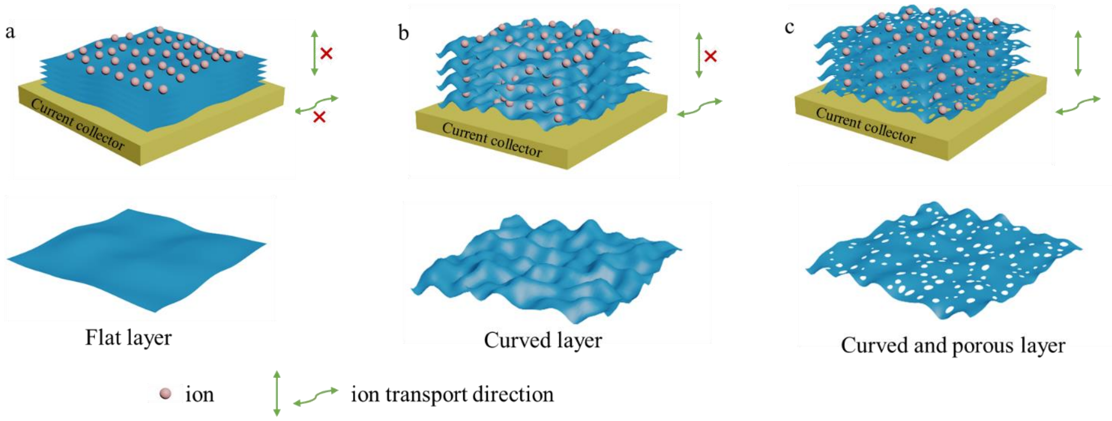

Figure 5.6 Schematic diagram of ion transport in different morphologies' electrode materials in supercapacitor.

The electrochemical performances of the prepared electrode materials can be rationalized by using Gogotsi statement on the various strategies to prevent nanosheet re-stacking to fully use the developed surface area and enhance the electrolytic ion diffusion and transport.[15] As shown in Figure 5.6a, the flat layers of the pristine MXene are the less favorable material design in the series as nothing, in such a case, can prevent the natural trend of the layers to self-assemble in a re-stacked structure. The diffusion of the electrolytic ions is hindered by the limited inter-layer space and most of the electrochemically active surface corresponds to the external surface of the material. Ion diffusion perpendicular to the layer surface is only possible along the edges of the MXene particle. As such, corresponding electrochemical performances, especially specific capacitance and rate capability, are fair but also leave many room for improvement. In contrast, the morphology of the expanded MXene is inherited by the shape and the size of the MgO particles used as hard template.

The open structure is promoted by the assembling of a composite made of exfoliated MXene layers wrapping MgO particles. After hard template removal in mild acidic conditions, its footprint remains, providing the assembled layers with a crumpled morphology and an enlarged interlayer space. The porosity generated in between the curved layers is obviously more favorable for in-plane fast ion transport and access to more active sites. As a consequence, both electrochemically active surface area and ion diffusion are greatly improved. So are the corresponding electrochemical performances. Unfortunately, diffusion through the plane is still limited to particle edges. This limitation can be overpassed by introducing porosity on the layers. The thermal decomposition of urea between or at MXene layers generate holes and promote a structure built on the assembly of curved porous layers. The resulting electrochemical performances of the prepared foam take advantage of this complexe 3D structure showing simultaneously large interlayer spaces and many connexions through the layers facilitating access of the electrolytic ions to the entire volume of the electrode.

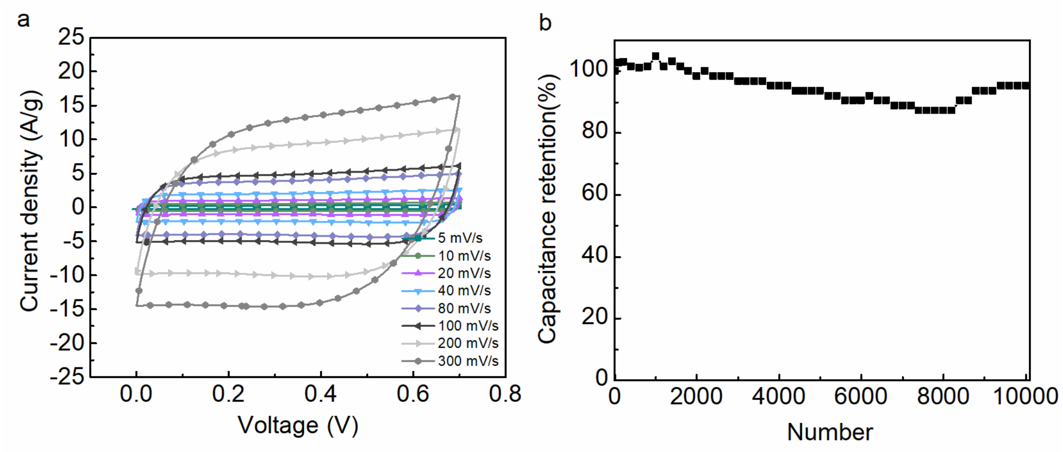

Figure 5.7 The electrochemical characteristic of symmetric MF//MF device. (a) CV curves at various scan rates. (b) Cycling performance over 8k cycles of charge discharge at 5 A g^{-1}.

The electrochemical performance of a symmetric device based on MXene foam –based electrodes (MF//MF) are shown in Figure 5.7 and Figure S14. The CV curves in KOH 1M at various scan rates are displayed in Figure 5.7(a). A decent device rate capability is anticipated since, up to 300 mV s^{-1}, distortions of the rectangular CV shape measured at low scan rate are very limited. Specific capacitance values were calculated from galvanostatic charging-discharging measurements at various current densities. Up to 20 A g^{-1} the signal kept the expected triangular shape with limited Ohmic drop (Figure S14a). Device energy and power densities were obtained from these measurements and reported in the Ragone plot shown in Figure S14b. With electrode loadings at about 3.5 mg cm^{-2}, the energy density of symmetric MF//MF device is about 3.6 Wh kg^{-1} at 350 W kg^{-1} of power density. When relative to the cumulative volume of MF in both electrodes, it translates as 2.5 Wh L^{-1} at 2.5 kW L^{-1}. Although these performances are limited, the aim of these measurements, either in 3- and 2- electrode setups, is to highlight the specific behavior of MF electrode, notwithstanding the potential limitations by any other “counter” electrode material. The cycle stability of device was measured at 5 A.g^{-1} over 8000 charge-discharge cycles. The calculated 87 % capacitance retention confirm the fair stability of the electrode materials when operated in the given conditions (Figure 5.7b). However, despite the promising electrochemical behavior of the electrode material, in such MF//MF symmetric device, the operating voltage is limited to 0.7 V with a severe impact on the available energy density, especially. To address this issue, an asymmetric device was considered. It was built on a MnO_2 positive electrode (Figure S15) and a MF negative electrode. Electrochemical results in KOH 1M are summarized in Figure 5.8. In comparison with the symmetric MF//MF device, MF//MnO_2 shows a great enhancement as a 1.6 V cell voltage was obtained. Both CV and galvanostatic series of curves are characteristic of the pseudocapacitive behavior of the electrode components but the signal distortions are characteristic of lower rate capabilities (Figure 5.8a and 5.8b). This was confirmed when calculating the device power density at 160 W Kg^{-1} or 8.5 kW L^{-1}. In contrast the effect of the larger cell voltage is expressed by an enhanced energy density at 16.5 Wh kg^{-1}, 2 to 3 times greater than that of a C//C symmetric device based on activated carbon electrodes in aqueous electrolyte[68]. When considering the volume of active materials in both electrode, the volumetric energy density reached 10 Wh L^{-1} (4 times greater than that of a C//C device). During the first 5000 charge-discharge cycles, the device capacitance progressively increased to reach more than 110% of the initial value at 25 F g^{-1} (Figure 5.8d). The observed capacitance increase over the first 5000 charge-discharge cycles can be assigned to a slow and progressive impregnation of both electrodes upon cycling.

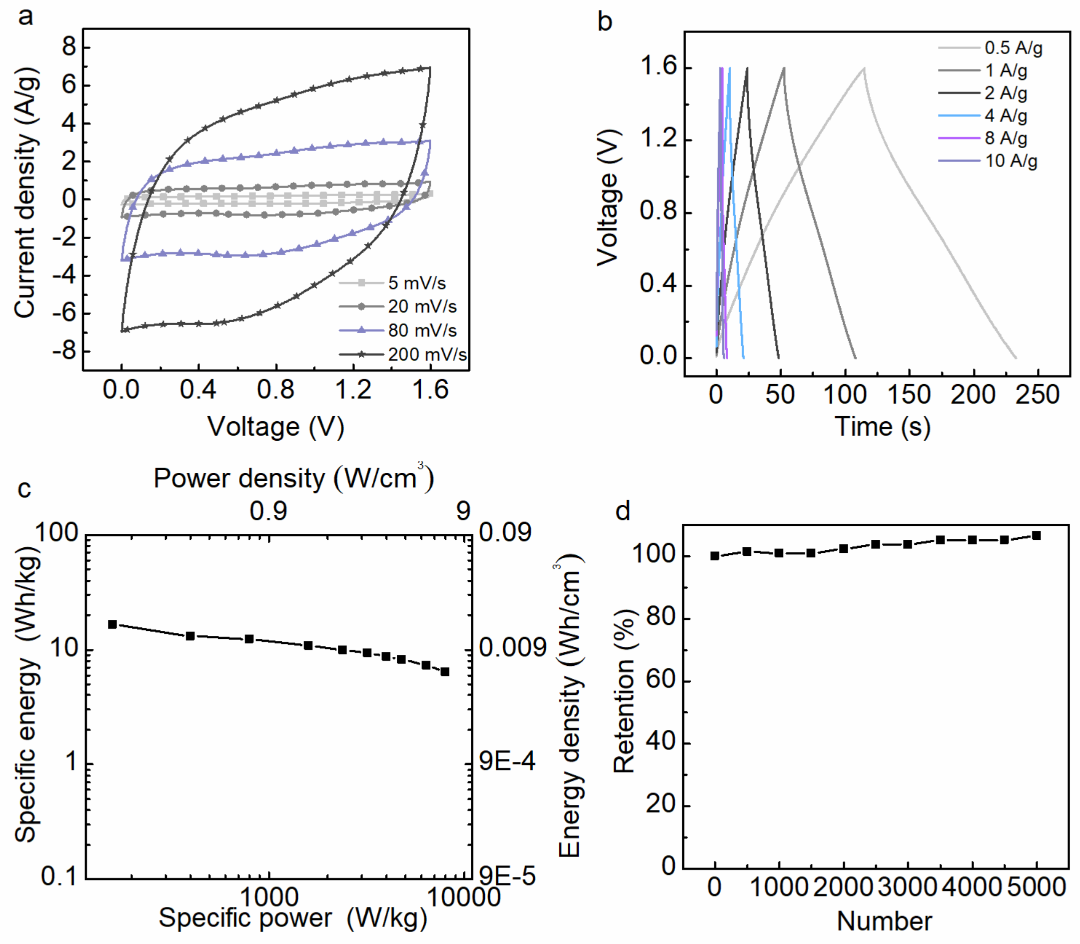

Figure 5.8 The electrochemical performance of asymmetric MF//MnO$_2$ device. (a) CV curves at various scan rates. (b) Galvanostatic charge-discharge test at various current densities. (c) Charge-discharge cycling performance at 5 A g^{-1} over 5k cycles.

5.5 Conclusion

To address the re-stacking issue of exfoliated MXene layers, we successfully prepared and engineered the expanded MXene and MXene foam materials by a hard template approach and a pore-forming method, respectively. As electrode materials, the binder-free MXene-based materials showed promising electrochemical performances in KOH 1M, either in terms of specific capacitance, rate capability and long term cycling. When moving from MXene to expanded MXene and MXene foam, the observed great improvement was assigned to the increase of the developed electroactive area and ion transport capability promoted by the morphology opening with larger interlayer space and pores through the MXene layers. MF was tested as electrode material in devices. Both symmetric MF//MF and asymmetric MF//MnO_2 devices displayed attractive rate capability and excellent cycle stability. Moreover, MF//MnO_2 device exhibited a fair energy density of 16.5 Wh kg^{-1} and 10 Wh L^{-1}.

Acknowledgements

Y. C. ZHU (NO. 201606240097) is supported by China Scholarship Council (CSC).

This chapter is already published as an article on Nano Energy.

5.6 Reference

1. Novoselov, K. S. Mishchenko, A. Carvalho, A. Castro Neto, A. H., Science 2016, 353 (6298), aac9439.

2. Lin, D. Liu, Y. Liang, Z. Lee, H. W. Sun, J. Wang, H. Yan, K. Xie, J. Cui, Y., Nat Nanotechnol 2016, 11 (7), 626-32.

3. N. Jabeen, A. Hussain, Q. Xia, S. Sun, J. Zhu, and H. Xia, Adv. Mater. 2017, 29, 1700804.

4. Y, Zhao, W, Ran, et al. D. Gao and F. Gao, Small 2015, 11, 1310–1319.

5. Y. Zhao, et al., W, Huang, and T, Zhang, Adv. Energy Mater. 2017, 7, 1700005.

6. Lv, R. Robinson, J. A. Schaak, R. E. Sun, D. Sun, Y. Mallouk, T. E. Terrones and M. Terrones, Acc. Chem. Res. 2015, 48 (1), 56-64.

7. S. Karunakaran, et al., B. Basu, and M. De, J. Am. Chem. Soc. 2018, 140, 12634−12644.

8. Alhabeb, M. Maleski, K. Anasori, B. Lelyukh, P. Clark, L. Sin, S. Gogotsi, Y., Chemistry of Materials 2017, 29 (18), 7633-7644.

9. C. Zhang, et al., Y. Gogotsi, and V. Nicolosi, Stamping of Flexible, Adv. Funct. Mater. 2018, 28, 1705506.

10. Ling, Zheng, et al., Proceedings of the National Academy of Sciences 111.47 (2014): 16676-16681.

11. Gupta, A. Sakthivel, T. Seal, S., Progress in Materials Science 2015, 73, 44-126.

12. Yang, Xiaowei, et al. science 341.6145 (2013): 534-537.

13. Coleman, Jonathan N., et al. Science 331.6017 (2011): 568-571.

14. Augustyn, Veronica, et al. Nature Materials 12.6 (2013): 518.

15. Mendoza-Sanchez, B. Gogotsi, Y., Adv Mater 2016, 28 (29), 6104-35.

16. Mas-Balleste, R. Gomez-Navarro, C. Gomez-Herrero, J. Zamora, F., Nanoscale 2011, 3 (1), 20-30.

17. Parvez, K. Wu, et al., R. Feng, X. Mullen, K., J Am Chem Soc 2014, 136 (16), 6083-91.

18. Lukatskaya, M. R. Mashtalir, O. Ren, C. E. Dall'Agnese, Y. Rozier, P. Taberna, P. L. Naguib, M. Simon, P. Barsoum, M. W. Gogotsi, Y., Science 2013, 341 (6153), 1502.

19. Wu, J. Zhang, Q. e. Wang, J. Huang, X. Bai, H., Energy & Environmental Science 2018.

20. W. Quan, C. Jiang, S. Wang, Y. Li, Z. Zhang, Z. Tang, and F. Favier, *Electrochimica Acta*, 2017, 247, 1072-1079.

21. Liu, Y. Lin, D. Liang, Z. Zhao, J. Yan, K. Cui, Y., Nat Commun 2016, 7, 10992.

22. Wang, Y. Song, Y. Xia, Y., Chem Soc Rev 2016, 45 (21), 5925-5950.

23. Yang, P. Sun, P. Mai, W., Materials Today 2016, 19 (7), 394-402.

24. Sun, Yiqing, Qiong Wu, and Gaoquan Shi. Energy & Environmental Science 4.4 (2011): 1113-1132.

25. Huang, Yi, Jiajie Liang, and Yongsheng Chen. Small 8.12 (2012): 1805-1834.

26. Stoller, Meryl D., et al. Nano letters 8.10 (2008): 3498-3502.

27. Hu, Liangbing, et al. ACS nano 5.11 (2011): 8904-8913.

28. Liu, Jinping, et al. Advanced Materials 23.18 (2011): 2076-2081.

29. Zhang, Xiong, et al. Electrochimica Acta 89 (2013): 523-529.

30. Zhang, Fan, et al. Energy & Environmental Science 6.5 (2013): 1623-1632.

31. Dubal, Deepak P., et al. Chemical Society Reviews 44.7 (2015): 1777-1790.

32. Wang, Yonggang, Yanfang Song, and Yongyao Xia. Chemical Society Reviews 45.21 (2016): 5925-5950.

33. Augustyn, Veronica, Patrice Simon, and Bruce Dunn. Energy & Environmental Science 7.5 (2014): 1597-1614.

34. Ding, L. Wei, Y. Li, L. Zhang, T. Wang, H. Xue, J. Ding, L. X. Wang, S. Caro, J. Gogotsi, Y., Nat Commun 2018, 9 (1), 155.

35. Lukatskaya, M. R. Kota, S. Lin, Z. Zhao, M.-Q. Shpigel, N. Levi, M. D. Halim, J. Taberna, P.-L. Barsoum, M. W. Simon, P. Gogotsi, Y., Nature Energy 2017, 2 (8), 17105.

36. Hu, H. Hua, T., Journal of Materials Chemistry A 2017, 5 (37), 19639-19648.

37. Li, H. Hou, Y. Wang, F. Lohe, M. R. Zhuang, X. Niu, L. Feng, X., Advanced Energy Materials 2017, 7 (4), 1601847.

38. Tian, Y. Yang, C. Que, W. He, Y. Liu, X. Luo, Y. Yin, X. Kong, L. B., Journal of Power Sources 2017, 369, 78-86.

39. Yan, J. Ren, C. E. Maleski, K. Hatter, C. B. Anasori, B. Urbankowski, P. Sarycheva, A. Gogotsi, Y., Advanced Functional Materials 20, 27 (30), 1701264.

40. Yang, Q. Xu, Z. Fang, B. Huang, T. Cai, S. Chen, H. Liu, Y. Gopalsamy, K. Gao, W. Gao, C., J. Mater. Chem. A 2017, 5 (42), 22113-22119.

41. Ahmed, B. Anjum, D. H. Hedhili, M. N. Gogotsi, Y. Alshareef, H. N., Nanoscale 2016, 8 (14), 7580-7.

42. Chaudhari, N. K. Jin, H. Kim, B. San Baek, D. Joo, S. H. Lee, K., Journal of Materials Chemistry A 2017, 5 (47), 24564-24579.

43. Couly, C. Alhabeb, M. Van Aken, K. L. Kurra, N. Gomes, L. Navarro-Suárez, A. M. Anasori, B. Alshareef, H. N. Gogotsi, Y., Advanced Electronic Materials 2018, 4 (1), 1700339.

44. Sang, X. Xie, Y. Lin, M. W. Alhabeb, M. Van Aken, K. L. Gogotsi, Y. Kent, P. R. Xiao, K. Unocic, R. R., ACS Nano 2016.

45. Shahzad, F. Alhabeb, M. Hatter, C. B. Anasori, B. Man Hong, S. Koo, C. M. Gogotsi, Y., Science 2016, 353 (6304), 1137.

46. X. He, R. Li, et al., M. Zheng, Carbon, 2012, 50, 4911-4921.

47. Y. Zhang, et al., M. Xie and X. Guo, J. Mater. Chem. A, 2018, 6, 2353-2359.

48. J. Wei, D. Zhou, et al., Y. Xia and D. Zhao, Advanced Functional Materials, 2013, 23, 2322-2328.

49. Y.Cong, J. Zhang, F. Chen and M. Anpo, J. Phys. Chem. C 2007, 111, 19, 6976-6982.

50. C. Yang, W. Que, et al., Y. Yang and M. Que, Electrochimica Acta, 2017, 225: 416-424.

51. D. Qu, M. Zheng, et al., Z. Xie and Z. Sun, Nanoscale, 2013, 5, 12272-12277.

52. D. Qu, M. Zheng, et al., H. Fan and Z. Sun, Scientific reports, 2014, 4: 5294.

53. Z. Gordon W. Liu, M. Liu and C. Wong, Advanced Energy Materials, 2012, 2, 884-888.

54. L. Sun, et al., M. Li and H. Fu, RSC Adv., 2012, 2, 4498-4506.

55. W. Bao, et al., D. Wang and G. Wang, Advanced Energy Materials, 2018, 8(13): 1702485.

56. Li, L. Zhang, M. Zhang, X. Zhang, Z., Journal of Power Sources 2017, 364, 234-241.

57. C. J. Zhao, et al., ACS Appl. Mater. Interfaces 2016, 8, 15661−15667.

58. J. F. Zhu, et al., Journal of The Electrochemical Society, 2016, 163 (5) A785-A791.

59. L. Yang, W. Zheng, P. Zhang et al., Journal of Electroanalytical Chemistry 2018, 1-6, 830-831.

60. L. Shi, S. Lin, W. Wu, et al., Ceramics International 44 (2018) 13901–13907.

61 J. Jian, X. T. Yuan, et al., J. H. Lin and J. L. Sun, Advanced Energy Materials, 2017, 7(15): 1602725.

62. X. Q. Xie, M. Q. Zhao, et al., G. X. Wang and Y. Gogotsi, Nano Energy, 2016, 26: 513-523.

63. Y. Yue, N. S. Liu, et al., J. Su and Y. H. Gao, ACS nano, 2018, 12(5): 4224-4232.

64. C. F. Zhang, et al., Y. Gogotsi and V. Nicolosi, Advanced Functional Materials, 2018, 28(9): 1705506.

65. C.-H. Lai, D. Ashby, M. Moz, Y. Gogotsi, L. Pilon, and B. Dunn Langmuir 2017 33 (37), 9407-9415.

66. P. Yu, C. Li, and X. Guo, The Journal of Physical Chemistry C 2014 118 (20), 10616-10624.

67. S.Y. Dong, et al., Q. Sheng and X.G. Zhang, J. Mater. Chem. A, 2015,3, 21277-21283

68. N. Goubard-Bretesché, O. Crosnier, F. Favier, T. Brousse, Electrochim. Acta. 206 (2016) 458–463.

Supporting information

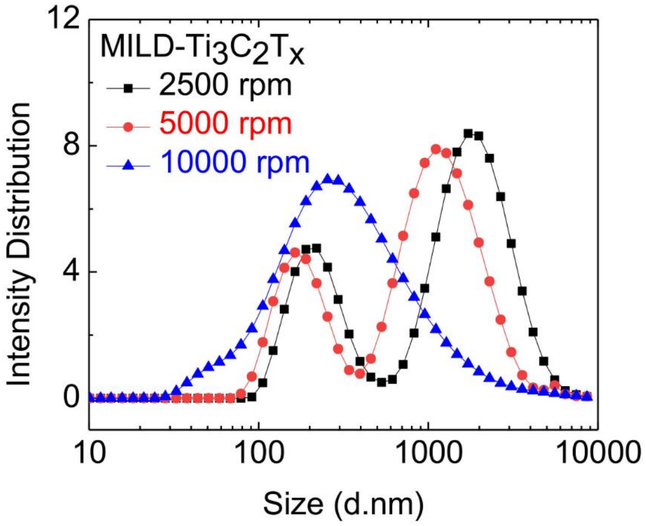

Figure S1 Ti3C2Tx flake size distribution after centrifuge step at 3 different rotating rates. from 3500 rpm to 5000 rpm, MXene colloidal solutions contain flakes with average size centered at 0.2 µm and 2 µm.[1]

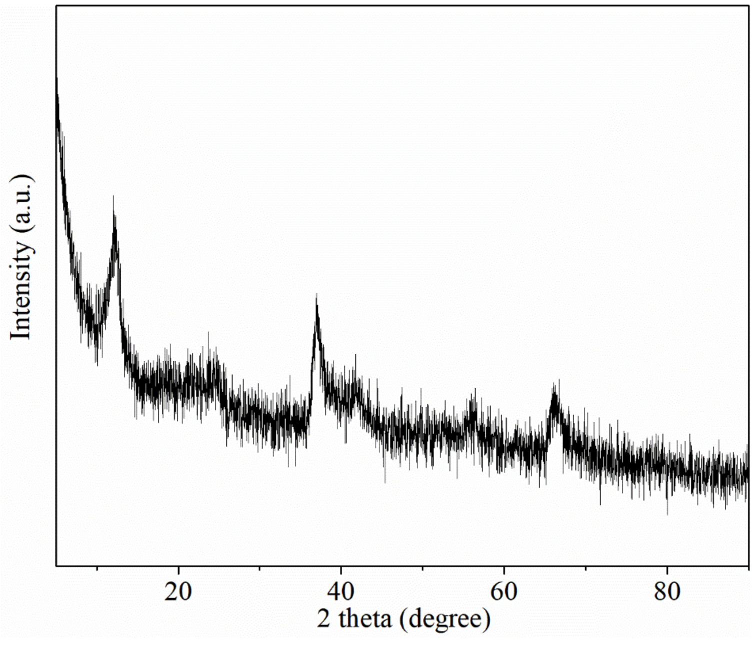

Figure S2 XRD pattern of prepared δ-MnO_2.

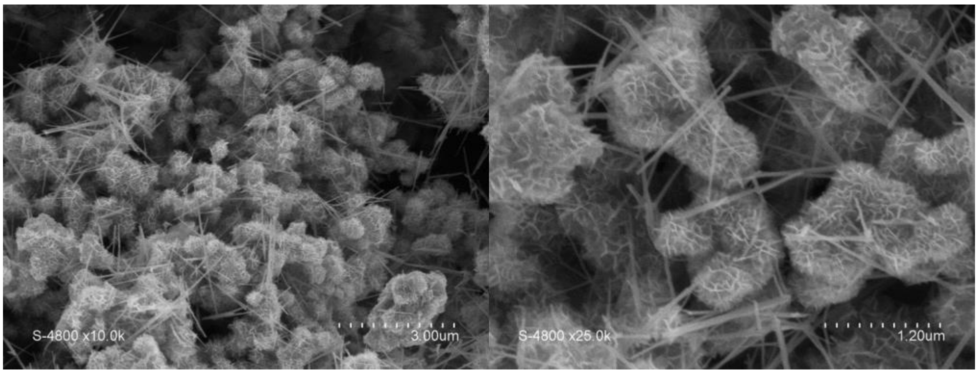

Figure S3 SEM images of prepared MnO_2.

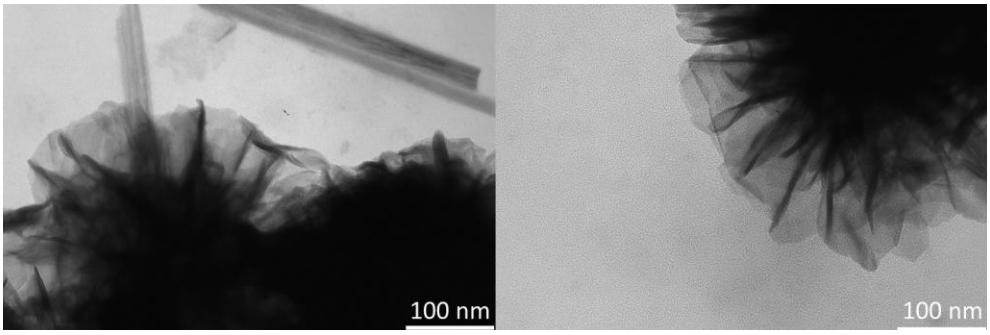

Figure S4 TEM images of prepared MnO2.

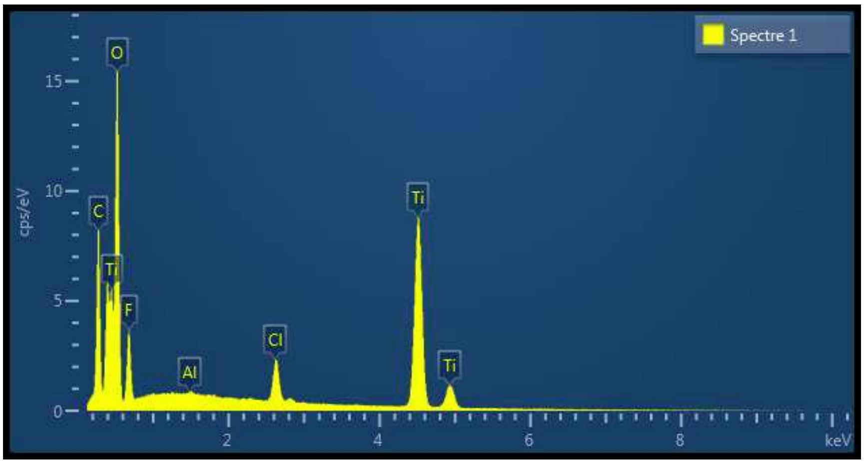

Figure S5 SEM Energy-dispersive X-ray spectroscopy (EDX) of Pure MXene.

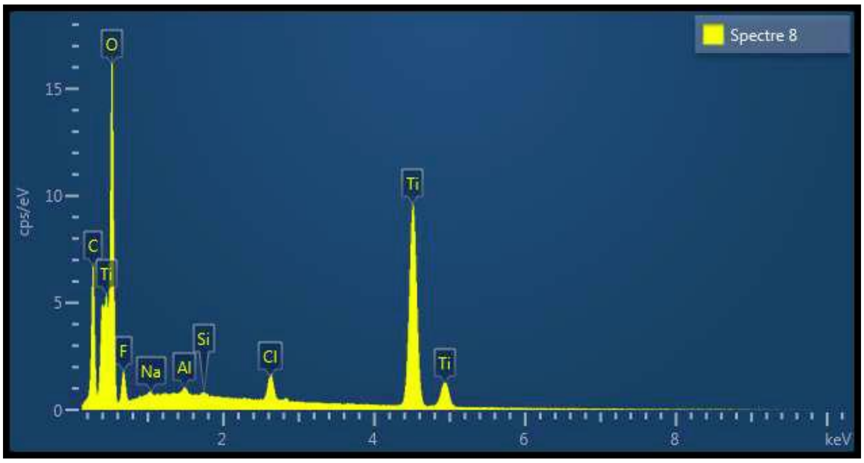

Figure S6 SEM Energy-dispersive X-ray spectroscopy (EDX) of MXene foam.

Table S1 EDX analysis of prepared MXene and MXene foam

Sample (mass %)	C	O	F	Al	Cl	Ti
Pure MXene	9.51	29.05	6.52	0.09	2.93	51.91
MXene foam	7.73	34.82	2.12	0.18	1.25	53.75

Sample (atomic %)	C	O	F	Al	Cl	Ti
Pure MXene	19.22	44.07	8.33	0.08	2.01	26.3
MXene foam	15.70	52.94	2.77	0.16	0.87	27.42

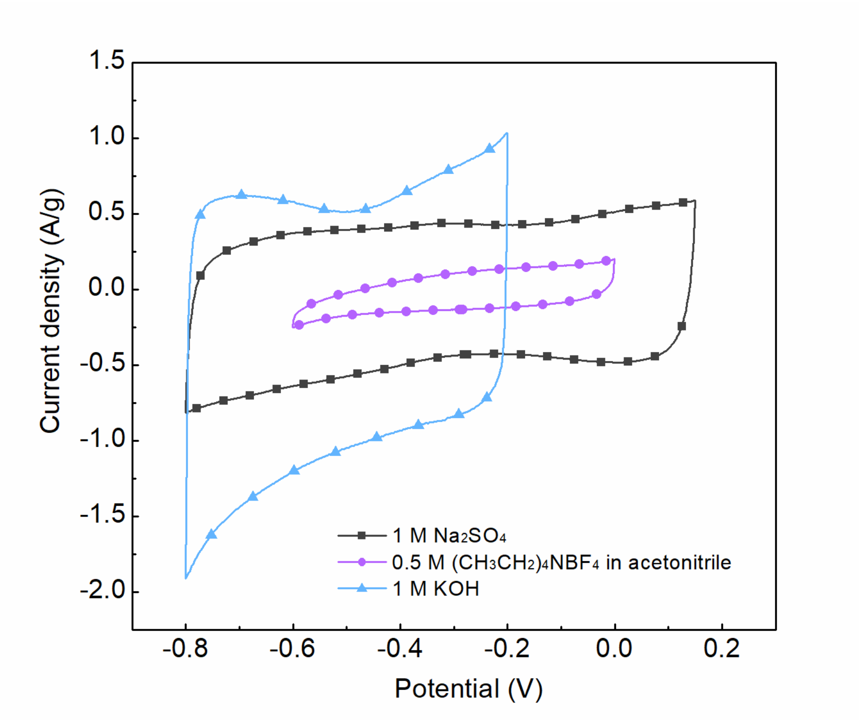

Figure S7 The CV curves of MXene foam at 5 mV/s in various electrolytes.

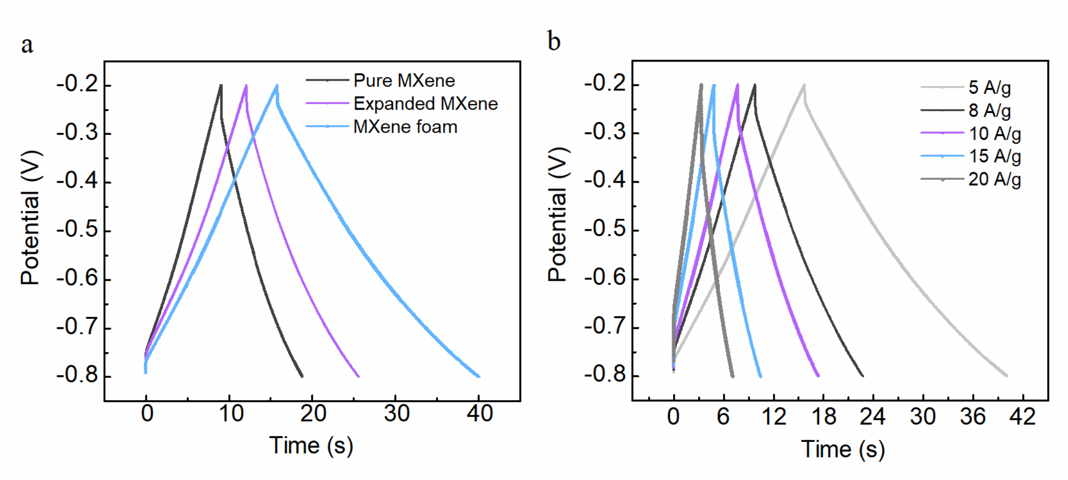

Figure S8 (a) Comparison of the galvanostatic charge-discharge (GCD) measurements of the prepared materials at 5 A.g^{-1} current density. (b) GCD measurements of MXene foam electrode at various current densities.

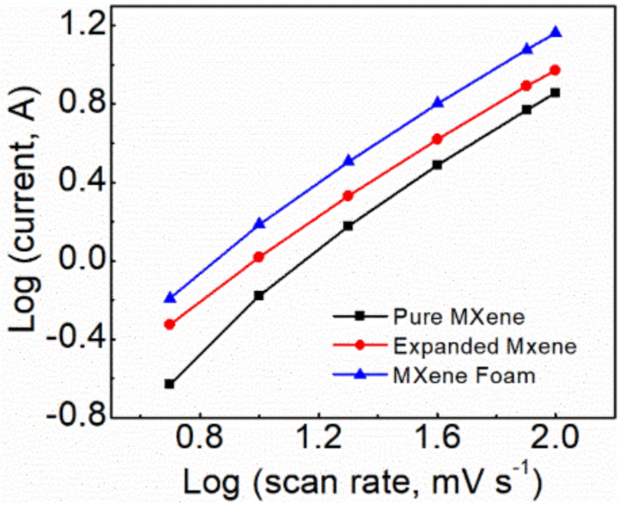

Figure S9 log/log current versus scan rate curves from CV data at various scan rates in 1 M Na2SO4. b slopes were calculated at 1.06 (pure MXene), 0.99 (Expanded MXene) and 1.02 (MXene foam) and correspond to $i = av^b$ relationship

A detailed analysis of the charge storage kinetics can be discussed from the cyclic voltammetry data of prepared electrode materials at various scan rates. It starts from the current-scan rate relationship in equation (1):

$$i = av^b(1)$$

where i is the current response following the applied voltage, a and b are adjustable parameters. When the b value is 0.5, it indicates a diffusion-controlled process. On the other hand, a b value at 1.0 implies a capacitive-controlled process. By plotting log v as the function with log i, b value corresponds to the curve slope. In the present case, b values were found close to 1.0, suggesting the kinetics of the three prepared electrodes to correspond to fast surface-controlled processes.

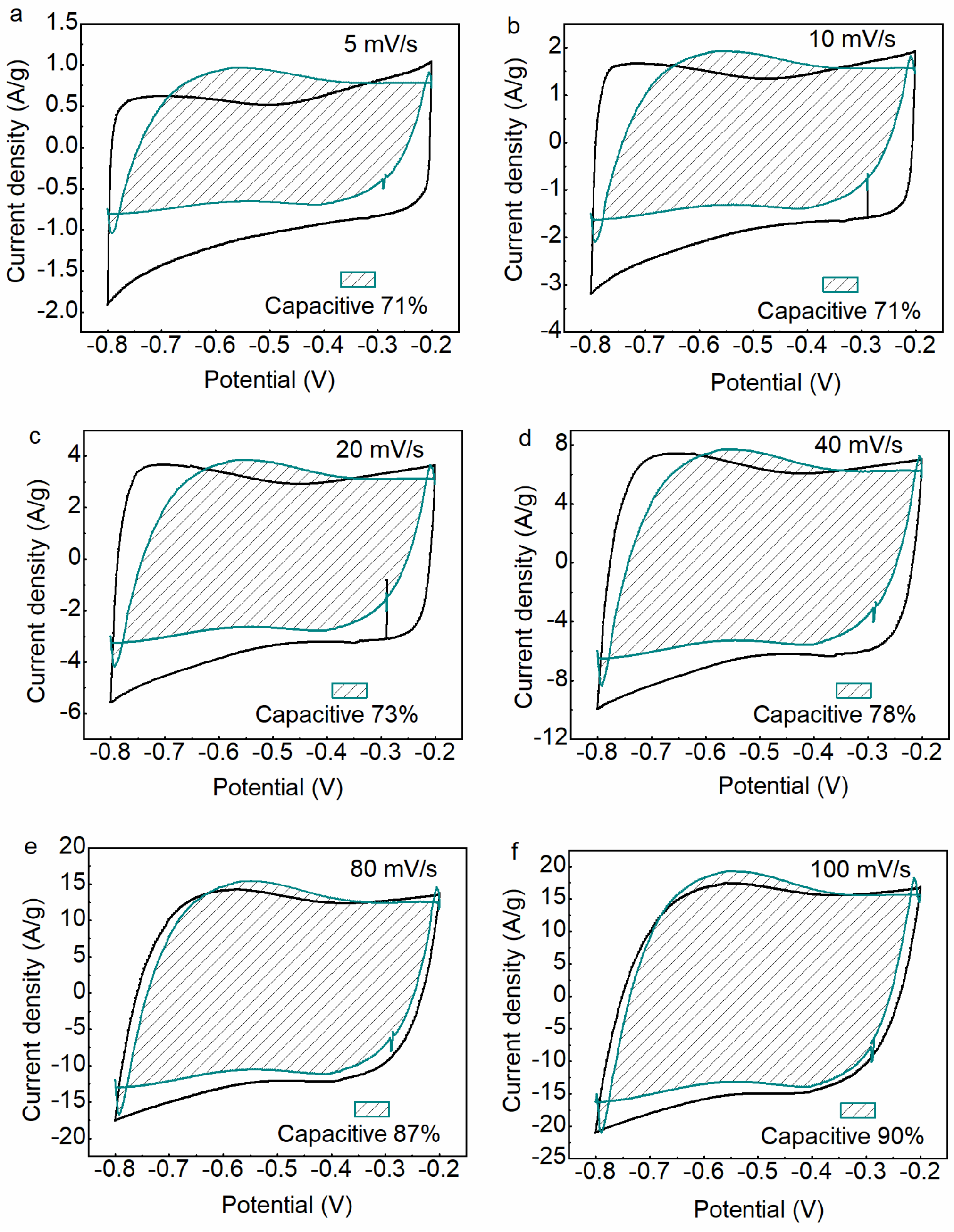

Figure S10 Capacitive and diffusion limited currents in MXene foam electrode operated at various scan rates in Na2SO4 1M.

Generally speaking, the total current can be divided into a capacitive contribution ($k_1 v$) and a diffusion contribution ($k_2 v^{1/2}$). The detailed relationship is shown in equation 2:

$$i(V) = k_1 v + k_2 v^{1/2} (2)$$

where i is the current at a fixed voltage, v is the scan rate, and k_1 and k_2 are the suitable values at the given voltage. To calculate the values of k_1 and k_2, equation 2 can be transformed into equation 3:

$$i\,(V)/v^{1/2} = k_1 v^{1/2} + k_2 (3)$$

By plotting the the $i\,(V)/v^{1/2}$ vs $v^{1/2}$, the k_1 and k_2 values can be achieved from the slopes and intercepts. Here, the separation of capacitive and diffusion currents for MXene foam are shown in Figure S10 and the capacitive contribution ratio at various scan rates in Figure S11. Relative contributions have been calculated by using an home-made fitting routine written in Python language. It is interestingly noticed that the capacitive ratio is 71% at low scan rate of 5 mV s^{-1}, implying a significant capacitive/surface contribution to the overall measured capacitance. Furthermore, the capacitive contribution improves with the increases of scan rates, signifying that, at high rates, MXene foam stores charges mostly through surface reactions in the EDL.

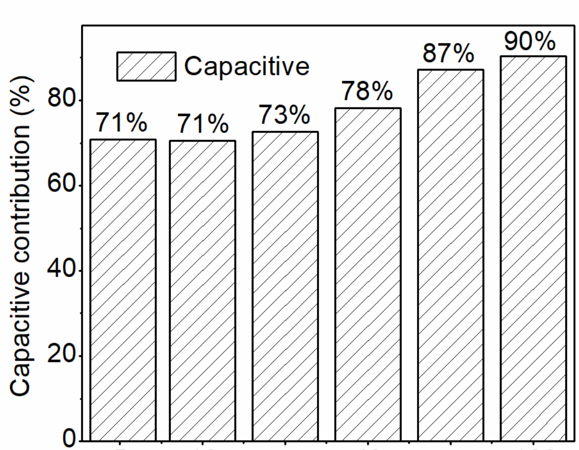

Figure S11 Capacitive contribution ratio of MXene foam at various scan rates.

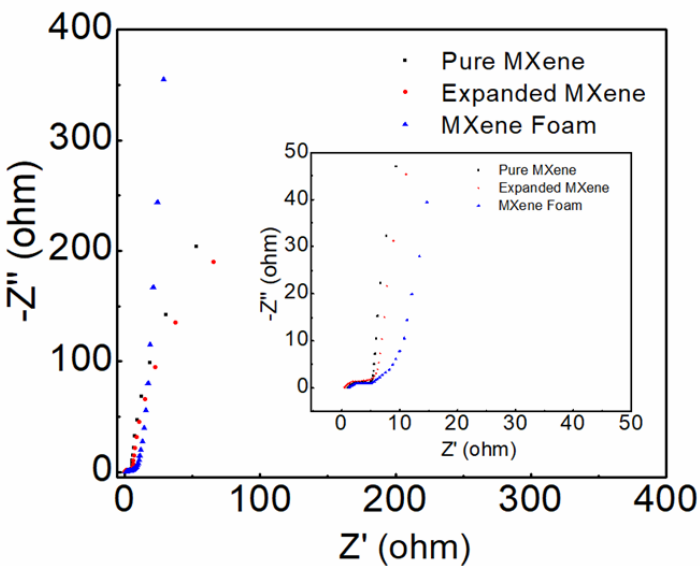

Figure S12 Myquist plots for electrodes based on prepared MXene materials. Measurements done at OCV in 1 M KOH after 10 min of stabilization with a 5 mV bias from 1000 Khz to 10 mHz.

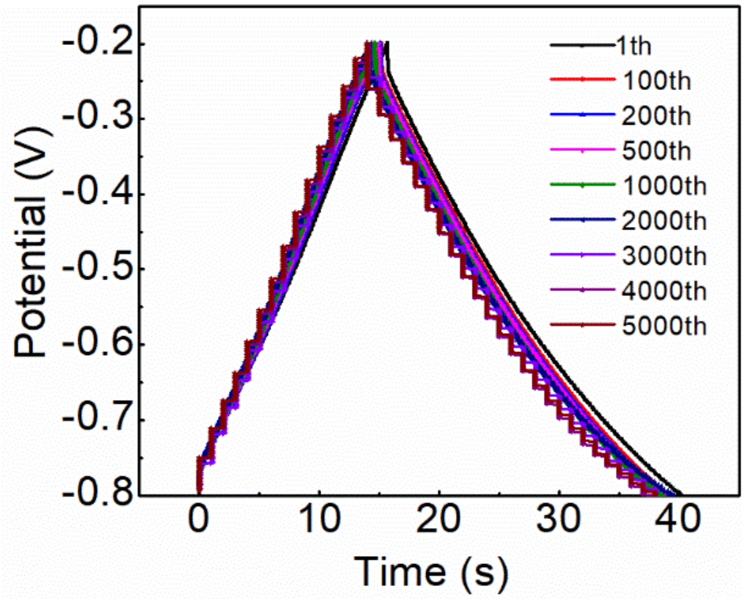

Figure S13 Galvanostatic charge-discharge cycling curves of MXene foam during 5000 cycles.

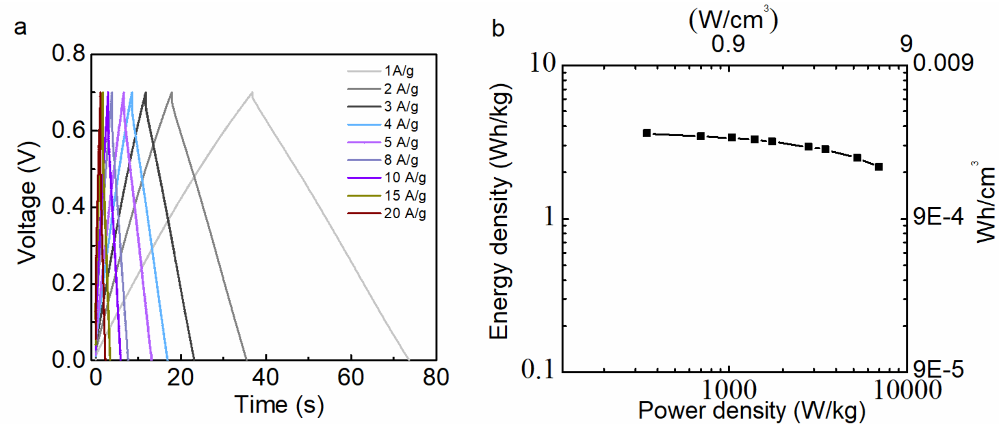

Figure S14 The electrochemical characteristic of symmetric MF//MF device. (a) Galvanostatic charge-discharge measurement at various current densities. (b) Ragone plot (energy density vs power density).

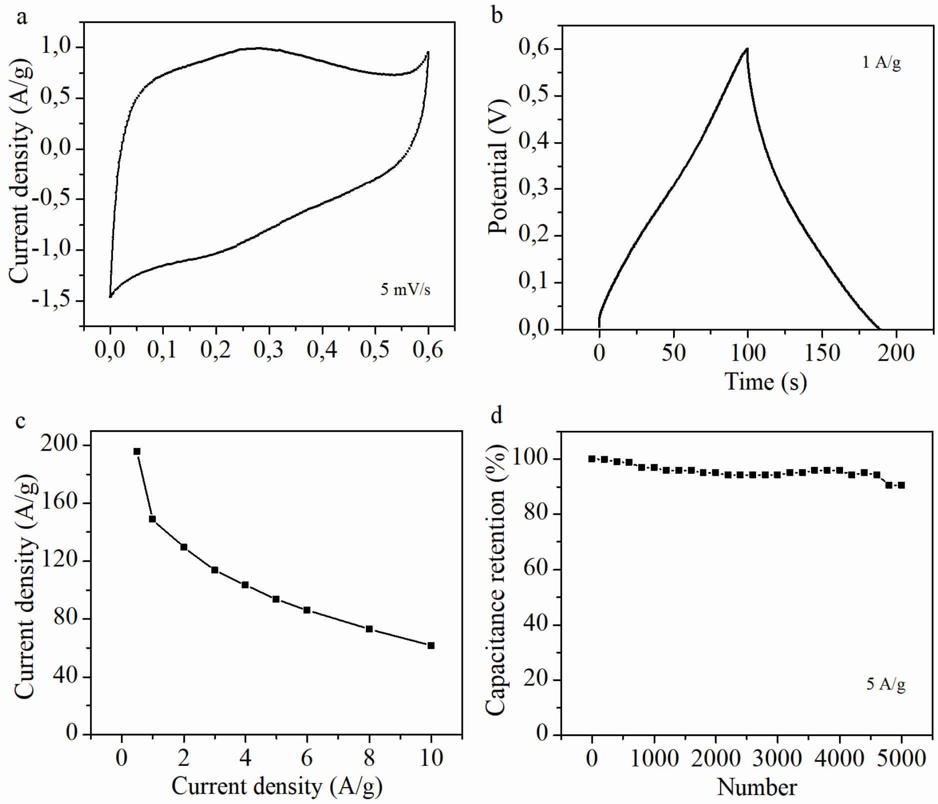

Figure S15 Electrochemical characterization of prepared δ-MnO_2 in 1M KOH. (a) CV curves. (b) GCD at 1A g^{-1}. (c) Capacitance at various current density. (d) Cycling property in 5000 cycles.

References

1. Chem. Mater. 2017, 29, 7633−7644

Chapter 6 Freestanding graphene-based electrode materials for supercapacitors

6.1 Introduction

In recent years, graphene[1-4] and the derived composites[5-9] have been the prevailing 2D materials in electrochemical energy storage because of their outstanding properties, including high conductivity, theoretical specific surface area, excellent mechanical flexibility and great chemical/thermal stability.[10-13] Intense researches focus on the construction of freestanding films/hydrogels with self-assembled frameworks for supercapacitors.[14-22] For example, Liu et al.[23] applied a dipping and drying procedure to build the freestanding graphene-based paper, in which the cellulose fiber (CF) can provide the conductive substrate for electron transport and the reduced graphene oxide (rGO) can boost the diffusion of electrolytes ions in the porous papers. Furthermore, the polyaniline (PANI) was polymerized on the surface of rGO/CF. The resulting composite with high flexible and foldable properties displayed enhanced performance with a greater capacitance and rate capability. Wu and co-workers[24] described a controlled method involving two consecutive self-assembly processes to produce a three-dimensional porous polyaniline/reduced graphene oxide composite which exhibited a suitable microframework to improve the electrolyte diffusion and the electron transport, therefore showing a great capacitance (808 F g^{-1} at 53.33 A g^{-1}) and excellent rate capability. Ma et al.[25] prepared hydroxyl-group graphene hydrogels by using various concentrations of phosphoric acid, exhibiting a pseudocapacitive behavior in cyclic voltammetry measurements. Thanks to the interconnected porous structure, the hydrogel displayed a high gravimetric capacitance (260 F g^{-1}), fair rate property (78% at 100 A g^{-1}) and excellent cycling durability (100% retention over 10k cycles). In the present study, we first prepared a freestanding and flexible graphene film by a simple reduction approach. It was then used as a positive electrode in the three-electrode supercapacitor, revealing a good capacitance performance and nice rate capability. The prepared reduced graphene hydrogels were fabricated and modified by a hydrothermal method in presence of urea. The porous graphene hydrogel exhibited a greater capacitance thanks to a greater permeability. Alternatively, a reduced graphene film was produced by evaporation followed by thermal reduction. Depending on the disparate thermal conditions, the film presented some structural changes which have been verified by characteristic diffraction peaks displacement. When treated at 400 ^{o}C, the resulting electrode showed an enhanced capacitance and improved cycling longevity. The above preparation method was further applied to synthesize MXene-graphene composites. With increasing MXene ratio, the capacitance performance showed a downward tendency.

6.2 The preparation of graphene film by the reduction method using hydrazine

12.5 mg GO (purchased from XFNAN0 company) was dispersed in 50 ml H_2O by ultrasonication for 2 hours. Then, the pH was adjusted to 10.5 by using ammonia, and 50 μl hydrazine was added as the reductant. The mixture was heated at 95 ^{o}C for 1h without stirring. Finally, the flexible graphene film was obtained by a simple filtration procedure.

Figure 6.1 The optical photographs of graphene films.

6.2.1 Electrochemical characterization

The electrochemical performances were measured in a three electrode system in 1 M KOH electrolytes, and the results are depicted in Figure 6.2. Regarding

CV curves, rectangular shapes are kept even at greater scan rate (Figure 6.2(a)). The capacitance was calculated from galvasnotic charge-discharge data at various current densities (Figure 6.2(b)), and the results are displayed in Figure 6.2 (c). At 0.5 A g-1 current density, the capacitance is 127 F g^{-1}. With73 F g^{-1} at 20 A g^{-1}, the capacitance is still able to keep 58 % of original value.

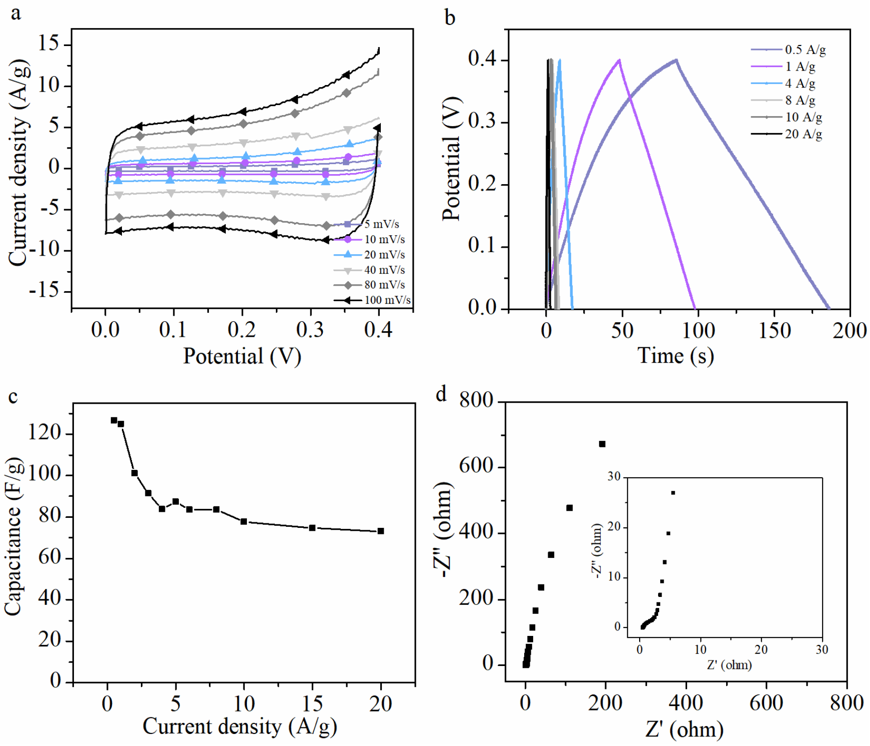

Figure 6.2 Electrochemical characteristics of graphene film. (a) CV curves at various scan rates. (b) Galvanostatic charge-discharge measurements at various current densities. (c) Capacitance performance. (d) Nyquist plot.

`6.3 The preparation of graphene hydrogels by a self-assembled hydrothermal method

30 mg GO was dispersed in 15 ml water under continuous ultrasonication treatment for 2 hours. Then, the brown solution with (H-1) or without (H-2), 900 mg of urea was transferred in a 20 ml stainless lined autoclave. The equipment was heated at 180 °C for 12 h in an oven. After washing with pure water, the targeted hydrogel was obtained.

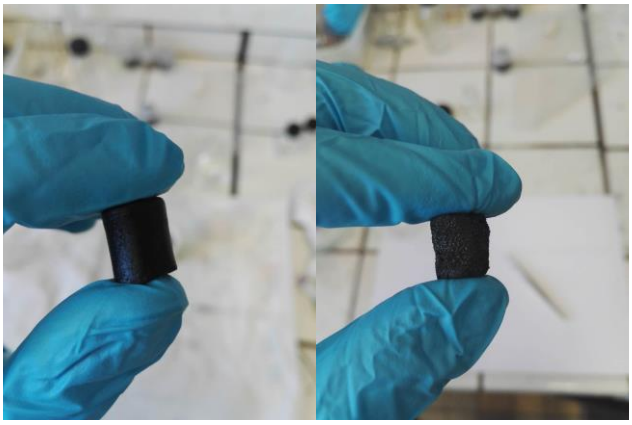

Figure 6.3 The photographs of graphene hydrogels without (left) or with (right) urea.

6.3.1 Electrochemical characterization

During the preparation process, it is found that the hydrogel without urea treatment (H-1) was settled at the bottom of glass bottle. In contrast, the hydrogel with urea treatment (H-2) was floating at the surface. This suggests that the introduction of urea triggers a more advanced reduction of GO and generates more pores in the graphene hydrogel.

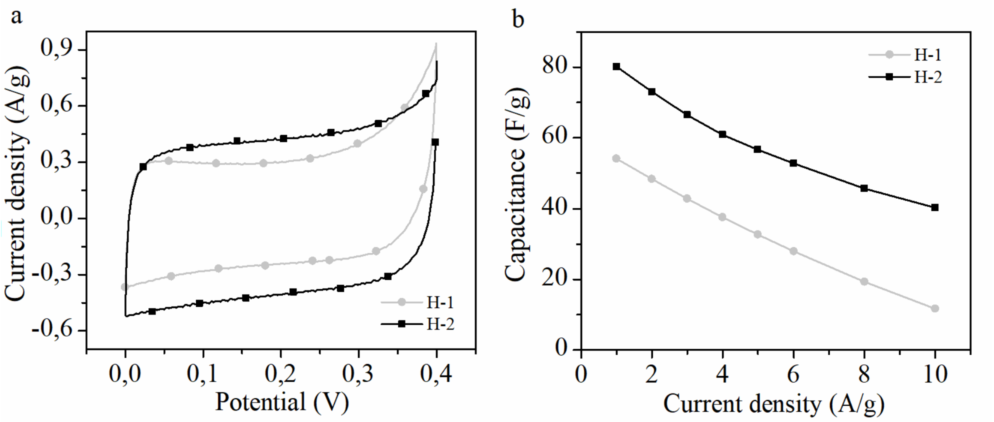

Figure 6.4 Electrochemical performance of graphene hydrogels. (a) CV curves at 5 mV/s. (b) Capacitance values at various current densities.

The electrochemical result was shown in Figure 6.4. Because of the enhanced reduction degree and porous structure characteristics, the CV of the H-2 electrode shows a larger integral area consistent with greater capacitance of H-2 either at lower or greater current densities (Figure 6.4 b).

6.4 The preparations of graphene film and MXene-graphene composites by evaporation and subsequent thermal-treated reduction approach

30 mg GO was dispersed in 15 ml H_2O by ultra-sonication for 2 hours. The resulting brown dispersion solution was transferred in a preheated glass dish vessel. The temperature was controlled and stable at 60 ^oC. After water evaporation and drying, a brown-black film was easilly peeled off and stored.

The film was cut in three slices of same size, which then were treated at Various temperatures of 200, 300 and 400 ^oC (termed as RGO-200, RGO-300 and RGO-400) for 1.5 h in a preheated oven under air atmosphere. Finally, the graphene film was successfully generated by this thermal reduction method.

The MXene-graphene composite was prepared by using a similar synthetic method, in which the quantity of MXene was varied (5 mg, 10 mg and 20 mg; termed as MXene-rGO-1, MXene-rGO-2 and MXene-rGO-3) keeping rGO at 30 mg to assemble freestanding complex films.

6.4.1 Results and discussion

The XRD result was shown in Figure 6.5. The black line is indexed as GO, which is confirmed by the characteristic peak at 12^o (2θ). It is clear that the increase of the reduction temperature induces a of peak shift as a proof of the reduction of graphene oxide by this thermal reduction approach. When raising the reduction temperature, a series of functional groups were actually removed from the GO layer. As these groups and water are gradually vanishing, the interlayer space corresponding shrunk, resulting in the observed shift of peak toward lower 2θ angles. RGO-400 shows a clear and intensive peak at around 23 degrees.

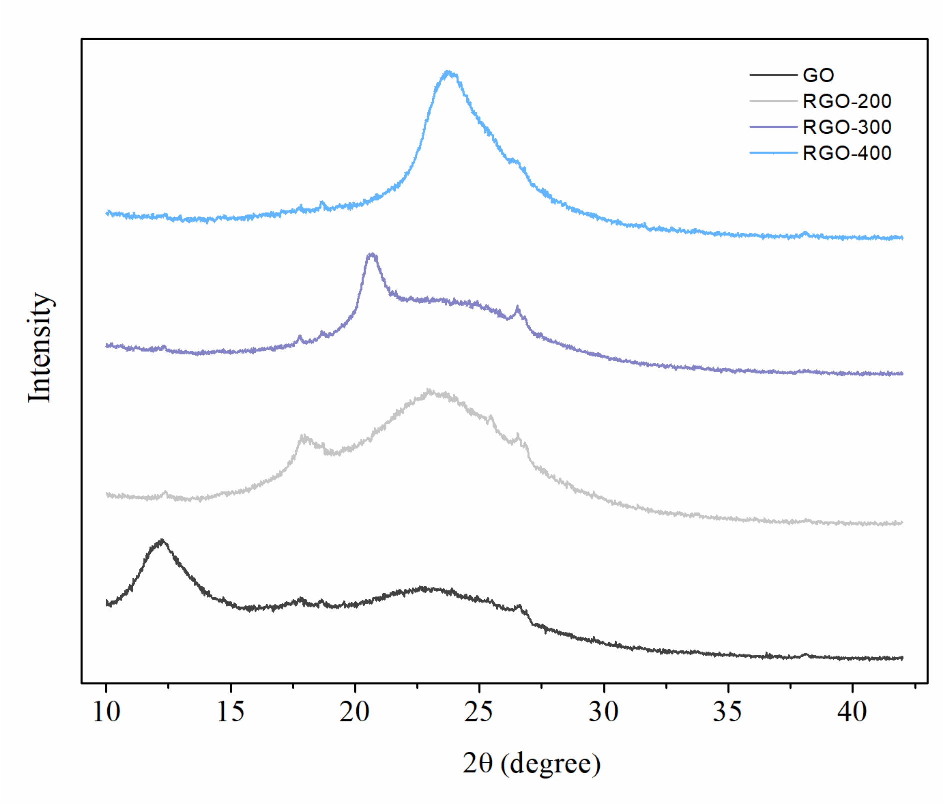

Figure 6.5 The XRD patterns of GO, RGO-200, RGO-300 and RGO-400.

The SEM images of RGO-400 are shown in Figure 6.6. It is found that the surface morphology of RGO-400 is flat and smooth. And the side view shows the stacked layered structure of prepared RGO.

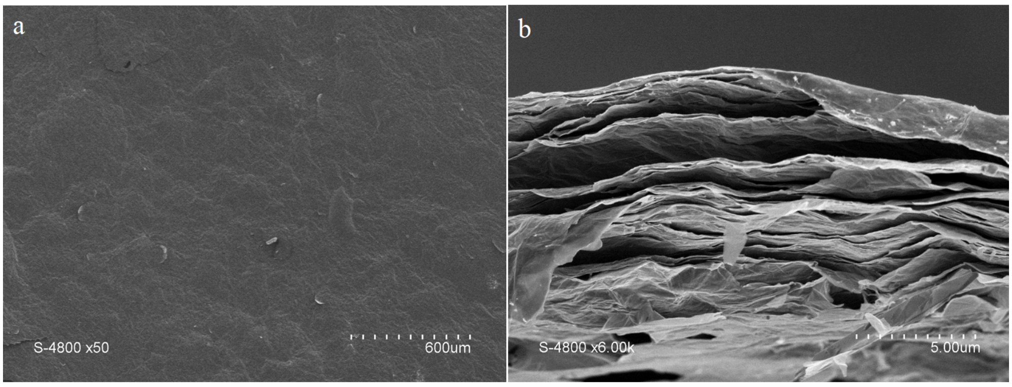

Figure 6.6 The SEM images of RGO-400 surface and section parts.

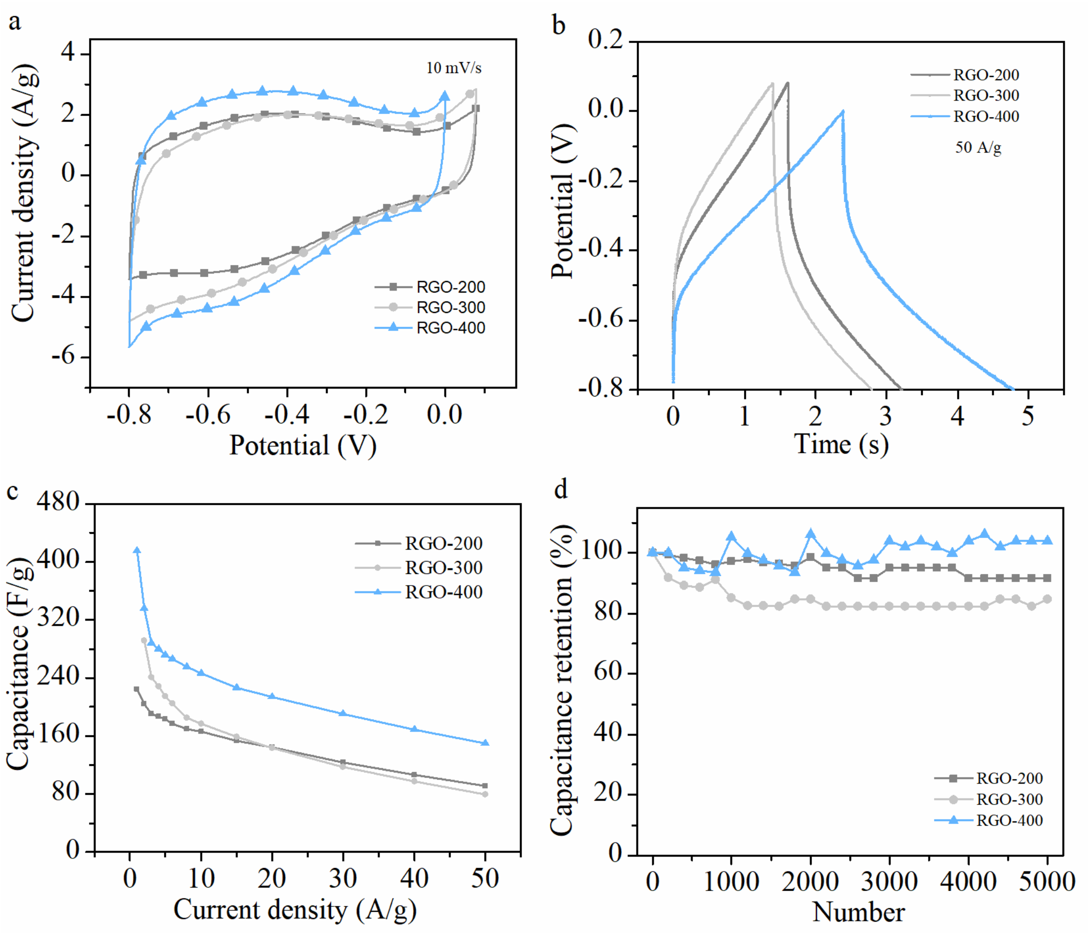

Figure 6.7 The electrochemical capabilities of RGO-200, RGO-300 and RGO-400. (a) CV curves comparisons at 10 mV s^{-1}. (b) Galvanostatic charge discharge measurement comparisons at the same current density of 50 A g^{-1}. (c) Capacitance values at various current densities. (d) Cycle stability comparisons over 5000 cycles at 5 A g^{-1}.

The electrochemical characterization was performed in three electrode system in 1 M KOH electrolyte. Figure 6.7 (a) shows the comparison of the CV curves for RGO-200, RGO-300 and RGO-400 at a scan rate of 10 mV s^{-1}. The RGO-400 integral area is slightly greater than those of the other samples. As such the capacitance of the former is the greatest in the series. This result is depicted in the capacitance plot in Figure 6.7 (c), which is calculated from galvanostatic charge-discharge measurements. As such, the capacitance of RGO-400 is 415 F g^{-1} at 1 A g^{-1}, while that of RGO-200 is 224 F g^{-1} at 1 A g^{-1} and that of RGO-300 is 291 F g^{-1} at 2 A g^{-1}. The cycle stability was tested over 5000 cycles at 5

A g^{-1} current density. After thousands of cycles, RGO-200 electrode capacitance decreases down to 92% of the initial capacitance, and RGO-300 retains 85% of its original capacitance. Interestingly, RGO-400 shows a steady capacitance retention, suggesting a very reliable and promising stability of corresponding supercapacitors. In addition, the electrochemical performance of MXene-RGO composites was measured and summarized in Figure 6.8 a and c, MXene-rGO-1 and MXene-rGO-2 display the close capacitance, 288 and 258 F g^{-1} at 1A g^{-1}, while MXene-rGO-3 has a lowest capacitance of 163 F g^{-1}. However, all are lower than that of pure reduced graphene (415 F g^{-1}), implying that the addition of MXene in the composite leads to a decrease in the capacitance. In Figure 8b, at 100 mV s-1, The quasi-rectangular shape MXene-rGO-1 is slightly distorted and a broad redox peak become apparent with scan rate increase, implying a microcosmic change of charge storage, which is needed to be explored in the future. On the other side, despite of similar capacitance at low scan rate or current density, MXene-rGO-1 still can have 119 F g^{-1} capacitance at 20 A g^{-1}, which is 41% of initial value, suggesting a fair rate capability. However, MXene-rGO-2 and MXene-rGO-3 display 79 F g^{-1} and 59 F g^{-1} at 20 A g^{-1}, meaning they could hold 31% and 36% of rate performances. It delivers that the quantity of MXene additives is a crucial factor for capacitive performance.

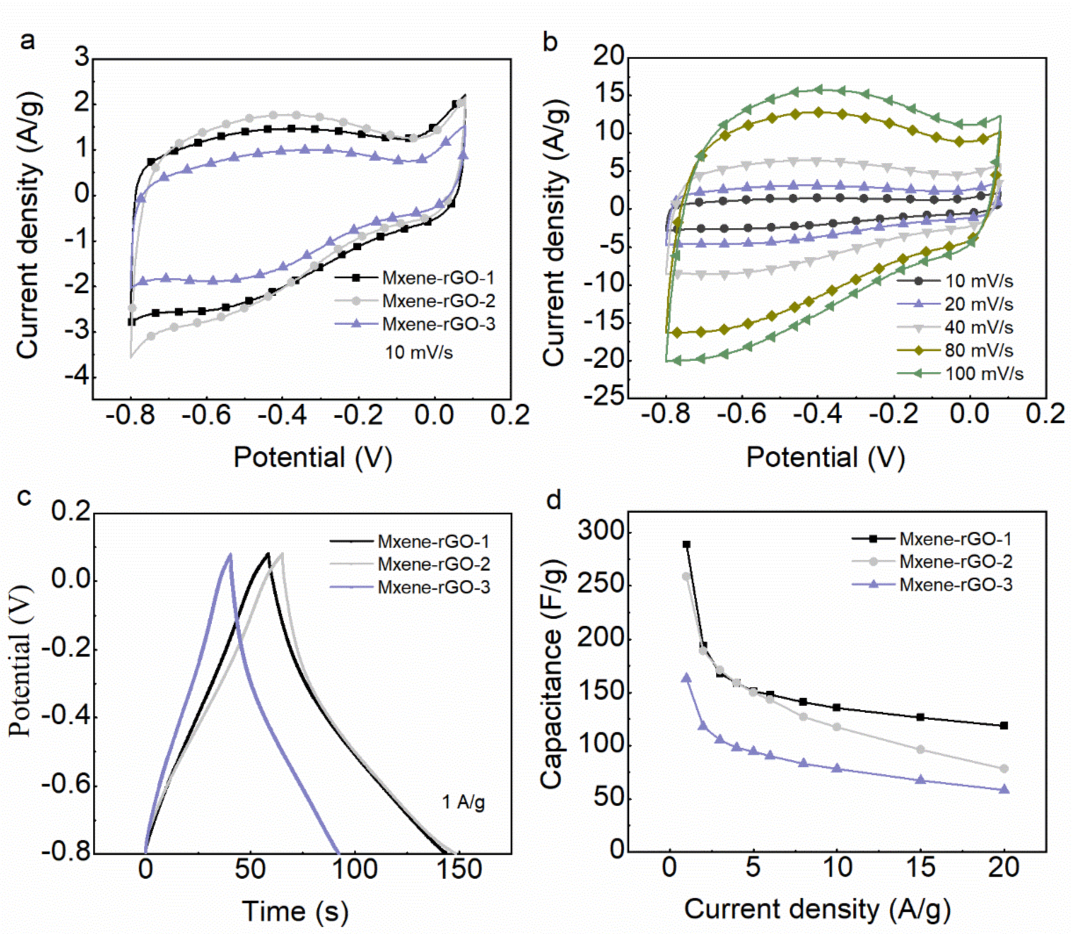

Figure 6.8 The electrochemical performance of MXene-rGO based- electrode materials. (a) CV curves comparisons at 10 mV s^{-1} in MXene-rGO materials. (b) CV curves of MXene-rGO-1 at various scan rates. (c) Galvanostatic charge-discharge measurements at 1 A g^{-1}. (d) Specific capacitances at various current densities.

6.5 Conclusion

In this chapter, a freestanding and flexible graphene film was first prepared via an easy thermal reduction method to discard the oxygen-containing functional groups at GO surface. As a positive electrode, the resulting rGO film displayed 127 F g^{-1} at 0.5 A g^{-1} and 73 F g^{-1} at 20 A g^{-1}, capacitances for a 58% rate retention. Alternatively, a freestanding reduced-graphene hydrogel from graphene oxide was self-assembled by the hydrothermal approach under undergoing high temperature and pressure procedures. In addition, urea was introduced to fabricate a porous architectural hydrogel. When used as the positive electrode, it showed a greater capacitance. Then, reduced graphene oxide was also prepared by a-thermal-reduction under air to eliminate the surface oxygen-containing functional groups. Depending on the reaction temperature, we found that the reduced graphene oxide film from a thermal treatment at 400 ^{o}C disclosed the greatest capacitance in the series, which is 415 F g^{-1} at 1 A g^{-1}. And the cycling stability was measured at 5 A g^{-1}, showing a quite steady capacitance retention during 5k charge-discharge cycles. Based on the above research result, the air-thermal-reduction method was applied to structure the MXene-graphene composites, which was investigated by increasing the ratio of MXenes. It is found that the quantity is a vital factor for capacitive performance. MXene-rGO-1 displays a fair rate capability that is 41%, while MXene-rGO-2 and MXene-rGO-3 hold 31% and 36% rate retention, respectively.

6.6 Reference

1. Dikin, D., Stankovich, S., Zimney, E. et al. Preparation and characterization of graphene oxide paper. Nature 448, 457–460 (2007) doi:10.1038/nature06016.

2. Li, D., Müller, M., Gilje, S. et al. Processable aqueous dispersions of graphene nanosheets. Nature Nanotech 3, 101–105 (2008) doi:10.1038/nnano.2007.451.

3. Meryl D. Stoller, Sungjin Park, Yanwu Zhu, Jinho An, and Rodney S. Ruoff, Graphene-Based Ultracapacitors, Nano Letters 2008 8 (10), 3498-3502, doi: 10.1021/nl802558y.

4. Meyer, J., Geim, A., Katsnelson, M. et al. The structure of suspended graphene sheets. Nature 446, 60–63 (2007) doi:10.1038/nature05545.

5. Stankovich, S., Dikin, D., Dommett, G. et al. Graphene-based composite materials. Nature 442, 282–286 (2006) doi:10.1038/nature04969.

6. Zhu, Y., Murali, S., Cai, W., Li, X., Suk, J.W., Potts, J.R. and Ruoff, R.S. (2010), Graphene and Graphene Oxide: Synthesis, Properties, and Applications. Adv. Mater., 22: 3906-3924. doi:10.1002/adma.201001068.

7. Yu, D., Prikhodchenko, P., Mason, C. et al. High-capacity antimony sulphide nanoparticle-decorated graphene composite as anode for sodium-ion batteries. Nat Commun 4, 2922 (2013) doi :10.1038/ncomms3922.

8. Sun, Z., Zhang, J., Yin, L. et al. Conductive porous vanadium nitride/graphene composite as chemical anchor of polysulfides for lithium-sulfur batteries. Nat Commun 8, 14627 (2017) doi :10.1038/ncomms14627.

9. David, L., Bhandavat, R., Barrera, U. et al. Silicon oxycarbide glass-graphene composite paper electrode for long-cycle lithium-ion batteries. Nat Commun 7, 10998 (2016) doi:10.1038/ncomms10998.

10. J. Cao, C. Chen, K. Chen, Q. Lu, Q. Wang, P. Zhou, D. Liu, L. Song, Z. Niu and J. Chen, High-strength graphene composite films by molecular level couplings for flexible supercapacitors with high volumetric capacitance. J. Mater. Chem. A, 2017, 5, 15008 doi: 10.1039/C7TA04920J.

11. Q. Zheng, A. Kvit, Z. Cai, Z. Ma and S. Gong, A freestanding cellulose nanofibril–reduced graphene oxide–molybdenum oxynitride aerogel film electrode for all-solid-state supercapacitors with ultrahigh energy density. J. Mater. Chem. A, 2017, 5, 12528 doi: 10.1039/C7TA03093B.

12. Qin, K., Liu, E., Li, J., Kang, J., Shi, C., He, C., He, F., Zhao, N. (2016). Free-Standing 3D Nanoporous Duct-Like and Hierarchical Nanoporous Graphene Films for Micron-Level Flexible Solid-State Asymmetric Supercapacitors. Adv. Energy Mater., 6: 1600755. doi: 10.1002/aenm.201600755.

13. N. Li, X. Huang, H. Zhang, Z. Shi and C. Wang, Graphene-hollow-cubes with network-faces assembled a 3D micro-structured transparent and free-standing film for high performance supercapacitors. J. Mater. Chem. A, 2017, 5, 16803 doi: 10.1039/C7TA03935B.

14. El-Kady, M., Shao, Y. & Kaner, R. Graphene for batteries, supercapacitors and beyond. Nat Rev Mater 1, 16033 (2016) doi:10.1038/natrevmats.2016.33.

15. Yang, X., Zhu, J., Qiu, L. and Li, D. (2011), Bioinspired Effective Prevention of Restacking in Multilayered Graphene Films: Towards the Next Generation of High-Performance Supercapacitors. Adv. Mater., 23: 2833-2838. doi:10.1002/adma.201100261.

16. Shao, Y., El-Kady, M.F., Lin, C.-W., Zhu, G., Marsh, K.L., Hwang, J.Y., Zhang, Q., Li, Y., Wang, H. and Kaner, R.B. (2016), 3D Freeze-Casting of Cellular Graphene Films for Ultrahigh-Power-Density Supercapacitors. Adv. Mater., 28: 6719-6726. doi:10.1002/adma.201506157.

17. Weng, Z., Su, Y., Wang, D.-W., Li, F., Du, J. and Cheng, H.-M. (2011), Graphene–Cellulose Paper Flexible Supercapacitors. Adv. Energy Mater., 1: 917-922. doi:10.1002/aenm.201100312.

18. Li, M., Tang, Z., Leng, M. and Xue, J. (2014), Flexible Solid-State Supercapacitor Based on Graphene-based Hybrid Films. Adv. Funct. Mater., 24: 7495-7502. doi:10.1002/adfm.201402442.

19. Xu, Y., Lin, Z., Huang, X., Wang, Y., Huang, Y. and Duan, X. (2013), Functionalized Graphene Hydrogel-Based High-Performance Supercapacitors. Adv. Mater., 25: 5779-5784. doi:10.1002/adma.201301928.

20. Bo, Z., Zhu, W., Ma, W., Wen, Z., Shuai, X., Chen, J., Yan, J., Wang, Z., Cen, K. and Feng, X. (2013), Vertically Oriented Graphene Bridging Active-Layer/Current-Collector Interface for Ultrahigh Rate Supercapacitors. Adv. Mater., 25: 5799-5806. doi:10.1002/adma.201301794.

21. Liu, L., Niu, Z., Zhang, L., Zhou, W., Chen, X. and Xie, S. (2014), Nanostructured Graphene Composite Papers for Highly Flexible and Foldable Supercapacitors. Adv. Mater., 26: 4855-4862. doi:10.1002/adma.201401513.

22. Maiti, U.N., Lim, J., Lee, K.E., Lee, W.J. and Kim, S.O. (2014), Three-Dimensional Shape Engineered, Interfacial Gelation of Reduced Graphene Oxide for High Rate, Large Capacity Supercapacitors. Adv. Mater., 26: 615-619. doi:10.1002/adma.201303503.

23. Liu, L., Niu, Z., Zhang, L., Zhou, W., Chen, X. and Xie, S. (2014), Nanostructured Graphene Composite Papers for Highly Flexible and Foldable Supercapacitors. Adv. Mater., 26: 4855-4862. doi:10.1002/adma.201401513.

24. J. Wu, Q. Zhang, J. Wang, X. Huang and H. Bai, A self-assembly route to porous polyaniline/reduced graphene oxide composite materials with molecular-level uniformity for high-performance supercapacitors. Energy Environ. Sci., 2018, 11, 1280 doi: 10.1039/C8EE00078F.

25. H. Ma, Q. Zhou, M. Wu, M. Zhang, B. Yao, T. Gao, H. Wang, C. Li, D. Sui, Y. Chen and G. Shi, Tailoring the oxygenated groups of graphene hydrogels for high-performance supercapacitors with large areal mass loadings. J. Mater. Chem. A, 2018, 6, 6587 doi: 10.1039/C7TA10843E.

Chapter 7 Freestanding 3D Mxene/AQ/Carbon Clothes for Supercapacitors

7.1 Abstract

Battery-like organic materials including electrochemically active quinone-based electrodes, have been introduced as electrode materials in supercapacitors because of their potentially performance economical, and sustainable merits. However, organic quinones are suffering a limited stability upon charge/discharge cycling originating from their intrinsic electrically insulating characteristics. Here, we report an anthraquinone/carbon cloth (AQ/CC) material, prepared by using simple heating procedure, in which anthraquinone was chemisorbed at the carbon cloth surface via non-covalent π–π interactions. The as-fabricated AQ/CC electrode presented a capacity of 35 mAh g^{-1} at 0.5 A g^{-1} in 1M sulfuric acid, greater than that of the pristine carbon cloth (24 mAh g^{-1}).Unfortunately , AQ/CC electrode suffered a low rate capability (9%) and rapid capacitive fading upon cycling (12% in 3000 cycles). To address these issues, a straightforward dipping procedure was applied to synthesize MXene/AQ/CC (M/AQ/CC), in which MXenes layer acts as a conductive layer facilitating electron transfersMoreover, cracks and openings in the MXene layer provide easy path for ions diffusion. Therefore, M/AQ/CC electrode displayed an attractive capacitance of 46 mAh g^{-1}(around 1 mAh cm^{-2} areal capacitance or 6 F L^{-1} volume) at 0.5 A g^{-1}, satisfactory rate performance and enhanced cyclability of 80% over 5k cycles. Our experimental work successfully shows a practical way to store more charges via redox reaction from organic quinones grafted at carbon surfaces and build up a protective shield to stabilize the Faradic behavior of quinones over charging-discharging process.

7.2 Introduction

Blue sky is being dyed by severe pollution arising from the intensive use of fossil fuels in human's daily life. Renewable approaches are urgently needed to meet the living consumptions and build a cleaner world.[1,2,3] In this regard, supercapacitors are part of these improved means, as energy-storage devices showing fast charging, great viability and lofty power density.[4,5] However, they are still suffering an unsatisfactory drawback, which is a degraded energy density in comparison with batteries.[6,7,8] To address this issue, one of the strategies is to incorporate redox-active compounds with capacitive materials, thereby promoting more efficient charges by fast Faradaic reactions to energy hosts.[9,10] For instance, quinones, having fully conjugated cyclic dione structure, are usually used as charge carriers thanks to theirs low cost and attractive redox-donating property.[11,12] However, the application of quinones is limited by theirs low conductivity, poor stability and rapid electrolytic dissolution.[13,14] To break through the wall, an effective way is to couple them with a conductive substrate, like two dimensional materials. [12,13,15,16,17] Thereinto, metallic 2D $Ti_3C_2T_x$[18], one of MXene species[19], is currently one of prevailing materials in supercapacitors.[20,21,22,23,24] The general formula is $M_{n+1}X_nT_x$, where M stands for early transition metal, X is carbon and/or nitrogen and T_x represents various surface terminations.[25,26] In MXenes, n+1 layers of M are associated with n layers of X in an $M_{n+1}X_n$ matrix.[27] Thanks to their metallic electrical conductivity, MXenes have been mainly used as a substrate to cooperate with other components to design enhanced materials.[28,29,30,31]

In this paper, we first covered anthraquinones onto a carbon cloth substrate (labelled AQ/CC) with non-covalent π–π interactions. The formed space-charge layer provides active redox sites for charge-discharge processes, thus delivering an improved specific capacitance in sulfuric acid -based electrolytes. However, the AQ/CC electrode exhibited a pretty low rate capability and a terrible cyclability. To address these issues, a protective and conductive MXene coating (M) was casted on the AQ/CC surface. This layer proved to not only stabilize anthraquinones but also to facilitate electron transfers. Although this MXene layer could have be detrimental to the diffusion of electrolytic species to the AQ redox sites, marked cracks offered an easy access. As a result, M/AQ/CC as an electrode represented a high capacitance, favorable rate performance and extended lifetime in acidic electrolytes.

7.3 Experimental details

The preparation of AQ/CC

First, the carbon cloth was washed and sonicated in acetone. Then the carbon cloth was immersed in 0.01M solutions of anthraquinones in the acetone (50 mL). The whole system was transferred in a laboratory reflux apparatus and heated up at 75 ^oC for 2 h. The AQ@CC sample was obtained after drying at 80 ^oC.

The preparation of MXene/AQ/CC

The dried AQ/CC was then immersed/dipped into as-prepared MXene flake suspensions for a few of minutes to ensure that the MXene unit can completely wet the CC framework. At last, the sample was dried at 80 ^oC in the oven. The immersion process was roughly repeated twice to obtain the uniform MXene@CC sample.

Material characterization

A JEOL JSM-6300F scanning electron microscope (SEM) was applied to image morphologies of samples. Sampling was done on freestanding disc on carbon tape. The Energy-dispersive X-ray spectroscopy (EDX) and mapping in SEM was applied to analyze elemental compositions and distributions.

Electrochemical characterization

Electrochemical measurements were carried out in Swagelok setup at ambient temperature by utilizing a VMP3 multi-channel Bio-Logic electrochemical workstation. In three electrode system, overcapacitive carbon was used as counter electrode, and Ag/AgCl was used as reference electrode. The working electrode was binder-free and freestanding carbon clothes-based disc. The electrochemical measurements were tested in 1 M sulfuric acid electrolyte.

The below related supporting information has been attached after reference.

7.4 Results and discussion

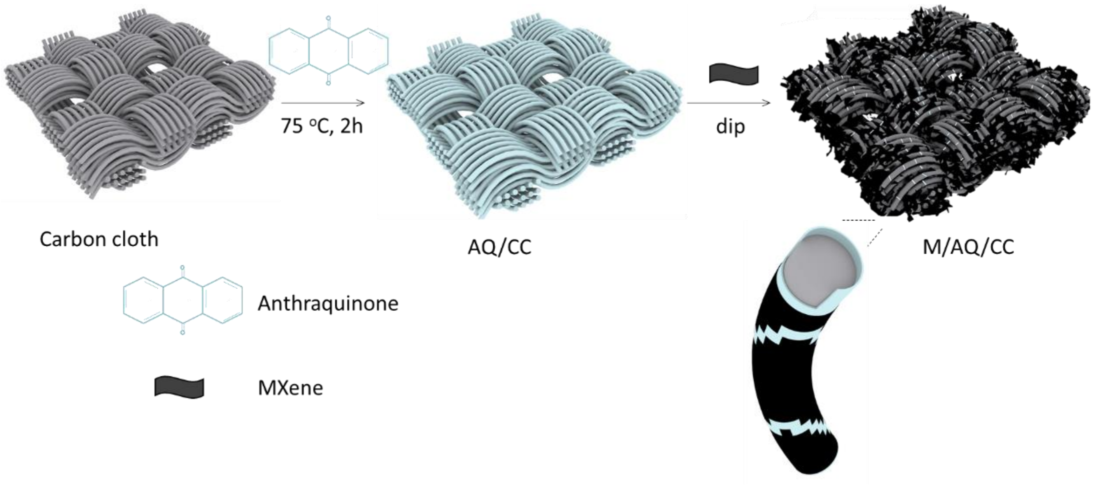

Figure 7.1 The schematic diagram of preparation process.

The sketchy synthetic process is summarily shown in Figure 7.1. The whole process proceeded by fairly easy procedures. First, the carbon cloth was pre-treated via a simple heating procedure and the whole framework was covered with anthraquinones to introduce sufficient Faradaic sites for storing more charges. Afterwards, a simple dipping procedure was used to deposit an MXene-protective layer on the resulting AQ/CC surfaces.

The morphology of AQ/CC surfaces was imaged by SEM measurement shown in Figure S3. Compared with general images of raw carbon clothes (Figure S1 a), AQ/CC displays a more ordered and non-stacked skeleton. The self-interlaced and loose framework is expected to provide many voids, suggesting it can expose more active sites with an easy access for the electrolytic species. On the other hand, after covering with organic reagents, the images of AQ/CC are blurred because of the intrinsic insulating property of anthraquinones. In the magnified Figure S3d, anthraquinone are uniformly coated on carbon clothes. The uniform coating of anthraquinone in AQ/CC can also be identified by SEM-EDX mapping measurements. As shown in Figure S4, oxygen elements (green), mostly from anthraquinones, are evenly distributed at the CC surface. In addition, it is observed that oxygen level increased from 7.9% in CC to 33.0 in AQ/CC based on the composition analysis of EDX/ This confirms this facile heating program to be a successful way to absorb anthraquinones at the CC surface. Afterwards, the subsequent and simple dipping procedure adopted to "wear" the protective conductive MXene layer led to the morphology structure of M/AQ/CC displayed in Figure 7.2. It shows the M/AQ/CC material to retain the interlaced and loose structures of pristine (AQ/)CC, in the meantime, a "glue-like" and uniform wrinkle of MXene layer is observed at the surface. Interestingly, there are many small cracks at the MXene layer surface. Besides, the uniform layer of MXene could also be detected by SEM-EDX mapping (Figure 7.3). It demonstrates the titanium element (blue) is uniformly distributed at the M/AQ/CC material surface. These results are also consistent with the elemental composition analysis in Table 7.1. The 41.7% (weight%) of titanium composition is measured, confirming the successful coating by MXene by the simple dipping method used during the present study.

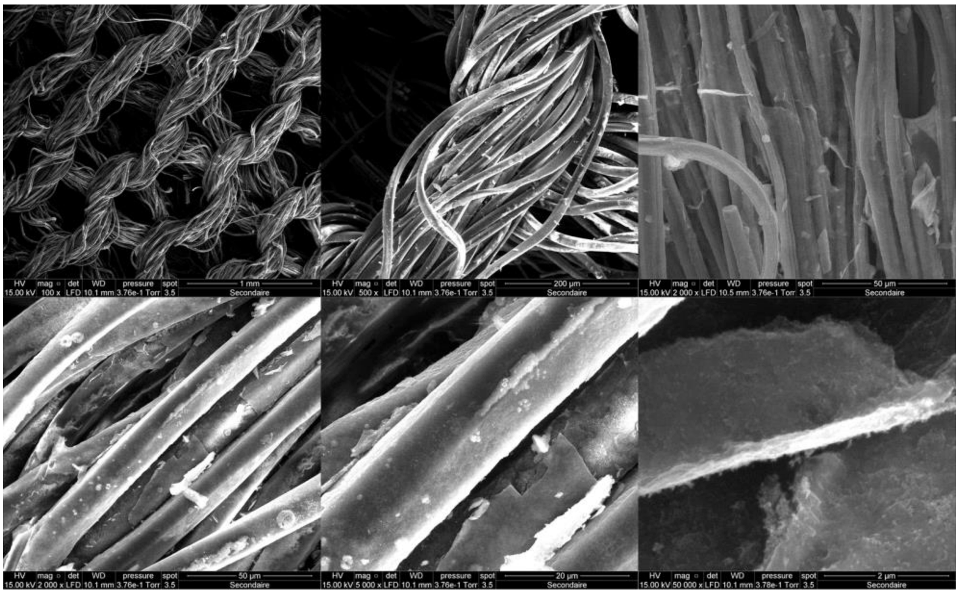

Figure 7.2 SEM images of M/AQ/CC.

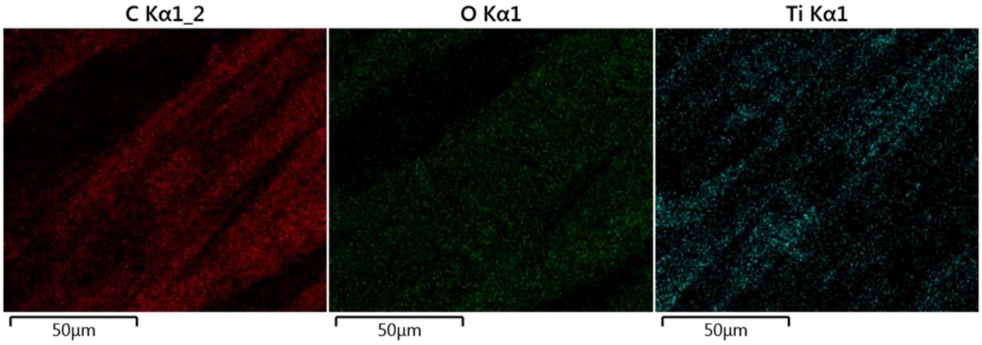

Figure 7.3 SEM-EDX mapping of elemental distribution in M/AQ/CC.

Table 7.1 Elemental composition analysis in M/AQ/CC.

Element	C	O	Na	Mg	Al	Cl	Ca	Ti	Zn
Atomic %	73.75	32.68	0.10	0.07	1.68	0.56	0.62	17.20	0.14
Weight %	66.83	36.33	0.16	0.08	2.30	1.01	1.32	41.67	0.50

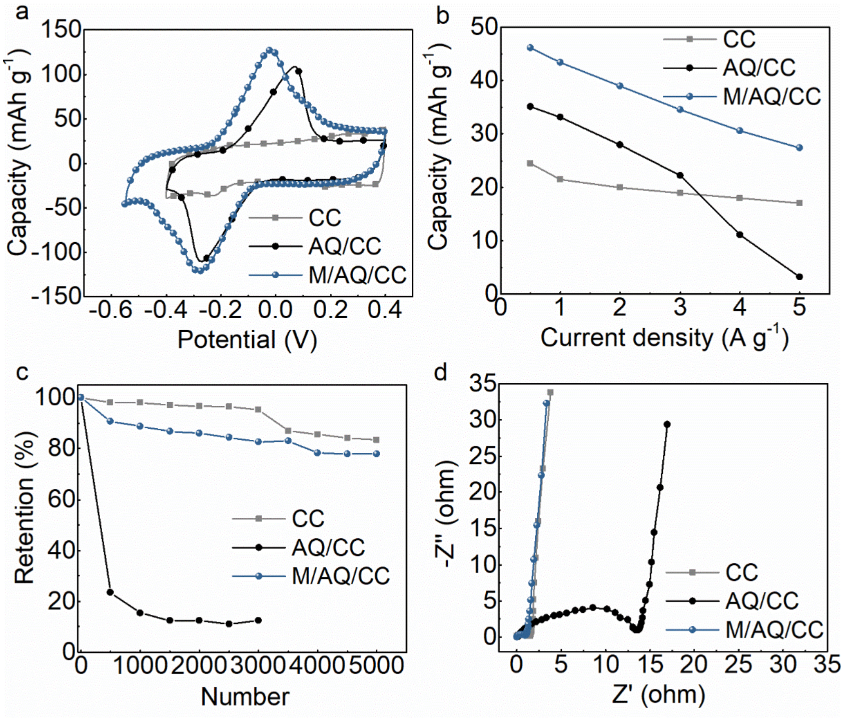

Figure 7.4 The electrochemical performance of prepared electrode material. (a) Cyclic voltammetry at 5 mV/s. (b) Specific capacitance at various current densities. (c) cycling stability. (d) Nyquist plot.

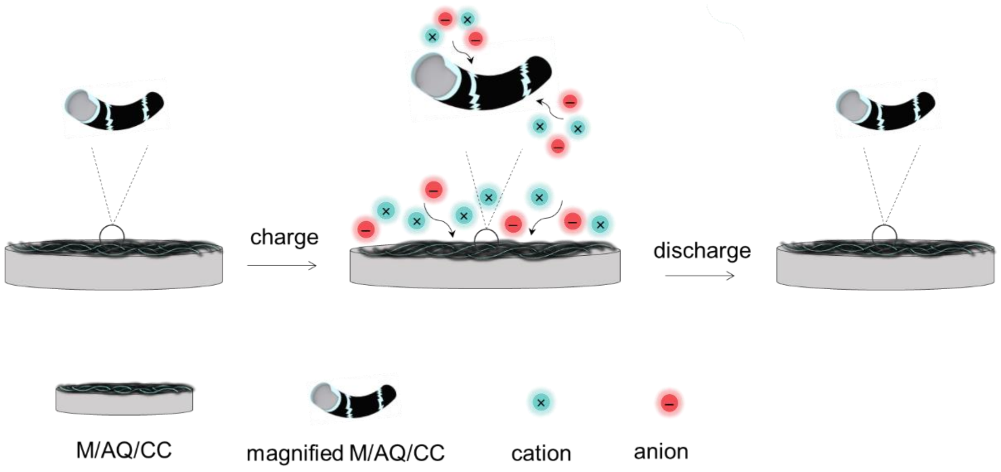

Figure 7.5 Schematic charging-discharging process of M/AQ/CC.

Electrochemical measurements were performed using a VMP3 multi-channel Bio-Logic electrochemical workstation at a constant temperature of 23 °C. Data were measured using a three-electrode Swagelok configuration. It includes a freestanding carbon cloth-based disc (7 mm diameter) as working electrode, an Ag/AgCl as reference electrode, and an overcapacitive YP-50 carbon as counter electrode. The weight loading of freestanding raw carbon cloth (CC), AQ/CC and M/AQ/CC discs were 15.6, 16.7 and 18.2 mg cm^{-2}, respectively. The disc thickness was 1.42 mm. Results are shown in Figure 7.4. In cyclic voltammetry plots (Figure 7.4a), two redox peaks are observed in AQ/CC material CV while that of raw cabon cloth is mostly capacitive, suggesting anthraquinones to be successfully absorbed. These efficiently contribute to the charge storage thanks to Faradaic redox contributions. The oxidation peak is measured at about 0.07 V vs Ag/AgCl. In addition, a slight distortion can be observed in AQ/CC electrode voltammetry. This thin warp is induced by unfavorable surface wetting and limited conductivity, arising from (mostly) hydrophobic and insulating anthraquinone.s The M/AQ/CC composite shows a similar redox signature as in AQ/CC CV, but the previous distortion is not observed. Furthermore, a broader voltage window was measured. We argue the contribution of the 2D MXene coating to originate from its remarkable conductivity and fair hydrophilic property. The wider potential window suggests a greater overpotential for hydrogen evolution because of the well-known limited catalytic properties of MXene towards HER. Afterwards, compared capacities were plotted as a function of the applied current density (Figure 7.4b). As expected, the AQ/CC electrode shows an improved capacity (35 mAh g^{-1} at 0.5 A g^{-1}) thanks to the redox contributions of anthraquinone. Unfortunately, it experiences a very strong fading as the current density was increased. For instance, the capacity at 5 A g^{-1} is 3 mAh g^{-1}, which is only 9% of the capacity at 0.5 A g^{-1}. This loss is caused by the limited conductivity of the bulk of electrodes at greater rates. Additionally, it is unsurprising that the AQ/CC -based electrode occurs a dramatic drop in cyclability (12% loss after 3000 cycles) during charge-discharge cycling at 3 A g^{-1} current density. It can be explained by a instability of AQ experiencing redox reactions during charge/discharge cycling. Oppositely, thanks to the MXene coating, M/AQ/CC exhibits a greater capacity at 46 mAh g^{-1} (1 mAh cm^{-2} of areal capacity) at 0.5 A g^{-1}, meanwhile maintaining 59% of it at 5 A g^{-1}. Moreover, this MXene-based material caould retain 80% of its initial capacity at 5 A g^{-1} over 5k charge-discharge cycles. We conclude that the MXene coating limit the AQ degradation upon cycling. The schematic of the charge-discharge process is depicted in Figure 7.5. It implies the diffusion of electrolytic ions through MXene narrow cracks towards the electrode bulk and more precisely AQ redox sites, even at greater rates. Meantime, the conductive MXene shell allows efficient electron transport, therefore contributing to the efficient redox reactions involved in charge storage. Thus, CVs and galvanostatic charge-discharge plots of M/AQ/CC electrode in Figure S5 can still retain similar shapes (except for a small drift) even after fast 5k charge-discharge cycles at a strong current density of 5 A g^{-1}. The resistance changes can be further investigated by Nyquist plots analysis (Figure 7.4d). In a Nyquist plot, R_e, the intercept with the real part at the high frequency region, stands for resistance of bulk electrolyte, electrode, and contact resistance between electrode and current collector. The R_c, diameter of semicircle, is the charge transfer resistance. Figure 7.4d shows the raw carbon cloth to simultaneously possess low resistances for electrolyte and charge transfer (from redox surface groups), suggesting good ion diffusion and charge transfer. However, when coated with anthraquinone, the AQ/CC electrode lied to a strong increase of the charge transfer resistance because of its organic (insulating) nature. In the presence of the MXene protective and conductive coating, there is a drastic decrease of resistances, either for electrode charge transfer and electrolyte resistances.

7.5 Conclusion

In summary, we successfully incorporated organic anthraquinones in carbon clothes by the noncovalent π–π interactions using a simple heating program. Thanks to involved Faradaic reactions from anthraquinones, the synthesized freestanding AQ/CC revealed 35mAh g^{-1} of capacitance at 0.5 A g^{-1} in 1M sulfuric acid. However, AQ/CC electrode occurred a rapid decay over long-term charge-discharge process, and the high current density dramatically slid its capacitance performance. To address this issue, conductive 2D MXene was used to cover the surface of the prepared 3D framework. It is disclosed that MXene can not only be a shield to shelter anthraquinones, but also improve the electronic conductivity. On the other hand, the observed cracks among MXenes provide a comfortable entrance for ions diffusion. As a result, the obtained M/AQ/CC delivered compelling capacitance of 46mAh g^{-1} (around 1mAh cm^{-2} of areal capacitance) at 0.5 A g^{-1}, favorable rate performance of 59% and pleasant cyclability of 80% over 5k cycles. Therefore, our work shows an encouraging way to construct conductive and freestanding 3D electrode material with plenty of Faradaic active sites for charge transfer.

Acknowledgements

Y. C. ZHU (NO. 201606240097) is supported by China Scholarship Council (CSC).

This chapter is submitting as an article.

7.6 Reference

1. Yoo, H. D.; Markevich, E.; Salitra, G.; Sharon, D.; Aurbach, D. On the Challenge of Developing Advanced Technologies for Electrochemical Energy Storage and Conversion. Mater. Today 2014, 17 (3), 110–121. https://doi.org/10.1016/j.mattod.2014.02.014.

2. Béguin, F.; Presser, V.; Balducci, A.; Frackowiak, E. Carbons and Electrolytes for Advanced Supercapacitors. Adv. Mater. 2014, 26 (14), 2219–2251. https://doi.org/10.1002/adma.201304137.

3. Lukatskaya, M. R.; Dunn, B.; Gogotsi, Y. Multidimensional Materials and Device Architectures for Future Hybrid Energy Storage. Nat. Commun. 2016, 7, 1–13. https://doi.org/10.1038/ncomms12647.

4. Gogotsi, Y.; Simon, P. Materials for Electrochemical Capacitors. Nat. Mater. 2008, 7, 845–854.

5. Wang, F.; Wu, X.; Yuan, X.; Liu, Z.; Zhang, Y.; Fu, L.; Zhu, Y.; Zhou, Q.; Wu, Y.; Huang, W. Latest Advances in Supercapacitors: From New Electrode Materials to Novel Device Designs. Chem. Soc. Rev. 2017, 46 (22), 6816–6854. https://doi.org/10.1039/C7CS00205J.

6. Wang, Y.; Song, Y.; Xia, Y. Electrochemical Capacitors: Mechanism, Materials, Systems, Characterization and Applications. Chem. Soc. Rev. 2016, 45 (21), 5925–5950. https://doi.org/10.1039/c5cs00580a.

7. Choi, N. S.; Chen, Z.; Freunberger, S. A.; Ji, X.; Sun, Y. K.; Amine, K.; Yushin, G.; Nazar, L. F.; Cho, J.; Bruce, P. G. Challenges Facing Lithium Batteries and Electrical Double-Layer Capacitors. Angew. Chemie - Int. Ed. 2012, 51 (40), 9994–10024. https://doi.org/10.1002/anie.201201429.

8. Xu, Y.; Duan, X.; Sun, H.; Peng, L.; Huang, Y.; Zhu, J.; Shakir, I.; Baumann, D. Hierarchical 3D Electrodes for Electrochemical Energy Storage. Nat. Rev. Mater. 2018, 4 (1), 45–60. https://doi.org/10.1038/s41578-018-0069-9.

9. Cho, S. Y.; Yoon, H. J.; Kim, N. R.; Yun, Y. S.; Jin, H. J. Sodium-Ion Supercapacitors Based on Nanoporous Pyroproteins Containing Redox-Active

Heteroatoms. J. Power Sources 2016, 329, 536–545. https://doi.org/10.1016/j.jpowsour.2016.08.114.

10. Kim, D.; Lee, G.; Kim, D.; Yun, J.; Lee, S. S.; Ha, J. S. High Performance Flexible Double-Sided Micro-Supercapacitors with an Organic Gel Electrolyte Containing a Redox-Active Additive. Nanoscale 2016, 8 (34), 15611–15620. https://doi.org/10.1039/c6nr04352f.

11. Wu, Q.; Sun, Y.; Bai, H.; Shi, G. High-Performance Supercapacitor Electrodes Based on Graphene Hydrogels Modified with 2-Aminoanthraquinone Moieties. Phys. Chem. Chem. Phys. 2011, 13 (23), 11193–11198. https://doi.org/10.1039/c1cp20980a.

12. Campbell, P. G.; Merrill, M. D.; Wood, B. C.; Montalvo, E.; Worsley, M. A.; Baumann, T. F.; Biener, J. Battery/Supercapacitor Hybrid via Non-Covalent Functionalization of Graphene Macro-Assemblies. J. Mater. Chem. A 2014, 2 (42), 17764–17770. https://doi.org/10.1039/c4ta03605k.

13. Shi, R.; Han, C.; Duan, H.; Xu, L.; Zhou, D.; Li, H.; Li, J.; Kang, F.; Li, B.; Wang, G. Redox-Active Organic Sodium Anthraquinone-2-Sulfonate (AQS) Anchored on Reduced Graphene Oxide for High-Performance Supercapacitors. Adv. Energy Mater. 2018, 8 (31), 1802088. https://doi.org/10.1002/aenm.201802088.

14. Peng, H.; Yu, Q.; Wang, S.; Kim, J.; Rowan, A. E.; Nanjundan, A. K.; Yamauchi, Y.; Yu, J. Molecular Design Strategies for Electrochemical Behavior of Aromatic Carbonyl Compounds in Organic and Aqueous Electrolytes. Adv. Sci. 2019, 6 (17), 1900431. https://doi.org/10.1002/advs.201900431.

15. Boota, M.; Chen, C.; Bécuwe, M.; Miao, L.; Gogotsi, Y. Pseudocapacitance and Excellent Cyclability of 2,5-Dimethoxy-1,4-Benzoquinone on Graphene. Energy Environ. Sci. 2016, 9 (8), 2586–2594. https://doi.org/10.1039/c6ee00793g.

16. Shabangoli, Y.; Rahmanifar, M. S.; El-Kady, M. F.; Noori, A.; Mousavi, M. F.; Kaner, R. B. Thionine Functionalized 3D Graphene Aerogel: Combining Simplicity and Efficiency in Fabrication of a Metal-Free Redox Supercapacitor.

Adv. Energy Mater. 2018, 8 (34), 1–12. https://doi.org/10.1002/aenm.201802869.

17. Luo, Z.; Liu, L.; Ning, J.; Lei, K.; Lu, Y.; Li, F.; Chen, J. A Microporous Covalent–Organic Framework with Abundant Accessible Carbonyl Groups for Lithium-Ion Batteries. Angew. Chemie - Int. Ed. 2018, 57 (30), 9443–9446. https://doi.org/10.1002/anie.201805540.

18. Shahzad, F.; Alhabeb, M.; Hatter, C. B.; Anasori, B.; Hong, S. M.; Koo, C. M.; Gogotsi, Y. Electromagnetic Interference Shielding with 2D Transition Metal Carbides (MXenes). Science (80-.). 2016, 353 (6304), 1137–1140. https://doi.org/10.1126/science.aag2421.

19. Naguib, M.; Mochalin, V. N.; Barsoum, M. W.; Gogotsi, Y. 25th Anniversary Article: MXenes: A New Family of Two-Dimensional Materials. Adv. Mater. 2014, 26 (7), 992–1005. https://doi.org/10.1002/adma.201304138.

20. Li, J.; Yuan, X.; Lin, C.; Yang, Y.; Xu, L.; Du, X.; Xie, J.; Lin, J.; Sun, J. Achieving High Pseudocapacitance of 2D Titanium Carbide (MXene) by Cation Intercalation and Surface Modification. Adv. Energy Mater. 2017, 7 (15). https://doi.org/10.1002/aenm.201602725.

21. Lukatskaya, M. R.; Kota, S.; Lin, Z.; Zhao, M. Q.; Shpigel, N.; Levi, M. D.; Halim, J.; Taberna, P. L.; Barsoum, M. W.; Simon, P.; Gogotsi, Y. Ultra-High-Rate Pseudocapacitive Energy Storage in Two-Dimensional Transition Metal Carbides. Nat. Energy 2017, 6 (July), 1–6. https://doi.org/10.1038/nenergy.2017.105.

22. Yoon, Y.; Lee, M.; Kim, S. K.; Bae, G.; Song, W.; Myung, S.; Lim, J.; Lee, S. S.; Zyung, T.; An, K. S. A Strategy for Synthesis of Carbon Nitride Induced Chemically Doped 2D MXene for High-Performance Supercapacitor Electrodes. Adv. Energy Mater. 2018, 8 (15), 1–11. https://doi.org/10.1002/aenm.201703173.

23. Zhang, C. J.; Anasori, B.; Seral-Ascaso, A.; Park, S. H.; McEvoy, N.; Shmeliov, A.; Duesberg, G. S.; Coleman, J. N.; Gogotsi, Y.; Nicolosi, V. Transparent, Flexible, and Conductive 2D Titanium Carbide (MXene) Films with

High Volumetric Capacitance. Adv. Mater. 2017, 29 (36), 1–9. https://doi.org/10.1002/adma.201702678.

24. Zhang, C. J.; Kremer, M. P.; Seral-Ascaso, A.; Park, S. H.; McEvoy, N.; Anasori, B.; Gogotsi, Y.; Nicolosi, V. Stamping of Flexible, Coplanar Micro-Supercapacitors Using MXene Inks. Adv. Funct. Mater. 2018, 28 (9), 1–10. https://doi.org/10.1002/adfm.201705506.

25. Seyedin, S.; Yanza, E. R. S.; Razal, J. M. Knittable Energy Storing Fiber with High Volumetric Performance Made from Predominantly MXene Nanosheets. J. Mater. Chem. A 2017, 5 (46), 24076–24082. https://doi.org/10.1039/c7ta08355f.

26. Chaudhari, N. K.; Jin, H.; Kim, B.; San Baek, D.; Joo, S. H.; Lee, K. MXene: An Emerging Two-Dimensional Material for Future Energy Conversion and Storage Applications. J. Mater. Chem. A 2017, 5 (47), 24564–24579. https://doi.org/10.1039/c7ta09094c.

27. Anasori, B.; Lukatskaya, M. R.; Gogotsi, Y. 2D Metal Carbides and Nitrides (MXenes) for Energy Storage. Nat. Rev. Mater. 2017, 2 (2). https://doi.org/10.1038/natrevmats.2016.98.

28. Zhao, M. Q.; Ren, C. E.; Ling, Z.; Lukatskaya, M. R.; Zhang, C.; Van Aken, K. L.; Barsoum, M. W.; Gogotsi, Y. Flexible MXene/Carbon Nanotube Composite Paper with High Volumetric Capacitance. Adv. Mater. 2015, 27 (2), 339–345. https://doi.org/10.1002/adma.201404140.

29. Zhu, M.; Huang, Y.; Deng, Q.; Zhou, J.; Pei, Z.; Xue, Q.; Huang, Y.; Wang, Z.; Li, H.; Huang, Q.; Zhi, C. Highly Flexible, Freestanding Supercapacitor Electrode with Enhanced Performance Obtained by Hybridizing Polypyrrole Chains with MXene. Adv. Energy Mater. 2016, 6 (21). https://doi.org/10.1002/aenm.201600969.

30. Zhao, D.; Zhao, R.; Dong, S.; Miao, X.; Zhang, Z.; Wang, C.; Yin, L. Alkali-Induced 3D Crinkled Porous Ti3C2 MXene Architectures Coupled with NiCoP Bimetallic Phosphide Nanoparticles as Anodes for High-Performance Sodium-Ion Batteries. Energy Environ. Sci. 2019, 12 (8), 2422–2432. https://doi.org/10.1039/c9ee00308h.

31. Zhang, J.; Seyedin, S.; Qin, S.; Wang, Z.; Moradi, S.; Yang, F.; Lynch, P. A.; Yang, W.; Liu, J.; Wang, X.; Razal, J. M. Highly Conductive Ti3C2Tx MXene Hybrid Fibers for Flexible and Elastic Fiber-Shaped Supercapacitors. Small 2019, 15 (8), 1–9. https://doi.org/10.1002/smll.201804732.

Supporting information

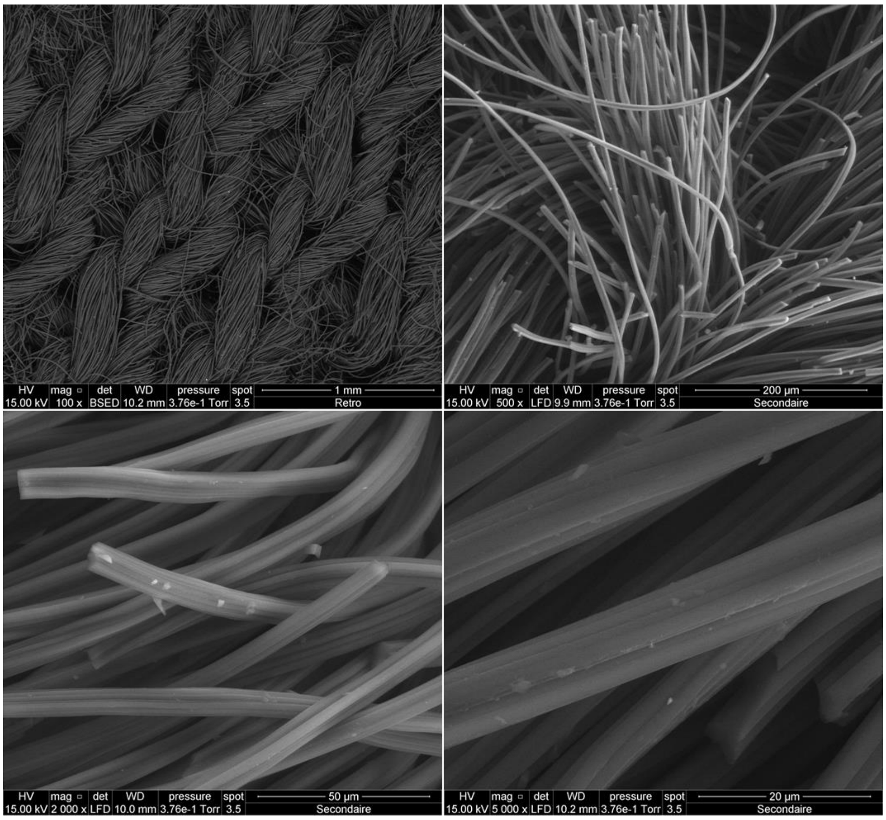

Figure S1 SEM images of pure carbon clothes.

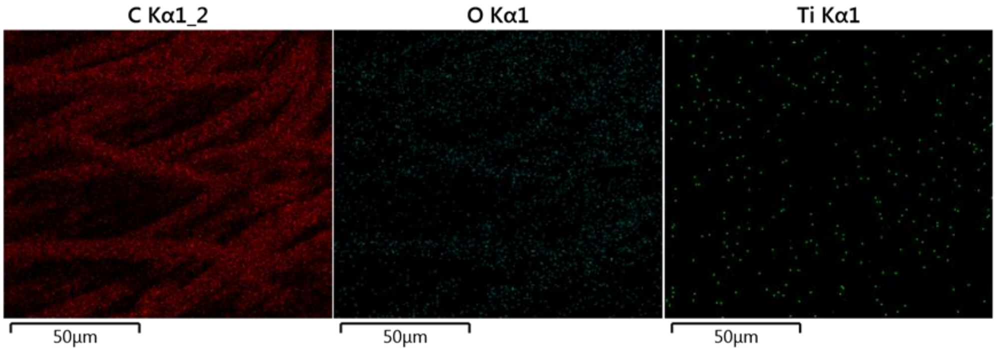

Figure S2 SEM-EDX mapping of elemental distribution in pure clothes.

Table S1 Elements composition analysis in pure clothes.

Element	C	O	Na	Mg	Al	Cl	Ca	Ti	Zn
Atomic %	91.26	6.25	0.12	0.00	0.49	0.47	0.07	0.00	0.16
Weight %	86.91	7.91	0.22	0.00	1.04	1.33	0.21	0.01	0.84

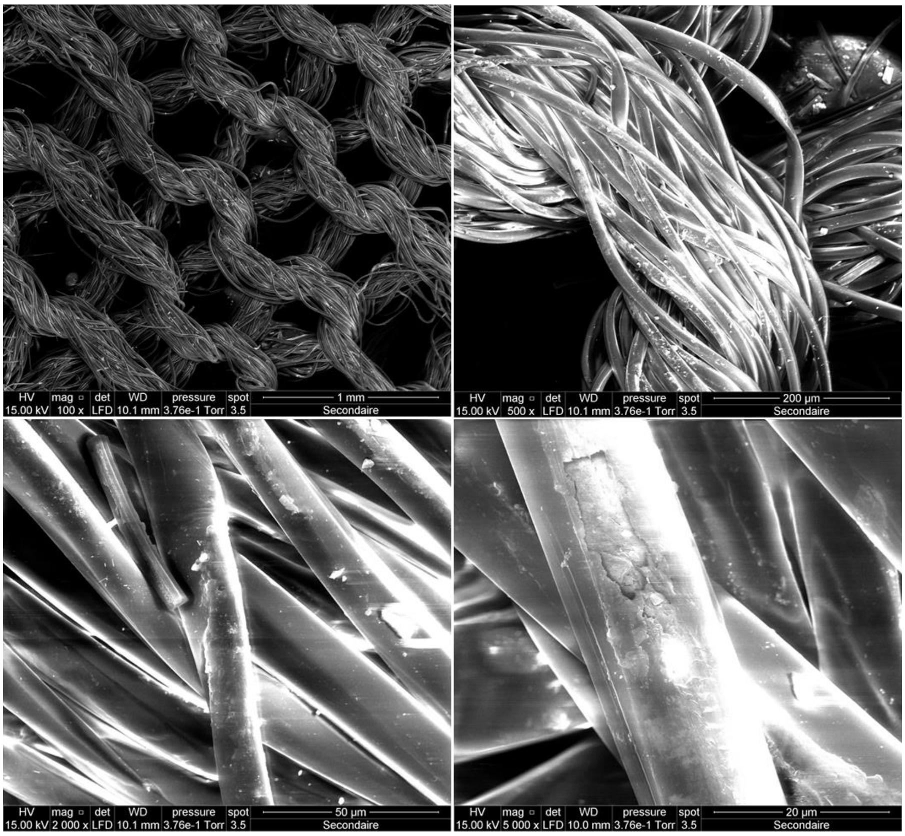

Figure S3 SEM images of AQ/CC.

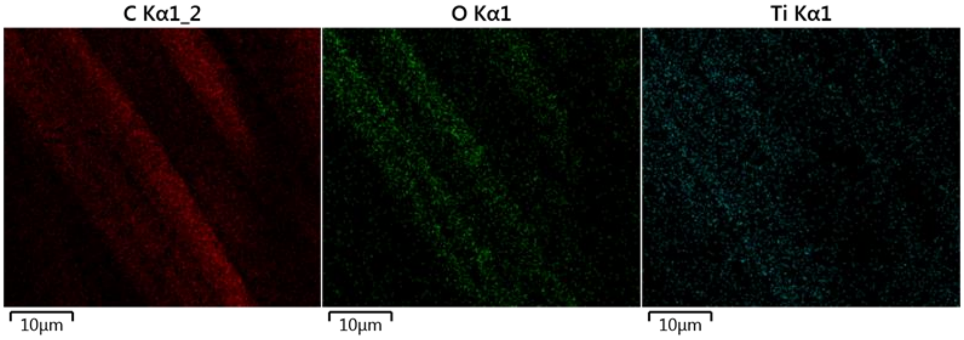

Figure S4 SEM-EDX mapping of elemental distribution in AQ/CC.

Table S2 Elements composition analysis in AQ/CC.

Element	C	O	Na	Mg	Al	Cl	Ca	Ti	Zn
Atomic %	73.01	27.22	0.08	0.02	0.18	0.06	0.02	0.05	0.04
Weight %	66.79	33.03	0.14	0.03	0.36	0.15	0.07	0.17	0.19

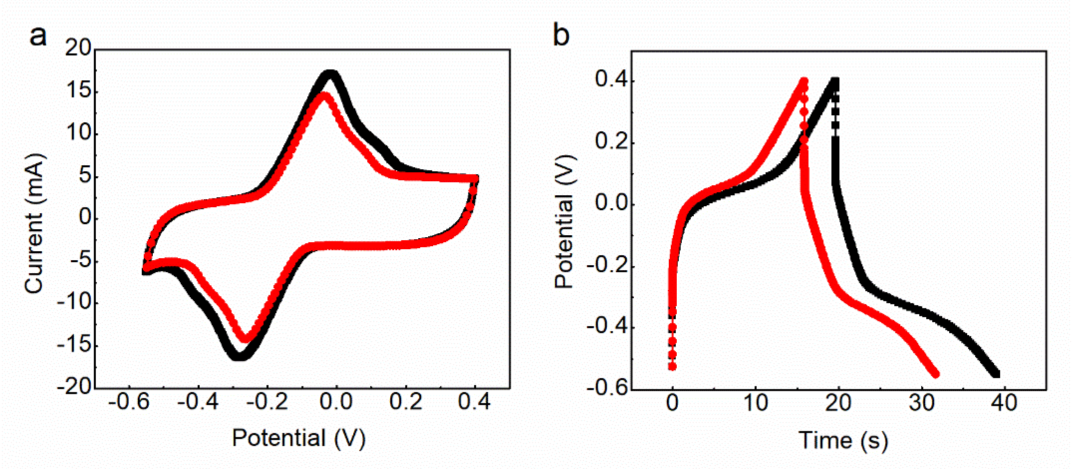

Figure S5 Cyclic voltammetry at 5 mV/s and galvanostatic charge-discharge of M/AQ/CC at 5 A/g comparisons of first (black) and 5000th (red) cycles.

Chapter 8 General conclusion

The main purposes of this thesis were to firstly apply copper ions to dope at 2D MnO_2 host. Alternatively, the growth mechanism of δ-MnO_2 was investigated and a delaminated LDH layered material was used to wrap MnO_2 particles. After that, conductive MXene was used as a substrate to grow MnO_2 coatings. Then, a series of surface engineering approaches was used design electrode materials from exfoliated graphene oxide or MXene layers by controlling the restacking issue to maximize the electrochemical performance of these 2D materials. Finally, a redox reaction, from anthraquinones, was introduced at the surface of carbon cloth to offer a fast pseudocapacitive behavior. Moreover, a MXene layer was used to inhibit the decay of anthraquinone, meantime improving the electronic conductivity.

Copper ions in suited conditions (proper concentration and temperature) can be inserted in between MnO_2 birnessite layers, consequently leading to a broader structural space, in which more active sites are exposed. The measured capacitance was 127 F g^{-1} at 0.5 A g^{-1} current density in KOH electrolyte. Interestingly, it showed 151 F g^{-1} at 2 A g^{-1} and 106 F g^{-1} capacitances at 10 A g^{-1} in Na_2SO_4 electrolytes, revealing an attractive 73% rate capability in this current density range. A manufactured device with Cu^{2+}-doped MnO_2 as positive electrode and commercial activated carbon as negative electrode offered an excellent 22 Wh kg^{-1} energy density at 450 W kg^{-1} power density.

The growth mechanism of 2D δ-MnO_2 was studied and exhibited a structural evolution process, in which the layered morphology gradually evolved as a fiber structure. However, to address the limited charge storage capability of the prepared MnO_2, it was associated to a battery-like LDH material. The latter can be delaminated by breaking weak van der Waals forces and used as a frame to wrap the spherical MnO_2 particles, thus generating a LDH@MnO_2 composite. Accordingly, it displayed 308 F g^{-1} capacitance at 0.5 A g^{-1} and kept 107 F g^{-1} at 10 A g^{-1}, while the pure MnO_2 just showed 50 F g^{-1} and 15 F g^{-1} at the same current densities. The strategy was successful to boost the charge capability of MnO_2 by a battery-like LDH material and, meantime, maintain an improved cycling stability. The supercapcacitor-battery hybrid device based on LDH@MnO_2 composite electrode and active carbon could retain 96% of its initial capacitance after 4000 charge-discharge cycles, while the device with pristine LDH electrode faded down to 42% of initial capacitance value. Meantime, the device delivered 19 Wh kg^{-1} energy density. The strategy to increase the charge capability of MnO_2 by coupling it with a Faradaic material was achieved and shown as efficient method to design composites from 2D layered materials for the fabrication of supercapacitor-battery hybrid devices.

Although the capacitance of MnO_2 can be improved in such a composite, the electrochemical capabilities are still hindered by the intrinsic limited conductivity. Hence, we applied the promising conductive MXene material as a substrate to improve the charge transfer and ions diffusion the corresponding composite materials. In the MnO_2eMXene composite, MnO_2 was embedded in/on the MXene layers. It revealed 272 F g^{-1} capacitance at 0.5 A g^{-1} current density in a three electrode system with KOH electrolytes and exhibited 93% capacitance retention after 5k charge-discharge cycles. Moreover, the composite presented an attractive rate capability in a neutral sodium-salt electrolyte. An asymmetric device was manufactured by applying a commercial activated carbon as the negative electrode and MnO_2eMXene as positive, either in alkaline and neutral electrolytes. The corresponding MeM//AC-Na device delivered 19 Wh kg^{-1} energy density and the MeM//AC-K produced 17 Wh kg^{-1} energy density at 400 W kg^{-1} power density, meantime maintaining 11 Wh kg^{-1} at 8kW kg^{-1}.

2D MXenes are known to show enhanced conductivity and great pseudocapacitance, though they suffer from the restacking issues during electrode fabrication. Thus, either hard and soft templating approaches were applied to settle the restacked flaws. First, nanosized MgO particles were employed to be trapped in between the MXene layers. A mild acetic acid was used to eliminate the nano template, therefore generating an MXene material with extended interlayer spacing. The resulting expanded and crumpled MXene showed 180 F g^{-1} capacitance at 1 A g^{-1} and displayed 99% retention after 5k charge-discharge cycles in KOH electrolytes. Furthermore, urea was used as green molecular template to craft a MXene foam material possessing a uniform porous framework, opening up a tridimensional space for ions diffusion. Thanks to this breaking of the spacial limits for ions diffusion, an attractive specific capacitance of 203 F g^{-1} at 5 A g^{-1} current density was obtained and it still exhibited 125 F g^{-1} at 20 A g^{-1}. The cycling steady MXene foam as negative electrode was packaged in the Swagelok device with 2D MnO_2 positive electrode in K$^+$-alkaline electrolytes. The resulting MF//MnO_2 asymmetric device showed a good cycling stability and generous energy density of 16 Wh kg^{-1}/10 Wh L^{-1}.

A freestanding reduced graphene oxide film was synthesized by reduction of exfoliated GO in hydrazine. In a three-electrode setup, the capacitive electrode delivers 127 F g^{-1} at 0.5 A g^{-1} and still retains 73 F g^{-1} at 20 A g^{-1}. On the other hand, the self-assembled graphene hydrogel, forming pores after urea decomposition, reveals improved capacitance and rate performance. In addition, the freestanding graphene film can be obtained by a simple heat-treatment approach, in which various temperatures were proceeded to induce a crystalline-shaped evolution. Accordingly, the graphene film, treated at 400 °C, displayed 415 F g^{-1} capacitance at 1 A g^{-1}, as well as a good cycling stability. Based on the easy method to prepare freestanding reduced graphene oxide films, the 2D MXene was introduced to synthesize a self-supported MXene-graphene composite. The composite showed decaying electrochemical performance while increasing the ratio of MXene, but still held a high capacitance at high current density and displayed fair rate capability just like raw graphene film.

Organic salts, having a battery-like redox behavior, were used to boost the electrochemical performance of a carbon-based capacitive material. Thus, anthraquinone was absorbed onto carbon cloth thanks to non-covalent π–π interactions. However, the organic salt shows a limited conductivity and are not stable upon charge/discharge processes. Aiming to solve the above issues, a coating made of exfoliated MXene was deposited on the surface of the 3D framework of organics/carbon cloth. MXene not only enhanced the conductivity for electrons transfer but also facilitate ions diffusion thanks to the reserved cracks in the coating. It thus resulted in greater capacity, meanwhile, improved cycling lifespan.

Perspectives

The thesis is focusing on the development of 2D materials, in which the reported materials with layered structures are modified, tailored and designed to allow to improve electrode materials for supercapacitors. However, there are still many projects and perspectives to be furthermore studied and understood.

In copper-MnO_2 based projects, the copper situation/role is needed to be investigated during charge-discharge processes. Obviously, the introduction of copper ions changed the surface morphologies of MnO_2 layers but they could be involved in redox reactions and act as active sites. Moreover, the variation of the Mn/O ratio after the copper doping is shown in the EDX measurements, suggesting Mn vacancies to be generated because of the intercallation of copper cations in the interlayer space. The vacancy case should be further investigated by in-situ measurements, like Mn K-edge X-ray absorption near-edge spectroscopy (XANES) or X-ray photoelectron spectroscopy (XPS). And, the pseudocapacitive mechanism of charge storage in M-1 is not clear in the present. Additionally, the rate capability of M-1 in KOH electrolytes is not as good as in neutral electrolytes. Moreover, the decay of capacitance was observed in both three-electrode systems and devices. The associated reasons should be figured out in the future.

In chapter 3, the LDH@MnO_2 was designed and fabricated by electrostatic interactions between negatively charged LDH layers and positively charged MnO_2 particles to get a composite material that possesses the high specific capacitance of pure LDH and the extended durability during charge-discharge processes. However, a greater energy density is needed before incorporation in a hybrid device and the battery and pseudocapacitive contributions to the mechanism of charge storage in LDH@MnO_2 is not clarified. During the charge storage process, the battery-behavior LDH was triggered by the redox reactions that promote some phase changes as evidenced by the potential plateau observed in charge-discharge curves. In the meantime, some redox reactions were also taking place in the pseudocapacitive MnO_2 but without any phase change. Therefore, there are many electrochemical reactions to be studied during the charge/discharge processes in these systems, which can lead to more detailed information to construct the enhanced composite electrode materials.

To upgrade the conductive property of MnO_2, the 2D layered MXene was used as a base to support a flaky MnO_2 deposit. In three-electrode system, the MnO_2eMXene composite retained an attractive cycling stability, while the longevity in the asymmetric device presented a sluggish fading. We proposed that the increase of ohmic drop caused the low energy efficiency and resulted in the observed decay. However, there possibly are other reasons to provoke this fading, such as the structural changes or phase transformation, which could be explored by in-situ measurements. In addition, a broader voltage window was obtained in neutral electrolytes in comparison with that in alkaline electrolytes, thus leading to a greater energy density. However, the energy density trend in KOH electrolytes exhibited a flatter line than that in Na_2SO_4. This related reason should be analyzed and explained more details from the different charge mechanism with two electrolytes.

In chapter 5, the stacked issue was settled by template methods, thus structuring the expanded MXene and MXene foam. The expanded MXene with the larger interlayer spacing can offer efficient 2D path for ions transport, while further work about adjusting the various d-spacing to match and accommodate different electrolytes (neutral or acidic electrolytes, organic electrolytes and ionic liquids) could be explored for fabricating enhanced MXene-based supercapacitors. Additionally, although the freestanding MXene foam presented remarkable performance, the host is fragile because of its thickness and tridimensional open structure (fragile as a foam). The applied strategy would be to decrease the total quantities to generate thinner film while keeping the steric effects, furthermore shortening the ions transport route and boosting the capacitance performance. On the other side, the charge storage mechanism of cations can be studied to evidence intercalation/deintercalation processes during charge-discharge.

Chapter 6 demonstrates that the capacitive performance of hydrogel can be boosted after using urea to create pores in the framework. The related morphological characterization should be studied to observe the porous structure and more electrochemical measurements should be done. We found that the capacitance of reduced graphene oxide film was improved at greater temperatures, but the reason why is still missing. The charge storage mechanism should be explored. Additionally, compared with raw reduced graphene oxide film, the introduction of MXene caused a loss of gravimetric capacitance. More measurements should be done to explain it, and, in the future, more work should be planned to improve the composite performance.

In chapter 7, we proposed that the conductivity could be improved by coating a MXene layer also playing a protective role but more physical measurements should be provided. Beside promoting the conductivity and facilitating ion diffusion, we have to figure out the mechanism of charge storage at the interface between electrolyte and electrode, which shows both capacitive and battery-like behaviors. At the microscopic scale, work should be focusing on probing the effect of MXene during the charge-discharge cycling process. More in situ tests should be done for that purpose.